DAMAGE INITIATION, PROGRESSION AND FAILURE OF POLYMER MATRIX COMPOSITES DUE TO MANUFACTURING INDUCED DEFECTS

A Dissertation

by

KHAIRUL ALAM CHOWDHURY

Submitted to the Office of Graduate Studies of
Texas A&M University
in partial fulfillment of the requirements for the degree of

DOCTOR OF PHILOSOPHY

May 2007

Major Subject: Aerospace Engineering

DAMAGE INITIATION, PROGRESSION AND FAILURE OF POLYMER MATRIX COMPOSITES DUE TO MANUFACTURING INDUCED DEFECTS

A Dissertation

by

KHAIRUL ALAM CHOWDHURY

Submitted to the Office of Graduate Studies of
Texas A&M University
in partial fulfillment of the requirements for the degree of

DOCTOR OF PHILOSOPHY

Approved by:

Co-Chairs of Committee,	Ramesh Talreja
	A. Amine Benzerga
Committee Members,	Vikram K. Kinra
	J. N. Reddy
Head of Department,	Helen Reed

May 2007

Major Subject: Aerospace Engineering

ABSTRACT

Damage Initiation, Progression and Failure of Polymer Matrix Composites due to Manufacturing Induced Defects. (May 2007)

Khairul Alam Chowdhury, B.S., BUET (Bangladesh);

M.S., The University of Alabama

Co–Chairs of Advisory Committee: Dr. Ramesh Talreja
Dr. Amine Benzerga

In polymer matrix composites (PMCs) manufacturing processes can induce defects, e.g., voids, fiber misalignment, irregular fiber distribution in the cross-section and broken fibers. The effects of such defects can be beneficial or deleterious depending on whether they cause failure suppression or enhancement by localized deformation processes e.g., crazing, shear yielding and fiber-matrix debonding. In this study, a computational approach is formulated and implemented to develop solutions for general boundary-value problems for PMC microstructures that accounts for micromechanics-based constitutive relations including fine scale mechanisms of material failure. The defects considered are voids, and the microstructure is explicitly represented by a distribution of fibers and voids embedded in a polymer matrix. Fiber is modeled as a linearly elastic material while the polymer matrix is modeled as an elastic-viscoplastic material. Two distinct models for the matrix behavior are implemented: (i) Drucker–Prager type Bodner model that accounts for rate and pressure-sensitivity, and (ii) improved macromolecular constitutive model that also accounts for temperature dependence, small-strain softening and large-strain hardening. Damage is simulated by the Gearing-Anand craze model as a reference model

and by a new micromechanical craze model, developed to account for craze initiation, growth and breakdown. Critical dilatational energy density criterion is utilized to predict fiber-matrix debonding through cavitation induced matrix cracking.

An extensive parametric study is conducted in which the roles of void shape, size and distribution relative to fiber in determining damage initiation and evolution are investigated under imposed temperature and strain rate conditions. Results show there are significant effects of voids on microstructural damage as well as on the overall deformational and failure response of composites.

To my father and my two sons, whom I lost during my Ph.D. studies

ACKNOWLEDGMENTS

First and foremost, I would like to pay deep gratitude to Allah and my parents for all endeavors in my life.

I would like to express my sincere thanks to my co-advisor, Dr. Ramesh Talreja, for his financial support and guidance throughout my Ph.D. studies. I would also like to express my sincere thanks and gratitude to my co-advisor, Dr. Amine Benzerga, not only for his wisdom and rigorous guidance but also for being my example of a brilliant hardworking scientist. Special thanks to my committee members: Drs. Vikram Kinra and J. N. Reddy for their contributions to my education and research. I also wish to thank Drs. A. Muliana and S. Lau for substituting for one of my committee members at the preliminary examination and final defense, respectively. Special thanks are due to my friend Gary Seidel for his support and all the scientific discussions. Special acknowledgement are due to my devoted friends Mr. Deepak Goyal, Mr. Guruprashad, Mr. Dawood Asad, Mr. Chandraveer Sing, Mr. Shantanu, Ms. Rebecca Stout, Mrs. Sara Khan and Mr. Zahid Afzal.

I deeply thank my wife, Shaila Khan, for her love and for helping me to overcome all the difficulties I faced during these years. I am grateful to her for all that she did for me.

Finally, I would like to acknowledge Karen Knabe for her administrative help.

TABLE OF CONTENTS

CHAPTER Page

CHAPTER Page

LIST OF TABLES

LIST OF FIGURES

FIGURE Page

FIGURE Page

FIGURE Page

FIGURE Page

FIGURE Page

FIGURE Page

FIGURE Page

CHAPTER I

INTRODUCTION

Polymer matrix composites has been gaining importance in aerospace and automotive applications due to their unique directional properties and weight saving potential. Increased use of polymer based composites has prompted extensive research for predicting their short term and long term performance as structural components. The scope of the research is to develop a methodology for structural design that include the fundamental knowledge of fine scale mechanisms of material failure. The specific material system addressed is polymer matrix composite. The aspects of modelling claimed to be novel are (i) the explicit incorporation of manufacturing induced voids into the analyses of polymers reinforced with oriented elements of relatively stiff elastic material; and (ii) the incorporation of matrix behavior at governing scales of physical mechanisms, which constitutes a first step toward characterizing damage in polymer-based composites. The material models utilized are sophisticated model needed to capture the essential molecular physics related to these mechanisms and therefore possess the predictive capability concerning localization and failure.

The significance of the research work will be the contribution to the advancement of capabilities essential to the prediction of damage initiation, progression and failure in polymer matrix composites as well as the assessment of manufacturing processes, their trade-offs with performance, and ultimately, to the design of cost-effective structures. The associated benefit of the conducted research will be an enhanced understanding of the physical mechanisms of deformation, localization and failure, which together will allow development of more advanced polymers and their composites.

The journal model is *IEEE Transactions on Automatic Control.*

A. Motivation

1. Processing-Structure Relationship

The research done here is a focused effort within the overall strategy of designing cost-effective composite structures. The result of the research can be utilized in developing acceptance/rejection criteria for a manufactured part.

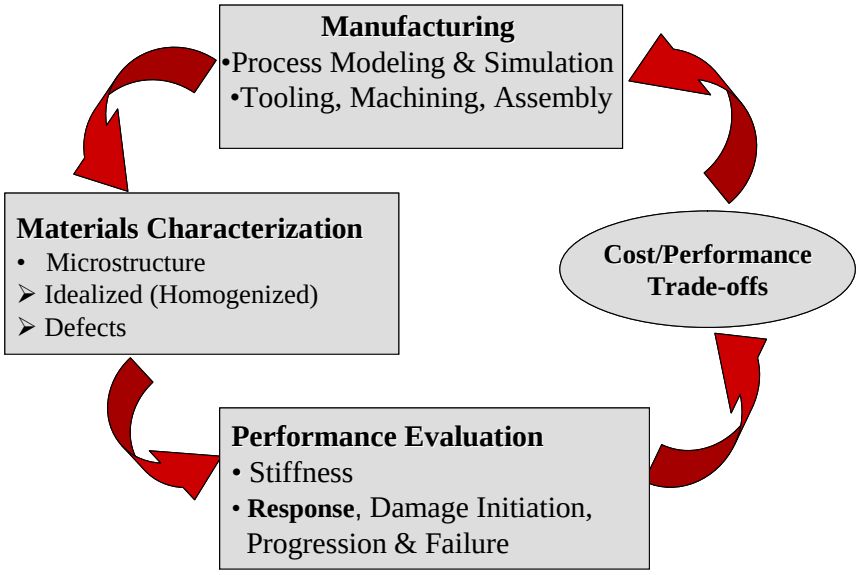

Fig. 1. The iterative process of cost-effectiveness assessment.

Figure 1 shows the elements involves in the process of making cost-effectiveness analysis of composite parts. First a given composite structure is characterized in terms the manufacturing processing parameters (e.g., temperature, pressure, and their time variations) as well as descriptors of machining, tooling, joining and assembly, as needed. Then, the manufactured part is described in terms of the composite microstructure and their corresponding properties. Conventionally, any composite microstructure are characterized in terms of the volume fractions of the constituents,

and of the fiber architecture, e.g., ply thickness, orientation and stacking sequence in a laminate, etc. But a composite structure, manufactured by any practical process, does not come out fully free of defects. There is a variety of manufacturing processes for composite structures, e.g., autoclave molding, compression molding, resin transfer molding, filament winding, chemical vapor deposition, etc. Defects are produced in the manufactured part from each of these processes that are usually attributes of that process. The defects induced by manufacturing can be in the fiber architecture, e.g., fiber misalignment, irregular fiber distribution in the cross-section and broken fibers; in the matrix, e.g., voids; and in the interfacial regions, e.g., disbonds and delaminations. Therefore, it is very important characterize composite structure by incorporating the defect state description (i.e. distributions of fiber misalignment and position, void size and location, fiber/matrix interfacial disbonds, delamination size and location, and any other defects of interest) with the conventional composite microstructure description for assessing manufacturing process.

Continuing the cost-effectiveness analysis with the characterization of the real material, the next step is to obtain material performance under loading condition that includes the changes in the material properties, overall response and failure under loading conditions. The manufacturing induced defects, discussed above, also have an major influence on damage initiation, progression and overall performance of composite structure which can be beneficial or deleterious.

Finally, the cost/performance trade-off, placed in the last box, in the manufacturing process assessment, is to evaluate the cost against the performance achieved. The trade-off between the cost and performance then provides an optimally affordable product.

To date, extensive efforts have been restricted to the effects of these defects on the composite stiffness and strength. Not many analyses have focused on the effects

of the defects on the mechanisms of failure in composites, which has important impact on cost-effectiveness of a composite structure. Our research is focused on performance evaluation of the composite structures with manufacturing induced voids.

2. Voids in Composites

The role of manufacturing induced defects is the key to satisfying the performance requirements while minimizing cost. The entire field of defect dependent structural performance is large and in a given application not all of it may be of critical importance. We focus on voids in this research as this class of defects is integral to the manufacturing processes using polymers and since voids form nucleation sites for localization of deformation and ensuing damage and failure. Voids are found in virtually all composite structures, whether matrix is thermoset [8] or thermoplastic [9]. The formation of voids is controlled by many manufacturing parameters, such as vacuum pressure, cure temperature, cure pressure and resin viscosity [10]. The presence of voids, even at low volume fractions has been found to degrade material properties [11]. Furthermore, more recent studies have shown that the properties are influenced by void size, shape and distribution in addition to the volume fraction. Thus at the same void volume fraction significantly different property reduction was found depending on the manufacturing process [12].

3. Effects of Voids

Harper [13] studied the effects of voids on the hygral and mechanical properties of AS4/3502 graphite/epoxy composite. Harper reported that void has significant influence in reduction of transverse and shear modulus. Bowles [14] studied the effects of void on the interlaminar shear strength of unidirectional Graphite-fiber- reinforced composites. Judd and Wright [11] experimentally showed that reduction of flexu-

ral, tensile, torsional shear, interlaminar shear and impact strength up to 30%, 3%, 9%, 7% and 8%, respectively for a void content as low as 1%. Suarez et al. [15] reported a 10% reduction of compressive strength per 1% increase of void volume fraction. Varna et al. [8] investigated the effect of void content and geometry on the macroscopic transverse mechanical behavior of unidirectional GF/VE fabric laminates. They found that low void content require higher stress, lower strain for failure but failure occurs in brittle manner. There are analytical models for predicting elastic properties in the presence of voids, which rely mostly on approaches that treat voids as inclusions having zero properties, see [16], [17] and [18] for reviews. These approaches do not account for void size, shape and distribution. Farouk et al. [19] used the Mori-Tanaka method based on the Eshelby tensor with voids as a distinct phase in addition to fibers and matrix. This approach allowed an account of the void length in the fiber direction. Further account of the void size and shape was made by Gowayed et al. [20] for voids of fixed geometry, also using the Mori-Tanaka method. These approaches is to consider only the initial properties and relate these to the material defects (microstructure). The changes in material properties do not always relate to the material defects the same way as the initial properties do. In fact, the initial properties may not show sensitivity to some of the material defects that may be significant when subjected to loading condition. Generally speaking, approaches of this nature fail to account for the fact that voids are not embedded in a homogeneous material but rearrange the local microstructure, e.g. by displacing fibers locally. Accounting for this was done by a computational method in Huang & Talreja [21], where displaced fibers around voids were modelled by varying the effective composite properties locally. Void shape and size were accounted for in a parametric study and the predictions of elastic moduli were found to agree well with experimental data. Most of the work described above involving in investigating the

effect of void are limited to stiffness degradation, there are very few work [8, 9, 22, 23] devoted for studying damage initiation and propagation of composites because of the presence of the manufacturing induced voids. Varna [8] et al. reported that void content effects the overall response of composites under transverse loading. Chamber et al. [23] reported the effect of voids in the initiation and propagation of static flexural and flexural fatigue failures of unidirectional carbon fibre composite. Though there is few experimental effort to understand damage initiation and evolution in the composite micro-structures with void, there is a little or no computational effort involving micromechanical analysis to investigate mechanism of damage initiation, progression and final failure of polymer based composites.

Among all the defects the voids are most detrimental for the sound performance of composites. Although a composite may display elastic response globally in the presence of voids, it can undergo inelastic deformation locally around voids. The inelastic deformation acts as a precursor to initiation of damage, which occurs through different mechanisms that are complex and usually involve interaction between micro-constituents and irreversible change of microstructure resulting from the application of thermo-mechanical loading. The damage in turn depends on the polymer molecular morphology, which generates crazing, fibrillation and local fracture. To capture these processes in a continuum model is a challenge, in particular when the model is to be used in a numerical simulation of initiation and progression of damage and that have a major influence on accurate prediction of deformation response and failure process of composite materials.

4. Research Approaches

One approach to address the effects of voids on damage initiation, propagation and failure of composite would be to develop a continuum constitutive model by incor-

porating a damage model into a viscoplastic model for the composite. There are a number of viscoplastic models available to date. Elasto-viscoplastic constitutive models for composite continuum to investigate overall response of several types of composite structures have been developed by [24–34]. The effect of voids could be included in the viscoplastic constitutive equation using homogenization. Then by incorporating damage model it would be possible to provide a framework to describe overall damage progression in the composite including material stiffness degradation. Kachanov [35] and Rabotnov [36] originated the framework of continuum damage mechanics (CDM), with this framework the deterioration of composite material results from the progression of a continuous damage variable can be obtained. The basic idea of the CDM approach is to express the overall response by incorporating the effects of damage. Figure 2 shows the schematics of the approach, where the stationary (e.g., fibers) microstructure of the composite material is first smeared into a homogeneous, anisotropic medium, then the evolving microstructure e.g., damage entities are represented by suitable internal variables and smeared into the previously homogenized field.

Chaboche et al. [37] pioneered the continuum damage mechanics approach for accounting the effect of ductile damage, creep damage and fatigue damage by developing thermodynamically consistent model. Talreja [38–40] incorporated damage (mainly due to fatigue) in the material response function as a set of vectorial damage variable. Fish [41] developed a continuum damage model using mathematical homogenization by introducing a double -scale asymptotic expansion of damage variable. Later Li et al. [42], Boutaous et al. [43] and Lannucci [44] further extended this technique by incorporating inelastic response of the matrix and applied to a variety of composite structures.

However, the major limitation of the CDM approach resides in its inability to

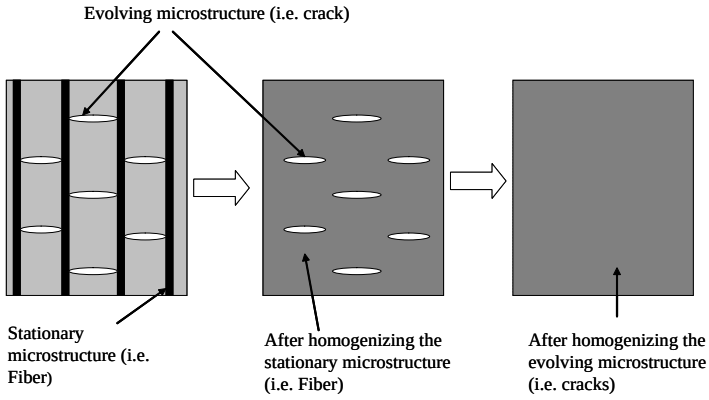

Fig. 2. Steps of continuum damage mechanics.

resolve localized modes of deformation especially when the mechanism (e.g. crazing and shear yielding for polymer matrix) of damage initiation and progression is poorly understood. Also the constraints and the interaction of the stresses/strains between each micro-phases in a lamina cannot be accounted for due to microphase homogenization. Also most CDM models are phenomenological model, which are not general enough to be applicable to different types of constitutive characteristics of composites because overall response is predicted for a particular set of constitutive and geometric characteristics of composite structures.

Prediction of damage is also addressed by Hashin [45, 46]; Yamada-Sun [47]; Shahid-Chang [48, 49]; Christensen [50]; Chandler et al. [51]. They developed failure criteria based on an average maximum stress and strain criteria for matrix failure. None of these models incorporate the basic mechanisms of damage initiation and progression by shear yielding or crazing in polymer matrix.

Generally shear yielding and crazing are the main localized deformation mechanisms at the fine scale. Ductile failure by shear yielding occurs by the formation

of shear bands due to intrinsic strain softening. Brittle failure preceded by crazing due to dominance of hydrostatic stress. The initiation and progression of damage in polymer is affected by the presence of voids and controlled by the fine scale physics of polymer deformation and fracture. Thus the deformation behavior and damage of a polymer matrix composite occur from localized deformation process, are essentially multiscale phenomena. Therefore at the macroscopic level it is very difficult to compute local stress-strain field and to capture the complicated mechanisms of failure using homogenized model.

Envisaged with such limitations of CDM model and fracture type we sought to follow a direct multiscale computational approach that employs large strain finite element computation to address such issue of inelastic constitutive behavior, irregularly shaped, randomly oriented fibers/voids and cracks by representing the microstructure explicitly by a distribution of fibers and voids, embedded in a polymer matrix. The field of approach permits to predict damage initiation and growth in a way (capturing damage at fine scale and predicting overall response at macroscopic scale) CDM would not, which will be very useful to guide the development of improved continuum damage model.

B. Literature Review

1. Deformation Behavior of Polymers

In an effort to understand the initiation and evolution of damage in polymer matrix due to manufacturing induced voids in composites, the deformation and failure mechanisms of polymers needed to be studied.

a. Experimental Facts

Polymers are a high molecular weight organic compounds consisting of large organic molecules formed by combining many millions of repeated linked units. From the morphological point of view polymers generally fall within two classes of molecular arrangement, e.g. amorphous or glassy polymers and semi-crystalline polymers. In the amorphous polymer at the macromolecular level polymer chains structurally oriented completely in a disorderly fashion, while in the semi-crystalline structure linear polymer chains are arranged in a uniform three-dimensional matrix. There are two major classes of amorphous polymer that are used in fiber reinforced composites i.e. thermosets and thermoplastics. Epoxy (e.g. Gr-Epoxy for aircraft flaps, rudder etc), Bismaleiemid (e.g. BMI composite, uses ranges from the Air Forces F-22 to engine parts of formula-l race cars), Bisphenol A (e.g. dental sealants), Phenolic (e.g. in naval submarines in the form of torpedo nose and tail cones, torpedo cradles), PS Polyimide, Vinyl ester (e.g. in a boat hull) etc are used in thermoset composites and Nylon 6 (e.g. in air intake manifolds of cars), Polyamide (PA) (e.g. in cycle pedals, fan blades for aircraft, nano-bio composites etc), Polybutylene terephthalate (PBT), Polyethersulfone (e.g. in PES composite membrane in bio application), Polyester (e.g. in GF/Polyester composite for dental post, in container for foods or medicine), Polysulfone (PSO-carbon fiber composites used in bio-application as in permanently implanted artificial limbs, bone plates, screws etc), Polycarbonate (e.g. in motorcycle helmets, in medical application in biocomposites i.e. arch wire and brackets, bone-plates and screws,), Polymethymethacrylate (PMMA composites in dental bridges, dental post, dental arch wire and brackets, bone cements, bone plates & screws etc, CNT-PMMA composite thin film for gas sensors), Polystyrene (PS composite in microwave substrate material) etc are used in the thermoplastic polymer composites.

Thermoset polymers consist of low molecular weight long polymer monomers, cross-linked with each other in a curing reaction which produces covalent bonds between the chains. The links between chains prevent them from sliding past one another resulting in a higher modulus. Thermoset polymer behavior shows strain rate and pressure dependent yielding [52]. Figure 3a shows quasi-static and moderate

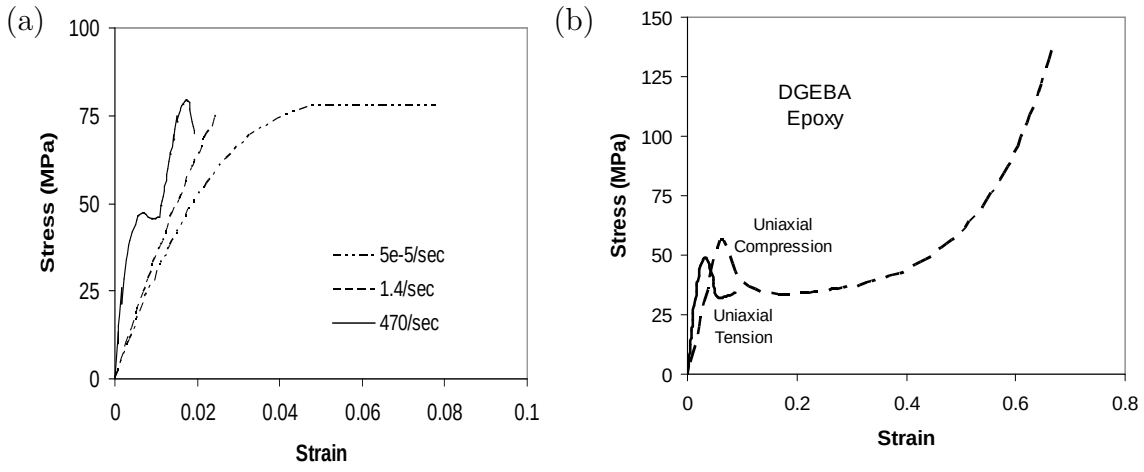

Fig. 3. (a) Effect of strain rate on stress–strain response under tension for Epoxy resin at room temperature [1]. (b) Large strain response of a DGEBA epoxy under uniaxial tension and compression at room temperature [2]

strain rate responses under uniaxial tension of PR520 epoxy resin. After yielding thermoset polymer exhibits isotropic hardening followed by saturation of hardening. Many typical commercial epoxies i.e. Diglycidyl ether of bisphenol-A (DGEBA) exhibit immediate strain softening followed by large strain hardening after reaching the peak yield stress [2, 53, 54]. Figure 3b shows that the response of uniaxial compression and tension of a DGEBA epoxy (LY556) exhibit strain softening and large strain hardening behavior.

However, thermoplastic polymers consist of high molecular weight long monomers

whose chains associate through weak van der Waals forces. The chains are free to slide past one another when sufficient thermal energy is supplied, resulting in ductile behavior. Depending on chain organization in the microstructure, thermoplastic polymers can be amorphous or semi-crystalline. The amorphous polymers exhibit rate, temperature and pressure sensitive flow.

The flow properties of polymer are strongly dependent upon strain rate, and this relationship is dependent on material characteristics including composition, molecular weight and thermal history. For amorphous polymers the yield strength is essentially linearly dependent on strain rate at a given temperature [3, 55]. Figure 4 shows the strain rate dependence on the polymer response for PMMA at T= 90^oC. Figure 5

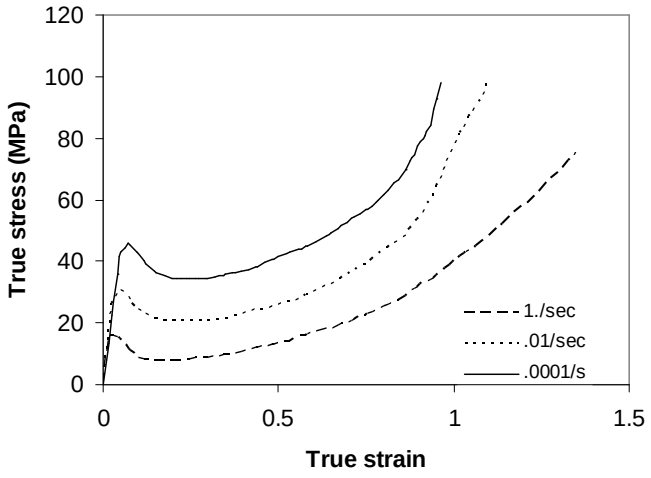

Fig. 4. Effect of strain rate on stress–strain response under uniaxial tension for PMMA at T= 90^oC [3].

shows the temperature dependance on the polymer response for PC. Ferry [56] reported from his experiments, which validated the dependence of yield stress with temperature. For a given strain rate, a given set of material constants and at suffi-

ciently low temperature(i.e. less than glass transition temperature T_g) the yield stress of amorphous polymers decreases approximately linearly with increasing temperature, and large drop of yield strength is observed after polymer reached above sufficiently high temperature (i.e. more than the T_g) [55, 56].

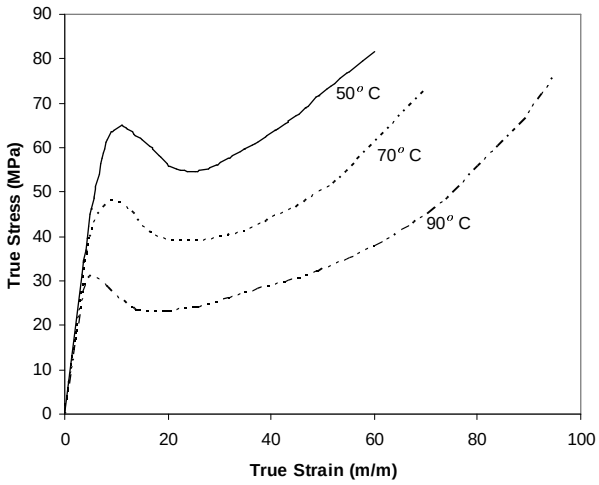

Fig. 5. Effect of temperature on uniaxial tension response of PMMA at a strain rate of 0.005/s [3].

With regard to pressure dependence Rabinowitz et al. [57], Sauer et al. [58], and Spitzig et al. [4] showed experimentally that the peak yield stress is linearly dependent on pressure for moderately large hydrostatic stress. Figure 6 shows effect of hydrostatic pressure under compression for Polycarbonate. Effect of Pressure is also observed (shown in Fig. 7) from tension and compression experiment conducted by G'Sell et al. [5]

At large strain the plastic flow in amorphous polymer occurs by overcoming two molecular resistance mechanisms [59]. Below glass transition temperature, prior to peak yield, amorphous polymer chains have to overcome intermolecular resistance to

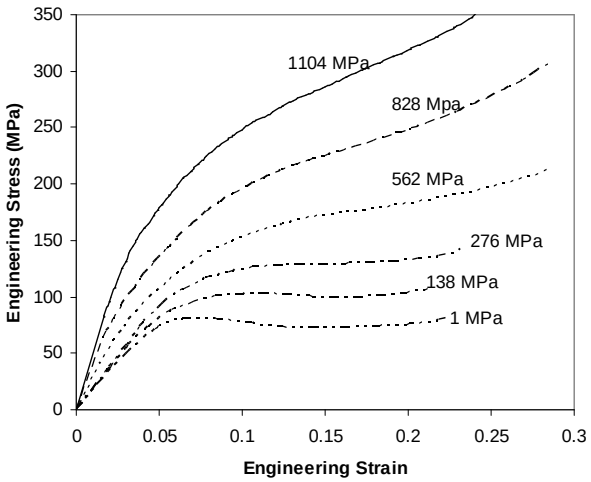

Fig. 6. Effect of pressure on stress–strain response under compression at room temperature and a strain rate of 7×10^{-4}/s for Polycarbonate (PC) [4].

segment rotation, after material begins to flow, causing the polymer chains to orient themselves in an affine manner that causes changes in configurational entropy, leading to anisotropic resistance to further inelastic deformation [55, 59]. Thermoplastic glassy polymer exhibits small scale nonlinear viscoplastic behavior before it reaches to peak yield due to evolution of free volume at the fine scale [60]. After the peak yield and before anisotropic orientational hardening the amorphous polymer undergoes intrinsic strain softening [55,61]. Intrinsic strain softening occurs when molecular chains rearrange them in a certain structure after polymer starts to flow plastically, causes actual drop of true stress, which may be accompanied by a band of localized inhomogeneous deformation i.e. shear banding [55]. Lu-Ravichandar [62] argued that drop of true stress is due to local inhomogeneous deformation (i.e. formation of neck during tension) within structure rather than intrinsic material softening. Ravichandar and coworkers [63] also performed uniaxial and confined compression test and

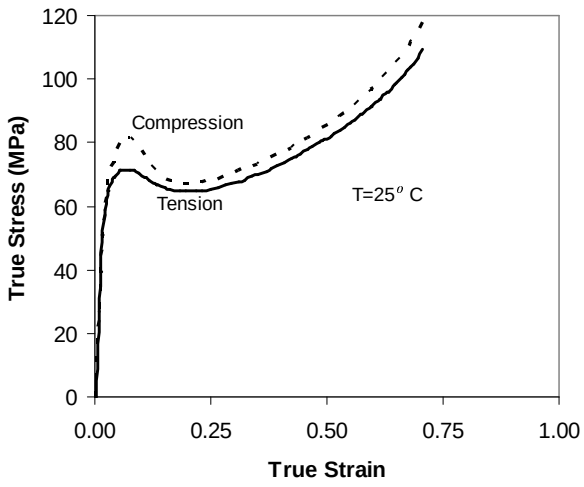

Fig. 7. True stress vs true strain response under compression and tension for PC at a strain rate of $1.7 \times 10^{-}3/\text{s}$ and room temperature [5].

showed that for the confined compression case strain softening does not occur. However, Spitzig's [4] compression experiment under different pressure (see Fig. 6) showed that under high pressure, response shows no strain softening indicates that Ravinchander's observation of no strain softening is because of the pressure effect due to the confined compression. However, Arruda et al. [6, 64] performed plane strain compression and uniaxial compression test for PC and observed homogenous deformation at very large strain for both the cases, which showed the drop of true stress without any localized deformation zone in the specimen. This observation offers more certainty in favor of the notion of intrinsic softening of polymers. The peak yield stress in plane strain compression is higher than in uniaxial compression because of the pressure dependence of the yield, which is the direct effect of the constraint applied by plane strain condition [6, 64]. Figure 8 shows the true stress-true strain response in uniaxial compression at constant strain rate with that in plane strain compression.

For both of these loading conditions strain softening occurs after yielding, followed by strain hardening. Under plane strain compression, the strain hardening progresses more rapidly with plastic deformation than under uniaxial compression. Because under uniaxial compression at large deformation polymer chains are free to align along any directions perpendicular to loading direction but for the plane strain condition free alignment of molecular chains occurs along only a single direction. Also, before

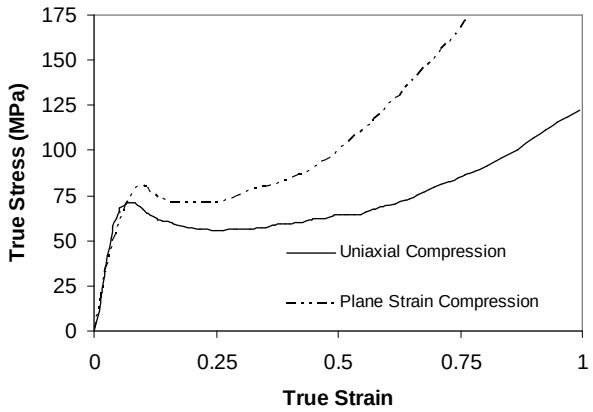

Fig. 8. Experimentally determined stress-strain response under uniaxial compression and plane strain compression for PC at a strain rate of 0.001/s and room temperature [6].

reaching peak yield point glassy polymer exhibit nonlinear isotropic hardening type plastic behavior [65–67]. Anand and Gurtin [66] stated that this nonlinear pre-peak yield behavior is due to the evolution of the local free–volume associated with the metastable state of these polymers.

Thus, the finite deformation response of amorphous polymers, such as thermoplastics, is characterized by rate, pressure and temperature sensitive yielding, pre–peak yield non-linear behavior, followed immediately by post yield behavior through intrinsic strain softening and, at large strains, by increasing strain hardening. The

small-strain softening behavior is inseparably connected with yielding by way of the molecular mechanisms of macroscopic yielding [61]. At the fine scale, yielding accompanied by small scale inhomogeneous deformation appears in the form of multiple narrow shear bands, and is usually referred to as "shear yielding". The increasing strain hardening behavior due to anisotropic resistance at large strain is associated with the stretching of the network of molecules between entanglements and the simultaneous development of a preferred orientation of the molecular chains.

b. Models

In order to model inelastic response of any material, two phenomena have to be considered i.e. i) yielding 2) post yield inelastic behavior of material. Yielding can occur at different stress state so, a criterion for prediction of yield may be a function, which is combination of the stress components. The von Mises and the Tresca yield criteria are two well known criteria for yield. According to Tresca, "yielding occurs when the resolved shear stress on any plane in the material reaches a critical value". The von Mises criterion states that yield will occur when the energy of distortion reaches a critical value for yield in uniaxial tension. Mathematically when the second invariant of the deviatoric stress tensor J_2 reaches a critical value yielding occurs. The Mohr-Coulomb criterion is another yield criterion, originally developed for soil plasticity, which has been used occasionally for polymer. According to the Mohr-Coulomb criterion yielding occurs if the shear stress on any plane in the material reaches a normal stress dependent critical value. But yielding of polymers is essentially hydrostatic stress dependent, so by utilizing these criteria without modification will not be useful to predict polymer yield. One modification could be adding a the pressure term and taking a linear variation of the pressure term in the von Mises yield function. The modified von Mises criterion is also known as Drucker-Prager yield criterion. Rottler-

Robbins [68] investigated different yield criteria by conducting molecular dynamics simulations of deformation in amorphous polymer glasses under triaxial stress states, and observed that the pressure-modified von Mises criterion has the better prediction of the onset of yielding, with the pressure coefficient nearly independent of many parameters.

Observed macroscopic yield behavior can be explained in terms of the change of detail molecular structure during yielding, which is known as Molecular theory of yielding. Among those theories, state transition theories developed by Eyring [69] is the earliest, which states that yielding occurs if molecular segments jumps from one equilibrium point to another. Duckett et al. [70] further refined this model by incorporating pressure sensitivity. Conformational change theory by Robertson [71] and Brereton [72] is based on the idea that the plastic flow of the polymer occurs as a sequence of change of molecular configurational or jumps governed by some kind of activated process. Bauwens [73] and Rush & Beck [74] developed a model based on the free volume theories, which states that yielding occurs when molecular structure reaches some critical free volume to flow plastically; dislocation theories by Bowden & Raha [75] describes yield stress as a critical stress for the formation of dislocation; segmental motion theories by Stacharuski [76] based on the idea that polymers deform by the transfer of rotational motion of the segments of polymer chains. Argon [59] developed a molecular model that states that yielding occurs when applied energy on the material overcomes the critical energy required to produce rotation of chain segments against the surrounding elastic medium.

A significant advance in modelling post-yield behavior, e.g. softening and orientational hardening of thermoplastic amorphous polymer has been made by Haward-Thackrey [77] , Argon-Boyce and their coworkers [55, 59, 78], Anand and Gurtin [66], and Wu and van der Giessen [79]. Haward and Thackrey developed a one dimensional

continuum model, by using the Eyring dashpot model to describe yield and Langevin spring model for the description of the post yield orientational hardening behavior. Argon [59] incorporated rate dependence in the Haward-Thackrey's model for post yield behavior. Later Boyce-Park-Argon [55] improved the model by incorporating pressure sensitivity, three dimensional effect, finite strain kinematics and classical three chain rubber elasticity model to describe the orientational hardening. This model will be referred to as macromolecular model. Wu-Gissen [79] refined Boyce's model by improving the orientational hardening by considering a statistical combination of three chain and eight chain rubber elasticity model. Anand-Gurtin [66] developed a continuum elasto-viscoplastic model for amorphous polymer to describe the rate, pressure and temperature dependent yield by introducing internal state variable for accounting for the pressure sensitivity related to the local free volume connected to certain metastable state.

Goldberg and his coworkers [80, 81] developed state variable constitutive equations, originally developed for metals [82], which have been modified for modelling strain rate and pressure dependent deformation of thermoset polymers. Their model combines pressure sensitivity of Drucker-Prager type and viscoplastic flow rule consisting of a state variable to describe isotropic hardening. This model will be referred to as DPB model.

2. Fracture in Polymers

a. Experimental Facts

In polymer local inelastic deformation act as a precursor to damage initiation and subsequent propagation, which occurs through irreversible change of microstructure through different complex mechanisms (i.e crazing, shear yielding). Ductile fracture

occurs by the formation of shear band or necking due to intense localized plastic deformation. Shear bands occur due to plane strain compression because of post-yield softening. Shear band may appear in two different ways [83]. When shear band has large width and has distinct boundary between sliding and surrounding area then it is called coarse shear band and fracture occurs along the deformation band. Shear band composed of fine multiple shear bands is identified as diffuse shear band, in this case fracture appears by forming a large kink [84]. For plane strain tension ductile fracture occurs through the formation of intense localized plastic deformation band, followed by necking.

Craze induced macroscopic brittle fracture is one of the fascinating aspects of fracture in both thermoset [85] and thermoplastic polymers, which has been studied in past four decades. Craze matters consist of strands of oriented micro-yielded material, known as fibrils, interspersed with micro-voids. Figure 9 shows a schematics at an advance stage of deformation of a crazed structure. Craze initiates through the nucleation of microvoids under dominance of local hydrostatic pressure. Craze initiation criterion is not well developed yet because it is very difficult to characterize the stress state at the craze initiation site at a microscopic level. Craze initiates due to the nucleation of void at a well defined temperature and presser dependent critical stress/strain [86], which is about 0.4 to 0.5 times the yield stress [87, 88]. Figure 10 shows the effect of pressure on craze initiation in PMMA plotted in principal stress space. Where 'P' denotes the pressure. The curve corresponding to $P = 0$ is obtained at T=70^{o}C under biaxial stress fields. However, curves corresponding to $P > 0$ and $P < 0$ are yield surface under imposed hydrostatic pressure and isotropic tension exhibit that craze formation is facilitated under positive pressure or tensile loading and is suppressed under negative pressure.

Craze grows due to the formation and widening of fibrils by drawing new polymer

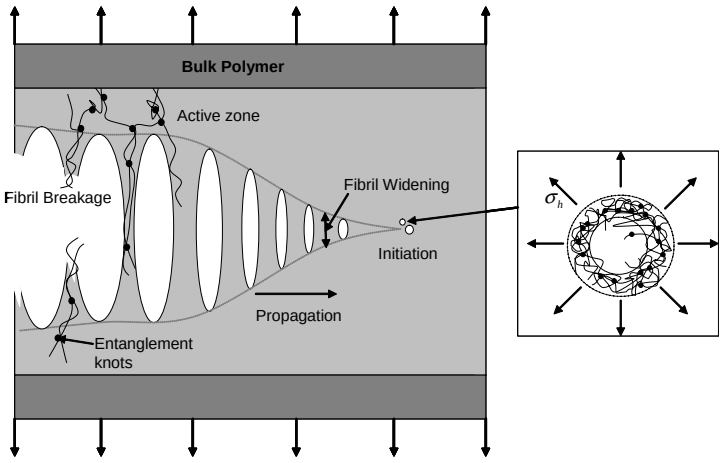

Fig. 9. Schematics of the formation and growth of a craze structure.

chains into the fibrils from the surrounding active polymer zone. Craze growth observed by experiment [89–91] suggesting that roughly cylindrical shaped craze fibrils have diameters ranging from approximately 5nm-40nm.

Finally, the craze fibrils starts to break, followed by the gradual fibril breakage that progresses perpendicular to the maximum principal stress direction and the craze structure losses the load bearing capacity accordingly. After the breakage of significant amount of fibrils the rest of the active fibrils break all together results in the formation of crack within the craze structure. Doll [92] shown by interferometric experiments breakage of craze fibrils after it reaches some craze opening displacement. Narisawa [83] suggested that fibril breakdown occurs because of formation multiple voids inside the fibril and coalescence of those voids. Kramer [91] reported that fibril breakdown starts at the interface of fibril and bulk polymer. This phenomenon is also supported by Rottler's [93] molecular dynamic simulation of craze structure. The fibril breakage may occur due to the breakdown of entanglement network either by disentanglement or scission of polymer chains [94].

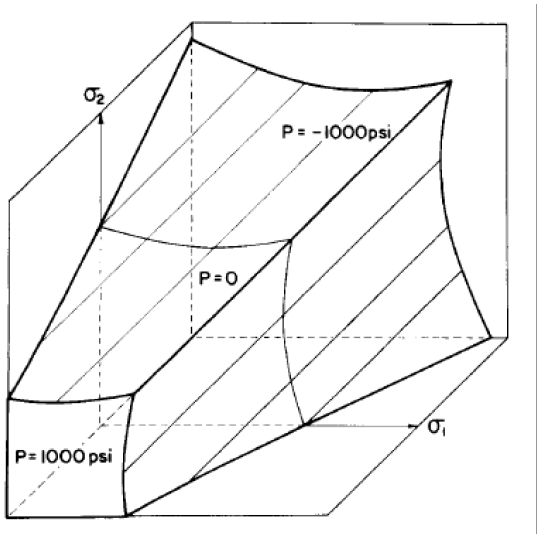

Fig. 10. Effects of pressure on craze yield surface for PMMA at T=70^{o}C [7].

Thus, craze life consisting of three distinct phases: initiation, growth and breakdown. After craze has initiated, it grows until it reaches the breakdown phase, during which the breakage of craze fibrils forms a crack. Though craze resembles crack by growing perpendicular to the major principal tensile stress, craze is not crack rather a precursor to crack because of the formation of fibrils connecting craze surfaces and its load bearing capacity due to this connection. Craze matter contains typically 40%-60% voids and widens extensionally due to elastic constraint of the surrounding undeformed polymer [86].

Argon-Hannoosh-Salama [88, 95, 96], Kramer [90]; Kinloch [97]; Williams [98] studied craze induced fracture on a linear elastic fracture mechanics framework. Estevez [99] mentioned in his work that mechanism of failure are concealed by linear fracture mechanics approach. If shear yielding occurs, this approach becomes inapplicable.

Apart crazing and shear yielding, another interesting fracture mechanism, ob-

served in the polymer matrix (especially in the interface region), is cavitation induced matrix cracking. This type of matrix cracking occurs mainly in the fiber–matrix interface region because of dominance of hydrostatic stress around the fiber region, which eventually results in fiber–matrix debonding. The interface regions within the bulk fiber and bulk matrix are created during the curing process of composite manufacture. The interface behaves harder than the bulk matrix [100]. Asp et al. [101] reported cavitation induced matrix cracking under dominance of hydrostatic stress. Under critical circumstances within the elastic regime, when deviatoric part of the stress is negligible and dilatational part is high enough to create microvoids, cavitation initiates followed by unstable growth and subsequent crack formation.

b. Models

Numerous theories and models have been developed during the last 40 years for modelling craze. One of the earliest craze initiation criterion is the stress based criterion (for planes stress condition) developed by Sternstein and Ongchin [7, 102] based on their idea that the dominance of dilative stresses increase the free volume associated with each chain, causes to increase in mobility of chain segments leading to the formation of voids and fibrils. Oxborough and Bowden [103] developed an alternative criterion of Sternstein and Ongchin's stress bias criterion for plane stress which postulates that craze initiates when maximum principal tensile strain reaches a mean normal stress dependant critical value. Argon-Hannoosh [88] developed craze initiation criterion suggested that craze initiates because of the formation of microcavity or pore due to molecular level stress concentration under influence of microshear band initiated by shear stress. Gearing and Anand [60] further modified the Bowden's craze initiation criterion from critical strain based criterion to critical stress based criterion. In which craze initiates when the maximum principal stress, mean princi-

pal stress are positive and the maximum principal stress reaches a mean stress and temperature dependant critical value.

After craze has initiated, it grows by advancing its tip due to the extension of craze periphery at a right angle to the maximum principal stress and fibril widening direction, which is the extension of the fibril length in the direction of maximum principal stress [90]. Kramer [90] postulates that craze fibrils widen due to drawing of new polymer chain, by the disentanglement of chains, into the fibril from the zone of undeformed polymer. Based on this postulates Kramer [91] developed a simple model of craze widening rate. Argon and Salama [96] developed craze widening model based on the phenomenon known as meniscus instability mechanism in which corrugated air-polymer interface appears that decreases with increase of hydrostatic tension, this interface is unstable to perturbations over a certain wavelength, and then new craze fibril are formed by repeated break up of convoluted interface and advance steadily forward. Lai-Giessen [104] developed a viscoplastic craze widening model based on Kramers postulates of craze widening, which is similar to Argon's viscoplastic model. Recently Basu-Giessen [105] and Rottler-Robins [93] also studied craze widening mechanism.

Recently continuum mechanics approach is utilized to address craze initiation, growth and breakdown. Estevez and his coworkers [99] developed an elasto-viscoplastic traction separation law, which is based on a concept of cohesive surface to model craze initiation, growth and breakdown leading to the failure by crack. Though cohesive surface technique is easy to implement, determination of parameters regarding sliding and opening of crack is difficult as crack path should be known a priori since crack can only initiate and propagate along the cohesive surface boundaries [60]. Gearing-Anand [60] adopted a viscoplastic continuum constitutive equation to represent craze initiation, widening and final breakdown. Their model switches from viscoplastic flow

rule [66] for polymer deformation to craze flow rule after craze initiation. There are two issues with this model. First, this model does not account for gradual loss of stress bearing capacity of craze structures. Second, craze breakdown is considered by sudden failure of craze structures through an empirical criterion. However, most of the craze breakdown criterion is also based on the idea that crack initiates when craze fibril breaks after reaching a critical value. Therefore, it is required to develop new model that accounts for craze initiation, craze growth process associated with fibril formation and breakdown accompanied by gradual loss of load bearing capacity and final failure of craze structure.

C. Research Outline

The objective of the research is to develop and implement a computational methodology to address the mechanical response and local state of a polymer based composite microstructure with initiation and growing damage. The implementation of the methodology requires specific plan of action, outlined below.

- The deformation behavior of polymers is implemented in an explicit finite element code.

  To assist us in the implementation of the deformation behavior of polymers, a reference model, Drucker–Prager type model is implemented that accounts for pressure-sensitive yielding [106] but rely on a relatively simple description of hardening [82, 107]. Then a physically based macromolecular model that accounts for rate, temperature and pressure sensitive yielding followed by intrinsic softening and, at large strain, increasing strain hardening. The model is based on a combination of a viscoplastic flow rule with an orientational hardening model [55] that draws upon an analogy with rubber elasticity. The compar-

ative study of the two models is conducted after the implementation. Later, the physically based macromolecular model is modified to incorporate initial viscoplastic behavior prior to peak yield.

- Polymer failure is implemented by developing continuum constitutive model for craze initiation and growth.

  Since failure in polymer matrix can occur either by ductile fracture through formation of shear bands or by craze induced brittle fracture, the formation and evolution of shear bands are a natural outcome of the macromolecular constitutive description and fracture initiation is implemented by imposing ad hoc based criterion. Brittle fracture through craze initiation, growth and craze fibril breakdown is implemented by utilizing a recently developed craze constitutive model [60] and then a new model is implemented with the development of a parameter-free continuum model of final craze breakdown. One feature of the new model is that the stress bearing capacity vanishes as a natural outcome to the craze breakdown process. This simplifies the numerical implementation of the crazing model in a finite element program beyond being more physical than currently used empirical failure criteria. In order to simulate fiber–matrix debonding through cavitation induced matrix cracking, the dilatational energy density criterion developed by Talreja and coworkers [101] is also implemented.

- The effects of manufacturing induced voids and their configurations on the initiation and growth of damage in ductile polymer based composites are investigated.

  To generate a basic understanding of the characteristic features of the competition between the void-generated damage and debonding of the reinforcing

elements in a composite, a parametric study is devised. The effects of voids on damage initiation and progression in a composite microstructure subjected to transverse plane strain tension loading at room temperature is investigated by considering void geometry (size, shape and distribution relative to fiber geometry), fiber geometry (location). Then the analyses are extended to investigate the effects of temperature and strain rate. Focused examination was conducted to investigate the effects of voids on cavitation induced debonding, deformation banding, and craze induced fracture. Influences of void and reinforcement structural parameters was clarified for specific loading conditions.

For all problems full transient analyses are carried out which employ a Lagrangian formulation of the field equations, with account taken of finite strains and rotations. A convective representation of finite deformations was used with the dynamic principle of virtual work [108]. In the plane strain specialization of this implementation, the discretization was based on linear displacement triangular elements arranged in quadrilaterals of four "crossed" triangles. The equations of motions was integrated numerically by Newmark-β method [109]. Once the (global) displacements and velocities are updated, the deformation gradient, the strain rate and other kinematic quantities can be directly calculated. The constitutive updating is based on the rate tangent modulus method of Peirce et al. 1984 [110], which is based on a forward gradient estimate of the effective viscoplastic strain rate. Extra boundary condition is implemented for composite unit cells to ensure zero lateral traction for uniaxial problem and prevent necking in the microstructure to maintain continuity of stress/strain fields between adjacent unit cells. Material failure subsequent to craze breakdown and debonding is implemented via an "element removal technique". In this approach when the failure condition is met in an element, the element is taken to vanish. All

the Numerical analysis were done using the Texas A&M university's Supercomputing facility.

D. Outline of Dissertation

Chapter I introduces the background, objective, and methodology of this research. Chapter II shows the development and capability of the computational framework for analyzing polymer deformation Chapter III illustrates extension of the computational framework developed in Chapter II by developing and implementing constitutive models to capture fracture behavior of polymers. Chapter IV features the investigation of the effects of voids on damage initiation and progression in composite microstructures utilizing the computational framework developed in chapter II and III. Chapter V presents the summary, conclusions, and limitations of this research, as well as comment on the direction of ongoing and future research that will extend the findings presented herein.

CHAPTER II

A COMPUTATIONAL FRAMEWORK FOR ANALYZING THE DEFORMATION BEHAVIOR OF GLASSY POLYMERS

A. Introduction

The deformation behavior of glassy polymers, such as polymethylmetacrylate (PMMA), polystyrene (PS), polycarbonate (PC) and some thermosets used in structural composites, exhibits rate and temperature dependence. At sufficiently high temperatures, yet below the glass transition temperature, the ductility is very large, typically reaching 100% in some polymers. In this regime, the behavior is characterized by post-yield softening at small strains followed by rapid hardening at large strains. At relatively low temperatures (or high strain rates) the small-strain softening is suppressed due to premature fracture and the behavior is rather brittle. In addition, differences arise between the tensile and compressive responses which are associated with intrinsic pressure-sensitivity and with craze formation under predominantly tensile stress states.

Over the past few decades, models have been developed which capture some peculiar features of deformation in glassy polymers. Pressure sensitivity is commonly accounted for through Mohr-Coulomb or Drucker-Prager type models, which are popular in composite applications [81]. These models, however, do not account for the phenomenology of deformation in glassy polymers as described above. More recently, physics-based models were developed which better capture the large strain behavior, including the intrinsic softening at small strains [55]. These material models are of levels of sophistication needed to carry the essential molecular physics related to deformation mechanisms and therefore possess the predictive capability concerning

localization and failure.

This chapter reports on the development of a computational framework for investigating deformation in amorphous glassy polymers, subject to quasi-static loading. Two classes of material models are considered: (i) Drucker-Prager like models that account for rate- and pressure-sensitivity; and (ii) improved constitutive models that also account for temperature dependence, small-strain softening and large-strain hardening. Both types of models are implemented in a unifying explicit finite-element framework using a Lagrangian formulation of the field equations and based on the constitutive updating method of [110].

The paper is organized as follows. We begin by formulating the field equations and numerical methods used. The specific constitutive models are then presented with implementation details regarding the rate tangent modulus method deferred to the appendix. Next, three applications are selected to demonstrate the capabilities of the framework: (i) full transient analyses of a polymeric block subject to impact; (ii) shear band formation and propagation in plane strain compression; and (iii) a study of the effect of strong contrast in material properties on strain localization, e.g. voids and stiff elements embedded in a polymer matrix.

B. Formulation

1. Field Equations and Numerical Methods

A Lagrangian formulation of the field equations is employed whereby a field variable is considered as a function of convected coordinates, y^i, and time t; see [108, 111, 112] The position of a material point in the initial configuration and current configuration, relative to the origin of a fixed cartesian frame is denoted by $\mathbf{X}$ and $\mathbf{x}$, respectively.

The displacement vector $\mathbf{u}$ and the deformation gradient $\mathbf{F}$ are given by,

$$\mathbf{u} = \mathbf{x} - \mathbf{X}, \quad \mathbf{F} = \frac{\partial \mathbf{x}}{\partial \mathbf{X}} \tag{2.1}$$

Denoting $\mathbf{G}_i$ and $\mathbf{g}_i$ the base vectors in the reference and current configurations, respectively, the relationships

$$\mathbf{G}_i = G^{ij}\mathbf{G}_j, \ \mathbf{g}_i = g^{ij}\mathbf{g}_j \tag{2.2}$$

define G^{ij} and g^{ij} as the inverse of the metric tensors $G_{ij} = \mathbf{G}_i \cdot \mathbf{G}_j$ and $g_{ij} = \mathbf{g}_i \cdot \mathbf{g}_j$, respectively.

In full transient analyses the dynamic principle of virtual work is written as:

$$\int_V \tau^{ij}\delta E_{ij}\mathrm{d}V = \int_S T^i \delta u_i \mathrm{d}S - \int_V \rho \frac{\partial^2 u_i}{\partial t^2}\delta u_i \mathrm{d}V \tag{2.3}$$

where τ^{ij} are the contravariant components of Kirchhoff stress, E_{ij} the covariant components of Green-Lagrange strain on the deformed, convected coordinate net, and T^i the contravariant surface tractions. Also, ρ is the mass density and V and S respectively denote the volume and surface of the body in the reference configuration. Specifically,

$$\tau^{ij} = J\sigma^{ij}; \quad J = \sqrt{\det(g_{ij})/\det(G_{ij})} \tag{2.4}$$

$$E_{ij} = \frac{1}{2}\left(u_{i,j} + u_{j,i} + u^k_{,i}u_{k,j}\right) \tag{2.5}$$

$$T^i = \left(\tau^{ij} + \tau^{kj}u^i_{,k}\right)\nu_j \tag{2.6}$$

with σ^{ij} the components of Cauchy stress, J the ratio of current to reference volume and ν_j the covariant components of the reference surface normal. $()_{,i}$ denotes covariant differentiation in the reference frame.

Discretization of (2.3) in the reference configuration using a finite element grid

results into equations of motion that take the form

$$\mathbf{M}\frac{\partial^2 \mathbf{U}}{\partial t^2} = \mathbf{R} \tag{2.7}$$

with $\mathbf{M}$ a symmetric definite-positive mass matrix, $\mathbf{U}$ the nodal displacement vector and $\mathbf{R}$ the nodal force vector. In the usual way, $\mathbf{U}$ results from substituting a suitable finite element approximation of the displacements u^i into (2.3) and from subsequent integration, and $\mathbf{R}$ is computed from the left hand side of (2.3) and from any applied boundary tractions, the surface integral in (2.3).

The discrete system (2.7) of equations of motion is integrated using a time stepping algorithm of the Newmark family [113]; also see [109, 114]. The sub-family of central difference schemes is written in the usual way. Let β be a real number, $0 \leq \beta \leq 1/2$, and $(\dot{})$ denote time differentiation $\partial(\ )/\partial t$, with components on appropriate base vectors. Given the nodal displacements and velocities $(\mathbf{U}_n, \dot{\mathbf{U}}_n)$ at time t_n, find $(\mathbf{U}_{n+1}, \dot{\mathbf{U}}_{n+1})$ such that:

$$\mathbf{U}_{n+1} = \mathbf{U}_n + \Delta t \dot{\mathbf{U}}_n + \frac{1}{2}\Delta t^2[(1-2\beta)\mathbf{A}_n + 2\beta \mathbf{A}_{n+1}] \tag{2.8}$$

$$\dot{\mathbf{U}}_{n+1} = \dot{\mathbf{U}}_n + \Delta t \left(\frac{\mathbf{A}_{n+1} + \mathbf{A}_n}{2}\right) \tag{2.9}$$

with $\Delta t = t_{n+1} - t_n$ the time step and $\mathbf{A}$ the acceleration vector given by:

$$\mathbf{A}_n = \ddot{\mathbf{U}}_n = \mathbf{M}^{-1}\mathbf{R}_n \tag{2.10}$$

Central difference Newmark schemes are second-order accurate [115]. They are generally implicit but for $\beta = 0$ equation (2.8) is explicit for $\mathbf{U}_{n+1}$ in terms of $(\mathbf{U}_n, \dot{\mathbf{U}}_n)$, making the $\beta = 0$ case known as *explicit Newmark*. As noted by Simo et al. [115], the implicit members of the Newmark family are not designed to conserve energy and also fail to conserve momentum. In this regard, it is somewhat para-

doxical that Newmark integrators work remarkably well and remain the most widely used schemes in nonlinear structural dynamics. Only relatively recently has the symplectic nature of the Newmark scheme been established, albeit in a non-trivial sense, by Marsden et al. [116], thus providing a rationale for the excellent performance of this class of integrators. Unlike implicit members of the Newmark family, the explicit method is known to preserve momentum stricto sensu [115]. Here we shall use this method. It has proven effective in various applications; e.g. dynamic shear banding [108], ductile-brittle transition [117, 118] and intersonic crack growth [119]. In addition, a lumped mass matrix $\mathbf{M}$ is used in (2.10) instead of the consistent one. This is preferable for explicit integrators because a diagonal mass matrix offers computational accuracy as well as storage efficiency [120].

After computation of displacements and velocities at time t_{n+1} the deformation gradient, the strain rate and other kinematic quantities are directly computed. The constitutive updating is based on the rate tangent modulus method of [110] giving the Jaumann rate of Cauchy stress given as

$$\overset{\nabla}{\boldsymbol{\sigma}} = \mathbf{L}_{\tan} : \dot{\mathbf{E}} + \dot{\mathbf{Q}} \tag{2.11}$$

where $\mathbf{L}_{\tan}$ and $\dot{\mathbf{Q}}$ are respectively fourth and second rank tensors, which depend on the constitutive model to be specified in Section 2.

Also $\dot{\mathbf{E}}$ is the rate of Green-Lagrange strain defined after equation 2.3 ; its covariant components are given by

$$\dot{E}_{ij} = \frac{1}{2}\left(F_i^k \dot{F}_{kj} + F_j^k \dot{F}_{kl}\right) \tag{2.12}$$

The updating of the Kirchhoff stress components in equilibrium equation (2.3) are then done by using $\tau^{ij}_{t+\triangle t} = \tau^{ij}_t + \triangle t \dot{\tau}^{ij}$ and a standard kinematic relation between the convected rate of Kirchhoff stress $\dot{\boldsymbol{\tau}}$ and the Jaumann rate of Cauchy stress $\overset{\nabla}{\boldsymbol{\sigma}}$,

given by

$$\dot{\tau}^{ij} = J\left[\overset{\nabla}{\sigma}{}^{ij} + g^{kl}\dot{E}_{kl}\sigma^{ij} - g^{ik}\sigma^{jl}\dot{E}_{kl} - g^{jk}\sigma^{il}\dot{E}_{kl}\right] \tag{2.13}$$

2. Constitutive Models

A number of models have been developed to simulate deformation behavior of polymers during the last half century. At large strain the inelastic flow of amorphous polymer occurs by overcoming two molecular resistance mechanisms [59]. Below glass transition temperature, prior to initial yield, amorphous polymer chains have to overcome intermolecular resistance to segment rotation, after material begins to flow, causing polymer chains to orient themselves in an affine manner that causes changes in configurational entropy, leading to anisotropic resistance to further inelastic deformation [55, 59]. Thus the finite deformation response of amorphous polymers, such as thermoplastics, is characterized by rate, pressure and temperature sensitive yielding, followed immediately by intrinsic strain softening and, at large strains, by increasing strain hardening. The small-strain softening behavior is inseparably connected with yielding by way of the molecular mechanisms of macroscopic yielding [61]. At the fine scale, yielding accompanied by small scale inhomogenous deformation appears in the form of multiple narrow shear bands, and is usually referred to as "shear yielding". The increasing strain hardening behavior due to anisotropic resistance at large strain is associated with the stretching of the network of molecules between entanglements and the simultaneous development of a preferred orientation of the molecular chains.

In this study, two distinct constitutive models are explored: (i) a reference material model, of the Drucker-Prager type, where pressure-sensitivity enters directly the plastic potential [106] with isotropic hardening as in [80, 82]; and (ii) a macromolecular model with kinematic hardening where pressure-sensitivity enters through the flow rule [55, 59, 78, 79, 121]

We begin with assuming additive decomposition of the total rate of deformation $\mathbf{D}$ into an elastic part $\mathbf{D}^{\mathrm{e}}$ and a viscoplastic part $\mathbf{D}^{\mathrm{p}}$. The former is taken to be governed by a hypoelastic law:

$$\mathbf{D}^{\mathrm{e}} = \mathbf{L}^{-1} : \overset{\nabla}{\boldsymbol{\sigma}} \tag{2.14}$$

where $\mathbf{L}$ is the tensor of elastic moduli with components on the deformed coordinates

$$\mathbf{L}^{ijkl} = \frac{E}{1+\nu}\left[\frac{1}{2}\left(g^{ik}g^{jl} + g^{il}g^{jk}\right) + \frac{\nu}{1-2\nu}g^{ij}g^{kl}\right] \tag{2.15}$$

with E Young's modulus and ν Poisson's ratio, and $\overset{\nabla}{\boldsymbol{\sigma}} = \dot{\boldsymbol{\sigma}} - \mathbf{W}\cdot\boldsymbol{\sigma} + \boldsymbol{\sigma}\cdot\mathbf{W}$ is the Jaumann rate of Cauchy stress $\boldsymbol{\sigma}$, $\mathbf{W}$ being the spin, i.e., the skew-symmetric part of the velocity gradient, and : denotes the dyadic product. Note that, as in (Eq. 1.13), explicit evaluation of the spin $\mathbf{W}$ is not required. For the glassy polymers of interest, this representation of elastic deformation is adequate within the range of temperature and strain rate considered and as long as the stresses remain small relative to Young's modulus.

The plastic rate of deformation tensor is specified through a viscoplastic flow rule, given by

$$\mathbf{D}^{\mathrm{p}} = \dot{\bar{\epsilon}}\,\mathbf{p} \tag{2.16}$$

where $\dot{\bar{\epsilon}}$ is the effective plastic strain rate, describe the magnitude of plastic flow, which is formally defined through:

$$\dot{\bar{\epsilon}} = \sqrt{\frac{2}{3}\mathbf{D}^{\mathrm{p}} : \mathbf{D}^{\mathrm{p}}} \tag{2.17}$$

and $\mathbf{p}$ is a tensor, defines the direction of plastic flow.

a. Drucker-Prager Type Model

First a viscoplastic model, particularly used in aerospace applications [80, 81], combines dilatant plasticity [106] with a viscoplastic flow rule developed by Bodner and co-workers [82, 107]. This model will be referred to as DPB model. In [80] a small-strain version of the model was used. In our work a finite-strain, rate dependent extension of this model is formulated in view of a finite-element implementation.

The plastic part of the rate of deformation is obtained from a pressure-sensitive flow potential, given by

$$\phi(\boldsymbol{\sigma}; \bar{\sigma}, \gamma) = \sigma_{\text{eq}} + \sqrt{3}\gamma\sigma_{kk} - \bar{\sigma} \tag{2.18}$$

where σ_{eq} is the Mises equivalent stress, i.e. $\sigma_{\text{eq}} = (3/2\,\boldsymbol{\sigma}' : \boldsymbol{\sigma}')^{1/2}$ with $\boldsymbol{\sigma}'$ the stress deviator. In the original DP model [106] the parameters γ and $\bar{\sigma}$ are constant. Here they are both taken to evolve with deformation. The evolution of γ permits a better representation of pressure-sensitivity in thermosetting polymers [81] while that of $\bar{\sigma}$, or rather some related variable to be defined below, allows for isotropic hardening to be represented. Thus, in the extended DP model, γ and $\bar{\sigma}$ are treated as state variables. The inelastic rate of deformation tensor is specified through the associative flow rule that is assumed to be proportional to the derivative of the potential function with respect to the components of stress tensor, $\boldsymbol{\sigma}$, given by

$$\mathbf{D}^{\text{p}} = \dot{\bar{\epsilon}}\frac{\partial\phi}{\partial\boldsymbol{\sigma}} = \dot{\bar{\epsilon}}\,\mathbf{p} \tag{2.19}$$

where $\mathbf{p}$ describes the direction of plastic flow:

$$\mathbf{p} = \frac{3}{2}\frac{\boldsymbol{\sigma}'}{\sigma_{\text{eq}}} + \sqrt{3}\delta\mathbf{I} \tag{2.20}$$

Here δ is a state variable that describes fine-scale structural arrangements associated

with a dilational component of plastic strain. If δ is identified with γ of equation (2.18) then flow is associative. By way of contrast, if $\delta = 0$ plastic flow is isochoric. Neither of these options seem to correspond to experimental measurements [4,122] so that in general $\delta \neq \gamma \neq 0$. Nonetheless, the assumption of volume-preserving plastic flow is more commonly adopted. The $'$ in the definition of $\dot{\bar{\epsilon}}$ is consistent with the flow rule (2.19).

The Strain rate hardening law originally derived by [82] on a physical basis to capture incubation, growth and saturation phenomenon of metal plasticity, later modified by [81] for polymer, where the effective strain-rate is expressed through following strain rate hardening law:

$$\dot{\bar{\epsilon}}(\bar{\sigma}; Z) = \frac{2}{\sqrt{3}}\,\dot{\epsilon_1}\exp\left[-\frac{1}{2}\left(\frac{Z}{\bar{\sigma}}\right)^{2n}\right] \tag{2.21}$$

where $\dot{\epsilon_1}$ is a material parameter describes the reference plastic strain rate, n represents the controlling parameter of rate dependance of polymer and Z is a state variable that represents isotropic hardening to represent resistance to plastic flow and is evolved as follows:

$$\dot{Z} = q\,(Z_1 - Z)\,\dot{\bar{\epsilon}} \tag{2.22}$$

where Z_1 is a material parameter, represents the saturation value of hardening. The evolution equation of the pressure sensitivity parameter γ given by:

$$\dot{\gamma} = q'(\gamma_1 - \gamma)\dot{\bar{\epsilon}} \tag{2.23}$$

where q' and γ_1 are material parameters, describes hardening rate and saturation value of pressure sensitivity, respectively. The stress-like variable $\bar{\sigma}$ is obtained implicitly through a consistency condition $\dot{\phi} = 0$. In the absence of dilatancy ($\gamma = 0$ in (2.18)), $\bar{\sigma}$ recovers the meaning of an effective stress as in the original Bodner-Partom model

[82, 107]. The model has two additional parameters, γ_0 and Z_0, which represent the initial values of γ and Z, respectively.

Although Drucker-Prager like plasticity was originally developed for soil material and Bodner-Partom like flow rules were initially developed for metals, the phenomenological model outlined above has recently been applied to polymers in composites [81]. The model in its current form does not account for kinematic-like hardening, clearly established for polymers [123]. A proposal for incorporating anisotropic hardening into the model has recently been made [107]. It is not included here for reasons that will become clear later in the discussion. In this study, the extended DPB model will essentially be used to investigate the effect of hydrostatic pressure on polymer behavior within an associative framework.

b. Macromolecular Model

The basis of this model is combining a rate-sensitive plastic flow rule by [59] with a 3D-anisotropic hardening model by [55] further refined by improving the hardening model by [79](94,95). First [77] developed a one dimensional continuum model, by using the Eyring dashpot model to describe yield and Langevin spring model to describe post yield orientational hardening behavior. [59] incorporated rate dependence in the Haward-Thackrey's model for post yield behavior. Later [55] improved the model by incorporating pressure sensitivity, three dimensional effect, finite strain kinematics and classical three chain rubber elasticity model to describe the orientational hardening. [65] further refined the model by considering thermal softening due to adiabatic heating. [79] refined Boyce's model by improving the orientational hardening by considering a statistical combination of three chain and eight chain rubber elasticity model.

The flow rule is taken such that plastic straining is in the direction of some

driving stress and that plastic deformation is incompressible, i.e.,

$$\mathbf{D}^{\mathrm{p}} = \frac{3}{2}\frac{\dot{\bar{\epsilon}}}{\sigma_{\mathrm{e}}}\boldsymbol{\sigma}'_{\mathrm{d}} \tag{2.24}$$

with $\dot{\bar{\epsilon}}$ the effective strain rate as above and σ_{e} is an effective stress defined as:

$$\sigma_{\mathrm{e}} = \sqrt{\frac{3}{2}\boldsymbol{\sigma}'_{\mathrm{d}} : \boldsymbol{\sigma}'_{\mathrm{d}}}, \qquad \boldsymbol{\sigma}_{\mathrm{d}} = \boldsymbol{\sigma} - \mathbf{b} \tag{2.25}$$

where $\boldsymbol{\sigma}'_{\mathrm{d}}$ is the deviatoric part of the driving stress, $\boldsymbol{\sigma}_{\mathrm{d}}$, and $\mathbf{b}$ is the back stress tensor that describes the orientation hardening of the material. This anisotropic hardening is modeled by making analogy with the stretching of cross-linked rubber elasticity [55, 79]. Introducing the unit principal directions, $\mathbf{e}_i^{\mathrm{p}}$, of the left plastic stretch tensor as base vectors, one can define the principle components of the back stress on that base. The constitutive equations for the back stress are written in terms of a functional dependence of the b_i's upon the principal plastic stretches, λ_i, associated with the principal directions $\mathbf{e}_i^{\mathrm{p}}$ of the left plastic stretch tensor . This dependence is specified as:

$$\mathbf{b} = \sum_i b_i \left(\mathbf{e}_i^{\mathrm{p}} \otimes \mathbf{e}_i^{\mathrm{p}}\right), b_i = b_i(\lambda_i) \tag{2.26}$$

The components of back stress is obtained from [79,121,124]'s description of full network model, which is a linear combination of the classical three-chain network model and the eight-chain model [78] that represent the fully three dimensional orientation distribution of molecular chains in non-Gaussian network, given as follows

$$b_i(\lambda_i) = (1-\rho)b_i^{3-ch} + \rho b_i^{8-ch} \tag{2.27}$$

where the functions b_i^{3-ch} [55] and b_i^{8-ch} [78] correspond to the three-chain and eight-

chain network models, respectively, given by (no sum on i here) :

$$b_i^{3-ch}(\lambda_i) = \frac{1}{3}C^R\sqrt{N}\lambda_i\mathcal{L}^{-1}(\frac{\lambda_i}{\sqrt{N}}) \tag{2.28}$$

$$b_i^{8-ch}(\lambda_i) = \frac{1}{3}C^R\sqrt{N}\frac{\lambda_i^2}{\lambda_c}\mathcal{L}^{-1}(\frac{\lambda_c}{\sqrt{N}}) \tag{2.29}$$

In these expressions, $\lambda_c = \sqrt{\frac{1}{3}\sum\lambda_i^2}$, C^R is the so-called rubbery modulus, N is the average number of links between entanglements, which determines the limit stretch of a molecular chain, and $\mathcal{L}$ is the Langevin function defined as $\mathcal{L}(\xi) = \coth\xi - \frac{1}{\xi}$. In equation (2.27), the factor ρ is determined by the maximum principal plastic stretch, $\bar{\lambda} = max(\lambda_1, \lambda_2, \lambda_3)$, through $\rho = 0.85\bar{\lambda}/\sqrt{N}$. Physically, when the value of either $\bar{\lambda}$ or λ_c approaches the average limit stretch (maximum principal stretch equal to $\sqrt{N}$ is identified as limit stretch) of a molecular chain, the network locks, no further viscoplastic flow occurs and the hardening rate increases dramatically.

Strain rate effects are accounted for through a specific strain-rate hardening law, first derived by [59] on a physical basis and later modified for pressure sensitivity and strain softening effects by [55]

$$\dot{\bar{\epsilon}} = \dot{\epsilon_0}\exp\left[-\frac{A\left(s-\alpha\sigma_{kk}\right)}{T}\left(1-\left(\frac{\sigma_{\mathrm{e}}}{s-\alpha\sigma_{kk}}\right)^{\frac{5}{6}}\right)\right] \tag{2.30}$$

where $\dot{\epsilon}_0$, and A are material parameters, α a factor describes the pressure sensitivity, T is the absolute temperature, σ_{kk} is the trace of Cauchy stress and s is an internal state variable, which may be interpreted as a micro-scale shear strength. The variable s evolves as follows

$$\dot{s} = h\left(1-\frac{s}{s_{ss}}\right)\dot{\bar{\epsilon}} \tag{2.31}$$

where h is an additional material parameter that describes the slope of the yield drop with respect to plastic strain and s_{ss} is the saturation value of s. The values used for α and s_{ss} are such that the term $s - \alpha\sigma_{kk}$ in (2.30) remains non-negative in

the course of deformation. We note, however, that incorporating pressure-sensitivity as in (2.30) may not be the most suitable choice, especially for extreme pressure-dominated loading.

The model presented in this section owes its macromolecular character to the fact that both the orientational and strain-rate hardening equations were developed based on macromolecular mechanisms. However, the effects of pressure sensitivity and softening, included in (2.30) and (2.31), are heuristic additions.

3. Rate Tangent Modulus Method

The rate tangent modulus method is a one step forward gradient time integration scheme by which we have estimated the effective strain rate, $\dot{\bar{\epsilon}}$. In general $\dot{\bar{\epsilon}}$ is a function of effective plastic strain, $\bar{\epsilon}$, and a finite number of scaler variable, ψ_i. However, in our case $\bar{\epsilon}$ is not included in the functional form of effective plastic strain rate, $\dot{\bar{\epsilon}}(\psi_i)$ (for Drucker-Prager type (DPB model) $\psi_1 = \bar{\sigma}, \psi_2 = Z$ and for macromolecular model $\psi_1 = \sigma_{\mathrm{e}}$) because $\bar{\epsilon}$ does not directly affect the strain rate hardening behavior (equation 2.21 and 2.30). Using the rate tangent method, $\bar{\epsilon}$ is obtained by expressing as a linear interpolation on the values between time t and $\triangle t$,

$$\triangle \bar{\epsilon} = \triangle t \left[(1-\theta)\, \dot{\bar{\epsilon}}_t + \theta \dot{\bar{\epsilon}}_{t+\triangle t} \right] \tag{2.32}$$

where θ being a numerical factor ranges from 0 to 1. Expressing the functional form of $\dot{\bar{\epsilon}}_{t+\triangle t}$ in equation(2.32) by Taylor-series-Expansion,

$$\dot{\bar{\epsilon}}_{t+\triangle t} = \dot{\bar{\epsilon}}_t + \theta \triangle t \left(\sum_i \frac{\partial \dot{\bar{\epsilon}}}{\partial \psi_i} \dot{\psi}_i \right) \tag{2.33}$$

The rate form of the scaler variables, $\dot{\psi}_i$, are obtained either by using consistency condition or from the evolution equation or taking time derivative of the variable

itself. The rate form of the scaler variable, $\dot{\bar{\sigma}}$, in the DPB model, is obtained using the consistency condition (considering the time derivative of the potential function, $\dot{\phi}$, equal to zero) and rate of isotropic variable, $\dot{Z}$, is substituted using the evolution law (Eq. 2.22). After substituting the rate form of the scaler variables and performing algebraic manipulation, following form of the effective strain rate at current time is obtained:

$$\dot{\bar{\epsilon}}_{t+\triangle t} = \frac{\dot{\bar{\epsilon}}_t}{1+\xi} + \frac{\xi}{1+\xi}\frac{\mathbf{PD}}{H} \tag{2.34}$$

where $\mathbf{P} = \mathbf{L} : \mathbf{p}$. Symmetry of $\mathbf{p}$ and $\mathbf{L}$ results in symmetric $\mathbf{P}$, which ultimately leads to symmetric tangent stiffness matrix, favorable for better convergence in solving nonlinear equations. ξ, and H are parameters, whose form dependent on particular material model.

Now rearranging equation 2.14 and taking outer product of $\mathbf{p}$ with Jaumann derivative of Cauchy stress, we obtain:

$$\mathbf{p} : \overset{\nabla}{\boldsymbol{\sigma}} = \mathbf{p} : \mathbf{L}_{\mathrm{e}} : \mathbf{D} - (\mathbf{p} : \mathbf{L}_{\mathrm{e}} : \mathbf{p})\,\dot{\bar{\epsilon}} \tag{2.35}$$

After substituting $\dot{\bar{\epsilon}}$ and conducting algebraic manipulation, the constitutive equation leads to the following expression,

$$\overset{\nabla}{\boldsymbol{\sigma}} = \mathbf{L}_{\tan} : \mathbf{D} + \dot{\mathbf{Q}} \tag{2.36}$$

where $\mathbf{L}_{\tan}$ and $\dot{\mathbf{Q}}$ have the following general form:

$$\mathbf{L}_{\tan} = \mathbf{L} - \frac{\xi}{1+\xi}\frac{\mathbf{PP}}{H}, \quad \dot{\mathbf{Q}} = \frac{\dot{\bar{\epsilon}}_t}{1+\xi}\mathbf{P} \tag{2.37}$$

An adaptive time stepping is used. First a conservative estimate of the stable time increment is given by the minimum dimension taken over all the elements.

$$\triangle t_{\mathrm{dyn}} = (L_{\min}/c_{\mathrm{d}}) \tag{2.38}$$

where $L_{\min}$ is the smallest element dimension in the mesh and c_{d} is the dilatational wave speed in terms of Young's moduli E and Poisson's ν , defined below:

$$c_{\mathrm{d}} = \sqrt{\frac{E(1-\nu)(1-2\nu)}{\rho(1+\nu)}} \tag{2.39}$$

Then maximum allowable time steps, was further refined by using two more criteria from [124]. First criteria is to ensure that effective plastic strain increment is lesser than the maximum effective plastic strain increment $\bar{\epsilon}_{\max}$ during a time step $\triangle t$. The second criterion ensures that the drop of the athermal shear strength is lesser than a fraction , ϵ_{s}, of current athermal shear strength s_t. For each increment, time step is taken to be the minimum of the three criteria, given by.

$$\triangle t = \min\left\{\triangle t_{\mathrm{dyn}}; \frac{\triangle \bar{\epsilon}_{\max}}{\dot{\bar{\epsilon}}}; \epsilon_{\mathrm{s_t}} \frac{s}{\dot{s}_t}\right\} \tag{2.40}$$

C. Illustrative Examples

In previous sections, a framework for analyzing the dynamic response of amorphous polymers was presented. The formulation accounts for nonlinear material behavior and finite transformations. Well tested numerical algorithms were also formulated to solve the discrete dynamics and integrate the constitutive equations. In this section, we demonstrate the capabilities of the modeling framework through three illustrative examples: response under dynamic impact, shear band formation under compression and uniaxial tension of a composite unit cell containing a void. A state of plane strain is assumed in all. Particular attention is given to time convergence and mesh sensitivity analyses.

The finite element discretization in convected coordinate is based on linear displacement triangular elements arranged in quadrilaterals of four "crossed" triangles. The "crossed" triangular quadrilateral is used to avoid volumetric locking at large

strain [125].

Before solving the three boundary value problems mentioned above, a single element problem subjected to plane strain uniaxial tension was analyzed to demonstrate the behavior of the homogenous polymer and to validate the implementation of the constitutive models. Figure. 11 shows the stress-strain response for uniaxial plane strain tensile loading for homogenous PS obtained from single element computation using both models. Material properties used in the Boyce-Argon (macromolecular) model are the similar to those values for PS provided by Wu and Giessen (1994,1995,1996) Table.I. The material parameters used for the Bodner-Partom (DPB) [Table.II] model were adjusted so that the saturation flow stress is approximately equal to the maximum flow stress at the initial yield point for PS in the small-strain regime.

Figure. 11a shows stress-strain response using the DPB model, where q (eqn. 2.22) and q'(eqn. 2.23) is assumed to be 10 and the initial value, Z_0, of the hardening parameter , Z, is varied. The true stress is normalized with a parameter σ_s (106 MPa), which is the saturation value of $\bar{\sigma}$ at $\dot{\epsilon} = 1/s$. The response curves (Fig. 11a) using the DPB model exhibits isotropic hardening after initial yield followed by the saturation of the flow stress. As Z_0 is the initial value of hardening parameter, $Z_0 = Z_1$ shows perfectly plastic behavior and the smallest Z_0 value shows viscoplastic deformation accompanied by isotropic hardening occurs almost from the beginning. Figure. 11b shows strain rate dependent yield and saturation of flow stress captured by the DPB model.

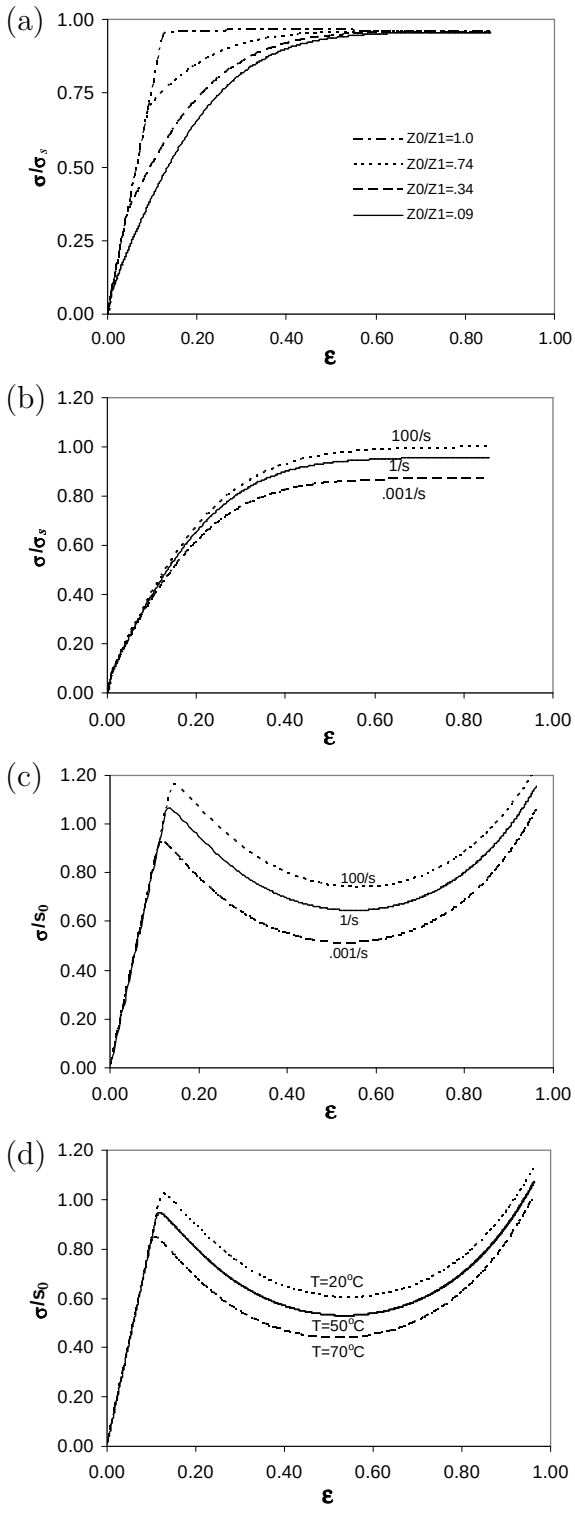

Fig. 11. Typical responses under homogeneous, plane-strain tension using the DPB model (a and b) and macromolecular model (c and d). (a) Effect of isotropic hardening parameters with $Z_1 = 1085$ MPa and $q = 10$. (b) Effect of strain rate with $Z_0/Z_1 = 0.1$ and $n = 0.9$. (c) Effect of strain rate at $T = 20°\text{C}$; and (d) effect of temperature at $\dot{\varepsilon} = 0.1\text{s}^{-1}$ for polystyrene (PS).

The homogenous deformation responses obtained by the computations using the macromolecular model (Fig. 11c and d) exhibit intrinsic softening after initial yield (at .0136 strain) followed by increasing strain hardening. Figure. 11c illustrates that with increase in strain rate, yielding occurs at larger stress and strain. Figure. 11d shows the temperature dependent yield and stress-strain responses using the macromolecular model. It should be noted that the effect of temperature on shear modulus is not considered here.

Figure 12 shows the cyclic response using the macromolecular model. Fig. 12a shows stress-strain response under cyclic strain between $\pm\epsilon = 0.20$, where unloading starts in the post yield isotropic softening regime. Throughout the loading cycle isotropic softening is dominant and reduces the elastic region via decreasing peak yield stress and therefore plastic strain increases from cycle to cycle. Cyclic response corresponding to kinematic hardening regime is shown the fig. 12b. In this case the cyclic strain is between $\pm\epsilon = 0.85$, where unloading starts from the kinematic hardening regime.

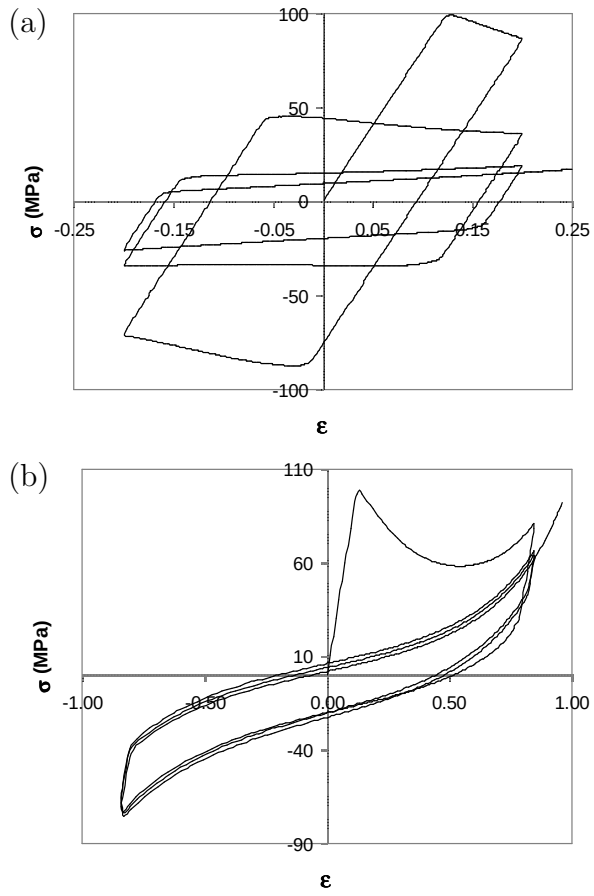

Fig. 12. Response of the macromolecular model to cyclic tension-compression at 0.1 s^{-1} strain rate: (a) cyclic strain $\varepsilon = \pm 0.2$; and (b) $\varepsilon = \pm 0.85$.

1. Impact-Response

First a planer PS polymer block subjected to plane strain three point dynamic bending was analyzed to observe the polymer response under dynamic impact loading. Fig. 13a

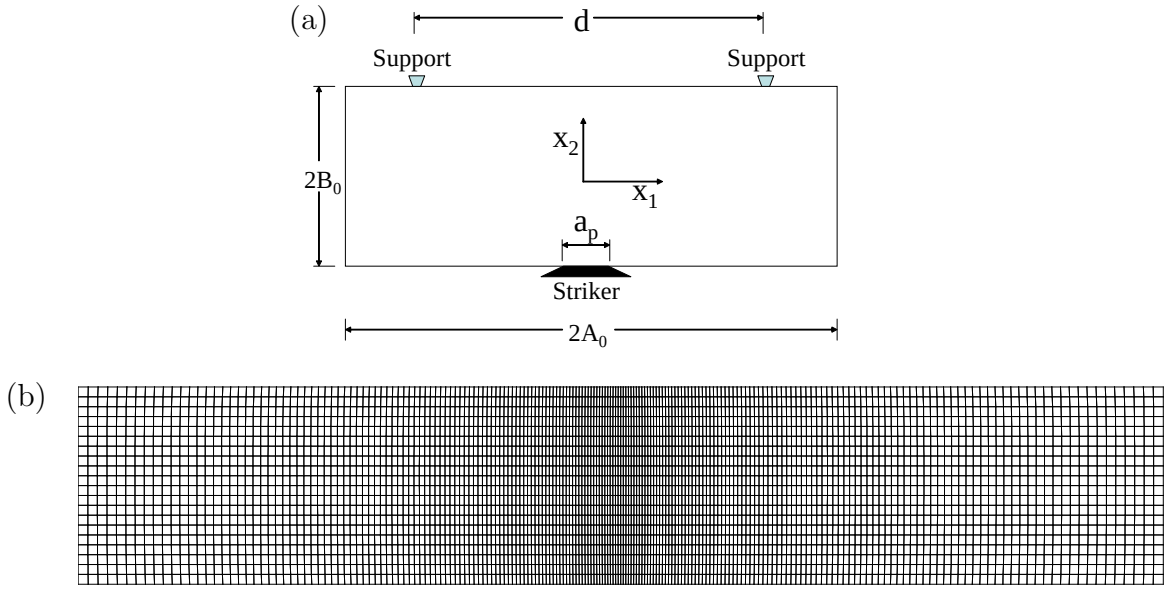

Fig. 13. (a) Geometry of the specimen and boundary conditions. (b) Finite element mesh (4000 elements).

illustrates the geometry of a planer polymeric block, which has been subjected to low to moderately high velocity (V_2 = 5m/s, 50m/s and 100m/s) impact in the x_1-x_2 plane, the finite element mesh used in the computations is also shown (Fig. 13b). The block has initial dimensions $2A_0 \times 2B_0$ and is simply supported by two anvils at a distance of d. The block of polymer is hit by the striker on the bottom surface over a finite width a_p. The striker and the anvils were accounted for by prescribing the following boundary conditions

$$U_2 = 0, \text{ at } x_1 = \pm d/2 \text{ and } x_2 = B_0 \tag{2.41}$$

$$\dot{U}_2 = V_2, \text{ for } x_2 = -B_0 \text{ and } -a_p/2 \leq x_1 \leq a_p/2 \tag{2.42}$$

All other surfaces are considered to be traction-free. The velocity function, $V(t)$, is a ramping function with a rise time of t_r and a final value of V_2. For the impact problem discussed here, the dimensions are : $A_0 = 27.5$ mm, $B_0 = 5$ mm, $d = 40$ mm, $a_p = 2$ mm and $t_r = 20\mu$s. The mesh shown in Fig. 13 consists of 4000 quadrilateral elements.

Figure 14 shows typical load displacement curves using the DPB (Fig. 14a) and macromolecular models (Fig. 14b) for PS material. The oscillations seen correspond to the amount of kinetic energy transmitted to the specimen upon impact, consistent with the impact velocities used in the computations. When the macromolecular model is used, the calculations are stopped at a striker displacement of 15.1mm, 17.5mm and 18.5mm for the impact velocity of 5m/s, 50m/s and 100m/s, respectively. Up to the striker displacement in all velocity impact considered here, both models yield similar load-displacement curves but substantial difference in the local behavior is observed, depending on which constitutive model is used. Fig. 15 shows the contours of the effective plastic strain, $\bar{\epsilon}$, obtained at three distinct loading velocities at an advance stage ($U = 14$mm) using the DPB model. The plots illustrate the distribution of plasticity within the polymer block, the penetration that occurs around the impact and the "bulging" in between the supports (anvils) at the top surface. Plastic deformation localizes near the anvils, where it is highest, on either side of the striker as well as on the outer fiber between the anvils. In the DPB model computation the maximum value of effective plastic strain for three different velocity impacts up to the $U = 14$mm are about $\bar{\epsilon} = 0.348$, $\bar{\epsilon} = 0.68$ and $\bar{\epsilon} = 1.068$ for the $V_2 = 5$m/s, 50m/s, 100m/s, respectively. For the DPB model, material is yielded from the beginning in the tensile regime, regardless of strain rate. Thus, for the higher velocity impact it

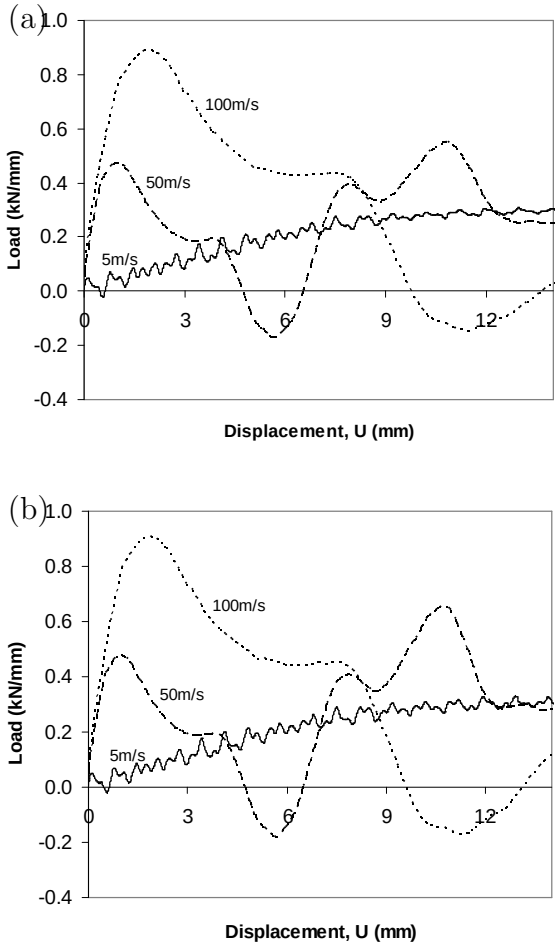

Fig. 14. Load versus displacement curves for V =5m/s, 50m/s and 100m/s velocity impact obtained using the (a) DPB model and (b) macromolecular model

shows larger plastic deformation in the tensile regime (at the corner of the anvil).

Interestingly, the deformation phenomenon of macromolecular model calculation is inherently different. Figure. 16 shows the distribution of $\bar{\epsilon}$ using the macromolecular model, at the three loading velocities corresponding to an advance stage (U = 14.0mm) of deformation . For the low velocity (V_2 = 5m/s) impact, the plastic zone rapidly expands because local yield is followed by immediate softening (see Fig. 11). As stated above, plastic shear activity emerges at the striker location, then a band of plastic deformation spreads towards the outer fiber, Fig. 16a. In addition,

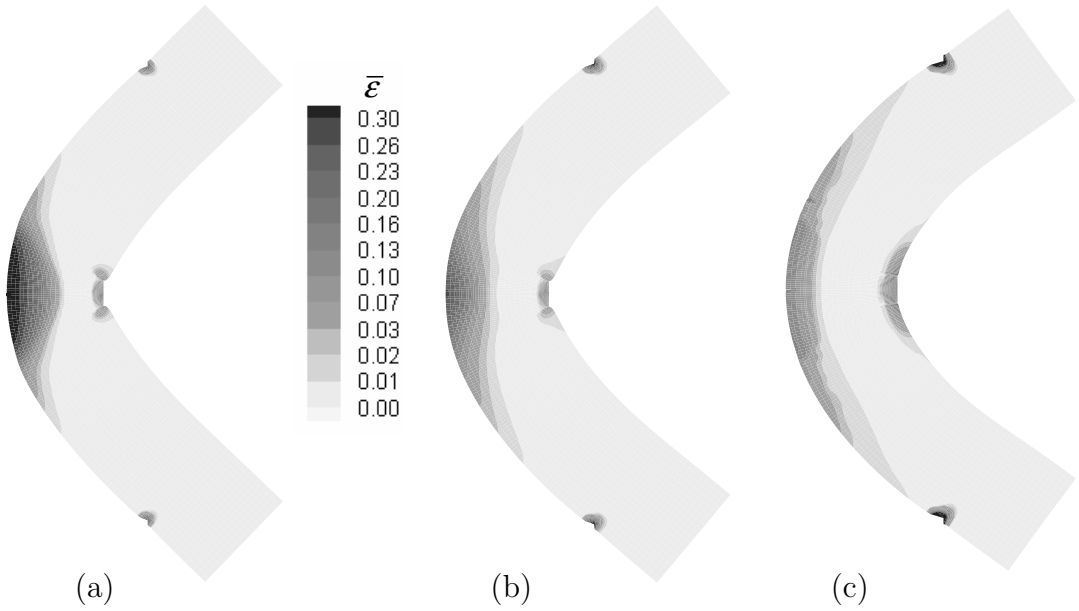

Fig. 15. Contours of effective plastic strain using the DPB model at 14mm striker displacement for the striker velocity, V, of (a) 5.0m/s (b) 50m/s and (c) 100m/s.

localization also occurs at the the outer fiber between supports and rapidly expands. The intensity of deformation increases within the "shear bands" until large-strain hardening occurs inside the band (recall the shape of the local stress-strain curve from Fig. 11c), which resists the intense flow of plastic deformation resulting in a maximum effective plastic strain, $\bar{\epsilon}$, of about 0.33. However, increase in impact velocity from 5m/s to 100m/s there is considerable increase of nominal strain rate, which results in high yield stress to initiate plasticity within the specimen. Thus, plastic localization within the block starts at the later stages with increase of impact velocity. The maximum value of effective plastic strain for three different velocity impacts up to the $U = 14$mm, computed using macromolecular model, are about $\bar{\epsilon} = 0.333$, $\bar{\epsilon} = 0.06$ and $\bar{\epsilon} = 0.032$ for $V_2 = 5$m/s, 50m/s, 100m/s, respectively.

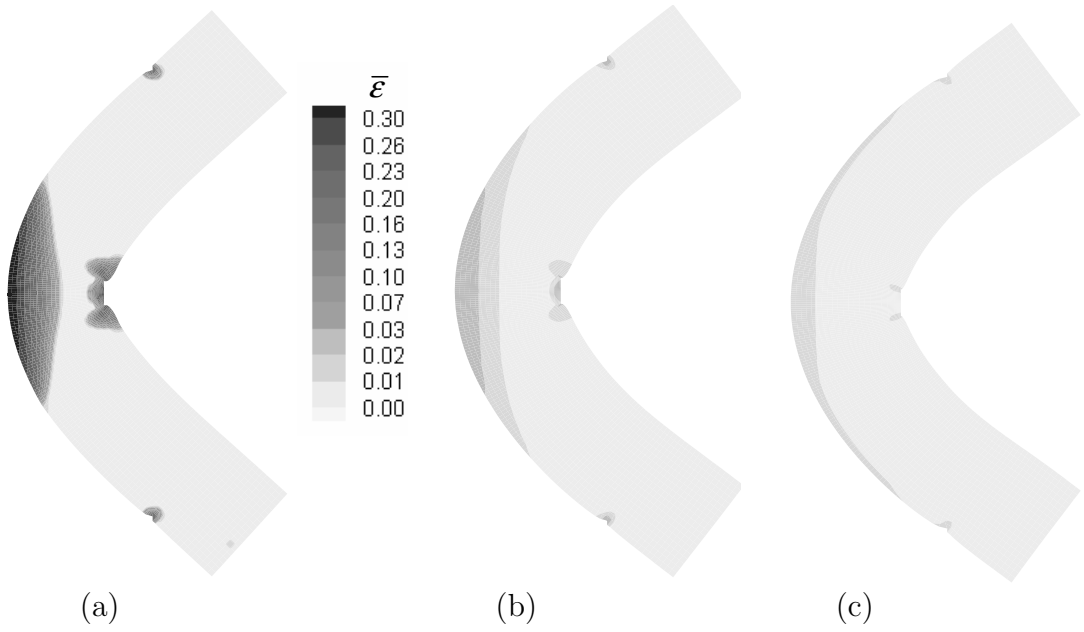

Fig. 16. Contours of effective plastic strain using the macromolecular model at 14 mm striker displacemnt for striker velocity, V, of (a) 5.0m/s (b) 50m/s and (c) 100m/s.

Fig. 17 shows the distributions of the maximum principal stress, σ_{I}, obtained using both models at the same striker displacement of 14mm. The plots suggesting that maximum principal tensile stress is higher for the macromolecular model as compared to the DPB model and compressive stress is lower than the DPB model computation. A better indication of the localization of plastic deformation is obtained by plotting the maximum principal compressive stress and tensile stress at any location of the specimen for the $V_2 = 5$m/s velocity impact Fig. 18. For the DPB model the tensile maximum σ_{I} reaches a saturation value of 125 MPa (outer fiber between the anvils) and in the compressive zone σ_{I} reaches a value about 800 MPa. In contrast for the macromolecular computation maximum tensile and compressive σ_{I} about 180 MPa and 600 MPa, respectively. The calculated tensile maximum σ_{I} is higher for the

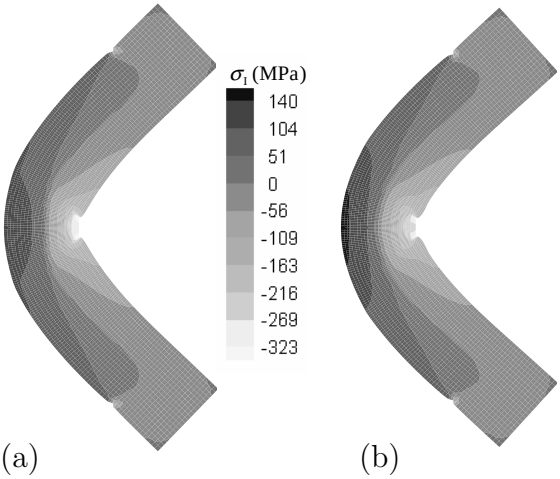

Fig. 17. Contours of maximum principal stress at a striker displacement of 14 mm for $V = 5$m/s obtained by the (a) DPB model (b) macromolecular model

macromolecular model due to the large strain hardening effect, not captured by the DPB model.

Thus, even though the global response is not significantly different between the two predictions at large deformations (see Fig. 14) the details of local deformation patterns, with associated propensity to plastic deformation, varying substantially from one prediction to the other.

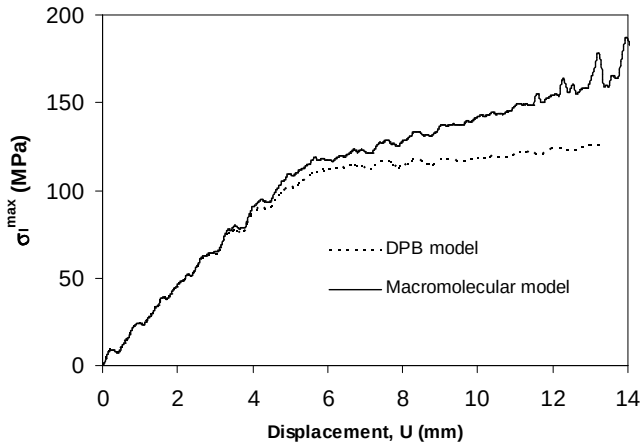

(a)

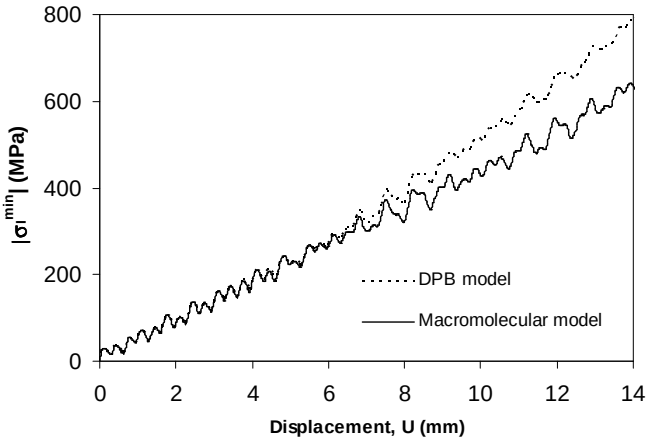

(b)

Fig. 18. Plots of (a) maximum and (b) minimum principal stress at any location of the specimen for $V = 5$m/s during impact

2. Shear-Band Formation by Plane-Strain Compression

In this section a plane strain strip under quasi-static plane strain compression were studied to observe a comparison of each models ability to capture shear band formation.

For the plane strain uniaxial compression problem shown in Fig. 19a, a polymer block of initial dimension $2A_0 \times 2B_0$ is considered. Due to a plane of symmetry about

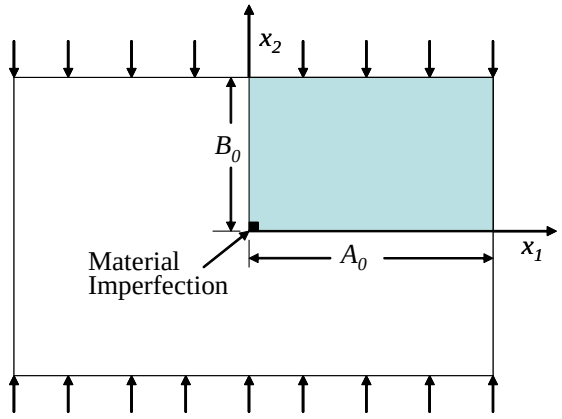

(a)

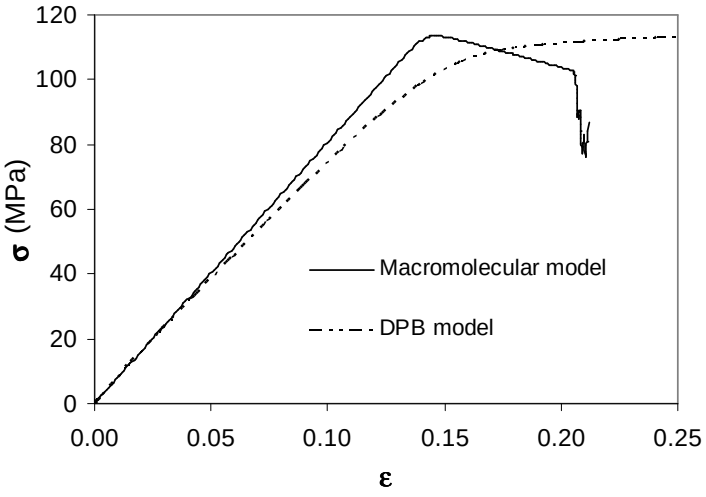

(b)

Fig. 19. (a) Geometry of the specimen and boundary conditions and (b) stress-strain response under plane strain compression for PS using the DPB and the macromolecular model.

$x_1 = 0$ and $x_2 = 0$, only the quarter symmetry of the block is analyzed. The boundary conditions, are given as

$$T_1(A_0, x_2) = 0, T_2(A_0, x_2) = 0, T_1(x_1, B_0) = 0, \dot{U}_2(x_1, B_0) = \pm V_2 \tag{2.43}$$

,where the velocity function, $V(t)$, is a ramping function with rise time t_r and final value V_2 was kept constant throughout the deformation process. T_1 is the traction over the boundary surface x_1. In all of the computations regarding the rest of the boundary value problems in this chapter, overall response is monitored by the macroscopic true strain and nominal strain rate, respectively

$$\epsilon = |ln(B/B_0)|, \quad \dot{\epsilon} = |V_2/B| \tag{2.44}$$

and by the applied true macroscopic stress,

$$\sigma = \pm \frac{1}{A} \int_0^A T_2 \left(x_1, B_0\right) dx_1 \tag{2.45}$$

where, V_2 is the applied velocity in the x_2 direction, A_0, B_0 and A, B are the original state and deformed state's dimension, respectively. To facilitate shear band initiation, localization is triggered by introducing an imperfection at the center $(x_1 = 0, x_2 = 0)$ of the specimen in a single quadrilateral element. The imperfection for the DPB and macromolecular model are prescribed by decreasing the Z_0 value and the flow stress s_0 by .01%, respectively, relative to the rest of the specimen. The material parameters are considered to be the same as those used in impact problem. To facilitate shear band initiation, element aspect ratios have been chosen to provide optimal orientation of the element diagonal [121]. Fig. 19b shows overall stress-strain response for the compressed block using the DPB and macromolecular model. The macroscopic stress-strain curves using the macromolecular model exhibit a sharp stress drop due to the initiation and rapid propagation of shear band, but the response corresponding to

the DPB model shows homogeneous response, as there is no occurrence of localized deformation due to lack of softening.

Figure. 20a shows overall stress-strain response for the three different mesh densities. The meshes consisted of 234, 2240 and 8960 elements, having 13, 40 and 80 elements in the x_1 direction and 18, 54 and 112 elements in the x_2 direction, respectively. The responses of the three meshes exhibit a sharp stress drop due to the initiation and rapid propagation of shear band without show substantial mesh sensitivity. The development and propagation of the shear band, however, differs significantly depending on mesh density. fig. 20b-d shows deformed mesh and contours of the effective plastic strain, $\bar{\epsilon}$, for different mesh densities. These plots illustrate that the course mesh of 2240 elements and the courser mesh of 234 elements are unable to exhibit multiple shear bands, in contrast to the finer mesh of 8960 elements, which captures the widening of the main shear band by the formation of multiple shear bands. This may be as the result of the finer mesh size. Analysis of the same boundary value problem using the DPB model exhibits homogenous deformation without forming any shear bands, since the this model does not account for any softening behavior.

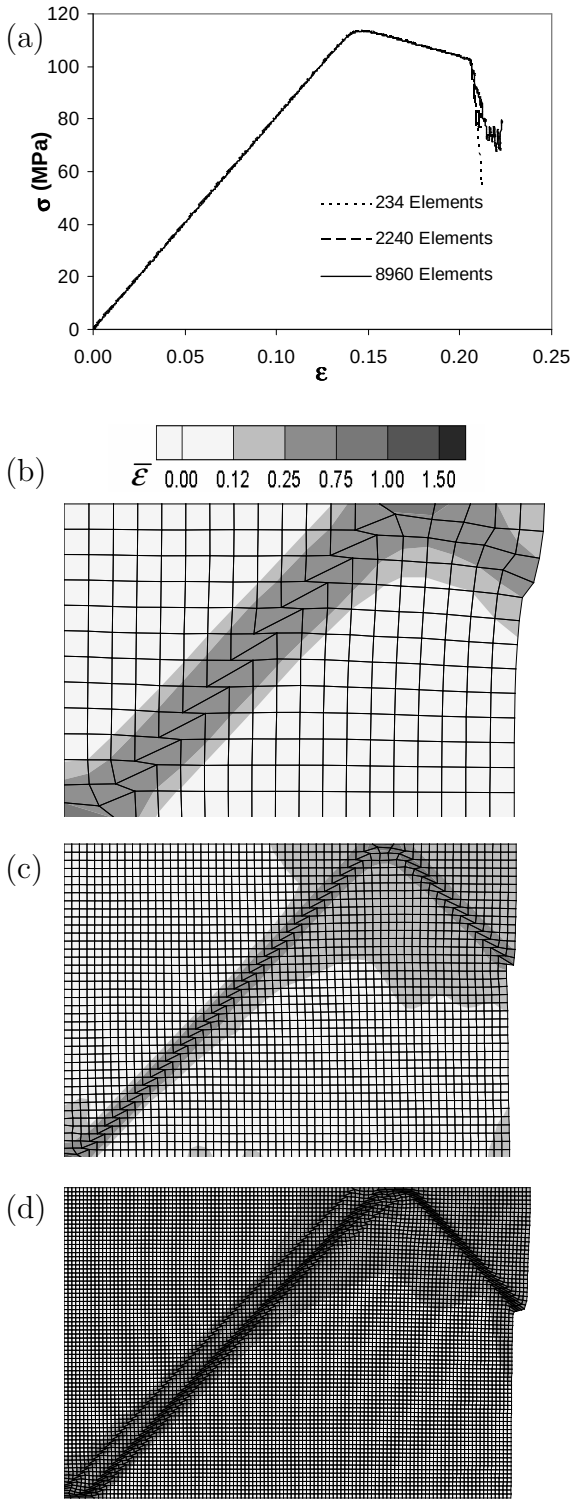

Fig. 20. Comparison of shear band propagation between different mesh densities (a) for 234 elements (b) 2240 elements and (c) 8960 elements.

Figure. 21 shows a sequences of deformed meshes and contours of effective plastic strain, $\bar{\epsilon}$, at different stages of straining(stages corresponding to the response curve is shown in the top plot in the fig. 21) for the 8960 elements mesh at various stages of straining using the macromolecular model. The plots illustrates the development of shear band within the polymer block which has initiated at 0.20 of overall strain at the location of imperfection fig. 21A. After the initial yield, the material starts to soften, and eventually large strain hardening occurs inside the band, thus, facilitating plasticity and subsequent softening in adjacent material. Thus, after the shear band initiates, it propagates further into the material fig. 21B, During propagation, the shear band is reflected from the rigid boundary fig. 21C. Upon further deformation, intense localized plastic deformation accumulates in the main shear band, which quickly strain hardens and apply a resistance to the further development of plastic deformation within the band. This results in the formation of an adjacent parallel shear band fig. 21D.

In addition, multiple fine shear bands also emerge from the imperfection, which also propagate parallel to the main shear band. These fine shear bands link up with each other and their propagation results in further widening of the main shear band.

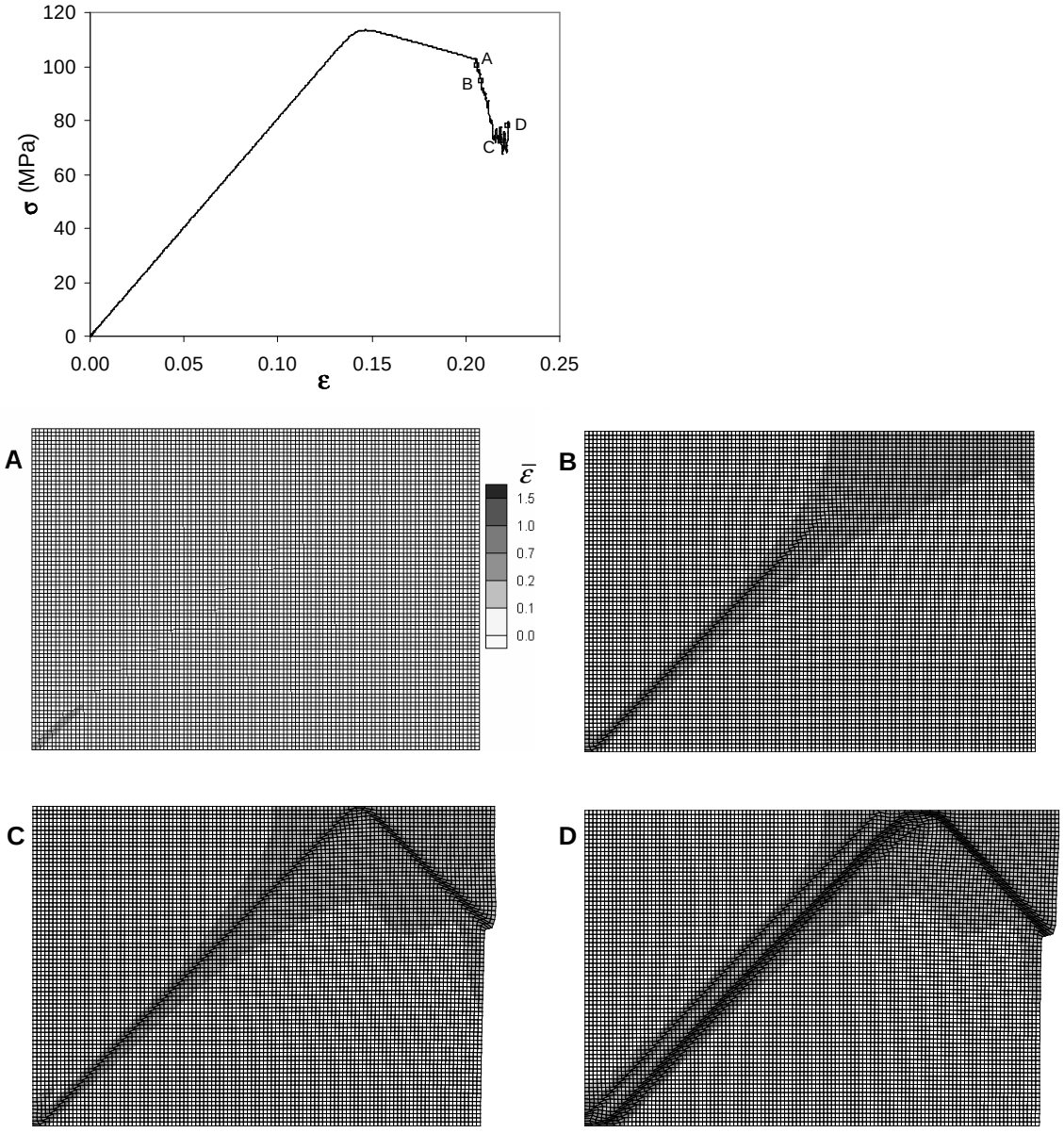

Fig. 21. Sequences of deformed meshes and effective plastic strain contours show shear band initiation and propagation under quasi-static plane strain compression.

3. The Effect of Strong Contrast in Material Properties

In addition, a unit-cell of a polymer composite with a void subjected to quasi-static plane strain uniaxial tension and zero lateral stress was analyzed to observe the effect of strong contrast in material properties on the local stress state.

To observe the effect of strong contrast in material properties, a unit-cell of a polymer composite with a void is considered (Fig. 22) for two cases. In the first case, only a polymer block with a void and in the second case, stiff fibers are embedded into the polymer block along with the void is considered, whereby the specimen is subjected to plane strain uniaxial tension along the x_2 direction. The problem is idealized for the sake of simplicity. The fibers are taken to be aligned with the loading direction and are assumed to be perfectly bonded to the matrix. Fig. 22 shows the geometry of the problem, the specified boundary conditions (Fig. 22a) and the finite element mesh (Fig. 22b). The block has a initial dimensions of $2W_0 \times 2H_0$ with a

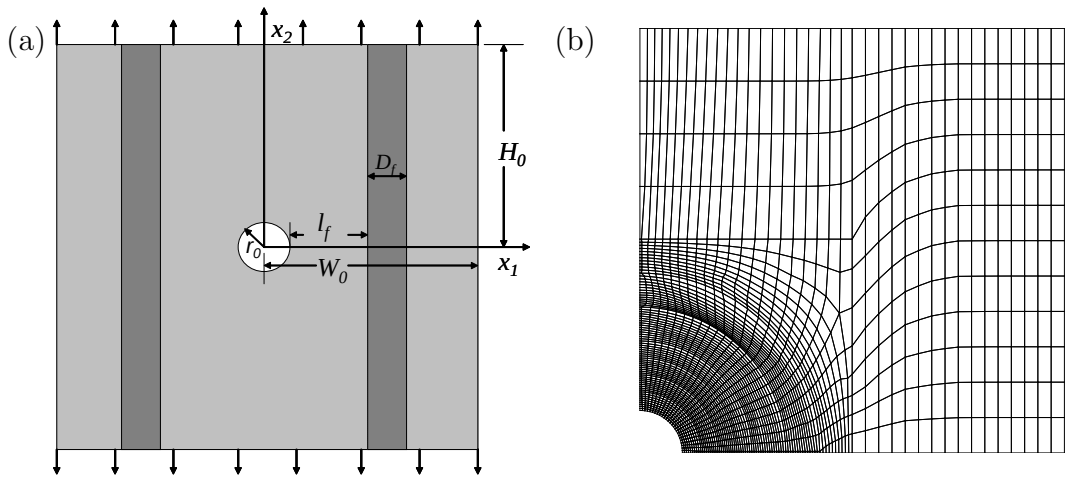

Fig. 22. (a) Boundary conditions, applied over a unit cell model containing a void and stiff fiber embedded in polymer (b) finite element mesh.

void of radius r_0. Stiff fibers of thickness D_f are placed at a distance of l_f from the

lateral edge of the void. Assuming the plane $x_2 = 0$ and $x_1 = 0$ be symmetry planes, only the quarter portion of the problem is considered. Applied boundary conditions are as follows

$$T_1(W_0, x_2) = 0, T_2(W_0, x_2) = 0, T_1(x_1, h_0) = 0 \tag{2.46}$$

$$\dot{U}_2(x_1, h_0) = +V, \dot{U}_2(x_1, 0) = 0, \dot{U}_1(0, x_2) = 0 \tag{2.47}$$

For this boundary value problem the dimensions are: $W_0/H_0 = 1$, $l_f/W0 = 0.45$, $D_f/r_0 = 1$, $r_0/W_0 = 0.05$, $V = 0.001$m/s and $t_r = 100\mu$s. The mesh shown in the Fig. 22b consists of 2222 quadrilateral elements. The material parameters used for the macromolecular model and DPB model are representative of Polycarbonate (PC) specified in table I and II.

Fig. 23 shows the overall stress-strain responses for the two cases using the DPB (Fig. 23a) and the macromolecular model (Fig. 23b). Polymer 'with fiber' (Case 2) shows stiffer response than polymer 'without fiber' (Case 1) because of the higher fiber

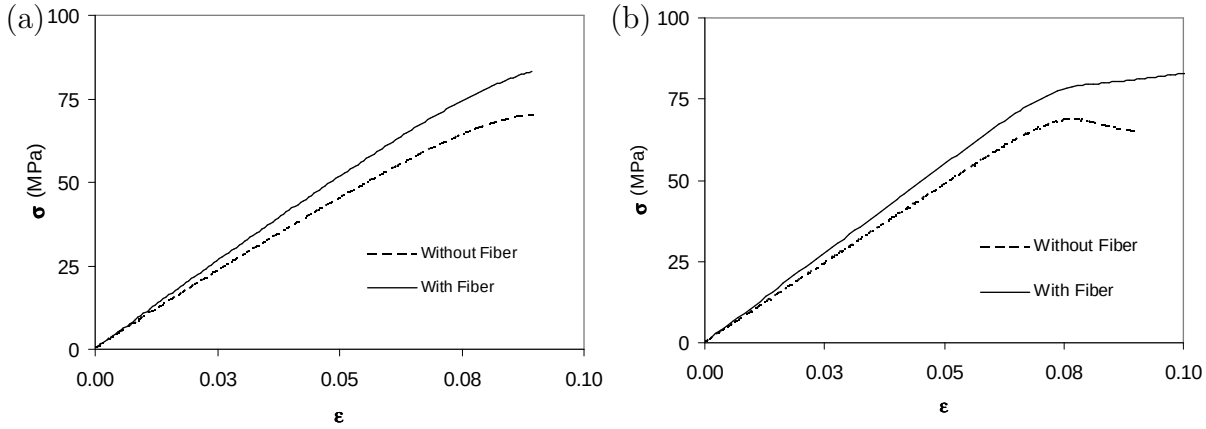

Fig. 23. Overall stress-strain response to uniaxial tension at $\dot{\epsilon} = 0.1/s$ obtained for with fiber and without fiber case by (a) the DPB model and (b) the macromolecular model

stiffness. In this case the fiber stiffness assumed, was twice (E=1820 MPa) as high as the polymer stiffness. The overall response computed using the macromolecular

model shows the softening due to local softening behavior.

Figure. 24 illustrates the effective plastic strain distributions using the DPB (Fig. 24a) and the macromolecular model(Fig. 24b) at the macroscopic strain of 0.075 for both the 'with fiber' and the 'without fiber' cases. For the 'without fiber' case both models show concentration of the plastic deformation at the lateral edge of the void, where this is highest. The plastic deformation zone then expands at an angle of 45° relative to the loading direction. The bottom figures of 24a and b illustrates the effect on the distribution of effective plastic strain due to the presence of a stiff fiber in the deformation zone. The plastic deformation zone near the fiber is suppressed slightly, suggesting that the presence of fiber only affects the deformations zone that are close to fiber. In the DPB model prediction, the maximum effective plastic strain, $\bar{\epsilon}$, at the lateral edge of the void is found to be 0.2954 for the 'with fiber' case, as compared to 0.3025 for the 'without fiber case. However, the maximum effective plastic strain is more intensive than in the DPB model prediction. The $\bar{\epsilon}$ obtained for the macromolecular model is about 0.5277 for the 'with fiber' computation, as compared to $\bar{\epsilon} = 0.53$ for the 'without fiber calculation. Very small difference in the amount of plasticity around the void edge between 'with fiber' and without fiber' computation indicates that the presence of fiber affect only the zone very near to fiber. However, intensive plastic deformation at the void's lateral edge occurs even though the global strain ($\epsilon = 0.075$) is below the strain at which the macroscopic stress-strain response achieves initial yield point ($\epsilon = 0.08$). For the macromolecular model the initial yield is followed by the immediate intrinsic softening, initially, the plastic deformation rapidly extends into the matrix in the form of narrow zone at an angle of approximately 45 degrees. As large strain hardening eventually occurs, adjacent materials become more prone to plastic deformation and subsequent strain softening, so the zone of localized plasticity propagates along the void surface. As

a result, the void changes its continuously growing elliptic shape by "bulging" out between its lateral and vertical edge. However, the DPB model computation shows that the shape of the deformed void is still elliptic like.

Fig. 25 shows the contours of the normalized effective plastic strain rate. The DPB model computation shows small traces of plastic strain rate at the void edge, however, for the macromolecular model an intense plastic flow is observed at the junction between "bulged" out and elliptic surface of the void. Fig 25 provides a closer snapshots, which illustrates a better demonstration of the change of the shape of the void using both models. Figure 26 shows the maximum principal stress , σ_{I}, contours for the 'with fiber' case obtained at different stage of straining using the DPB (Fig. 26a) and the macromolecular model(Fig. 26b). This plot illustrates that the development of a stress concentrated zone between the void and fiber region predicted by both the models. For the DPB model stress concentration initiates (Fig. 26a-top at $\epsilon = 0.03$) at the void's lateral edge, upon continuing deformation the high stress zone around the edge moves away from the void(Fig. 26a-bottom at $\epsilon = 0.075$). However, in the macromolecular prediction the stress concentration initiates (Fig. 26b-top at $\epsilon = 0.03$) at the region near void's lateral edge, then, due to on going deformation, this region undergoes local yield followed by intrinsic softening. Therefore the highly stress concentrated zone shifts away from the edge (Fig. 26b-middle at $\epsilon = 0.05$) soon thereafter, this region undergoes orientational strain hardening leading to the reestablishment of the highly stress concentrated zone at the lateral edge (Fig. 26b-bottom at $\epsilon = 0.075$). Due to this strain hardening, the maximum value of σ_{I} at the lateral edge of the void is about 173 MPa for the macromolecular model as compared to 99 MPa for the DPB model.

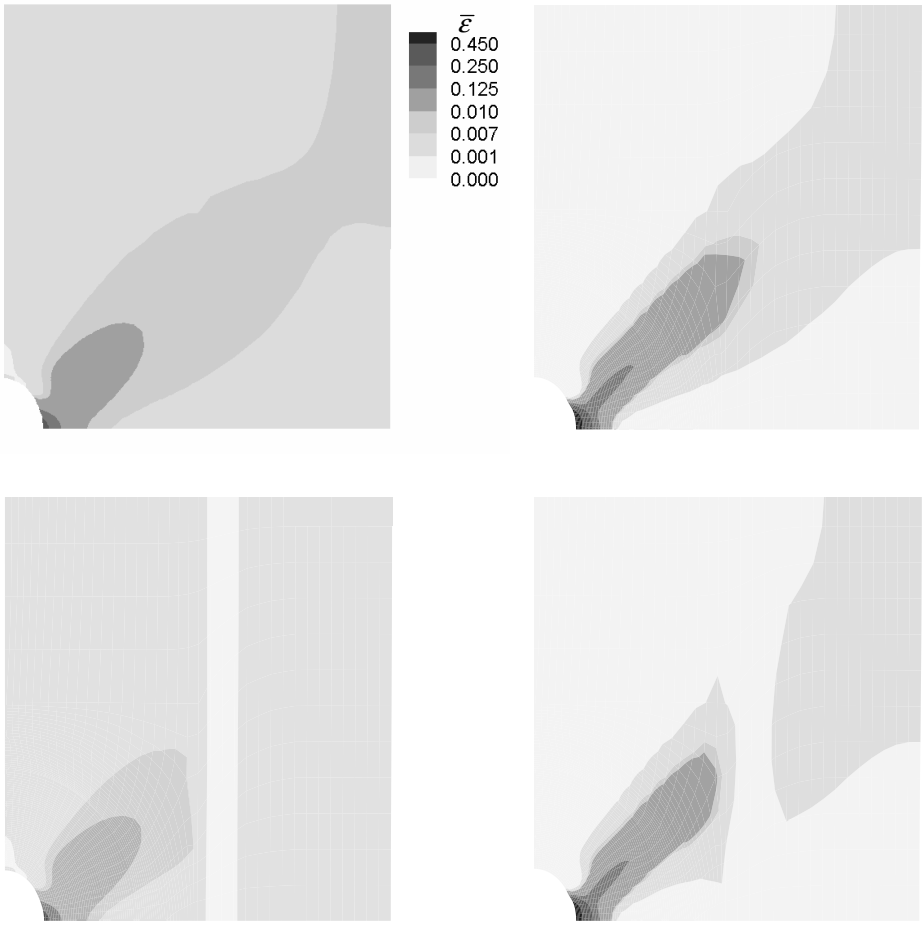

(a) (b)

Fig. 24. Contours of effective plastic strain obtained at $\epsilon = 0.075$ using (a) the DPB model and (b) the macromolecular model for "without fiber" (top) and "with fiber"(bottom) case

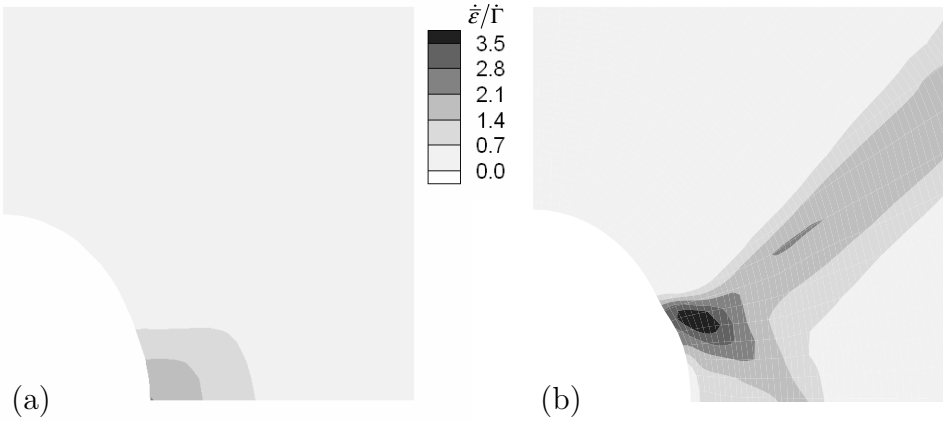

Fig. 25. Contours of normalized effective plastic strain rate at $\epsilon = 0.075$ obtained using (a) the DPB model (b) the macromolecular model.

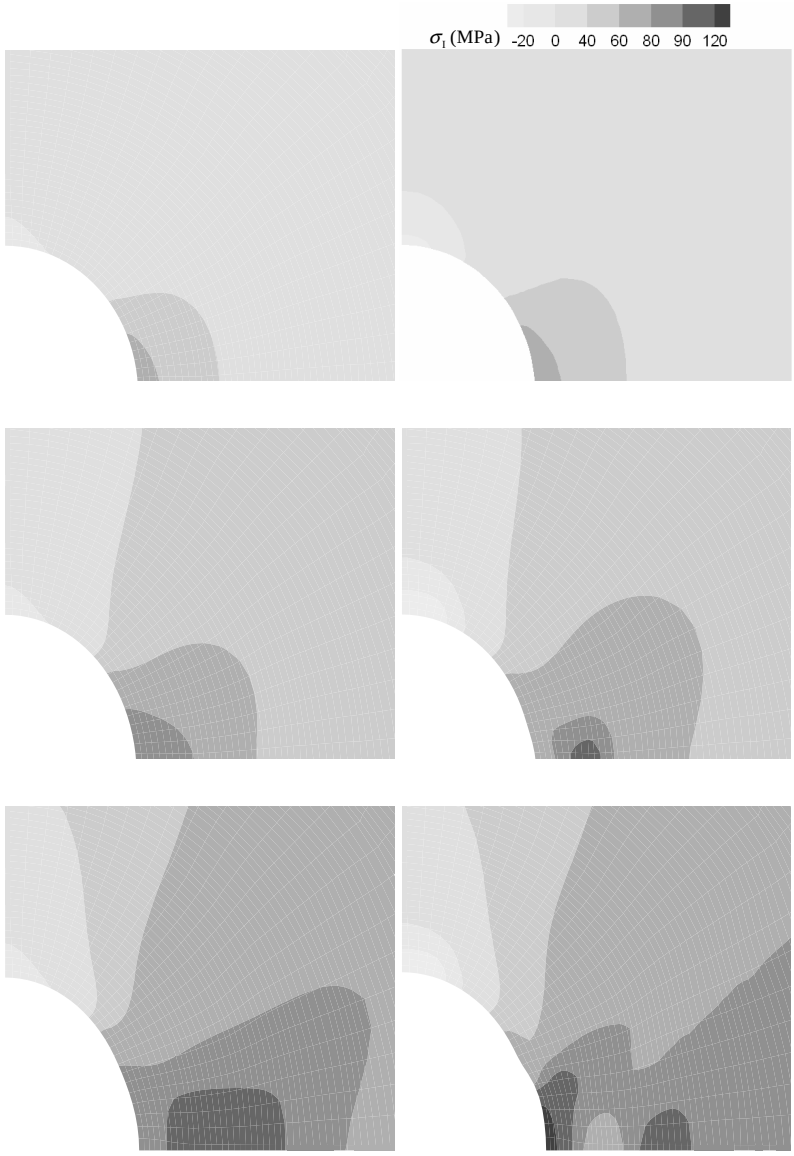

Fig. 26. Close snapshot of maximum principal stress contours using the (a) DPB model and (b) macromolecular model at the macroscopic strains of (from top to bottom) 0.03, 0.05 and 0.075

D. Discussion

Physically based constitutive equations for polymer deformation were implemented in a finite element computational framework at finite strain. The first model belongs to the Drucker-Prager type [106], with respect to how pressure-sensitive yielding is accounted for. It relies on a description of hardening proposed by Bodner and co-workers [82, 107] that has been successful in capturing aspects of metal plasticity. The second model investigated in this study belongs to the group of macromolecular models, as per the classification adopted in [123]. It combines a pressure-sensitive, disclination based strain-rate hardening law [59] with an orientational hardening model [55, 78, 79] that draws on an analogy with rubber elasticity. The macromolecular model accounts for rate- and temperature-sensitive yielding, intrinsic post-yield softening, rapid strain hardening at large deformations and anisotropic hardening. In that respect, it captures more faithfully the behavior of amorphous glassy polymers below the glass transition temperature.

Although not elaborated upon in this article, the constitutive models developed here are thermodynamically consistent. In that regard, the reader may refer to Ref. [66] in what concerns the macromolecular model for instance. Also, the constitutive equations for rate hardening in the DPB model can be improved to account for kinematic hardening as proposed in [107]. The improved model would be appropriate for metals but it would not capture the large strain behavior of polymers.

Using the constitutive models developed here the finite deformation response of a planar block of polymer material subject to dynamic impact, plane strain compression and uniaxial tension of a composite unit cell containing a void were analyzed with full account taken of the transient response.

Under dynamic impact both models exhibit similar load-displacement response,

however, locally they show significantly different behavior. The DPB model shows a more expanded plastically deformed zone due to the occurrence of the early visco-plasticity associated with isotropic hardening. With the increase of impact velocity from low to moderate level, the macromolecular model shows decrease of localized plastic deformation while the DPB model shows increasing amount of plastic deformation.

Shear band formation in a polymer block under plane strain compression is successfully captured by the macromolecular model. The intrinsic small strain softening increases the propensity to the formation and propagation of shear bands. Under such circumstances the use of a model that fully incorporates the small strain softening behavior is necessary in order to predict the shear bands. However, The DPB model did not able to predict shear band and exhibits homogeneous response under plane strain compression.

Both models yield substantially different predictions for a stiff reinforcement with a void embedded in polymer because the macromolecular model shows macroscopic softening behavior but the DPB model is not able to show. Also, the details of local deformation and subsequent deformation pattern around the void edge may substantially vary depending on which model is used. According to the observation from the analysis, the stress field around the hole is affected by the softening and re-hardening associated with polymer behavior.

Although the rate-hardening law, used in the DPB model, was initially developed for metals [82,107], it has recently been applied to polymers in composite applications [81]. In view of the small macroscopic strains supported by a composite material, the use of the DPB model to describe deformation of the polymer matrix appears as a reasonable undertaking. It should be noted, however, that although the macroscopic strains in composites are small local strains in the polymer matrix may be substantial.

The constraints imposed by stiff reinforcing elements, i.e. the fibers, may lead to the emergence and growth of localized deformation zones and consequent failure. In addition to that the DPB model does not account for strain softening which is observed in some thermoset epoxy response.

E. Conclusion

Viscoplastic models of the large strain polymer deformation were developed and used to investigate the impact, plane strain compression response of a planar block of material and local behavior of a composite unit cell with a void under plane strain tension. Constitutive models of polymer behavior were implemented in a finite element code within a unifying framework. Full transient analyses were carried out at finite strain.

- The macromolecular model captures successfully the rate, temperature and pressure sensitive yield, intrinsic strain softening followed by orientational hardening behavior of glassy polymer. The DPB model demonstrates initial viscoplastic flow accompanied by isotropic strain hardening followed by saturation of the flow stress except the strain softening phenomenon of glassy polymers.

- Both models yield similar macroscopic behavior under low and moderately high velocity impact loading. But local behaviors may vary substantially depending on which model is used.

- The response to compression of a polymer block is very much dependent upon the type of model used. The intrinsic softening behavior characteristic of glassy polymers at small strains favors the formation and propagation of bands of intense deformation. This behavior is only captured by the macromolecular model.

- The presence of a stiff reinforcement in a unit cell of polymer containing a void effects only the region near the reinforcement. The macromolecular model captures interesting macroscopic and microscopic behavior including the "bulging out" of void due to the strain softening effect.

The results compiled in this study are part of an ongoing effort at investigating the damage in polymer based composites with the presence of manufacturing induced defects. The focus here was demonstrate the capability of the framework to capture the deformation behavior of glassy polymers.

Table I. The material parameters of Polycarbonate (PC) and Polystyrene (PS) used in the macromolecular model

Material parameter	Units	Description	PS	PC
s_0	MPa	initial value of athermal shear strength	97	97
s_{ss}	MPa	saturation value of athermal shear strength	45	76
h	MPa	slope of yield drop	81	500
$\dot{\epsilon}_0$	s^{-1}	reference strain rate	2×10^{15}	2×10^{15}
A	K^{-1}	rate-sensitivity factor	296	240
α	–	pressure sensitivity parameter	0.08	0.08
C^R	MPa	rubbery modulus	7.25	12.8
N	–	number of rigid links between entanglements	7.0	2.8

Table II. The material parameters of Polycarbonate (PC) and Polystyrene (PS) used in the DPB model

Material parameter	Units	Description	PS	PC
Z_0	MPa	Initial value of hardening	400	100
Z_1	MPa	Saturation value of hardening	1085	895
q	–	Slope of the hardening	200	279
γ_0	–	Initial value of pressure parameter	.08	.08
γ_1	–	Saturation value of pressure parameter	.08	.08
q'	–	slope of the pressure parameter	200	279
$\dot{\epsilon}_1$	s^{-1}	Reference strain rate	2×10^{15}	2×10^{15}
n	–	Rate sensitivity parameter	.93	.93

CHAPTER III

A COMPUTATIONAL FRAMEWORK FOR ANALYZING FRACTURE IN GLASSY POLYMERS

A. Introduction

Damage in composite materials and structures is, in general, very complicated. Evaluating such damage involves multiple modes such as matrix cracking, fiber matrix debonding and delamination between plies. Understanding the mechanisms of damage initiation and progression are important for analyzing the cost effectiveness of composite structures, since these mechanisms depend upon the defects produced by manufacturing that mainly determine cost. The damage processes in polymers and their composites are, essentially, multi-scale in nature. At the nanometer scale, damage occurs by the formation and breakage of craze structures or through shear yielding that can be predicted by using a molecular dynamic simulation [93]. At the macroscopic level, damage is treated using continuum mechanics based on homogenized models [37–41, 126]. In spite of the development of efficient computational software and hardware, investigation of failure mechanisms at the nanometer scale through MD simulation is very expensive and is limited by the size of the microstructure. At the other extreme, continuum damage models, by their nature, do not provide any knowledge of damage initiation and progression. In between, at the mesoscopic level, individual representations of fibers and matrix appear to be efficient in predicting damage initiations and progressions in polymer based composites [127–129]. However, most of this type of work does not incorporate the mechanisms at fine scales (crazing, shear yielding) in predicting matrix crack initiation.

The objective of this study is to develop and implement a methodology for inves-

tigating the failure of amorphous glassy polymers by incorporating fine scale damage mechanisms. Failure in glassy polymers can occur either by crazing or by a ductile fracture process through shear band formation. Craze formation is favored at low homologous temperatures and is sensitive to pressure [7, 90, 130]. On the other hand, at a sufficiently moderate temperature, the polymer undergoes large strain with a distinct softening regime [55]. During this softening stage, the available molecular free volume is rearranged in such a way that any possibility of craze formation is essentially precluded at larger strains, even if the stress is high. Instead, final fracture occurs by a ductile failure mechanism preceded by shear banding.

The study of craze formation and growth has received much attention over the past three decades [7, 60, 88, 90, 95, 96, 99, 103–105, 130], each dealing with one or more stages of crazing. In essence, a craze is a planar crack like defect, where the two faces are linked by thin fibrils with a stress bearing capacity. Figure 27 shows a schematic picture of the stress strain response of an assumed craze continuum and the development of the craze structure under tensile stress. Craze initiates by the formation of voids under the dominance of local hydrostatic stress due to the presence of any flaws or defects (Fig 27A). The craze growth process involves two mechanism, i.e., i) the widening of craze structures in an extensional deformation mode by widening the already formed fibril due to a drawing of new polymer chains from the bulk to the craze structure (Fig 27B) and ii) advancement of the craze tip perpendicular to the maximum principal stress direction by forming new voids and fibrils through the craze initiation. Upon continuing the craze growth process, the crack initiates in the craze structure due to the breakage of the old thin fibrils (Fig 27C). The craze growth process accompanied by the old fibril breakage causes a gradual loss (see the schematics of the response of a craze structure in Fig 27) of the load bearing capacity of the craze structure (Fig 27D). Finally, when the

remaining active fibrils are unable to bear any load, all of them break at once and the whole continuum fails (Fig 27E). The craze initiation mechanism is probably the most

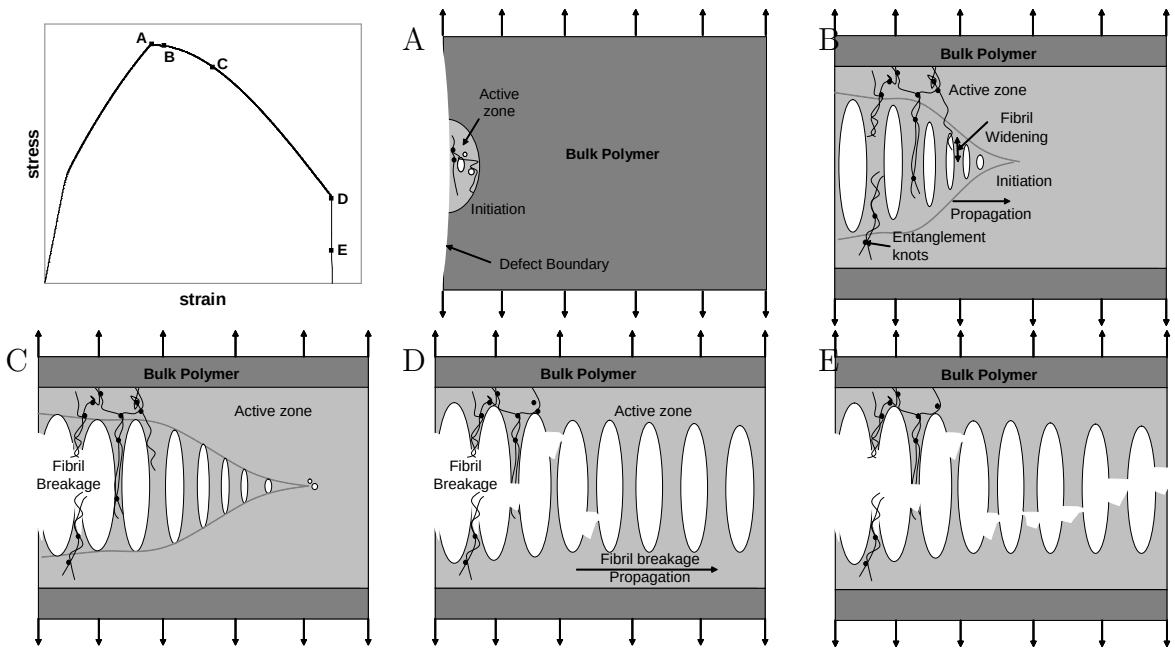

Fig. 27. Schematics of stress-strain response and different stages of craze life for a crazed structure. Stage A: Craze initiation near defect, Stage B: Formation of new fibrils, their widening and propagation to the direction perpendicular to the loading C:Widening and Breakdown of old fibrils, formation of new fibril through initiation, Stage D: Breakdown and widening of old fibrils only, Stage E: sudden breakage of all the remaining fibrils in the structure.

controversial stage of the craze structure. A number of craze initiation models have been developed during the past several decades [7,60,88,96,102,103]. Though almost all the criteria included temperature dependant material parameters, none of the parameters is the function of temperature, as we will see discussed below. Sternstein et al. [7,102] developed the earliest craze initiation criteria based on an experiment on PMMA plates with a circular hole under a biaxial plane stress, which states that the

craze initiates when a stress bias 'σ_{b}' reaches a pressure and temperature dependant critical value, $\sigma^c(\sigma_{kk})$,given by

$$\sigma^c\left(\sigma_{kk}\right) = A_1 + \frac{A_2}{\sigma_{kk}} \tag{3.1}$$

where A_1 and A_2 are temperature dependant material parameters and $\sigma_{\mathrm{b}} = |\sigma_1 - \sigma_2|$. The physical interpretation of 'σ_{b}' is not clear as mentioned by Oxborough [103] because this quantity is the difference between the maximum and intermediate principal stresses for tensile stress state and between the maximum and the minimum principal stresses when either σ_1 or σ_2 is compressive. Thus, the evaluation of 'σ_{b}' under triaxial stress state is also unclear. Therefore, this criterion is only applicable for the plane stress case, i.e., when $\sigma_3 = 0$. Oxborough-Bowden developed a critical strain based craze initiation criterion based on their experiments on PS. They postulated that the critical condition for craze nucleation is when maximum principal tensile strain, ϵ_1, reaches a mean normal stress dependent critical value, $\epsilon_{cr}\left(\sigma_{kk}\right)$.

$$\epsilon_1 = \epsilon_{\mathrm{cr}}\left(\sigma_{kk}\right) > 0, \qquad \epsilon_{\mathrm{cr}} = X' + \frac{Y'}{\sigma_{kk}} \tag{3.2}$$

where X' and Y' are temperature dependant material parameters. ϵ_1 is obtained from the isotropic elastic relationship, given by

$$\epsilon_1 = \frac{1}{E}\{\sigma_1 - \nu\left(\sigma_2 + \sigma_3\right)\} \tag{3.3}$$

where E and ν are the Young's modulus and Poisson's ratio, respectively.

Geometrical imperfections or heterogeneities (e.g., voids) in the material have a major role in influencing the local stress states and the sites of craze initiation. Therefore, critical values of stress or strain based criteria of craze initiation are difficult to determine with precision from experiments [88, 95]. Argon and his co-workers postulated that craze initiation will occur when the local mean normal stress is positive,

$\sigma_{kk} > 0$, and when the local equivalent shear stress reaches, $\bar{\tau}$, a pressure dependent critical value given by

$$\bar{\tau} = \sqrt{(1/2)\boldsymbol{\sigma}' : \boldsymbol{\sigma}'} = \bar{\tau}_{\rm cr}\left(\sigma_{kk}\right) > 0, \qquad \bar{\tau}_{\rm cr} = \frac{A'\sigma_y}{B' + 3\sigma_{kk}/2\sigma_y Q} \tag{3.4}$$

where $\boldsymbol{\sigma}'$ is the deviatoric part of the Cauchy stress, $\boldsymbol{\sigma}$, A' and B' are temperature dependant material parameters, σ_y is the yield stress, and $Q = .0133$ is a factor describing resistance to further cavitation in a porous region when a large deviatoric stress near the yield level is present. Although this model is associated with the molecular physics of craze initiation, as noted by Gearing et. al., this criterion does not reveal the required microscopic state of stress during craze initiation. In our study, we have utilized the craze initiation model recently developed by Gearing-Anand [60].

The craze growth process involves two mechanisms, i.e., i) craze tip advancement by the expansion of the craze structure forming new fibrils, and ii) craze thickening by separating the craze surfaces due to widening of the fibrils. Argon [88, 96] postulates that the craze tip advance occurs by Talyor's meniscus instability, by repeated formation and expansion of voids at the front of the craze tip. More recently, Kramer [90] suggested that fibril formation and widening occurs due to the drawing of new polymer chains from a zone called the 'active zone', near the craze boundary, into the fibrils, because of the disentanglement of polymer chains in the active zone. Based on this mechanism, Kramer assumed that the 'active zone' of the craze structure acts like a non-newtonian fluid and several viscoplastic flow laws have been developed. Recently van der Giessen and co-workers [99, 131] developed a rate dependant, craze widening law which was implemented in a 'cohesive surface' framework, based on the same idea of craze growth process suggested by Argon and Kramer. Their craze widening model accounts for both the craze widening and craze tip advancement. One significant aspect of their model is the incorporation of softening behavior in the

craze structure, which ensures that the craze tip advancement is the natural outcome of the craze widening process. On the basis of the previous literature of Knauss [132], Telenkov et al. [133] and Warren [134], van der Giessen and his co-worker assumed that craze structures undergo softening after initiation, followed by a constant stress. Knauss [132] assumed a continuum, which consists of a crack, a cracked tip bridged with fibrils, and a craze tip which assumes that stress drops after craze initiation and continues to drop until the whole structure fails. One peculiar feature of craze flow behavior is the predominantly extensional deformation that accompanies craze growth and breakdown, a behavior that is reminiscent of the final stages of fracture by void coalescence in plastically deforming solids [135]. Recently, Anand and Gearing developed a craze widening model that incorporates this deformation mode in a constitutive framework [60].

The craze breakdown mechanism is also highly debated among the researchers who are involved in describing polymer fracture through crazing. Many criteria [60,91, 98,99,104,105,131] have been developed to capture craze breakdown at the individual fibril level incorporating the mechanism of disentanglement of polymer chains, the fibril extension ratio, the effect of cross tie fibrils, the scission of polymer chains, etc. Williams [98] suggested that craze breakdown occurs when the craze fibril elongation reaches a critical value. Kramer and Berger [91] observed through experiment that fibril breakdown follows Weibull distribution with respect to the plastic strain within the craze structure, and the maximum width of the craze fibril at breakdown depends upon the molecular weight due to entanglement loss during craze widening. According to Doll et al. [92],], the maximum craze opening displacement during breakdown has been found to be constant over a wide range of crack tip velocities. Based on their [91,92,98] observations, van der Giessen and coworkers [99,104,131], Boyce and coworkers [136], and Anand and coworkers [60] all followed an ad-hoc critical craze

width for the craze breakdown. The value of these ad-hoc criteria governing the breakdown is difficult to determine with a satisfactory level of precision from current experiments. Also, the conversion of the critical craze width from the individual fibril level to a continuum of craze structure that contains many fibrils is not clear.

The purpose of this study is to implement an existing model, to be called the reference model, and a new model of the crazing behavior to constitute a computational framework to predict the fracture response of glassy polymers. For the new model, we have utilized a continuum constitutive relationship that accounts for three ingredients of crazing: craze initiation, widening and breakdown. Instead of modeling each stage of craze separately, we have followed an existing criterion for craze initiation and supplemented it with a new craze flow rule [60] for craze widening, with craze breakdown already taken care of. The new craze model does not account for details fine scale craze micromechanism, but rather presents an average over a representative volume element (see Fig 27) considered to describe inelastic deformation of a craze structure. Prior to implementation of the crazing model, we have modified the original macromolecular model described in Chapter II. The original version of the large strain polymer deformation model is supplemented with a modified version of the evolution equation of athermal shear strength in order to allow nonlinear viscoplastic behavior before craze initiation.

The organization of this chapter is as follows. In Section B we will describe the reference craze model and the new craze model. The modification of the original macromolecular model will be described in Section C. In Section D, finite element implementation of the models will be discussed. Section E will be used to demonstrate the capability of the computational framework to predict polymer deformation and fracture. Discussion of the results will be presented in Section F. Finally, we will draw conclusions in Section G.

B. Constitutive Models for Polymer Fracture

1. Reference Craze Model

First, we have started with a reference craze model developed by [60] that accounts for craze initiation, growth and breakdown. Their craze initiation criterion is based on the original idea of Oxborough-Bowden [103]. Gearing-Anand modified Oxborough-Bowden's critical strain based craze initiation criterion (Eq. 3.2) to critical stress based criterion, where craze initiation is taken to occur when the maximum principal stress σ_{I} attains or exceeds a (positive) pressure–dependent critical value, σ^c, while the mean normal stress $\frac{1}{3}\sigma_{kk}$ is positive. The pressure dependence of σ^c is specified by

$$\sigma^c\left(\sigma_{kk}\right) = c_1 + \frac{c_2}{\sigma_{kk}} + c_3\sigma_{kk} \tag{3.5}$$

The craze flow rule developed by Gearing accounts for the purely extensional deformation mode that is associated with the drawing of new polymer chains from an "active zone" near the craze/bulk boundary into the craze fibrils leading to a widening of the craze fibril. Therefore, after craze initiation there will be a transition from the viscoplastic flow rule to the craze flow rule. This extension of the craze fibrils occurs along the direction, $\hat{\mathbf{e}}_{\mathbf{1}}$, of the maximum principal stress

$$\mathbf{D^p} = \dot{\epsilon}^{\mathrm{cr}}\hat{\mathbf{e}}_{\mathbf{1}} \otimes \hat{\mathbf{e}}_{\mathbf{1}} \tag{3.6}$$

The evolution of the effective strain rate, $\dot{\epsilon}^{\mathrm{cr}}$, specifies the rate-dependent response during craze flow as:

$$\dot{\epsilon}^{\mathrm{cr}} = \dot{\epsilon}_0^{\mathrm{cr}}\left\{\sigma_{\mathrm{I}}/s_{\mathrm{cr}}\right\}^{\frac{1}{m}} \tag{3.7}$$

where $\dot{\epsilon}_0^{\mathrm{cr}} = \dot{\bar{\epsilon}}/\dot{\epsilon}^{\mathrm{cr}}$ is a reference craze strain rate chosen to ensure continuity of plastic stretching at the transition from shear flow to craze flow. Also, m is a strain-rate

sensitivity parameter and $s_{\rm cr}$ is the craze flow resistance taken as a constant [60]. Following [13], a final fracture is imposed using an ad hoc critical strain criterion:

$$\bar{\epsilon} \geq \bar{\epsilon}_{\rm f}. \tag{3.8}$$

2. New Craze Model

For the new craze model we have considered the craze initiation criterion developed by Gearing-Anand [60]. Here, in this case, also after the craze initiates, there will be a transition from the viscoplastic flow rule to the craze flow rule. The craze flow rule developed here accounts for the purely extensional deformation mode that is associated with the cumulative effect of the craze fibril growth and breakdown. This extension of craze fibrils occurs along the direction, $\hat{\mathbf{e}}_{\mathbf{1}}$, of the maximum principal stress, and craze flow is governed by following the craze potential. A single craze flow potential is used for the form:

$$\Phi_{\rm c} = \sigma_{\rm I} - \eta\bar{\sigma} \tag{3.9}$$

consistent with the change in deformation mode that accompanies craze growth and breakdown, where $\bar{\sigma}$ is an effective craze stress and η is a function of damage variable χ, controls the drop of stress with damage, assumed to be

$$\eta = f(\chi) = 1 + n_1\chi^2 \tag{3.10}$$

where, χ is the damage variable that describes the volume fraction of active fibrils in the craze structure that is a cumulative effect of the fibril formation and fibril breakdown. n_1 is a parameter that depends upon the fraction of active fibrils remaining in the craze structure that suffers a complete loss of stress bearing capacity. The

following evolution equation is adopted for the damage variable χ:

$$\dot{\chi} = C\,(\chi_1 - \chi)\,\dot{\bar{\epsilon}} \tag{3.11}$$

where χ_1 is the final value of the damage variable, the value χ ranges from 0 to 1 from a no damage point to a fully damaged continuum, respectively, and C is the slope of change in the χ value. The evolution of the effective strain rate, $\dot{\bar{\epsilon}}^{\rm cr}$,is assumed to be of the following form

$$\dot{\bar{\epsilon}}^{\rm cr} = \dot{\bar{\epsilon}}_0^{\rm cr} \left\{ \frac{\bar{\sigma}}{s_{\rm cr}} \right\}^{\frac{1}{m}} \tag{3.12}$$

One feature of the new model is that the stress bearing capacity vanishes as a natural outcome to the craze growth process (as described by the variable χ). This simplifies the numerical implementation of the crazing model in a finite element program beyond being more physical than currently used empirical failure criteria.

C. Modification of the Original Macromolecular Model

The model we have used in Section 2 for large strain polymer deformation is linear before it reaches the yield peak. However, in reality, the polymer exhibits a nonlinear plastic stress-strain response before the peak yield [6, 60, 78]. This small scale plastic deformation can be neglected for very large strains but crazing in glassy polymers occurs before the polymer reaches the yield peak, and at the small strain regime where the effect of the small viscoplastic deformation may play a role in the fracture mechanism. We have modified the original model by changing the evolution equation of athermal shear strength, s, given as

$$\dot{s} = h(\bar{\epsilon}) \left(1 - \frac{s}{s_1} \right) \dot{\bar{\epsilon}} + g(\bar{\epsilon}) \left(1 - \frac{s}{s_2} \right) \dot{\bar{\epsilon}} \tag{3.13}$$

where, s_1 is the saturation value of s when material reaches the peak yield and s_2 is the saturation value of the isotropic softening. The initial value of s is s_0. $h(\bar{\epsilon})$ and $g(\bar{\epsilon})$ are heaviside like functions (see Fig 28) that controls the isotropic hardening before the peak yield and the isotropic softening after the peak yield, respectively, given as

$$h(\bar{\epsilon}) = -h_0 \left\{ \tanh\left(\frac{\bar{\epsilon} - \bar{\epsilon}_p}{f\bar{\epsilon}_p} \right) - 1 \right\} \tag{3.14}$$

$$g(\bar{\epsilon}) = h_0 \left\{ \tanh\left(\frac{\bar{\epsilon} - \bar{\epsilon}_p}{f\bar{\epsilon}_p} \right) + 1 \right\} \tag{3.15}$$

where h_0 is the slope of the hardening and softening, f controls the slope of the tran-

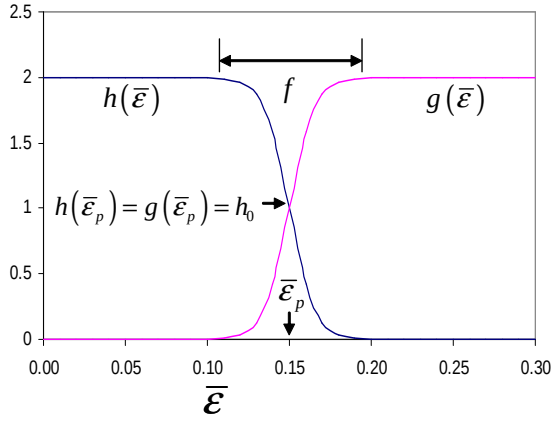

Fig. 28. Functions $h(\bar{\epsilon})$ and $g(\bar{\epsilon})$

sition from isotropic hardening to isotropic softening and $\bar{\epsilon}_p$ controls the accumulation of plastic deformation before the upper yield point.

D. Implementation

We have implemented the constitutive models, described above, in the stand alone explicit finite element code, suitable for large strain analysis. Detailed descriptions of the explicit finite element formulation are offered in Section 2. In the plane strain

specialization of this implementation, the discretization is based on the linear displacement of triangular elements arranged in quadrilaterals of four crossed triangles [108]. The constitutive updating is based on the rate tangent modulus method of [110] giving the Jaumann rate of Cauchy stress as

$$\overset{\nabla}{\boldsymbol{\sigma}} = \mathbf{L}_{\tan} : \dot{\mathbf{D}} + \dot{\mathbf{Q}} \tag{3.16}$$

where $\mathbf{L}_{\tan}$ and $\dot{\mathbf{Q}}$ are tensors of rank 4 and 2, respectively, which depend upon the constitutive model. $\mathbf{L}_{\tan}$ is given by

$$\mathbf{L}_{\tan} = \mathbf{L} - \frac{\xi}{1+\xi}\frac{\mathbf{PP}}{H}, \quad \dot{\mathbf{Q}} = \frac{\dot{\bar{\epsilon}}_t}{1+\xi}\mathbf{P} \tag{3.17}$$

Further details about the rate tangent formulation of crazing models are given in the Appendix. The constitutive updating method permits a unifying presentation of both macromolecular and crazing models. In our implementation, initially the pre-craze viscoplastic flow of material due to the modified macromolecular model is allowed. When the maximum principal stress reaches a pressure and temperature dependent critical value, craze will initiate and after craze initiation there will be a transition from the macromolecular based viscoplastic flow rule to the craze flow rule, in which craze widening and breakdown will be taken care of in the direction of maximum principal stress. Passing from the viscoplastic to craze flow behavior is presently dealt with in an explicit way, whenever the craze initiation criterion is reached at the current integration point.

This method is similar to that used in [137] for implementing improved ductile fracture models. The simultaneous occurrence of inelastic deformation due to shear yielding and crazing were allowed in the implementation.

Finally in order to simulate complete failure of the craze structure, we have used a simple rule: for circumstances in which the local damage, χ, reaches a critical value,

χ_f, fracture will be taken to occur. Material failure subsequent to craze breakdown is implemented via an element vanish technique. When the failure condition is met in an element, the element is taken to vanish.

E. Results

1. The Modified Macromolecular Model

We start out by illustrating the behavior prediction using the modified macromolecular model under plane strain compression. The values of shear modulus μ of the material is determined from the relationship given by [65]:

$$log(\mu) = log(1205) - .00118/[K](T - 298[K]) \tag{3.18}$$

The parameter $s_0 = 70$MPa is assumed constant for all temperatures, s_1 is estimated from the relation $s_1 = .063\mu/(1-\nu)$, here the factor .063 and $s_1/s_2 = .90$ estimated from the reasonable fit with the experimental data for plane strain compression for PMMA [6]. The parameter $\nu = .33$, $\alpha = .2$ is specified in the literature [55, 65] for PMMA. Rate sensitivity parameter $\dot{\epsilon}_0 = 2 \times 10^{13}$, and other parameters $A = 225K/$MPa, $\bar{\epsilon}_p = .15$, $f = .1$, $h_0 = 1300$MPa, $C^R = 9.5$ and $N = 4.1$ are also estimated for reasonable fit. Figure 29 illustrates the stress-strain curves which are generated by a single element computation of plane strain compression using the original and modified macromolecular models, and are compared to experimental stress-strain curves [6].

The responses obtained by using both of the models are able to capture the intrinsic strain softening, followed by strain hardening. However, the original macromolecular model is not able to demonstrate the non-linear regime before the peak yield, as observed in the experimental curves; the original macromolecular model

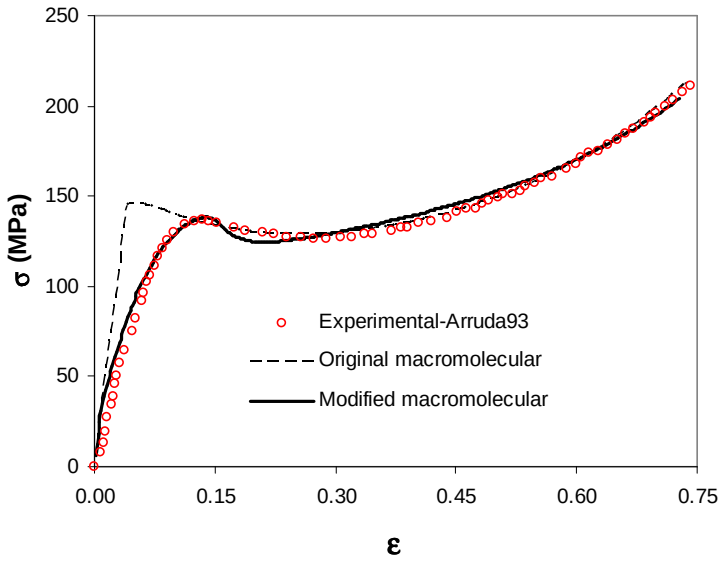

Fig. 29. Comparison between the stress-strain responses of PMMA, using the original macromolecular model, modified macromolecular model and the experimental response under plane strain compression

predicts linear elasticity before the peak yield. The modified macromolecular model successfully captures the early non-linear visco-plasticity before peak yield and predicts yield as a distributed event rather than a sudden event, as in the original case. The macroscopic strain at the onset of peak yield is observed to be approximately 13.3% in the experimental curve, while the original model predicts the peak yield at 5% (65% less than the experimental prediction), and the modified model predicts the value to be 13.65%. Because of this, at a strain lesser than the peak yield, the original model predicts strain softening, while the experimental observation and the modified model predict a strain hardening response. This can be critical for any strain based fracture mechanism that occurs before peak yield.

Figure 30 demonstrates the ability of the modified model to predict the strain rate and temperature dependant initial yield, the viscoplastic behavior before peak yield and the peak yield. Figure 30a illustrated the rate dependent yield and stiffer

response for higher strain rate. Figure 30b illustrates the rate dependent yield

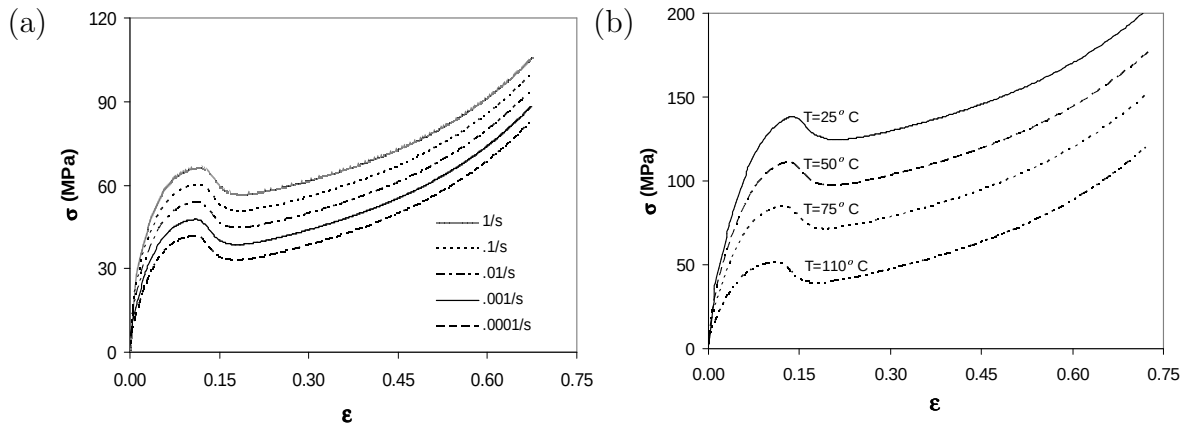

Fig. 30. Stress-strain responses of PMMA for (a) plane strain tension at T= 90°C for different strain rates (b) plane strain compression for different temperatures at $\dot{\epsilon} = .001/\text{s}$

and stiffer response for the higher strain rate. Figure 4b demonstrates the temperature dependent yield during the plane strain compression for a very low strain rate ($\dot{\epsilon}$ =.001/s) case.

2. Crazing Models

Single element computation is done to understand the behavior of the craze structure using the reference craze model and the new craze model. For both cases, the modified macromolecular model is used to obtain pre-craze behavior. The uniaxial tensile response, with crazing fully accounted for, is shown in Fig. 31. The material parameters used for the reference craze model were taken from [60] and are representative of PMMA with $c_1 = 45$ MPa, $c_2 = 786$ MPa^2, $c_3 = 0$, $m = 0.04$, $s_{\text{cr}} = 200$ MPa and $\bar{\epsilon}_{\text{f}} = .005$. The material parameters for the new craze model that are common to the reference craze model are taken to be the same. The additional material parameters

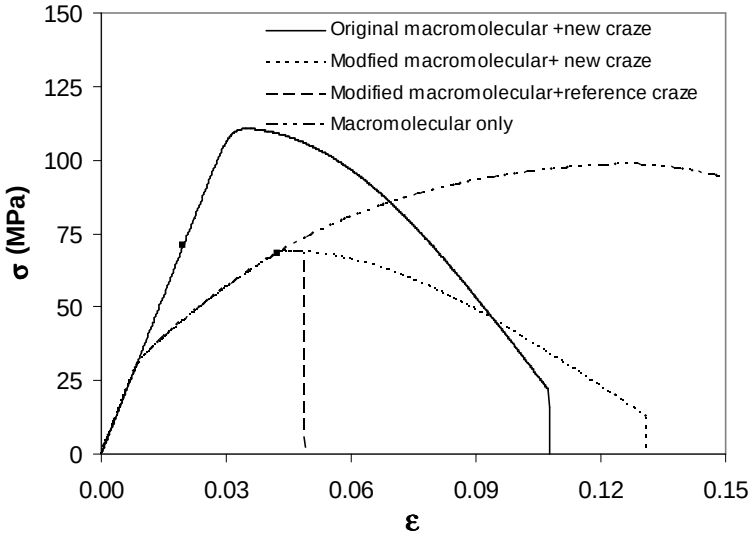

Fig. 31. Stress-strain responses using the crazing models. Solid squares denote craze initiation point

have the following values: $C = 7.5$ and $n_1 = 2.78$. The value of n_1 is estimated from the state of damage, $\chi = \chi_f$, that corresponds to a complete loss of the stress bearing capacity of the craze structure. Typical fibril volume fractions for glassy polymers craze structure ranges from .1 to .6 [90,130,138]. Thus, we have considered $\chi_f = .60$, at which the stress in the craze structure will drop down to zero. For both crazing models, the material failure subsequent to craze breakdown is implemented via an element vanish technique. When the failure condition is met in an element, nodal forces in that element are gradually reduced to zero. For the case of the new craze model, element vanishing is activated when χ reaches 80% of χ_f for better numerical stability.

The dashed line corresponds to the response using the reference craze model with the modified macromolecular model. Clearly, before the breakdown (Eq. 3.8) the stress saturates to some value equal to the critical stress necessary for craze initiation (black solid squares). This is so because under uniaxial tension, the hydrostatic

component of the stress and resistance to the craze flow remain constant, which is not effective at causing softening. In Fig. 31 the dotted line corresponds to the response using the new craze model. After the initiation of craze, stress gradually drops upon continuing deformation, which demonstrates the capability of the new model to capture the cumulative damage process of a craze structure due to fibril breakage. Behavior of a craze structure using the original macromolecular model with the modified craze model is also shown for comparison purposes. The response of the original macromolecular model with the new craze model continues to show linear elastic behavior after the craze initiation until craze induced softening takes place. For the original at the onset of craze initiation there is almost a little or no accumulation of plastic strain. The response remains almost linear before the accumulation of necessary plastic strain for the softening to occur. Also, the peak stress (110 MPa) in the element supersedes the value of the peak yield stress (98 MPa) of that temperature ($T = 25^o$C) and strain rate($\dot{\epsilon} = .01/s$). Figure 32 shows the stress strain behavior obtained by the single element computation for plane strain tension, using the new craze model with the modified macromolecular model. Craze initiation stress decreases with an increase in temperature [86, 102, 103], so we have assumed linear dependence of the c_1 and c_2 parameters given by:

$$c_1(t) = m_1 \times T + k_1 \tag{3.19}$$

$$c_2(t) = m_2 \times T + k_2 \tag{3.20}$$

where m_1 and m_2 are the slopes and k_1 and k_2 are the intercepts of the linear equations. Oxborough-Bowden [103] obtained c_1 and c_2 value from the craze initiation stress at different temperatures. $m_1 = m_2 = -.065$ is estimated from the slope of the c_1 vs. the Temperature curve [103]. The value of intercept $k_1 = 65$ MPa and

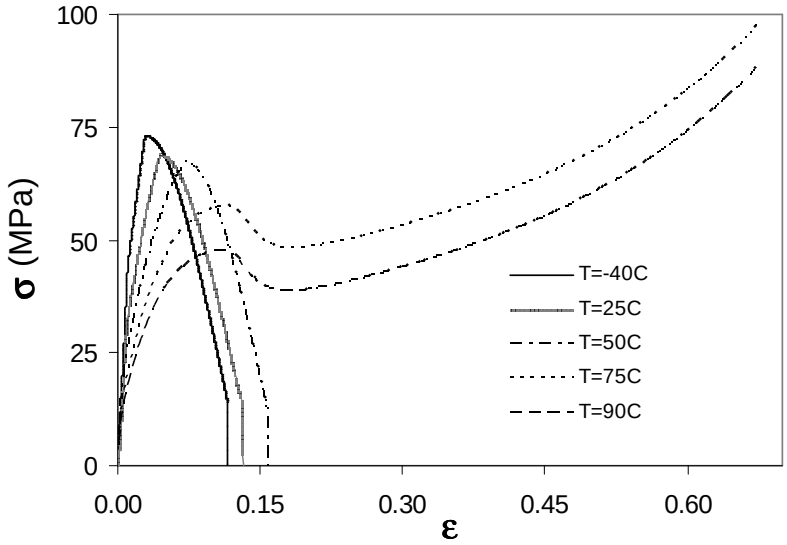

Fig. 32. Stress-strain responses using the new craze model for different temperatures at $\dot{\epsilon} = 0.001$/s

$k_2 = 806$ MPa^2 is estimated by considering $c_1$and c_2 values at room temperature (25^oC) obtained by Gearing-Anand [60]. Figure 32 illustrates that at sufficiently low temperature of $T = -40^o$C, 25^oC, 50^oC, crazing occurs and at a sufficiently moderate temperature of $T = 75^o$C and 90^oC, shear yielding occurs.

3. Crazing in a Unit Cell with a Void

A unit cell of a polymer plate with a void subjected to low strain rate, plane strain, uniaxial tension and zero lateral stress was analyzed to observe the effects of the craze model in predicting a fracture in polymer material. Fig. 33 shows the geometry of the problem, the specified boundary conditions (Fig. 33a) and the finite element mesh (Fig. 33b). The block has an initial dimensions of $2W_0 \times 2h_0$ with a void with a radius of r_0. Assuming the planes $x_2 = 0$ and $x_1 = 0$ to be symmetry planes, only the quarter portion of the problem is considered. Applied boundary conditions are

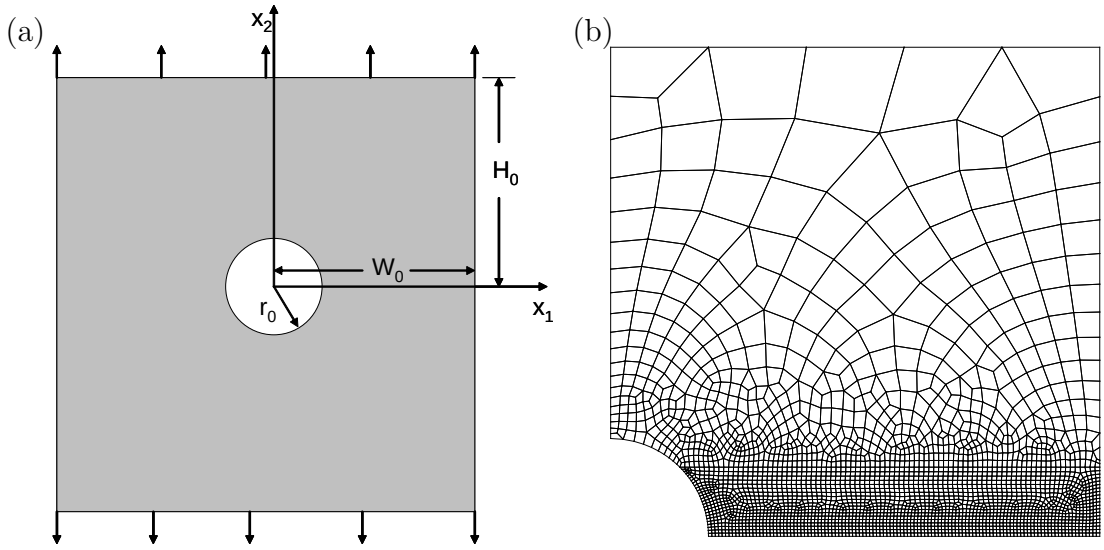

Fig. 33. (a) Unit cell with a void geometry and the boundary value problem (b) finite element mesh (2702 quadrilateral elements)

as follows

$$T_1(W_0, x_2) = 0, T_2(W_0, x_2) = 0, T_1(x_1, h_0) = 0 \tag{3.21}$$

$$\dot{U}_2(x_1, h_0) = V_2, \dot{U}_2(x_1, 0) = 0, \dot{U}_1(0, x_2) = 0, \dot{U}_1(W_0, x_2) = V_1 \tag{3.22}$$

Here, V_2 is a prescribed constant while V_1 is determined from the condition that the average lateral traction vanishes, i.e

$$\int_0^{H_0} T_1 dx_2 = 0 \tag{3.23}$$

We have considered the above boundary condition to ensure that the straight lines bounding each cell remain straight after deformation and also preserve the mirror symmetry of the array so that straight lines connecting the centers of the cells remain straight. For this boundary value problem the dimensions are: $r_0/W_0 = .2$ and $H_0/W_0 = 1$. The mesh shown in Fig. 33b consists of 2702 quadrilateral elements. The material parameters used for the pre-craze model and craze model are representative

of the PMMA specified in the previous section.

Overall response is monitored by the macroscopic overall stress and macroscopic logarithmic strain,

$$\Sigma_{22} = \frac{1}{2W}\int_0^W T_2(x_1, H_0)dx_1 = 0 \tag{3.24}$$

$$\Sigma_{11} = \frac{1}{2H}\int_0^H T_1(W_0, x_2)dx_2 = 0 \tag{3.25}$$

and

$$\mathrm{E}_{22} = ln(H/H_0) \tag{3.26}$$

Figure. 34a shows the macroscopic stress strain response of the unit cell, using the three combinations of macromolecular and craze models. Case 1: the original macromolecular model with the new craze model; Case 2: the modified macromolecular model with the reference craze model; and Case 3: the modified macromolecular model with the new craze model. For Case 1 and Case 2 the macroscopic stress strain response is linear until the final failure of the unit cell. The effect of craze plasticity is visible in the response of Case 3. Macroscopic crack initiation strains for the three cases are $\mathrm{E_i} = 0.0235$, 0.0095 and 0.0134.

For Case 3, where the original macromolecular model is used, numerical instability occurred when the crack had propagated about halfway through the specimen. Figure 34 the numerical simulations obtained for the three cases (Figs. 34b-d). The crack initiates from the lateral edge of the void for all the three cases but propagated in a different manner in each case. For the cases, where the modified macromolecular model is used branching of the crack is observed (Fig. 34c and d).

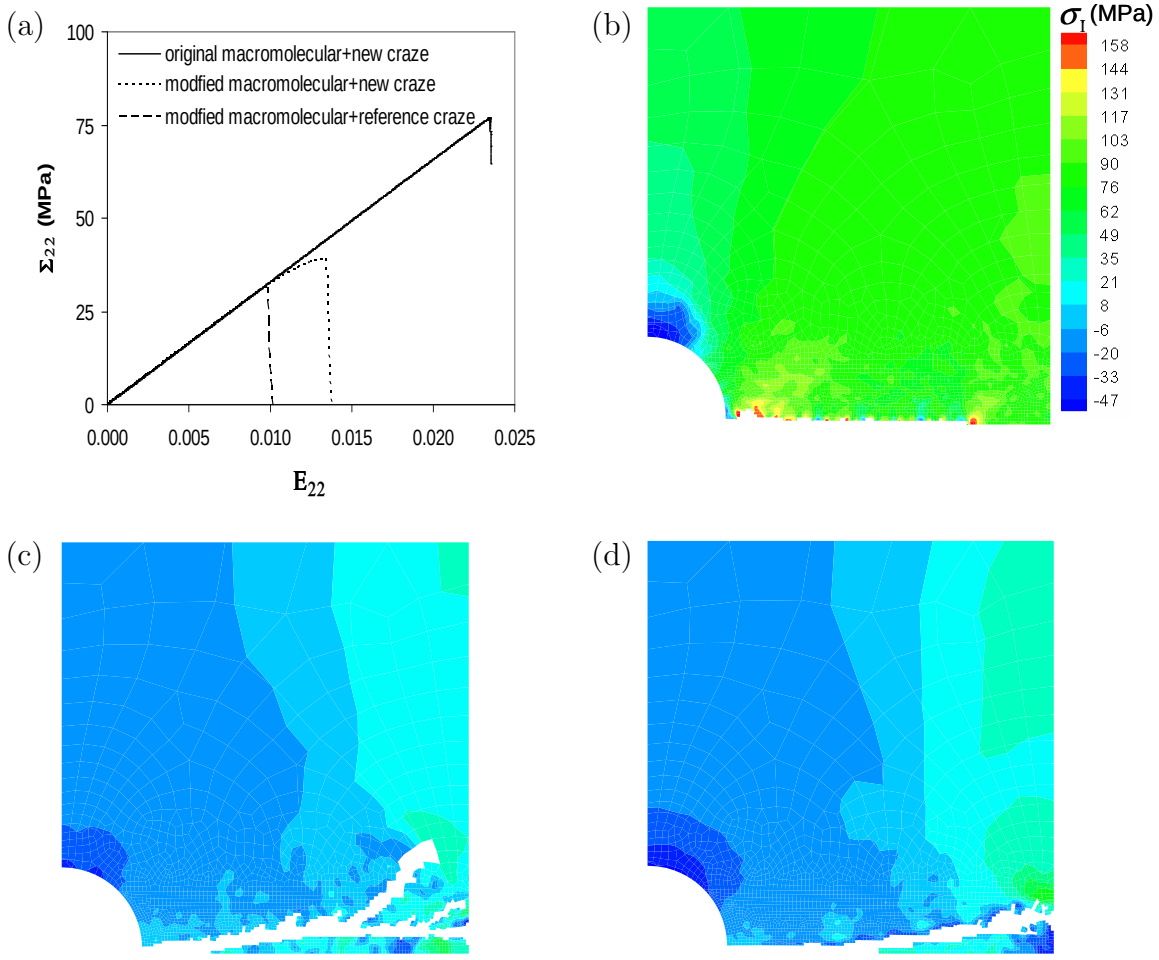

Fig. 34. (a) Macroscopic stress-strain ($\Sigma_{22} - E_{22}$) responses for the three combinations of the macromolecular model with the crazing models for the plate with a hole under plane strain tension and σ_I contours at the advance stage of cracked specimen obtained by using (b) original pre-craze model with the modified craze at $E_{22} = 0.0245$ (c) modified pre-craze model with the reference craze at $E_{22} = 0.0139$, (d) modified pre-craze model with the modified craze model at $E_{22} = 0.0101$

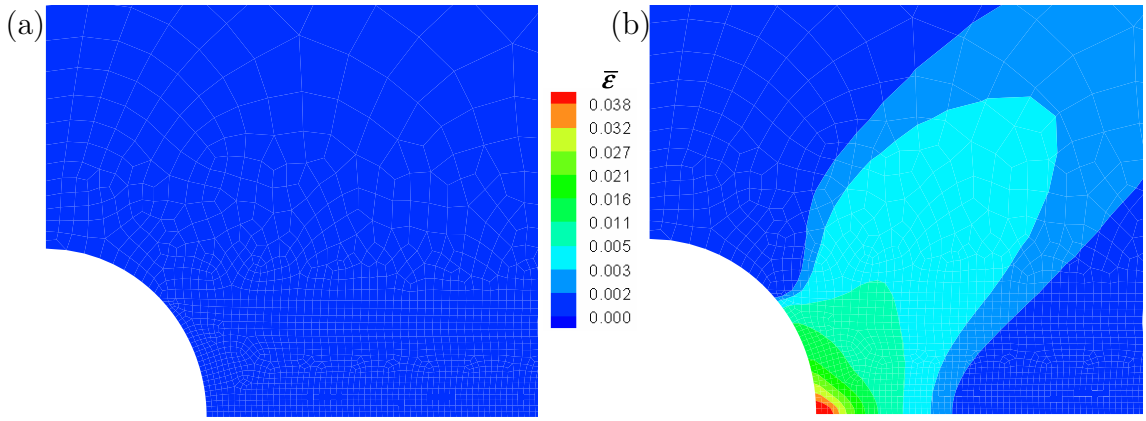

Fig. 35. Close snapshots of effective plastic strain contours at $E_{22} = 0.013$ before craze initiation using the (a) original and (b) modified macromolecular model with the new craze model

The original macromolecular model crack propagates in a similar manner without forming any branches (Fig. 34b). Figure 35 shows close snapshots of the effective plastic strain contours for the three cases. For the original macromolecular model (Fig. 35a) there is no pre-craze plasticity occurring but for the modified macromolecular model (Figs. 35b) significant plasticity occurs and expanded within the specimen.

After the specimen starts deforming, stress is concentrated around the lateral edges of voids by forming oblate zones, and upon continuing deformation this zone goes through isotropic hardening due to pre-craze plasticity followed by the initiation of craze. After craze initiation, strain softening occurs in the oblate zone due to post-craze plastic flow followed by the initiation of a crack. As the crack front advances, the oblate craze zone expands by "bulging out" and allows the main crack to propagate in a similar manner. When the crack front crosses the expanded oblate shaped craze zone, at the front of the crack tip there exists a crazed zone. At the front of that crazed zone there exists a pre-craze plasticized zone that is undergoing isotropic hardening

dominant by the deviatoric part of the stress state, which also might have small intrinsic softening behavior. During the crack advancement through the craze tip the crack front may come into the contact of craze tip material that is undergoing pre-craze viscoplastic flow. Thus, facilitating plasticity and subsequent initiation of crazing at an angle to the main crack path followed by the diversion of the crack. For the reference (Gearing-Anand) craze model, crack diversion occurs at a closer distance from the void edge than in the new craze model. Just before the crack initiation, the size of the oblate crazed zone, predicted by the reference craze model, is smaller than the new craze model. As the reference craze model predicts the final craze breakdown at an earlier stages than the new craze model, the crack tip comes into the contact of pre-craze viscoplastic material more frequent and causes more branching. For the case of the original macromolecular model, there is no plasticity in the surrounding zone of the craze tip; therefore, no branching of the crack occurs.

The PMMA plate with a void problem also was analyzed at a moderate temperature (T= 90^oC) using the modified macromolecular model and the new crazing model. Figure 36a shows a comparison of the stress-strain response between room temperature, T= 25^oC and moderate temperature, T= 90^oC. At moderate temperature, the response exhibits more ductile behavior and crack initiation occurs at the later stages of deformation. Crack branching (Fig. 36b) also occurs at moderate temperatures but the crack branching occurs at a greater distance from the void edge than in the room temperature case.

F. Discussion

Physically based constitutive equations after modification for polymer deformation and craze constitutive models were implemented in a finite element computational

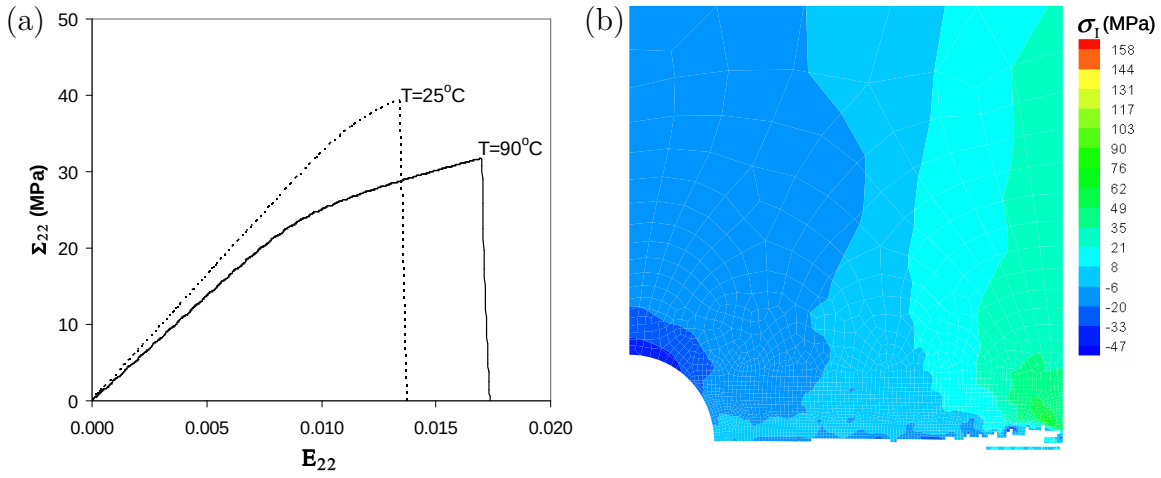

Fig. 36. (a) Macroscopic stress-strain responses at T= 25^{o}C and T= 90^{o}C and (b) $\sigma_{\rm I}$ contours at an advance stage ($E_{22} = 0.0172$) of cracked specimen obtained at T= 90^{o}C

framework at finite strain. The modified macromolecular model accounts for rate and temperature sensitive yielding, isotropic hardening before the peak yield, intrinsic post-yield softening, rapid strain hardening at larger deformations and anisotropic hardening. In that respect, it captures more faithfully the behavior of amorphous glassy polymers below the glass transition temperature. It combines a pressure sensitive rate dependant viscoplastic flow law [59] with an orientational hardening model [55, 78, 79] that draws on an analogy with rubber elasticity. The original model would be appropriate for compression or where large strain deformation occurs locally, but for tension loading it would not capture the branching of a craze induced crack, due to its inability to capture pre-craze inelastic deformation.

The first crazing model (the reference craze model) implemented here was developed by Gearing-Anand [60], which separately accounts for the three stages of crazing, i.e., craze initiation, craze widening and craze breakdown. It should be rec-

ognized, however, that the loss of stress carrying capacity in the reference craze model is not due to the craze flow constitutive equations but rather to the empirical craze failure criterion (3.8). Here, instead of attempting to represent each individual stage of craze, we have developed a continuum model that combines craze fibril widening and breakdown, where craze breakdown is a continuous process instead of an instantaneous process. For the modified model, craze induced failure occurs as a natural outcome of the solution.

Using the constitutive models discussed here, the finite deformation response of a planar plate of polymer material with a void subjected to uniaxial load was analyzed with full account taken of the transient response. At sufficiently low temperatures, diffuse deformation ceases shortly after yielding. Localization takes place through craze initiation and growth which results in craze induced crack. Both the crazing models with the same macromolecular pre-craze model yield similar predictions for craze propagation, but the macroscopic response, as well as the details of local deformation and subsequent crack growth, substantially vary depending on which model is used. For the new craze model with different pre-craze models, i.e., the original macromolecular model and the modified macromolecular model, we get significantly different predictions for macroscopic and local behaviors, involving macroscopic response, and crack initiation and propagation patterns, as described in Section 5. At relatively moderate temperatures, the material response shows more ductile behavior and the intrinsic small strain softening increases the propensity to a formation and propagation of shear bands. Under such circumstances the use of a model that fully incorporates the small strain softening behavior is necessary in order to predict the shear bands.

G. Conclusion

The objective of the work presented here was to develop models of the deformation and failure mechanisms in polymers and to apply the models to investigate the behavior of a polymer plate containing a void subjected to uniaxial tension. A finite element implementation of the models led to the following conclusions.

- The original macromolecular model with the new craze model were unable to capture macroscopic nonlinear responses, as well as local crack propagation patterns.

- The modified macromolecular model with both the crazing models successfully captured crack initiation and crack propagation patterns for a PMMA polymer plate with a void.

- The modified macromolecular model for polymer deformation and the new crazing model are most efficient in predicting local crack initiation, propagation and macroscopic nonlinear responses due to local inelastic deformation.

In view of the small macroscopic strains supported by a composite material, the use of the modified macromolecular model with the new crazing model to describe deformation and fracture of the polymer matrix appears to be a reasonable undertaking. It should be noted, however, that although the macroscopic strains in composites are small, local strains in the polymer matrix may be substantial. The constraints imposed by stiff reinforcing elements, i.e., the fibers, may lead to the emergence and growth of localized deformation zones and consequent failure. It remains to be seen how the deformation and fracture models would perform in predicting damage initiation and growth in a composite. This is the subject of another study described later in this report.

CHAPTER IV

EFFECTS OF VOIDS ON DAMAGE IN POLYMER BASED COMPOSITES

A. Introduction

Composite materials are tailored to possess unique directional properties, such as high strength or stiffness, and weight saving potential, which offer a huge advantage over conventional materials. But a composite structure, manufactured by any practical process, comes out with defects e.g. voids and fiber misalignment. The presence of defects plays a major role in determining damage initiation, strain to failure and on their failure properties such as fracture toughness. The search for a rational design procedure to reduce the manufacturing cost, particularly through optimizing the material properties by trade-off with manufacturing cost to realize the best performance/cost ratio, drives an accelerated development of experimental and computational methodology to obtain a relationship between the microstructure and the material's mechanical behavior including failure. Damage in polymer based composites may occur in multiple modes involving complex micromechanisms due to nonuniform distribution and geometry of micro-constituents and defects and complex behavior of polymer matrix. Under different loading conditions such as loading rate and temperature, the microstructural features, such as presence of voids, their size, length and orientation distributions, determine the properties, especially the failure properties, of the composites through their affects on the initiation and evolution of the micro-damages. Several observations of the various micro-damage mechanisms have been reported during past two decades [8, 139–143]. These studies have reported several modes of damages at the micro scale such as matrix crack initiation from void [8, 141] and crack propagation to fiber to form debonding (see

Fig. 37), cavitation induced matrix cracking near the fiber surface and subsequent propagation through matrix cracking, fiber/matrix decohesion, matrix cracking due to fiber breakage, etc. Understanding the damage initiation and evolution process under the cumulative effect of void and fiber microstructural variation with different temperature and loading rate, by the design of experiments (DOE) approach is a very challenging task. In addition to this, experimental observation can be costly and inefficient. There have been few computational works [128, 129, 144–148] done on understanding matrix cracking in the polymer composite micro-structure but with typically little or no understanding of the underlying mechanisms of polymer fracture.

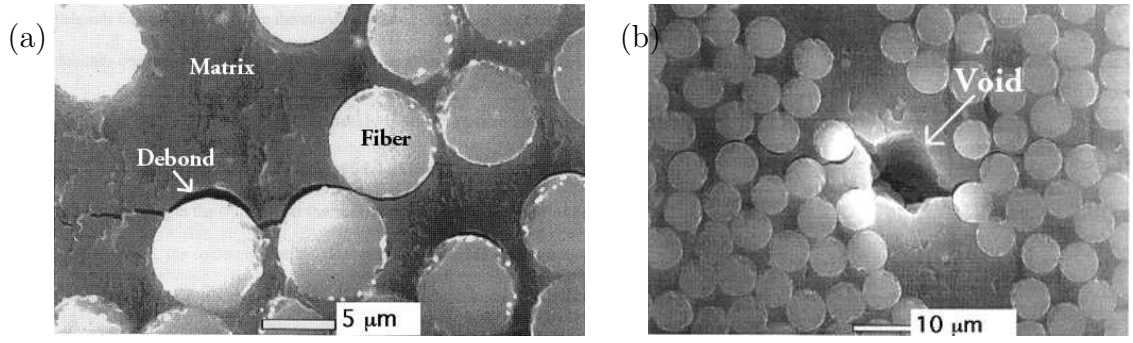

Fig. 37. Matrix crack initiated (a) from fiber debonding in a Gr/Epoxy composite and (b) from void results in fiber debonding. [Wood and Bradley, 1997]

Govaert et al [144] studied the yield and fracture behavior of an epoxy system under various multiaxial loading conditions. They used 3-D Eyring model that accounts for pressure sensitivity of polymer yield and simple maximum strain criterion for polymer fracture. Seidel et al [146] investigated damage in a two-phase viscoelastic particle-reinforced composite material with a viscoelastic cohesive zone model for polymer damage that draws an analogy with crazing micromechanism in an average

sense. But their model did not consider three stages of craze life i.e craze initiation, growth and breakdown. Zhang et al [147] simulated matrix cracking of a polymer composite, where a non-linear viscoelastic model was used to model polymer deformation, crack initiation was modeled based on an ad-hoc maximum principal strain criterion and progression of crack was modeled using smeared crack method which allows loss of stress carrying capacity and stiffness reduction under continuing loading. Sirivedin et al [148] studied matrix cracking in a polymer composite initiated from fiber breakage. They simulated crack initiation and crack growth employing minimum strain energy density criterion for crack initiation. Huang et al [128] analyzed matrix micro-cracking in short fiber reinforced polymer composites based on finite element simulation. In order to simulate matrix cracking they utilized the Rice-Tracey ductile fracture model where plastic deformation involves growth of voids and crack initiates when local plastic deformation reaches a critical plastic strain.

All of the computational framework discussed above, involved with simulating failure of polymer-matrix composite microstructure, did not completely consider key mechanisms of polymer deformation i.e. rate, temperature and pressure dependent yielding, failure through craze initiation, growth and breakdown. The matrix debonds from the fiber ends at an early stage of loading is a key damage initiation mechanism in composite microstructure. Asp and his coworker [101] observed that in many cases debonding like separation of fiber–matrix interface occurs due to cavitation induced matrix cracking rather than complete separation of fiber-matrix interface, which is termed as debonding. This debonding like phenomenon may arrest somewhere on the fiber–matrix interface and results in intense localized plastic deformation followed by matrix crack propagation [128]. Several models to predict failure initiation through debonding have been successfully developed [101, 149–151]. A majority of these studies included complex micromechanism involving fiber matrix debonding and used

"cohesive surface" methodology. Recently this methodology has been widely used to simulate damage initiation and progression. Implementation of the complex micromechanism using cohesive finite elements requires substantial amount of technical effort. The purpose of the present computational framework is to demonstrate the competition between fiber–matrix interface separation and manufacturing defects induced matrix cracking. For this purpose we employ a simple criterion developed by Asp [101] to capture the phenomenon of fiber and matrix interface separation. According to their model, when dilatational energy density reaches a critical value, the cavitation within elastic field in a glassy polymer grows unstably, results in debonding like crack on the fiber-matrix interface. For the sake of simplicity we will denote this debonding-like cavitation induced matrix cracking over the periphery of the fiber-matrix interface as cavitation induced debonding.

Substantial experimental effort have been devoted to understanding matrix cracking and debonding in the polymer composite microstructure by considering ideal situations or defect free situations. Very few of them have been involved in investigating the effect of voids in composite [8, 9, 11, 13–23, 152]. Most of the works involved in studying the effect of void have been limited to stiffness degradation, while very few works [8, 9, 22, 23] have been devoted to investigating failure properties through damage initiation and evolution of composites in the presence of manufacturing induced voids. Varna [8] et al studied the effects of void on damage initiation and evolution under transverse loading for unidirectional Gr/VE epoxy composite. They observed that high void content exhibits low strength ductile macroscopic response, which is associated with formation of numerous small transverse cracks and low void content shows more brittle behavior associated with the formation of few large and well defined transverse cracks connected to large voids leading to early failure. Berglund and coworker [9] investigated the effect of voids in damage mechanism for the Glass

mat thermoplastic (GMT) composites. They reported that void content up to 5% does not have significant effect on damage initiation, but that failure occurs due to presence of locally soft region. However, it was unclear as to what caused locally soft region, and also the effect of void size and shape in damage initiation and progression was not investigated. Chamber et al [23] studied the the role of voids in the initiation and propagation of static and flexural fatigue failures of unidirectional carbon fiber composite. They hypothesize that void size, shape and distribution have major role in crack initiation and progression in composites. But the effects of those parameters on the mechanism of damage formation and growth were not clearly understood.

Though there is experimental effort to determine the relationship between the composite micro-structures with void and the failure properties of composites, there is little or no computational effort for systematic analysis of damage initiation and growth due to manufacturing induced voids in polymer based composites. Our objective is to investigate the effect of the presence of voids, their distribution, geometry and size on damage initiation and progression in a polymer matrix composite system under different temperatures and loading rates. Fibers and voids embedded in a thermoplastic polymer are explicitly represented in the microstructure. The modified macromolecular model, the modified crazing model and the critical dilatational energy density criterion are employed in a finite element computational framework at finite strain to capture large strain polymer deformation behavior and in simulation of damage due to crazing and cavitation induced debonding. The modified macromolecular model accounts for rate, pressure and temperature-sensitive yielding, isotropic hardening before peak yield, intrinsic post-yield softening and rapid anisotropic strain hardening at large deformations. The modified craze model accounts for the three stages of crazing, i.e. craze initiation, craze growth and craze breakdown.

The organization of this chapter is as follows. In Section 2 we will describe

critical dilatational energy density criterion to predict cavitation induced debonding. Implementation issues of the cavitation induced debonding model will be described in Section 3. Section 4 will be used to describe the analysis of the effect of the presence of voids in a composite microstructure by considering variations of size, shape and location of the void relative to the fiber under variation of temperature and loading rate. Discussion of the results will be made in Section 5 and finally we will draw conclusion in Section 6.

B. Fiber-Matrix Separation due to Cavitation Induced Cracking

Asp and coworkers [153] observed through numerical simulation that hydrostatic stress concentration near the fiber surface leads to cavitation, which in turn initiates cracks. In a composite microstructure in most cases the fiber shape is circular, which causes hydrostatic stress concentration at the interface around the fiber during transverse tension. Upon continuing the loading, the increasing hydrostatic stress may result in a critical condition to form microcavity when the interfacial behavior is still in the elastic regime. Such cavitation may grow unstably at a critical hydrostatic stress state. The growth of this cavitation may then form a crack that may lead to separation of fiber–matrix interface through matrix cracking. They proposed a criterion which states that microcavitation will occur when dilatational energy density reaches a critical value

$$U_v = \frac{1-2\nu}{6E}\left(\sigma_1+\sigma_2+\sigma_3\right)^2 \geq U_v^{\text{crit}} \tag{4.1}$$

where σ_1, σ_2 and σ_3 are principal stresses. ν and E are Poisson's ratio and Young's modulus, respectively. U_v^{crit} is the critical dilatational energy required for cavitation, which is observed to be approximately constant with temperature

C. Implementation

Important implementation issues regarding the modified macromolecular model and the modified crazing model are discussed in Chapter III. Identification of the material parameters for polymer deformation and crazing of PMMA is also discussed in that chapter. For the cavitation induced debonding, the dilatational energy density is computed from equation (4.1). Crack initiates when dilatational energy density reaches the critical value of the dilatational energy density. The value of U_v^{crit} For PMMA is not known at this point. We have used $U_v^{\text{crit}} = .2$ of DGEBA/APTA matrix, which is obtained from the poker chip test. Because DGEBA/APTA and PMMA matrix have similar stiffness, and cavitation induced debonding occurs when the polymer behavior is mostly within the elastic regime, the value considered for U_v^{crit} for PMMA is a reasonable assumption. Crazing and shear yielding are allowed only in the matrix region, while cavitation induced debonding failure is only allowed in the interface region, which has thickness of t_I. Material failure subsequent to cavitation induced cracking is implemented via an element vanish technique. When the failure condition is met in an element, the element is taken to vanish.

D. Results

For all problems analyzed in this chapter, the microstructure considered is a unit-cell of a composite containing a void and a fiber, subjected to plane strain uniaxial tension and zero lateral traction, under neck prevention condition. Fig. 38 shows the geometry of the problem with the specified boundary conditions. The unit cell has an initial dimensions of $2W_0 \times 2H_0$ with a void of radius r_v, a fiber of radius r_f and a fiber interface of thickness t_I. The fiber is situated at a distance, $l_f = W_0 - (r_v + r_f)$, from the void edge. Assuming the plane $x_2 = 0$ and $x_1 = 0$ to be symmetry planes,

only the quarter portion of the geometry is considered. Applied boundary conditions are as follows

$$T_1(W_0, x_2) = 0, T_2(W_0, x_2) = 0, T_1(x_1, H_0) = 0 \tag{4.2}$$

$$\dot{U}_2(x_1, H_0) = V_2, \dot{U}_2(x_1, 0) = 0, \dot{U}_1(0, x_2) = 0, \dot{U}_1(W_0, x_2) = V_1 \tag{4.3}$$

Here, V_2 is a prescribed constant, while V_1 is determined from the condition that the

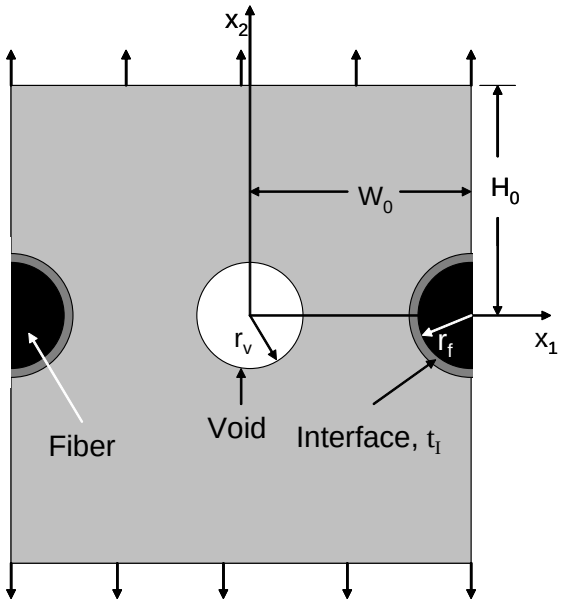

Fig. 38. Geometry of a composite microstructure with void and the boundary value problem.

average lateral traction vanishes, i.e

$$\int_0^{H_0} T_1 dx_2 = 0 \tag{4.4}$$

For all the analysis considered here, overall response is monitored by the macroscopic overall stress and macroscopic logarithmic strain,

$$\Sigma_{22} = \frac{1}{2W} \int_{-W}^{+W} T_2(x_1, H_0) dx_1 = 0 \tag{4.5}$$

$$\Sigma_{11} = \frac{1}{2H}\int_{-H}^{+H} T_1(W_0, x_2)dx_2 = 0 \tag{4.6}$$

and

$$\mathrm{E}_{22} = ln(H/H_0) \tag{4.7}$$

with macroscopic strain rate

$$\dot{\mathrm{E}} = |V_2/H_0| \tag{4.8}$$

1. Prediction at Room Temperature

In this section the effects of void on damage at room temperature in a composite microstructure are investigated and compared to the case of no voids. Various structural parameters related to voids, e.g. void proximity with fiber, void size relative to fiber size and void shape are considered at the strain rate of 1/s and at the room temperature (T= 25^{o}C).

a. Reference Case

The damage under uniaxial plane strain loading in a composite microstructure containing a circular fiber and with a void of same diameter in the polymer matrix is investigated and compared with the case of no void. The void is located at the side ($x_2 = 0$ plane) of the fiber such that the ratio of void-fiber distance to void radius, l_f/r_v, ratio of 6.0. Figure. 39 shows the finite element mesh used for the without void case(Fig. 39a) and with void case(Fig. 39b).The mesh shown in the Fig. 39 consists of 2014 and 4047 quadrilateral elements for the 'without void' and 'with void' cases, respectively. Figure 40a shows the macroscopic stress strain response under uniaxial tension at room temperature for 'without void' and 'with void' case. Figure 40b shows a close snapshot of the response at T= 25^{o}C. Comparison of the stress-strain response of the two cases shows that without voids the response is stiffer than with

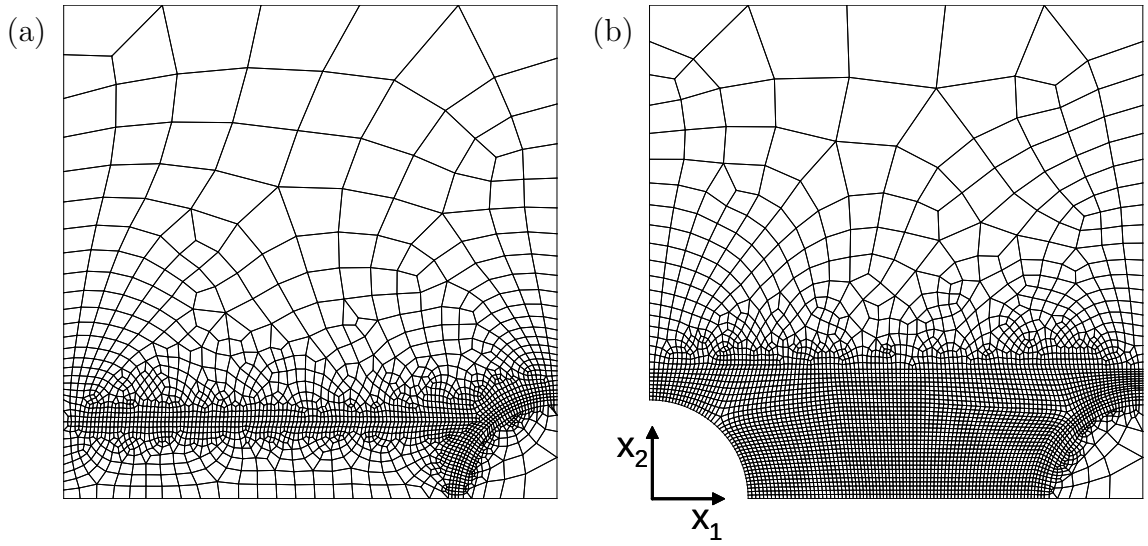

Fig. 39. Finite element mesh (a) without void (2014 quadrilateral elements) (b) with void (4047 elements).

voids. Also, a sharp drop of the macroscopic stress occurs at a larger stress and smaller strain without voids than with voids.

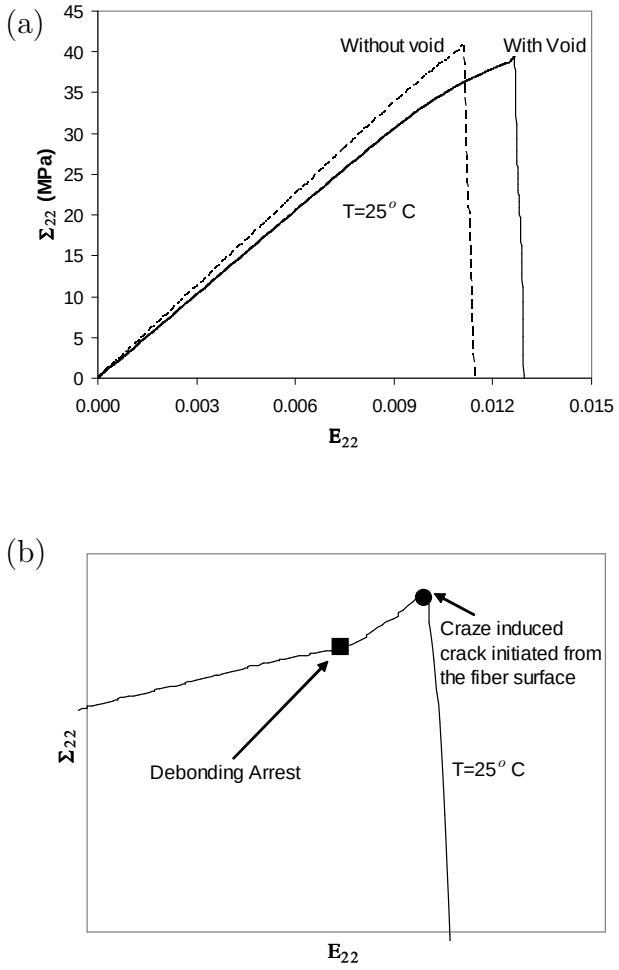

Fig. 40. Macroscopic stress strain responses at macroscopic strain rate, $\dot{E}$ of 1/s for the PMMA composite for the 'without void' and the 'with void' cases (b) close snapshot of the stress strain response of the 'with void' case.

Figure 41 exhibits the development of damage and maximum principal stress, σ_{I}, distribution of the unit cell at different stage of straining. Figs 41a and 41b shows σ_{I} distribution for the 'without void' and 'with void' case corresponding to 0.01 macroscopic strain. Due to the presence of the void, high stress concentration occurs at the void's lateral edge and the maximum principal stress is lower on the top edge of fiber than in the 'without void' case. Higher stress on the top edge of the fiber for the 'without void' case (Fig. 41a at $\mathrm{E}_{22} = 0.011$) causes earlier debonding initiation due to cavitation induced cracking than in the 'with void' case (Fig. 41b at $\mathrm{E}_{22} = 0.0125$). For both the 'without void' and 'with void' cases crack initiates from the cavitation induced debonding at the top edge of the fiber when dilatational energy reaches a critical value, following which debonding continues on the fiber surface and is eventually arrested. Due to this crack arrest, there is a small rise of macroscopic stress (Fig. 40b) and the stress at the point of arrest starts to concentrate and craze initiation occurs. After that, crack initiates and starts progressing through the matrix, while debonding continues over rest of the fiber surface. The craze induced crack propagated perpendicular to the loading direction, and travels through the specimen for the 'without void' case (Fig. 41b at $\mathrm{E}_{22} = 0.012$), while it merges in the void for the 'with void' case(Fig. 41b at $\mathrm{E}_{22} = 0.013$). Before merging into the void the main crack shows several branches due the highly stressed zone around the void's lateral edge, where another craze induced crack initiated and progresses towards the fiber. Soon after, the crack from the void edge takes a sharp turn along the loading direction (x_2 direction). The reason of the sharp turning of a crack will be discussed in a later section.

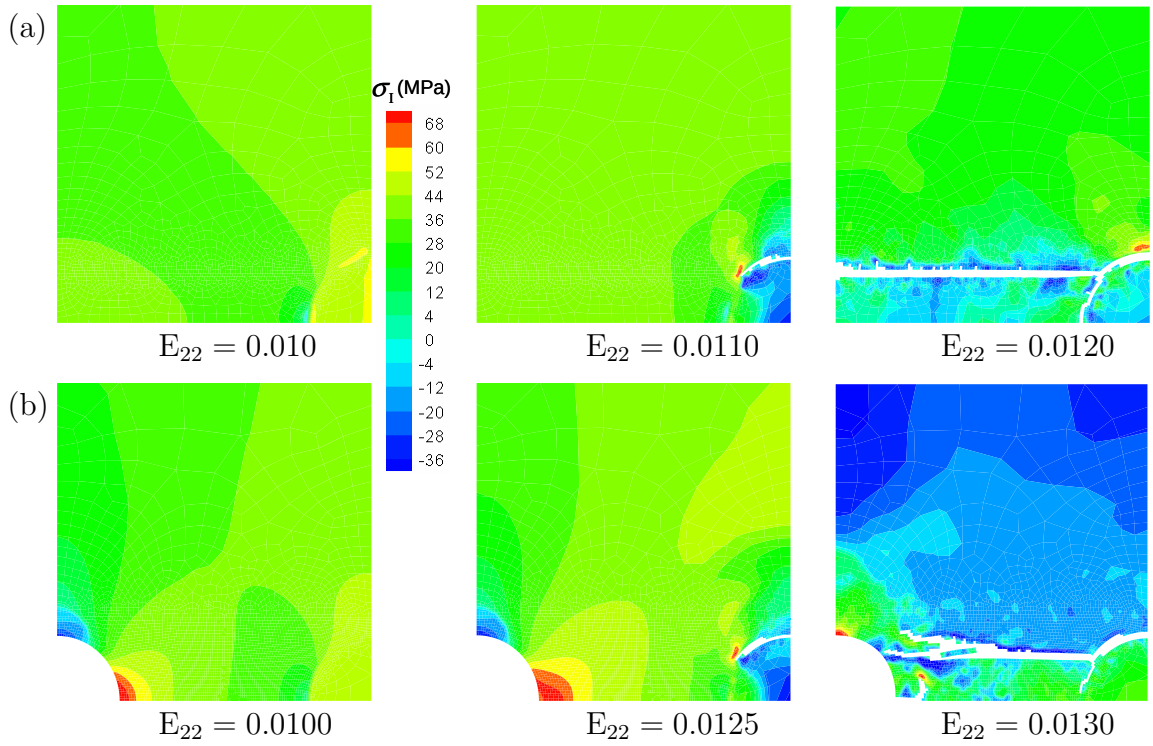

Fig. 41. Development of fracture and the maximum principal stress, σ_{I}, contours of the composite microstructure at T= 25^{o}C for (a) 'without void' and (b) 'with void'.

b. Effects of Void–Fiber Spacing

In the problem of the previous subsection, void was located away from the fiber. Here we study the case where the void is very close to the fiber. In this case, the ratio of fiber-void distance to void radius l_f/r_v, is 0.4 instead of the previous value of 6.0. All other parameters are kept the same. Figure 42 shows the finite element mesh used for the 'without void' case (Fig. 42a) and with void case(Fig. 42b).The meshes shown in the Fig. 42 consists of 2569 and 2334 quadrilateral elements for the 'without void' and 'with void' cases, respectively.

Figure 43 shows the macroscopic stress-strain response under uniaxial tension

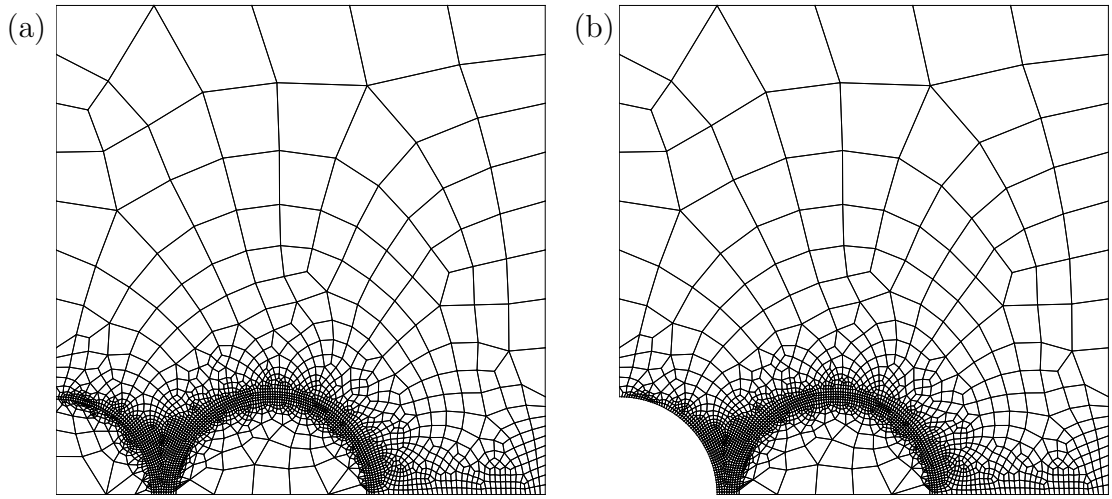

Fig. 42. Finite element meshes for the near fiber case (a) without void (2569 elements) (b) with void (2334 elements).

at room temperature for 'without void' and 'with void' cases. The response corresponding to 'with void' case is softer and has a sharp drop of macroscopic stress at a smaller stress and strain values than in the 'without void' case. On the contrary, the same void situated farther from the fiber causes failure at a much larger strain than in the 'without void' case, as we have seen in the previous section. Figure 44 shows the development of damage and hydrostatic stress, σ_{kk}, distribution of the unit cell at different stages of straining. σ_{kk} distribution for the 'without void' and 'with void' case at 0.0095 macroscopic strain are shown in the first figure of figs. 44a and 44b, respectively . As fiber is situated very near to the void there is not much stress at the void's lateral edge and σ_{kk} is a little lower on the top edge of fiber than in the 'with void' case. Higher stress on the top edge of the fiber due to the presence of a closely placed void (Fig. 44a at $E_{22} = 0.01$) causes later debonding initiation due to cavitation induced cracking than in the 'without void' case (Fig. 44b at $E_{22} = 0.0108$).

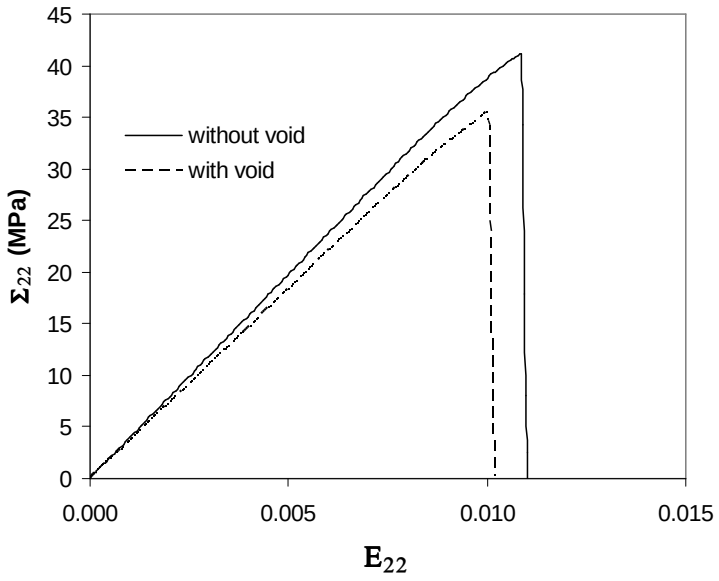

Fig. 43. Macroscopic stress–strain responses at room temperature (T= 25^{o}C) and $\dot{\mathrm{E}} = 1/\mathrm{s}$ for the 'without void' and the 'with void' cases, where the fiber located very near the void.

Though there is difference in macroscopic response, the local fracture pattern is very similar in both cases. In this case of closely placed void also, crack initiates through cavitation induced debonding at the fiber top-edge and progresses through the matrix due to crazing. However, no crack is observed from the void's lateral edge due to crazing, as fiber's lateral edge is very close to the void, which inhibits development of high stress concentration around the void. Perturbation of plastic strain field due to presence of the void very near to fiber is also shown in the Fig. 45. Figures. 45a and 45b show the effective plastic strain distribution in the 'without void' and 'with void' cases. For the 'without void' case, distribution of effective plastic strain is symmetric about the fiber (Fig. 45a) but inclusion of a void perturbs the plastic strain field of the fiber and increases the intensity of the local inelastic deformation on one side of the fiber where the void is located (Fig. 45b).

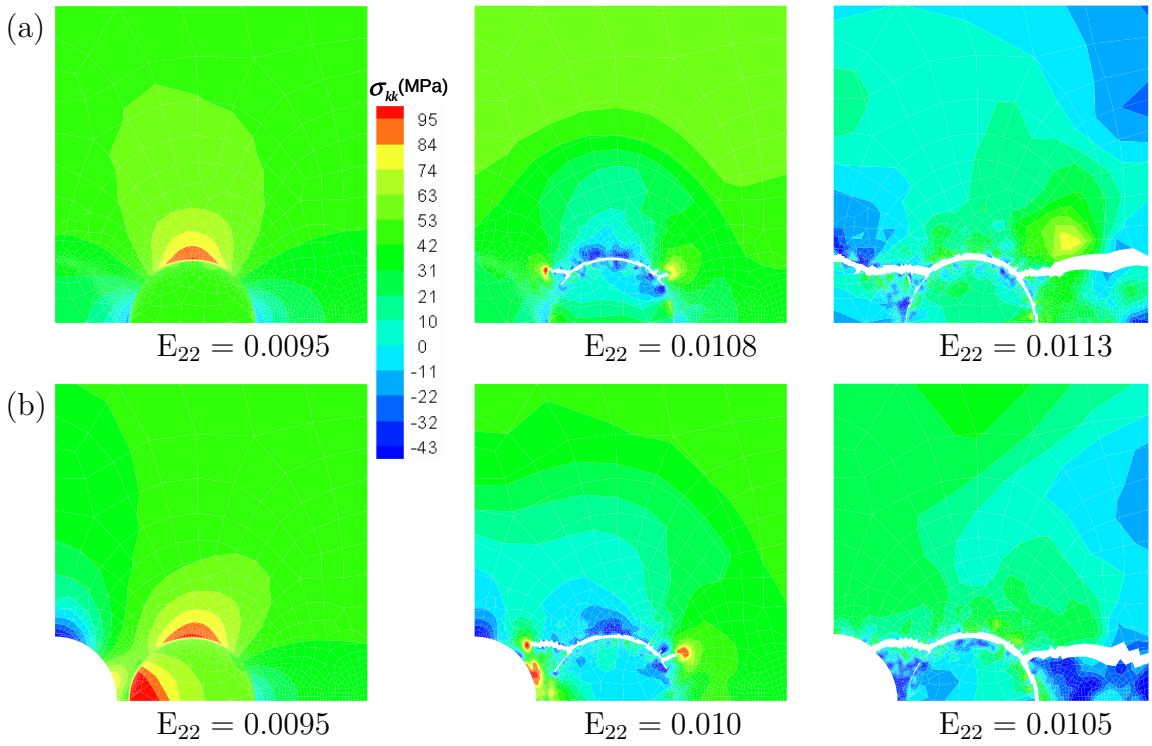

Fig. 44. Development of fracture and hydrostatic stress, σ_{kk}, contours for the (a) 'without void' and (b) 'with void' near the fiber at room temperature.

c. Effects of Relative Void Size

In this section the effect of void size relative to fiber on damage in a composite microstructure is analyzed by considering a unit cell containing a circular shaped void and a fiber of constant diameter located at the side of the void ($x_2 = 0$ plane). Figure 46 shows the finite element mesh used for different ratios of void to fiber radii, ($r_v = 0.5$) (Fig. 46a), 1.0 (Fig. 46b), 1.5 (Fig. 46c) and 2.0. (Fig. 46d). The meshes shown in Fig. 46 consist of 4941, 4047, 3756 and 3159 quadrilateral elements corresponding to r_v/r_f ratio of 0.5, 1.0, 1.5 and 2.0, respectively.

Figure 47 shows the macroscopic stress-strain response under uniaxial tension at room temperature for different void sizes. With the decrease of void size the unit cell

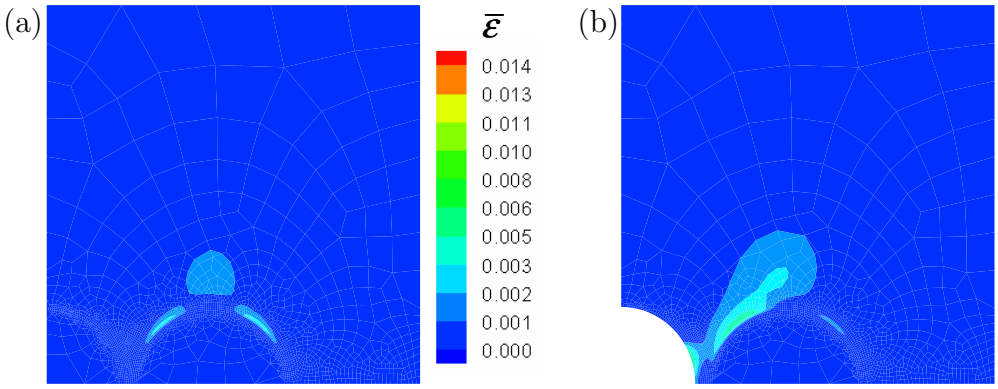

Fig. 45. Effect of void on effective plastic strain, $\bar{\epsilon}$, field for the (a) without void and (b) with void case.

shows stiffer response due to decrease of volume fraction of the void. Stress-strain response obtained for the 'without void' case at T= 25^{o}C is also shown for comparison, which shows stiffer response and sharp drop of macroscopic stress occurring at larger stress and smaller strain than in all the cases of voids.

The development of crack initiation and propagation and distribution of maximum principal stress, σ_{I}, in unit cells of different r_v/r_f ratios at different stages of failure are shown in the Fig. 48. For the r_v/r_f ratio of 0.5 (Fig. 48a) crack initiates from the top edge of the fiber due to cavitation-induced debonding followed by debonding arrest on the fiber matrix interface. Upon continuing deformation, craze induced crack initiated at the arrested debonding site and propagated along the perpendicular direction of the loading. At the same time, debonding continues to the peripheral interface of the fiber.

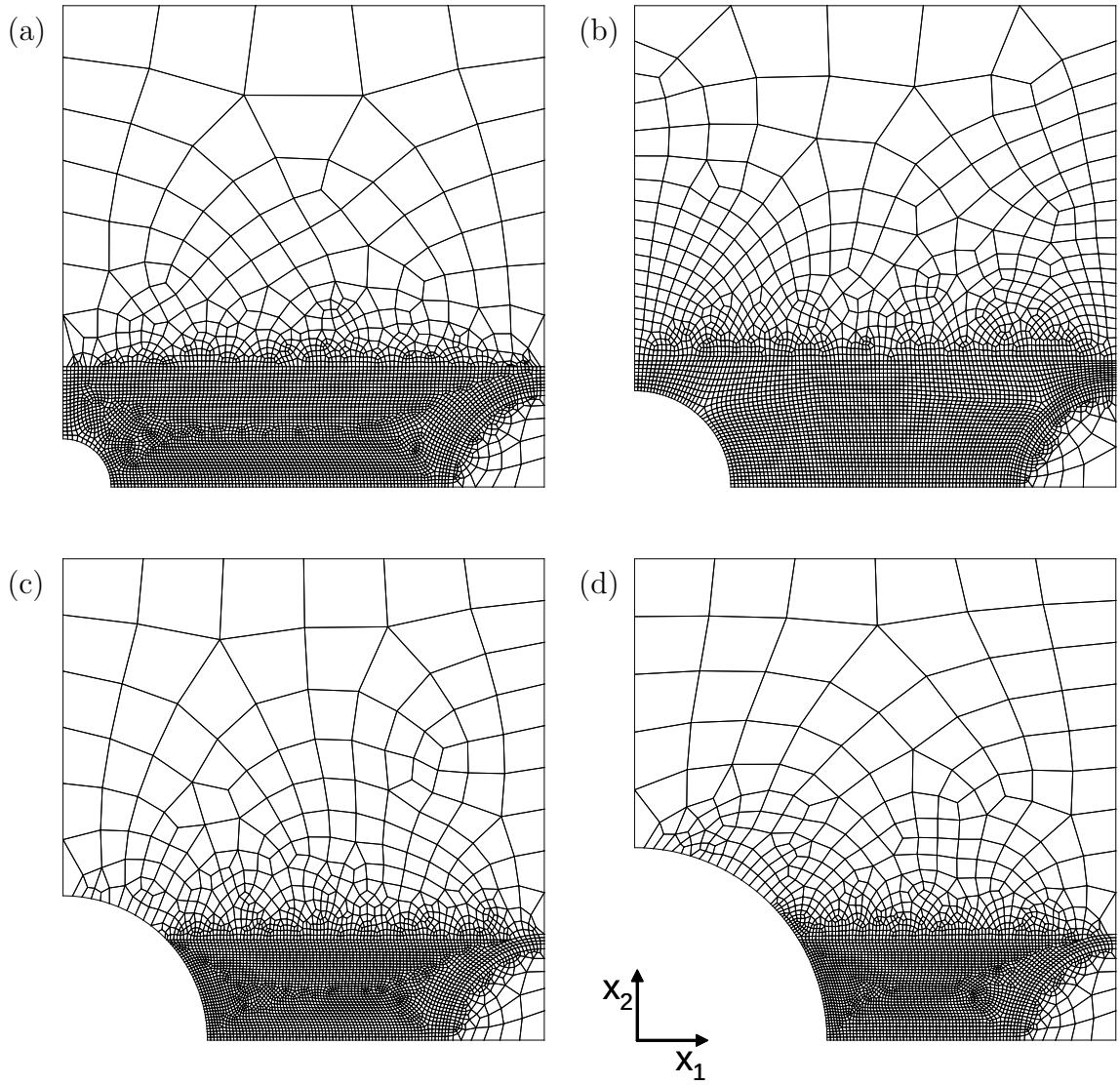

Fig. 46. Finite element meshes for the void radius (r_v) to the fiber radius (r_f) ratio of (a) 0.5 (b) 1.0 (c) 1.5 and (d) 2.0.

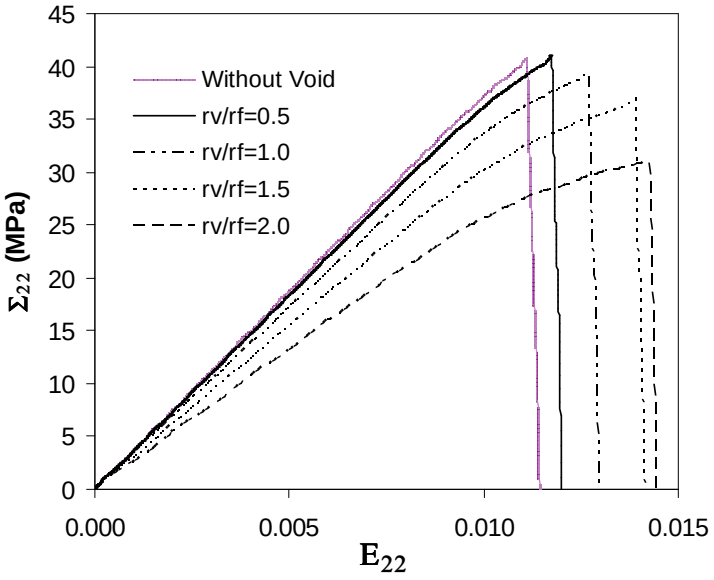

Fig. 47. Macroscopic stress-strain response for different void sizes at T= 25^{o}C and $\dot{\mathrm{E}} = 1.0/\mathrm{s}$.

Soon thereafter, another crack initiates from the void's lateral edge due to craze formation and continues to propagates towards the fiber edge (Fig. 48a at E_{22} = 0.0118). Simultaneously, two cracks from the opposite ends move towards each other on a parallel plane. At a certain stage they come to the same longitudinal plane, when their redistributed stress fields at the crack tip perturb each other's stress fields, increasing their concentration and resulting in formation of craze along the zone of higher stress concentration. Thus, the crack that is initiated from the void edge diverts from its original path and progresses at an angle and after a while the crack again propagates perpendicular to the loading. Upon propagating further in a similar manner the crack again turns towards the loading direction. At the same time, the crack from the fiber surface continues to propagate laterally until it reaches compressive stress field created on top of the void and in its surrounding area. Now this crack turns away from the void's longitudinal edge because of compressive stress around that edge.

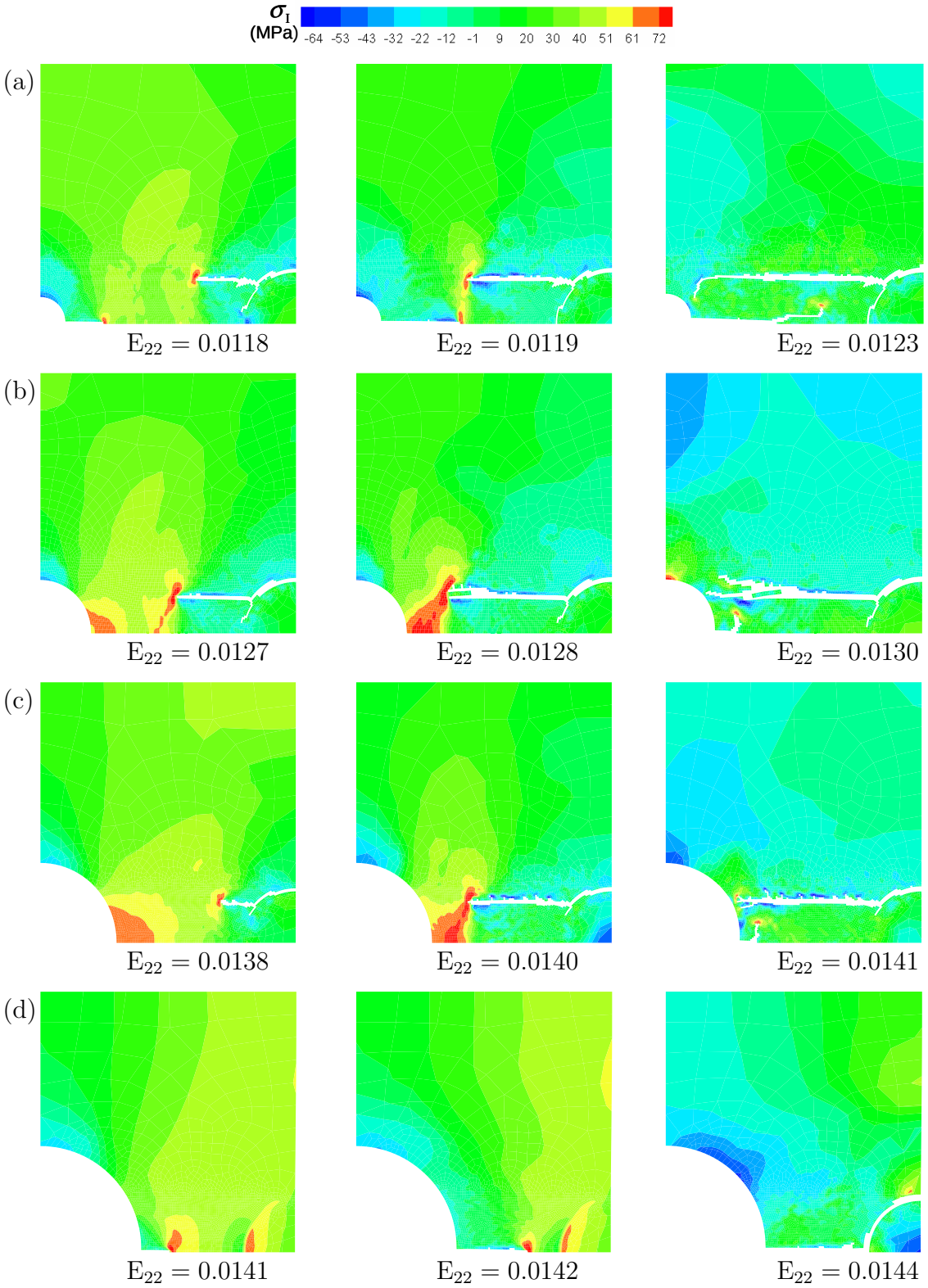

Fig. 48. σ_I contours and crack propagation patterns for the r_v/r_f ratio of (a) 0.5 (b) 1.0 (c) 1.5 and (d) 2.0 at T= 25°C at the strain rate of 1/s.

Figure. 48b shows the development of fracture for the $r_v/r_f = 1.0$, where craze induced crack from void initiates much later than in the previous case. Also the craze induced crack (Fig. 48b at $E_{22} = 0.0127$), which initiates from the debonded fiber branches out two cracks due to interaction between redistributed stress field around the crack tip and stress concentration around the lateral edge of the void (Fig. 48b at $E_{22} = 0.0128$). Diversion of the void induced crack towards the loading direction also occurs (Fig. 48b at $E_{22} = 0.013$) when the parallel crack from the debonding zone comes to the same longitudinal (x_1) plane. Fracture behavior corresponding to the $r_v/r_f = 1.5$ (Fig. 48c) shows similar pattern as for $r_v/r_f = 1$. except the craze induced crack from the debonding zone shows less number of branching. For $r_v/r_f = 2.0$, fracture pattern is very different from the previous three cases, as in this case crack initiates due to crazing at the void's lateral edge and propagates perpendicular to the loading, towards the fiber, when finally the craze induced crack reaches the fiber's lateral edge and cavitation induced matrix cracking takes place over the fiber surface.

Figure 49 shows the distribution of σ_{kk} for different void size at macroscopic $E_{22} = 1.0\%$ before any crack initiation, which illustrates that the larger the void, the lower the level of hydrostatic stress at the top edge of the fiber. The stress concentration zone at the lateral edge of void increases in highly stressed area and in intensity as void size increases.

Thus, the propensity of craze formation is higher for the larger-sized void. For better understanding, the contours of dilatational energy density, U_v, for different r_v/r_f ratios at $E_{22} = 0.01$ are shown in the Fig. 50, , which illustrates that the level of dilatational energy density on the top edge of the fiber is lower due to the presence of the larger void. Thus, the increase of the void size relative to the fiber size lowers the possibility of cavitation induced debonding.

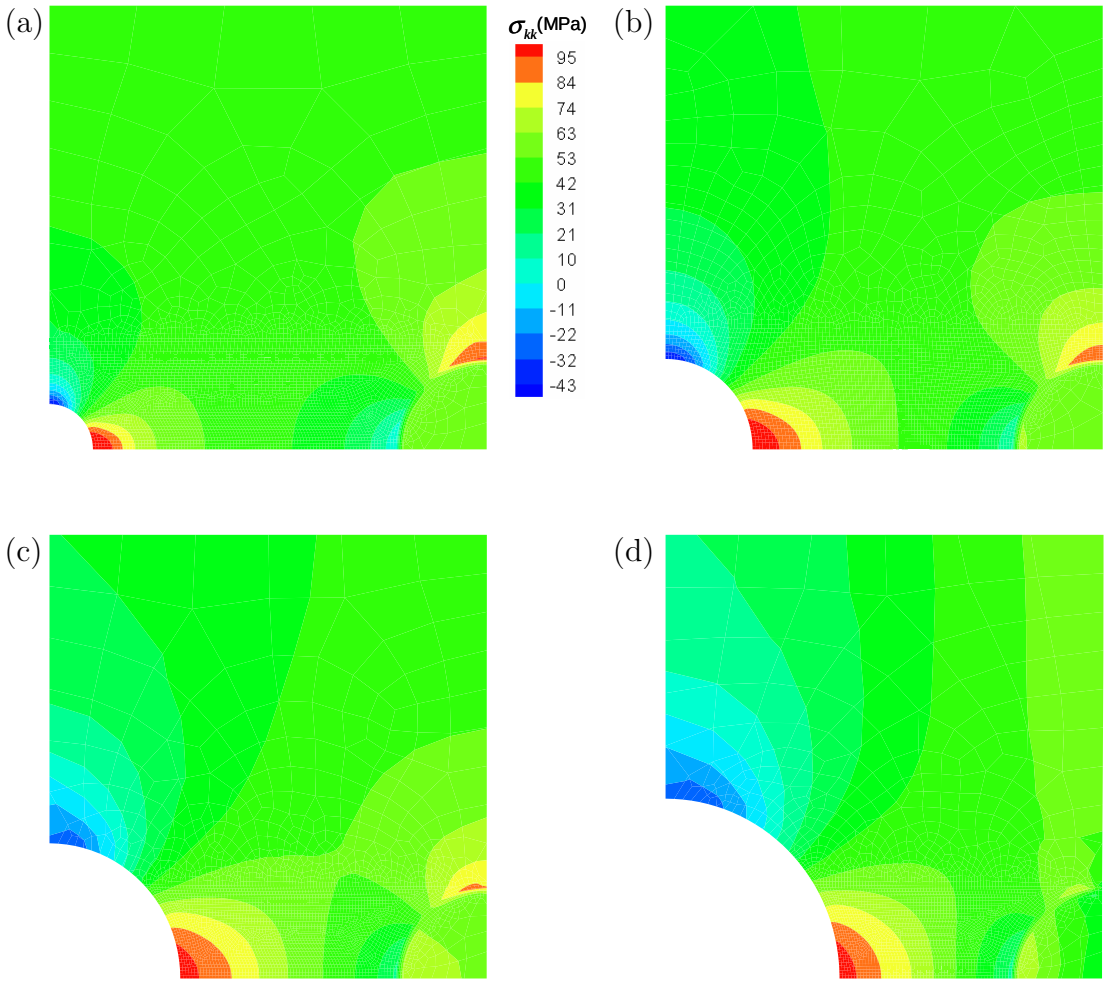

Fig. 49. Hydrostatic stress, σ_{kk}, contours at the macroscopic strain, E_{22} of 0.01 for r_v/r_f ratios of (a) 0.5 (b) 1.0 (c) 1.5 and (d) 2.0.

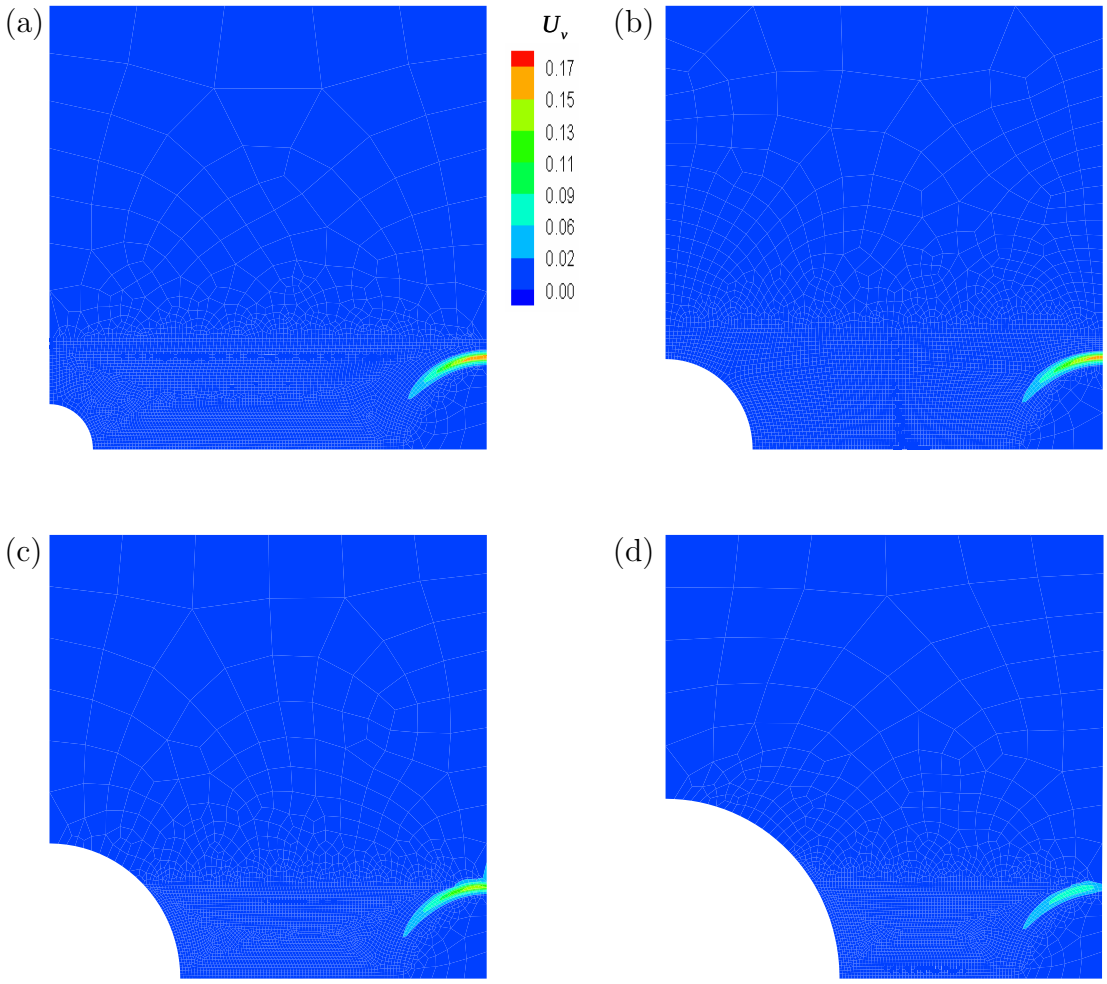

Fig. 50. Dilatational energy density, U_v, contours at $E_{22} = 0.01$ for r_v/r_f ratios of (a) 0.5 (b) 1.0 (c) 1.5 and (d) 2.0.

Therefore, void size relative to fiber size also plays an important role in the competition between craze induced fracture and cavitation induced debonding.

Figure 51a shows E_i/E_i^0 versus temperature plot. The black solid squares and the hollow squares correspond to craze induced fracture initiation and debonding induced fracture initiation, respectively. The plot illustrates that the crack initiation strain increases with the r_v/r_f ratio. But the change of crack initiation strain with respect to void size decreases when crazing is the mechanism of crack initiation. Figure 51b exhibits $\Sigma_{max}/\Sigma_{max}^0$ versus temperature variation. The plot illustrates that the maximum macroscopic stress carried by the unit cell decreases with increase of void size. Change of stress carrying capacity with respect to r_v/r_f ratio increases for crack initiation dominated by craze induced fracture from the void edge. Thus, the analysis conducted here indicates that the void size relative to fiber size has a deleterious effect on crack initiation and stress carrying capacity.

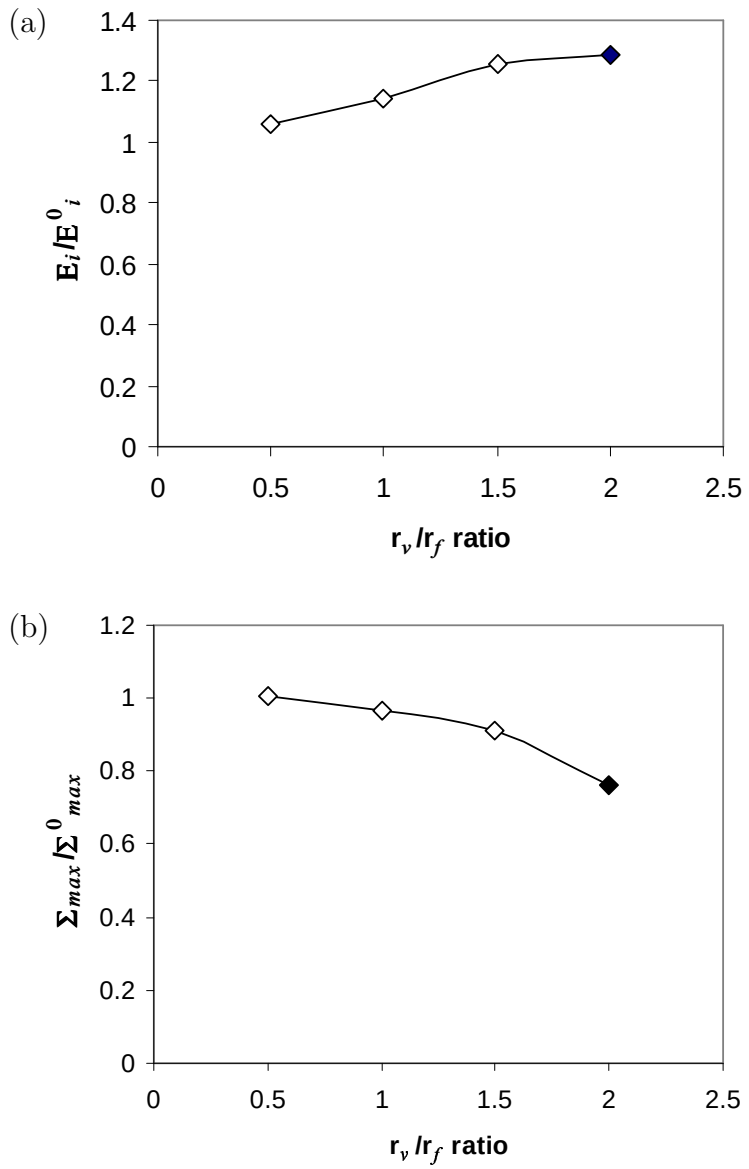

Fig. 51. (a) Normalized crack initiation strain, E_i/E_i^0, vs. r_v/r_f ratio (b) $\Sigma_{max}/\Sigma_{max}^0$ vs. r_v/r_f ratio. E_i and E_i^0 are the macroscopic strain at the onset of crack initiation for the 'with void' and 'without void' cases, repectively. Σ_{max} and Σ_{max}^0 are the maximum macroscopic stress attained by the unit cell before failure for the 'with void' and 'without void' case, repectively.

d. Effects of Void Shape

In this section, the effect of void shape on damage under plane strain tension at room temperature is investigated. Void shape is varied from prolate to oblate by changing the ratio of the major axis (a) to the minor axis (b), a/b, ratio while keeping the area constant. Four a/b ratios of 0.5, 1.0, 2.0 and 4.0 are considered. The circular-shaped

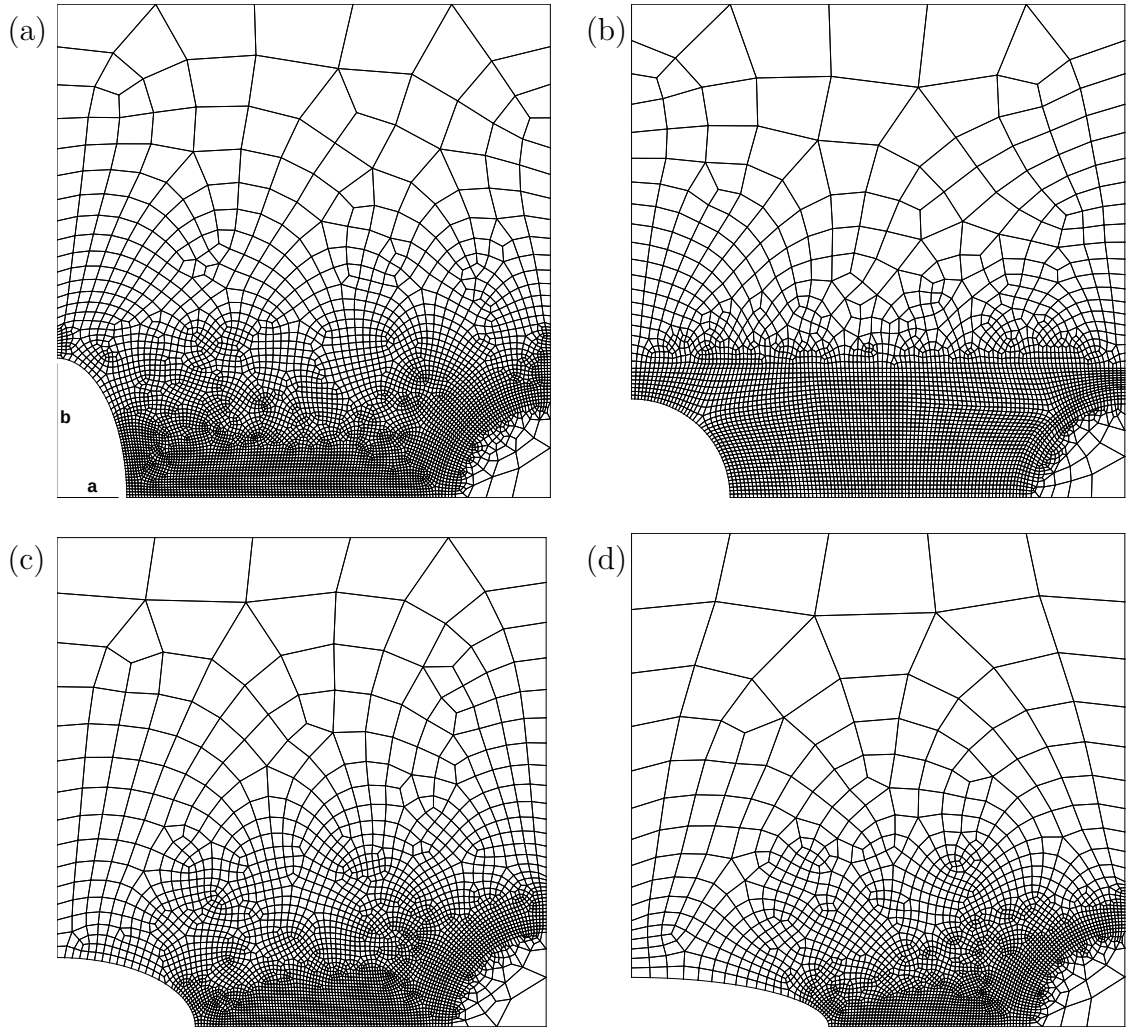

Fig. 52. Finite element meshes for different void shapes from prolate to oblate (a) $a/b = 0.5$ (b) $a/b = 1.0$ (c) $a/b = 2.0$ and (d) $a/b = 4.0$.

fiber is placed at the side of the void. The meshes corresponding to the a/b ratios of

0.5, 1.0, 2.0 and 4.0 are shown in the Figures. 52a, 52b, 52c and 52d, respectively. The number of quadrilateral elements is 5381, 4047, 3714 and 2807 for $a/b = 0.5, 1.0, 2.0$ and 4.0, respectively.

Figure 53 shows the macroscopic stress strain response under uniaxial tension for the a/b ratio of 0.5, 1.0, 1.5 and 2.0 at T= 25^{o}C and $\dot{\mathrm{E}}_{22} = 1./\mathrm{s}$. This figure illustrates that with an increase in the a/b ratio, the macroscopic responses show stiffer behavior. This indicates that the macroscopic behavior can change with the void shape due to changes in the local inelastic behavior, in spite of the constant volume fraction of the micro-constituents. For all a/b ratio at T=25^{o}C, a kink is observed in the stress-strain curve due to the change in the damage mechanism during a sharp stress drop, following a crack initiation.

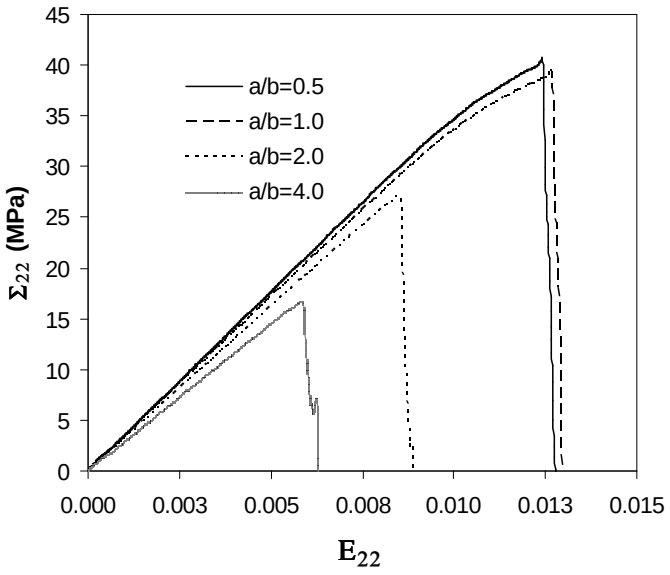

Fig. 53. Macroscopic stress strain responses under plane strain tension at room temperature, T=25^{o}C and $\dot{\mathrm{E}} = 1/\mathrm{s}$ for different void shapes.

Figure 54 shows the maximum principal stress contours and development of the crack propagation for the two extreme cases of void shapes corresponding to

prolate ($a/b = 0.5$) and oblate($a/b = 4.0$) at the T= 25^{o}C. In the prolate shaped void of $a/b = 0.5$ (Fig. 54a at $E_{22} = 0.0125$) the crack initiates from debonding on the top edge of the fiber. The crack further progresses (Fig. 54a at $E_{22} = 0.0127$) through the matrix due to crazing, and finally merges into the oblate void (Fig. 54a at $E_{22} = 0.0129$). During the crack propagation, the main crack forms several branches because the crack tip stress field is redistributed and perturbed due to the influence on the stress field by the void. The crack propagation pattern corresponding to $a/b = 4.0$

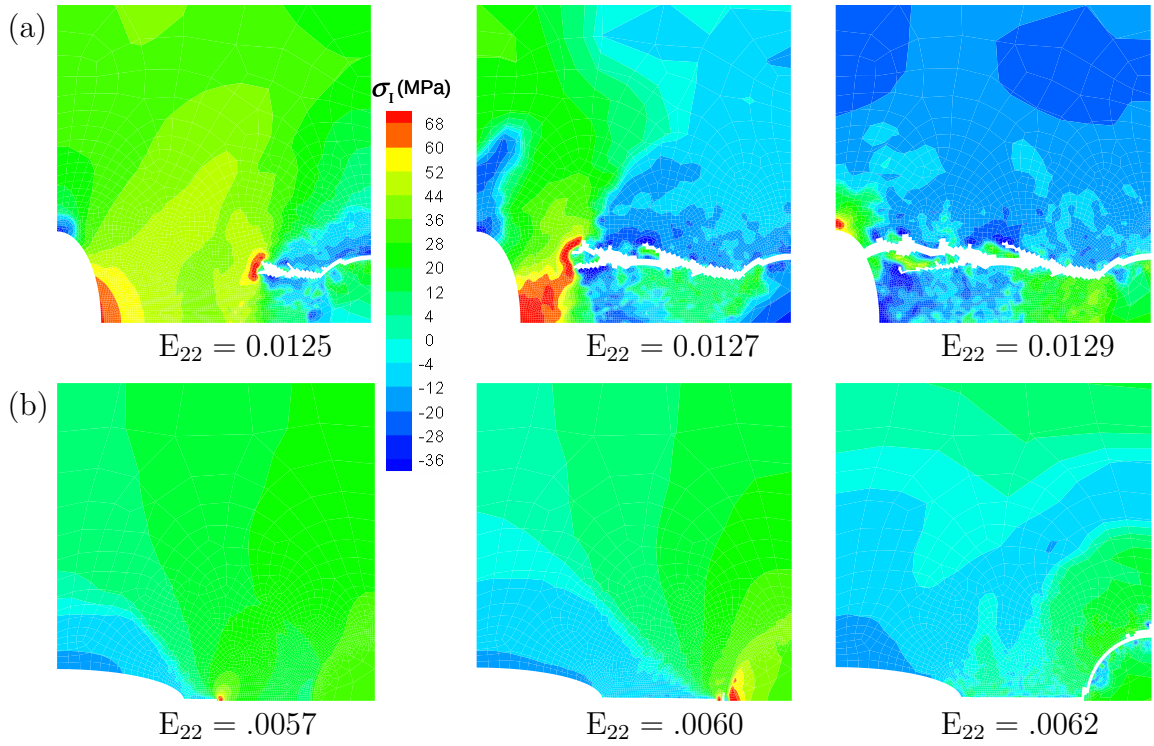

Fig. 54. Development of fracture and σ_1 contours for (a) prolate ($a/b = 0.5$) and (b) oblate ($a/b = 4.0$) shaped void in a composite at $\dot{E} = 1/s$ and T= 25^{o}C.

is shown in Figure 54b, in which case the crack initiates (Fig. 54b at $E_{22} = 0.0057$) from the lateral edge of the void because of crazing, and propagates (Fig. 54b at $E_{22} = 0.0060$) towards the fiber along the plane perpendicular to the loading plane.

When the crack merges into the fiber edge, the mechanism of damage changes from crazing to debonding and the fiber surface debonds from the matrix (Fig. 54b at $E_{22} = 0.0063$). The cracking pattern at an advanced stage of strain is also shown for $a/b = 1.0$ (Fig. 55a) and $a/b = 2.0$(Fig. 55b). $a/b = 2.0$ also shows similar behavior to another oblate shape case, $a/b = 4.0$.

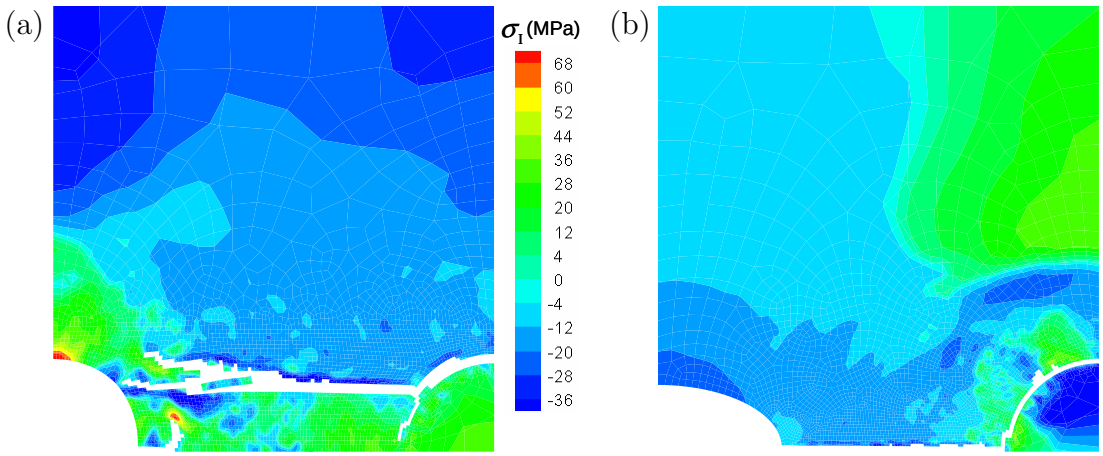

Fig. 55. Crack propagation patterns for the void shape aspect ratio, a/b, of (a) 1.0 and (b) 2.0.

Figure 56 shows the distribution of effective plastic strains at an intermediate stage of crack propagation for different void shapes. For the case of $a/b = 0.5$ and 1.0 the stress–strain response (Fig. 53) shows nonlinear behavior because the effective plastic strain spreads (see Fig. 56a and 56b) throughout the specimen in addition to local in-elastic behavior around the void edge and at the fiber's top edge. With an increase in the a/b ratio, the response curve becomes almost linear because for these two cases the effective plastic strain is only concentrated at the lateral edge and at the crack tip, as shown in Figures 56c and 56d. The red zone in the contours indicates that the zone went through the crazing mechanism. The remaining zones (yellow and light blue), where material behaves plastically, corresponds to a pre-craze

viscoplastic behavior. Changing the void shape from prolate to oblate increases the stress concentration at the lateral edge of the void, which is shown in Figure 57. This figure shows the distribution of hydrostatic stress at $E_{22} = 0.005$ for the void shapes corresponding to the $a/b = 0.5, 1.0, 2.0$ and 4.0. For $a/b = 2.0$ and 4.0,the void edge undergoes a highly localized in-elastic deformation process due to high triaxiality, resulting in craze formation and subsequent failure.

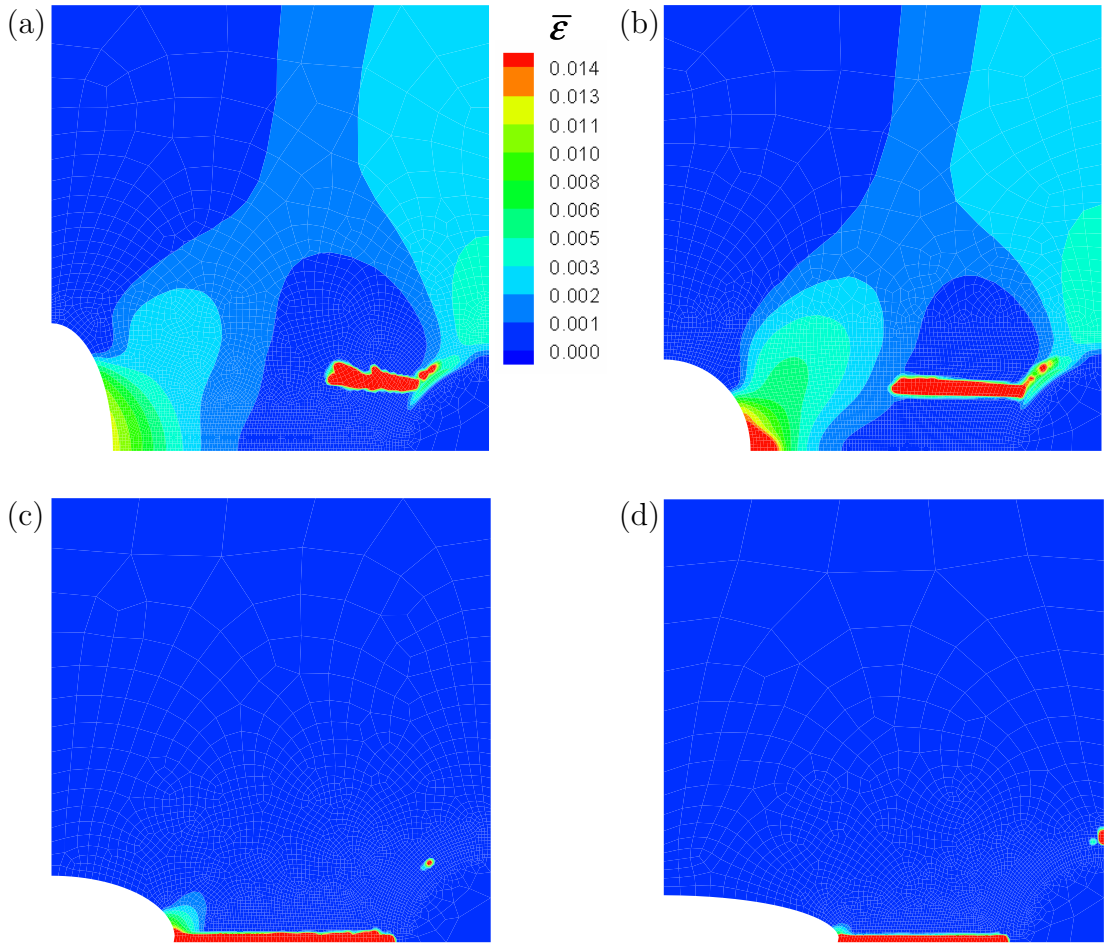

Fig. 56. Distribution of effective plastic strain at an advance stage of crack propagation at T= 25^{o}C for different void aspect ratios, a/b,of (a) 0.5 (b) 1.0 (c) 2.0 and (d) 4.0. The red zone contours corresponds to crazed zone.

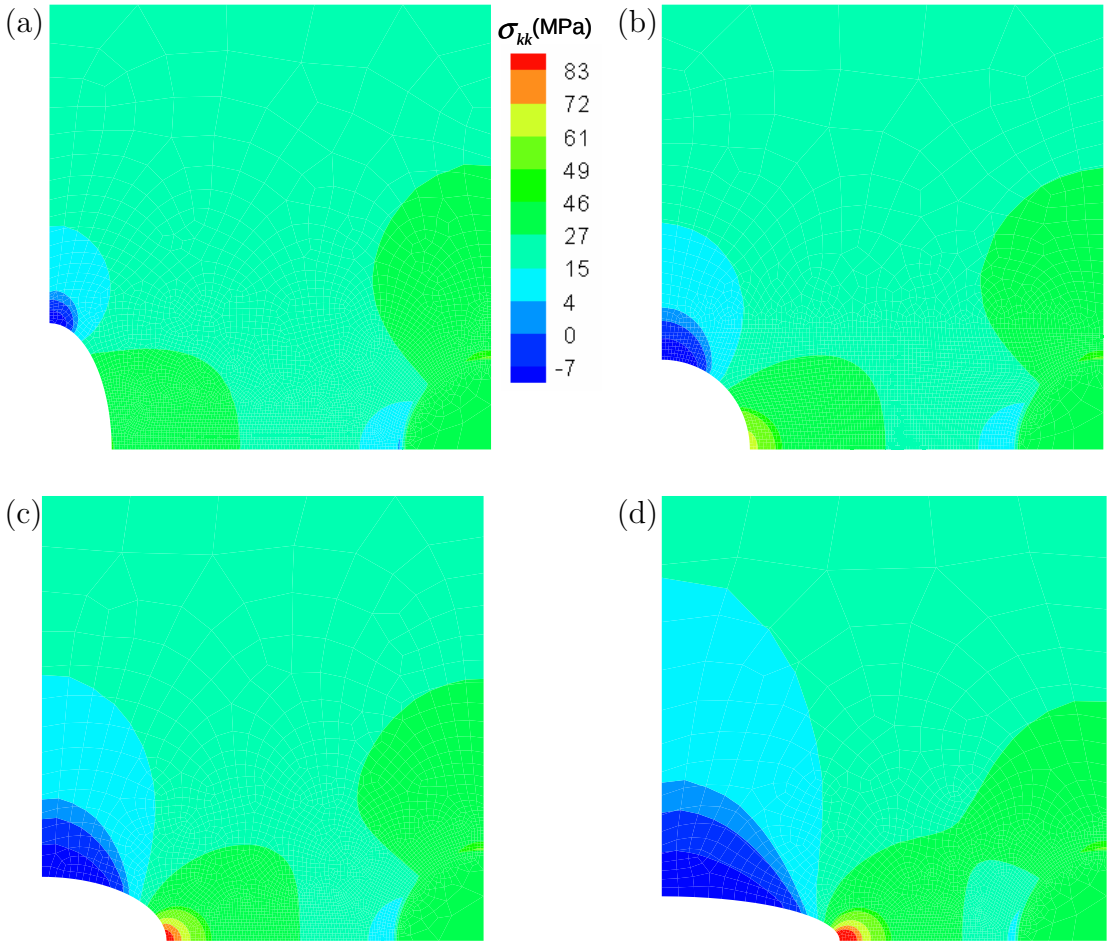

Fig. 57. Hydrostatic stress contours at T= 25^{o}C for the void shape aspect ratios, a/b,of (a) 0.5 (b) 1.0 (c) 2.0 and (d) 4.0.

Figure 58a shows E_i/E_i^0 versus the a/b ratio for a different temperature. The black solid triangles and the hollow squares correspond to craze-induced and debonding-induced fracture initiations, respectively. This plot mainly illustrates the direct effect of the presence of differently shaped voids against the no void case. Due to the presence of a void from prolate to spheroid, the crack initiates at a larger strain than without the presence of a void. Crack initiation strain reduced drastically as the shape of the void became oblate. The curve shows that the crack initiation strain increases with an increase of the a/b ratio up to $a/b = 1.0$, then decreases with an increase of the a/b ratio. When $a/b = 0.5$ and 1.0 the crack initiation occurs through cavitation-induced debonding and when $a/b = 2.0$ and 4.0 craze-induced fracture at the void edge is responsible for crack initiation. This pattern conforms to previous trends indicating that fracture initiation occurs earlier if crazing is the fracture initiation mechanism, and later if debonding is the fracture initiation mechanism.

Figure 58b exhibits $\Sigma_{max}/\Sigma_{max}^0$ versus a/b ratios at the room temperature. The plot illustrates that the maximum macroscopic stress, Σ_{max}, carried by the unit cell is lower for the 'with void' case, corresponding to the all shapes considered here, as opposed to the 'without void' case. Σ_{max} decreases with an increase in the a/b ratio. Change in the stress carrying capacity with respect to the a/b ratio decreases for crack initiation dominated by craze induced fracture from the void edge. A drop in Σ_{max} is not significant as long the void shape remain prolate or close to spheroid. The drop in Σ_{max} increases sharply as the void become more oblate. The difference in the maximum stress carrying capacity between the 'without void' and the 'with void' of $a/b = 0.5$ and 4.0 is -1% and -60%, respectively. The difference in crack initiation strain between the 'without void' and the 'with void' of $a/b = 0.5$ and 4.0 is $+12\%$ and -49%, respectively.

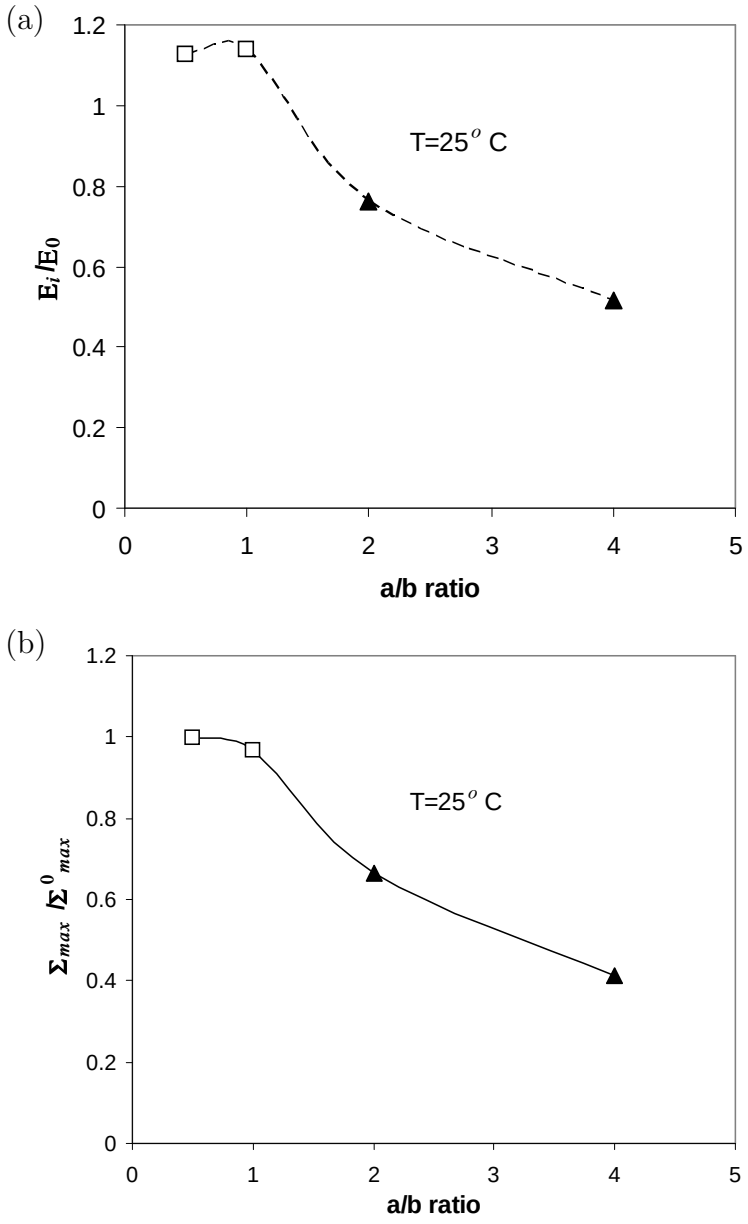

Fig. 58. Plots of (a) normalized crack initiation strain, E_i/E_i^0, vs. a/b ratio and (b) $\Sigma_{max}/\Sigma^0_{max}$ vs. a/b ratio.

The void shape has a severe effect on the damage initiation mechanism, the crack initiation strain and the stress-carrying capacity. As the void shape changes from prolate to oblate, the effect of the void becomes more severe.

e. Effects of Void–Fiber Configuration

In this section the effect of void location relative to the fiber on damage in a composite microstructure is analyzed by considering a unit cell containing a circular-shaped void and a fiber of constant diameter located above the void. For the case where the fiber is located above, the center-to-center distance between the fiber and the void remain the same as in the case where the fiber is located on the side. Figure 59a shows

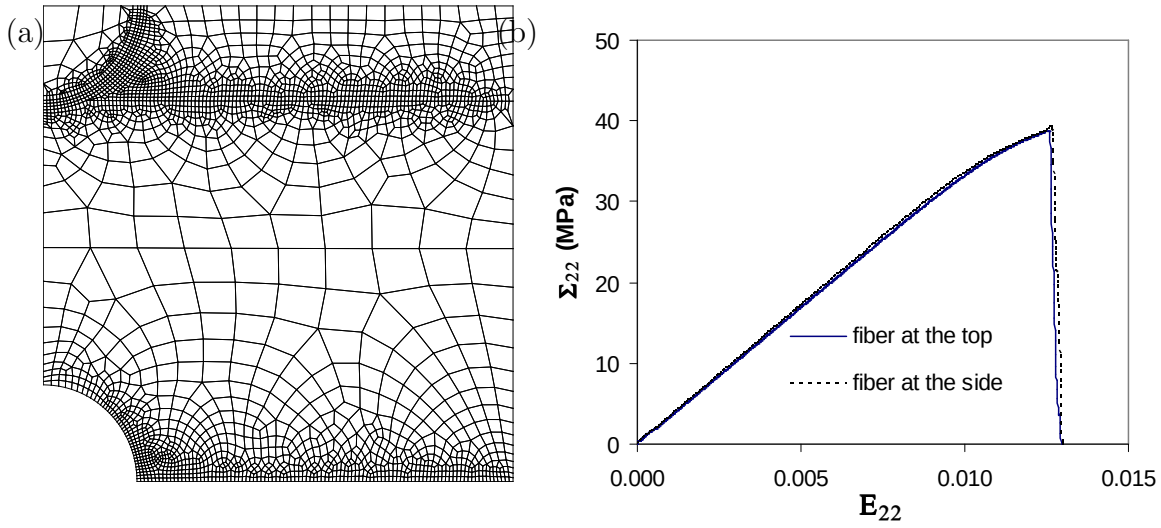

Fig. 59. (a) Finite element mesh of the unit cell, where fiber located at the top of the void (b) macroscopic stress-strain responses for different fiber locations at T= 25^{o}C and $\dot{\mathrm{E}} = 1/\mathrm{s}$.

the finite element mesh corresponding to the former case. The mesh consists of 2638 quadrilateral elements. Figure 59b shows the macroscopic stress-strain response under uniaxial tension at room temperature for different fiber locations. For both top

and side fibers the stress-strain responses, crack initiation strains and the maximum macroscopic stresses are almost the same. However, locally they show completely different behaviors in damage initiation and propagation patterns. Figure 60 shows the cracking pattern for the fiber location at the top (Fig. 60a) and the side (Fig. 60b). Cracks initiate from the lateral edge of the void due to crazing for the top-located fiber, whereas crack initiates from the cavitation-induced debonding from the fiber for the side location. For the top-located fiber there is the appearance of several little branches of cracks, but ultimately the main crack travels through the specimen.

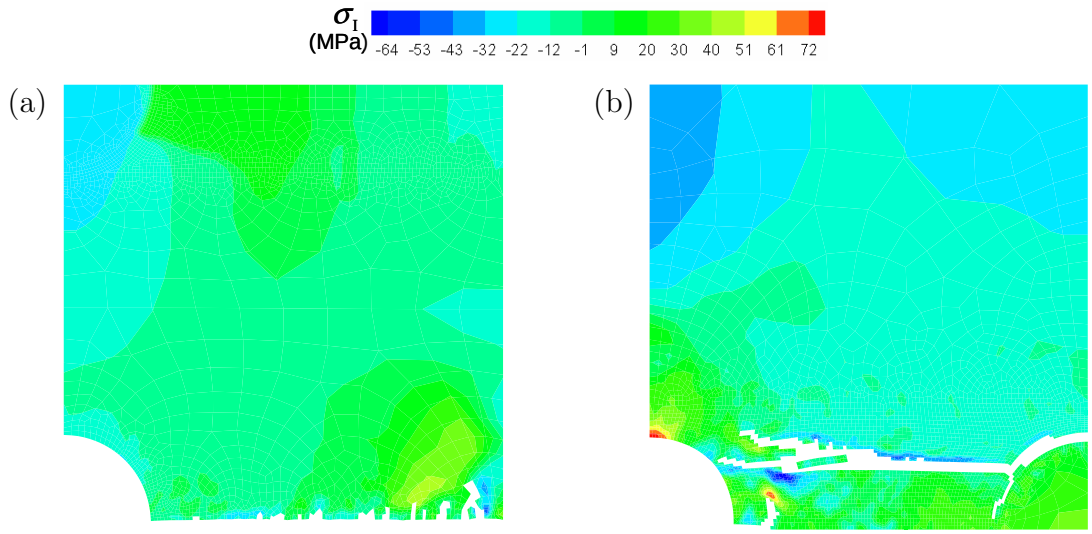

Fig. 60. Maximum principal stress contours at an advance stage of fracture for the fiber located at the (a) top and (b) side of the void.

2. Prediction at Varying Temperature

In this section we extended the investigation of the effects of voids in a composite microstructure, described in Section 1.a, by considering uniaxial plane-strain tension loading at different temperatures. In this case, six temperatures, T= 0^oC, 25^oC, 50^oC, 75^oC, 90^oC and 110^oC are considered. The finite element mesh of the problem is shown in Figure 39b.

Figure 61a shows the macroscopic stress-strain responses under uniaxial tension for different temperatures. All of the curves corresponding to different temperatures show this macroscopic non-linear behavior. With the increase in temperature, the microstructures shows more ductile behavior as glassy polymers exhibit softer responses and reach earlier initial yielding.

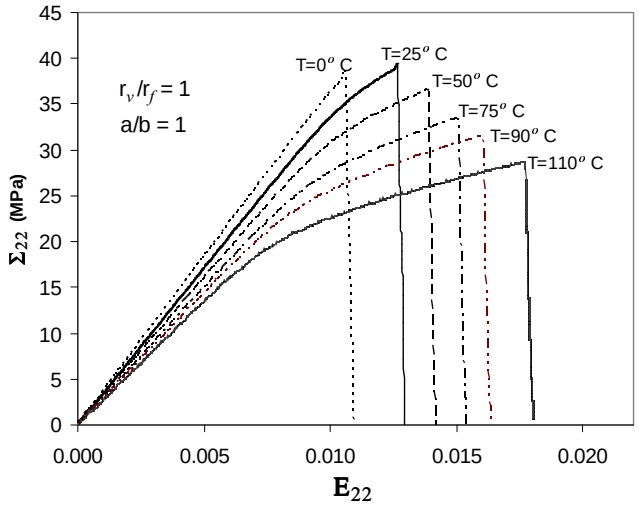

Fig. 61. Macroscopic stress–strain responses at different temperatures for circular ($a/b = 1$) shaped void and fiber located at the side.

Figure 62 exhibits the development of crack initiation and propagation, and the distribution of maximum principal stress, σ_{I}, in the microstructure for T=0^oC and 90^oC cases at different stages of straining, after damage initiation. For T=

0^oC(Fig. 62a at $E_{22} = 0.0105$) the crack initiates from the cavitation-induced debonding, followed by the lateral progression of craze-induced cracks from the fiber surface (Fig. 62a at $E_{22} = 0.0107$) and merges into the void edge (Fig. 62a at $E_{22} = 0.0109$). Before merging into the void

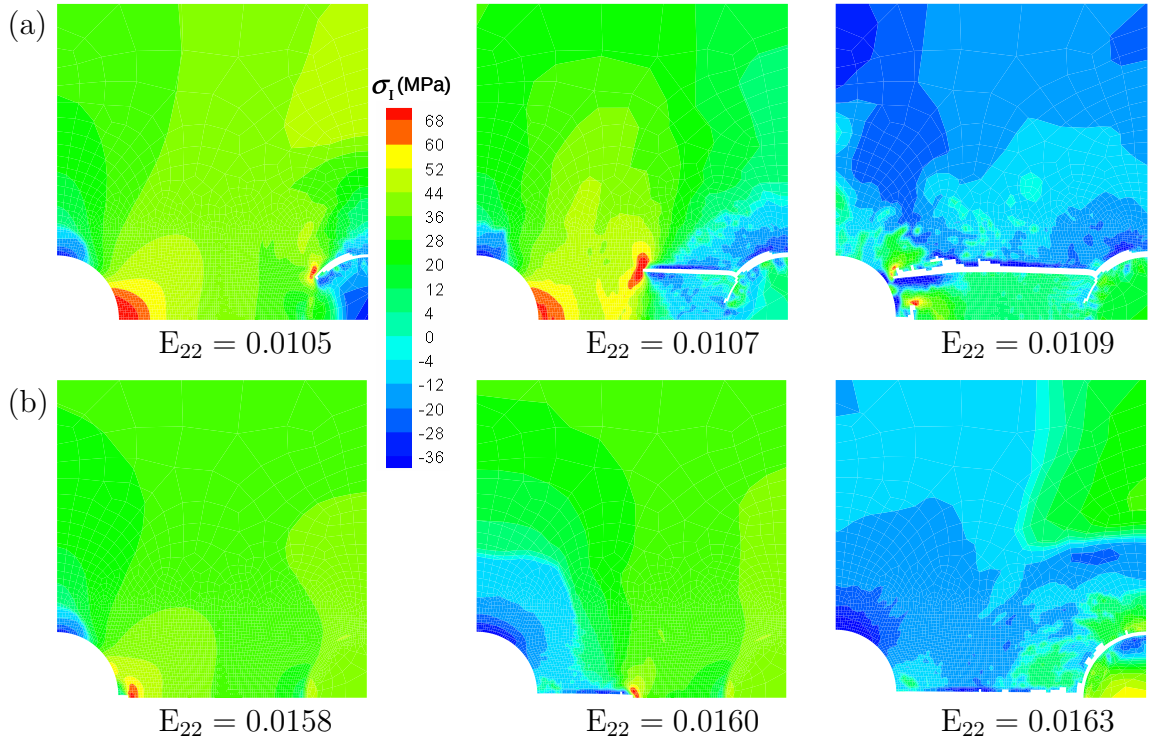

Fig. 62. Development of fracture and σ_I contours at (a) T= 0^oC and (b) T= 90^oC.

the main crack shows several branches. For T= 90^oC, the crack initiates due to crazing at the lateral edge of the void (Fig. 62b at $E_{22} = 0.0158$) and progresses toward the fiber along the direction perpendicular to the loading axis (Fig. 62b at $E_{22} = 0.016$). Finally, the craze induced crack merges into the fiber's edge and debonding (Fig. 62b at $E_{22} = 0.0163$) over the fiber surface occurs due to cavitation induced matrix cracking. Figure. 63 shows the fracture at an advance stage of failure for other

temperature cases (T= 25^{o}C, 50^{o}C, 75^{o}C and 110^{o}C) considered for analysis. Up to T= 25^{o}C, a crack initiates due to cavitation induced debonding. If the temperature is increased to 50^{o}C (Fig. 63b),75^{o}C (Fig. 63c) and 110^{o}C (Fig. 63d) initiation of the crack occurs from the void's lateral edge, due to crazing.

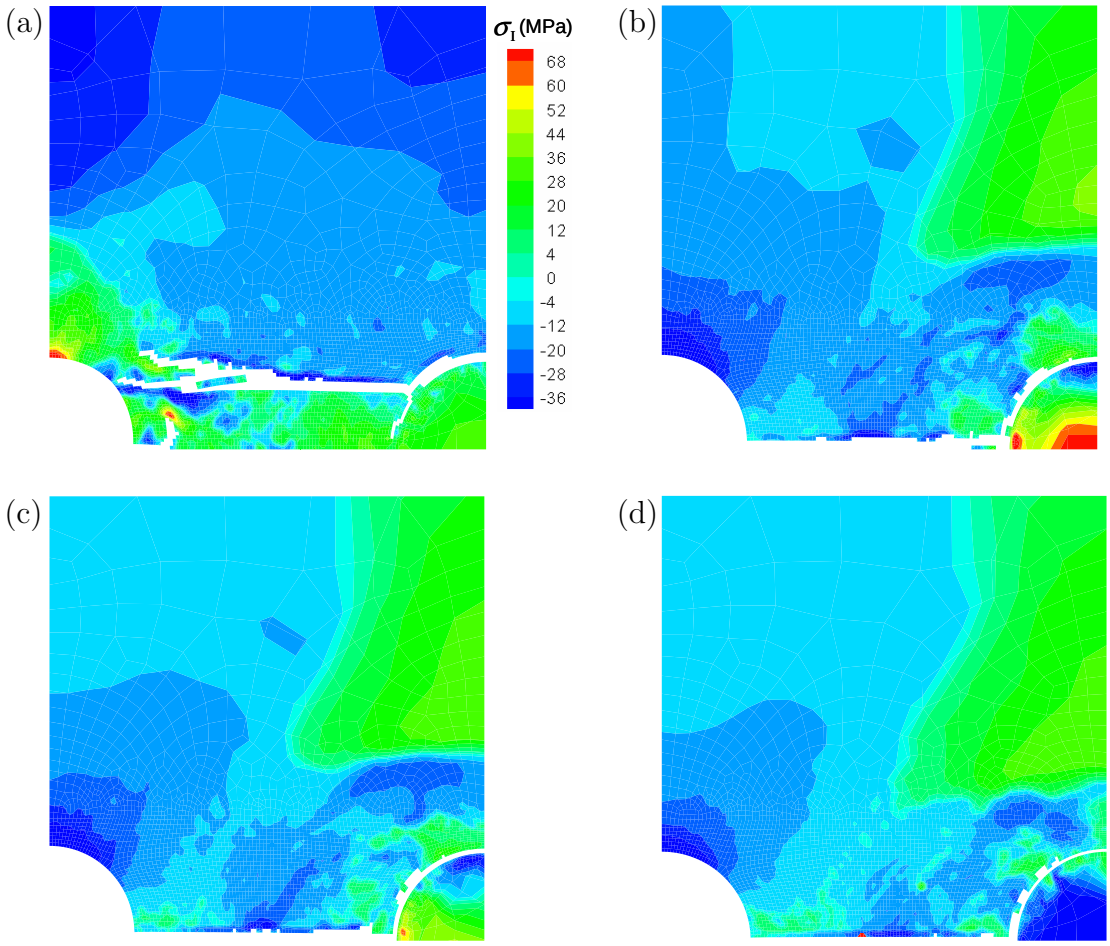

Fig. 63. Fracture patterns and σ_I contours at an advance stage of failure for different temperatures T=(a) 25^{o}C (b) 50^{o}C (c) 75^{o}C and (d) 110^{o}C.

Local behaviors also contribute to the ductile responses and damage initiation mechanisms at moderate temperatures. In figure 64, effective plastic contours is

shown at an advance stage of failure for different temperature cases, which illustrates that with the increase of temperature, the plastically deformed zone within the unit cell increases. As a result, the effective plastic strain, $\bar{\epsilon}$, has a wider distribution within the microstructure for T= 90^{o}C, than in the T= 0^{o}C case. Figure 65 shows distribution of hydrostatic stress for different temperatures at $E_{22} = 0.01$ before any crack initiation, which illustrates that the higher the temperature, the lower the level of hydrostatic stress at the lateral edge of the void and the fiber's top edge. Thus, the propensity of craze formation increases with the increase in temperature, while the possibility of the cavitation-induced debonding decreases. Craze initiation criteria and debonding criteria are dependent upon linear and quadratic terms of hydrostatic stress, respectively. Therefore, there is a competition between craze-induced fractures and cavitation-induced debonding, depending upon temperature.

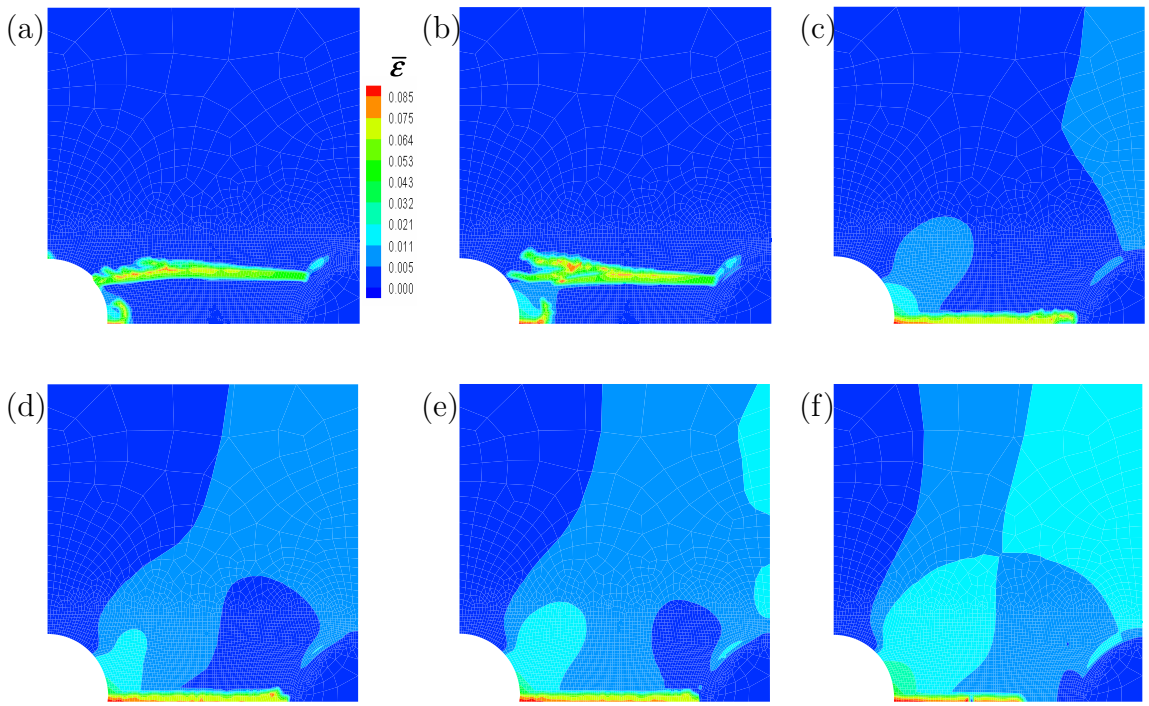

Fig. 64. Effective plastic strain, $\bar{\epsilon}$, contours at an advance stage of failure for different temperatures of T=(a) 0^{o}C (b) 25^{o}C (c) 50^{o}C (d) 75^{o}C (e) 90^{o}C and (f) 110^{o}C.

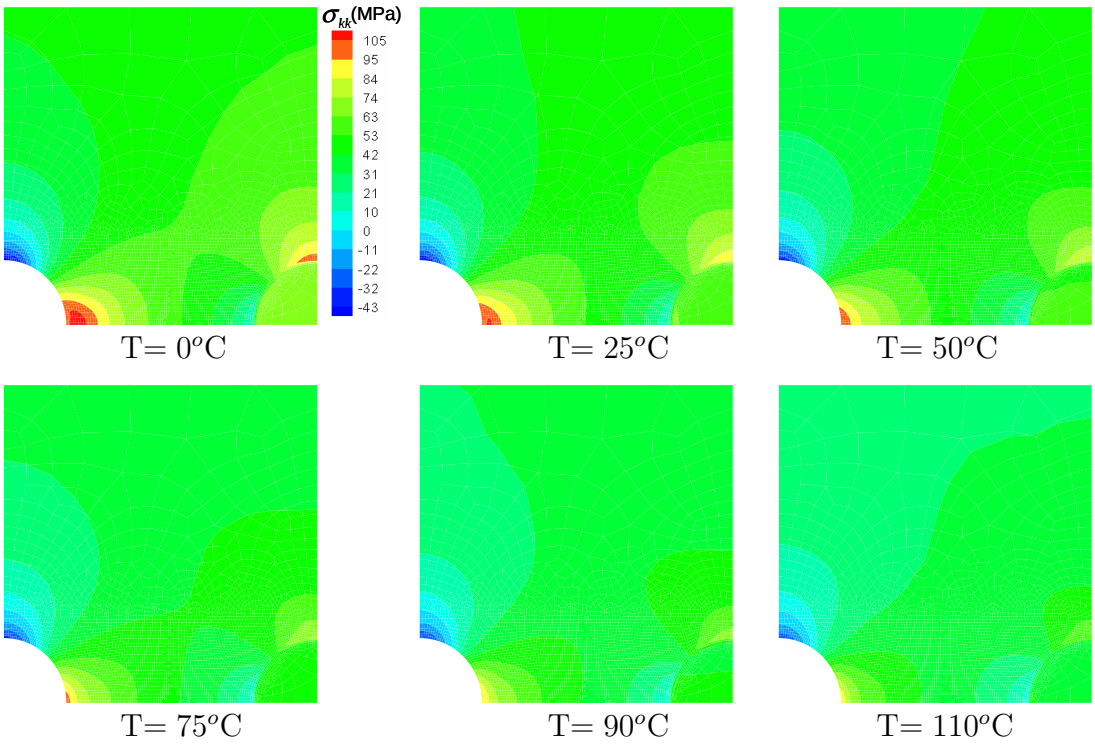

Fig. 65. Hydrostatic stress distribution at $E_{22} = 0.010$ for different temperatures.

Figure 66a shows E_i versus the temperature plot, where E_i is the macroscopic strain at the onset of fracture initiation. The black solid squares and the hollow squares correspond to craze-induced and debonding-induced fracture initiations, respectively. The plot illustrates that the crack initiation strain increases with an increase in temperature. At room temperature (T= 25^{o}C), the presence of a void causes fracture initiation at the larger strains than in the 'without void' case.

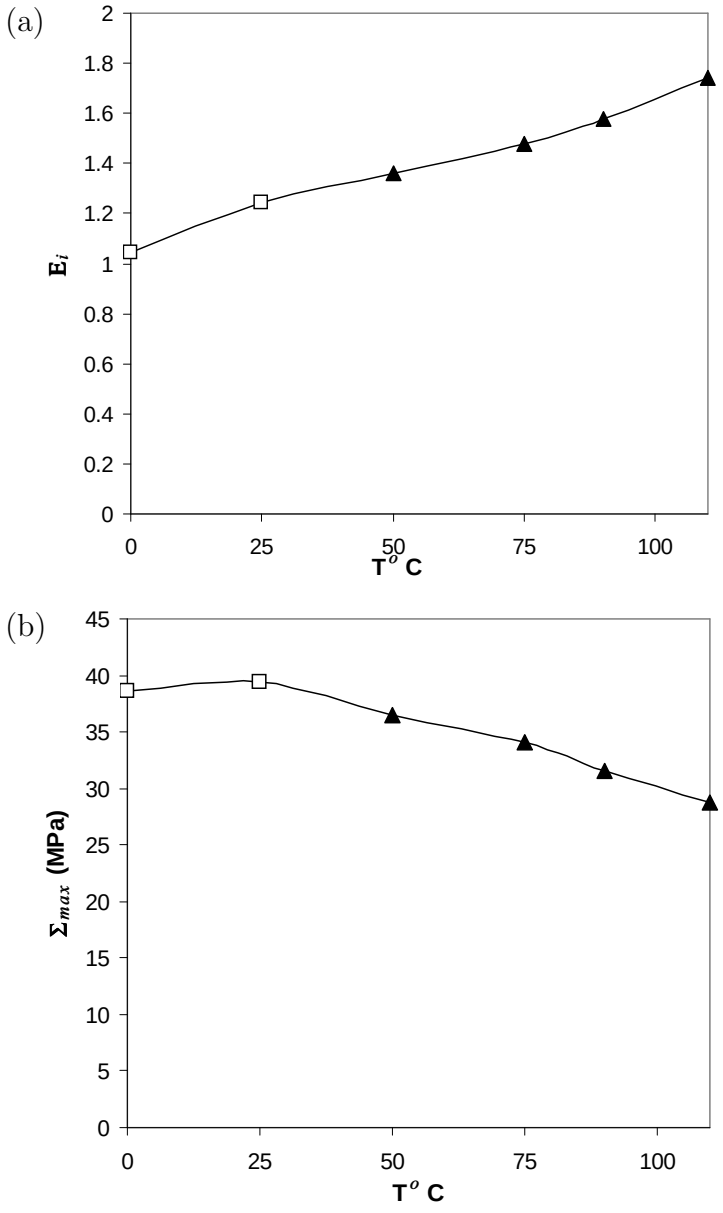

Fig. 66. Plots of (a) E_i vs. temperature (b) Σ_{max} vs. temperature. Here E_i and Σ_{max} is crack initiation strain and maximum macroscopic stress carried by the unit cell, respectively.

Figure 66a exhibits $\Sigma_{\max}$ versus the temperature plot, where $\Sigma_{\max}$ is the maximum macroscopic stress carried by the unit cell. The plot illustrates that the maximum macroscopic stress carried by the unit cell increases with an increase in temperature up to T= 25^oC, then decreases with a further increase in temperature.

Mechanisms behind the damage formation have the key role in demonstrating the above behavior regarding the stress-carrying capacity of the microstructure. The stress-carrying capacity increases with increasing temperature when damage initiation occurs from the cavitation-induced fiber debonding, and decreases with the increasing temperature if the damage initiates through the crazing at the void's lateral edge.

a. Effects of Temperature and Void-Fiber Spacing

In this section the effects of void fiber proximity on damage at different temperatures subjected to plane-strain tension are investigated. The ratio of the shortest distance (l_f) between the fiber and the void edge to the void radius (r_v), l_f/r_v, is varied, while keeping the fiber and void areas the same. Five l_f/r_v ratio of 0.40, 0.72, 1.20, 2.00 and 3.60 are considered. The circular-shaped fiber with the same area as the void is placed at the side. To study the temperature effect, T= 0^oC, 25^oC, 50^oC, 75^oC, and 90^oC are considered for all fiber distance. The meshes corresponding to the l_f/r_v ratio of 0.72, 1.20, 2.00 and 3.60 are shown in Figures 67a, 67b, 67c and 67d, respectively. The number of quadrilateral elements are 3573, 3639, 3744 and 3512 for $l_f/r_v = 0.72, 1.20, 2.00$ and 3.60, respectively.

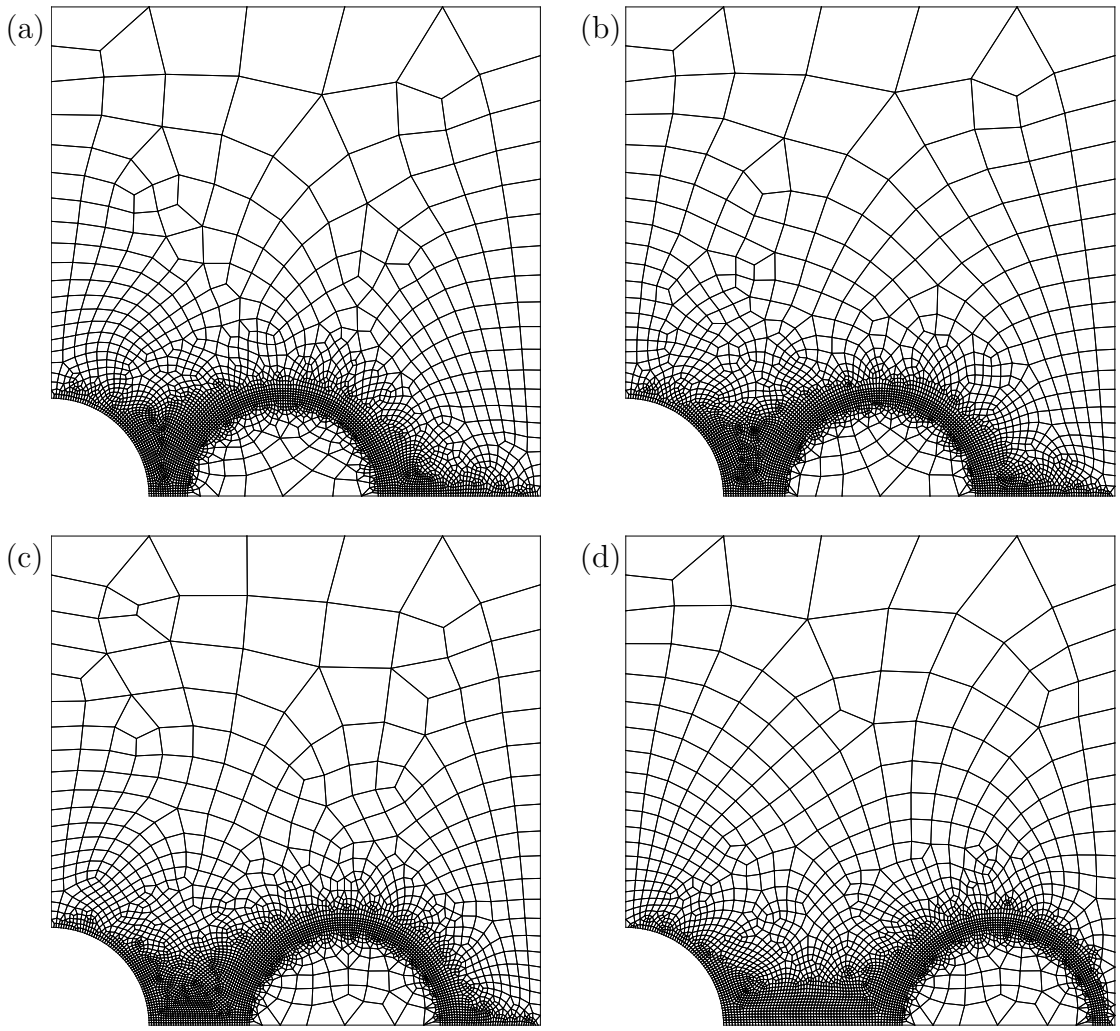

Fig. 67. Finite element meshes of different distances (l_f) of fiber from the void edge to the void radius (r_v), l_f/r_v, ratio of (a) 0.72 (3573 elements) (b) 1.20 (3639 elements) (c) 2.0 (3744 elements) and (d) 3.6 (3512 elements).

Figure 68 shows the macroscopic stress-strain response under uniaxial tension for $l_f/r_v = 0.40, 0.72, 1.20, 2.00$ and 3.60 at T= 25^{o}C at $\dot{\text{E}} = 1./\text{s}$. This figure illustrates that macroscopic responses corresponding to different l_f/r_v ratios show similar behaviors, but the sharp stress drop (due to damage initiation and progression) occurs at a larger strain and stress with the increase of the fiber distance from the void edge.

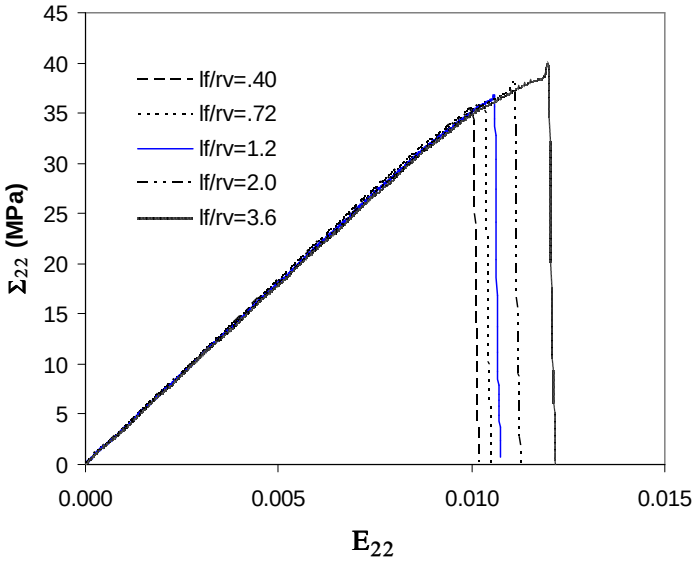

Fig. 68. Macroscopic stress strain responses at T=25^{o}C and $\dot{\text{E}}$ =1/s for different l_f/r_v ratios.

Crack propagation patterns were investigated for $l_f/r_v = 0.40, 0.72, 1.20, 2.00$ and 3.60 at temperature of 0^{o}C, 25^{o}C, 50^{o}C, 75^{o}C and 90^{o}C. For l_f/r_v ratios less than 3.60 for all temperatures considered here yield similar crack initiation and propagation patterns. In these cases, the crack initiates by cavitation-induced debonding (not shown here), followed by the initiation and lateral progression of a new craze-induced crack, which ends up merging into the void edge. Only $l_f/r_v = 3.6$ shows interesting variation of crack initiation mechanisms with an increase in temperature.

Figure 69 shows the maximum principal stress contours and crack propagations for all l_f/r_v ratio T= 50^{o}C at an advance stage of failure. For the case of $l_f/r_v = 0.40, 0.72, 1.20$ and 2.0 (Fig. 69b, 69c, 69d and 69e) the crack initiates from debonding on the top edge of the fiber. The crack further progresses through the matrix due to the crazing, and finally merges into the void. During the crack propa-

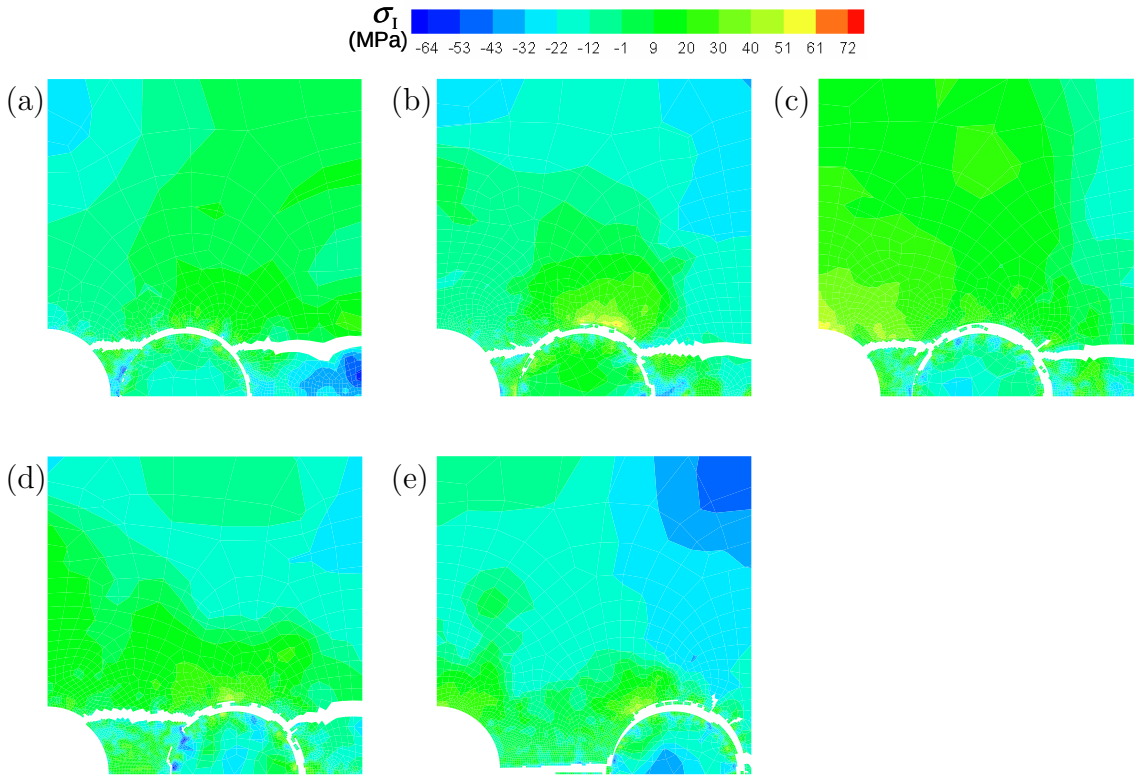

Fig. 69. Crack propagation patterns at T=50^{o}C and $\dot{\text{E}} = 1.0$/s for l_f/r_v ratio of (a) 0.40 (b) 0.72 (c) 1.20 (d) 2.00 and (e) 3.60.

gation, the main crack shows several small branches because the crack tip stress field is redistributed due to the influence of the stress field created by void. However, no branches corresponding to those l_f/r_v ratios grow any further. Crack propagation patterns corresponding to $l_f/r_v = 3.6$ for T= 50^{o}C are shown in the Figure. 69e.

In this case, the crack initiates from the lateral edge of the void due to crazing, and propagates towards the fiber along the plane perpendicular to the loading plane. Soon thereafter, the crack diverts at an angle and merges at the fiber edge. Then the mechanism of damage changes from crazing to debonding, and the fiber surface debonds from the matrix.

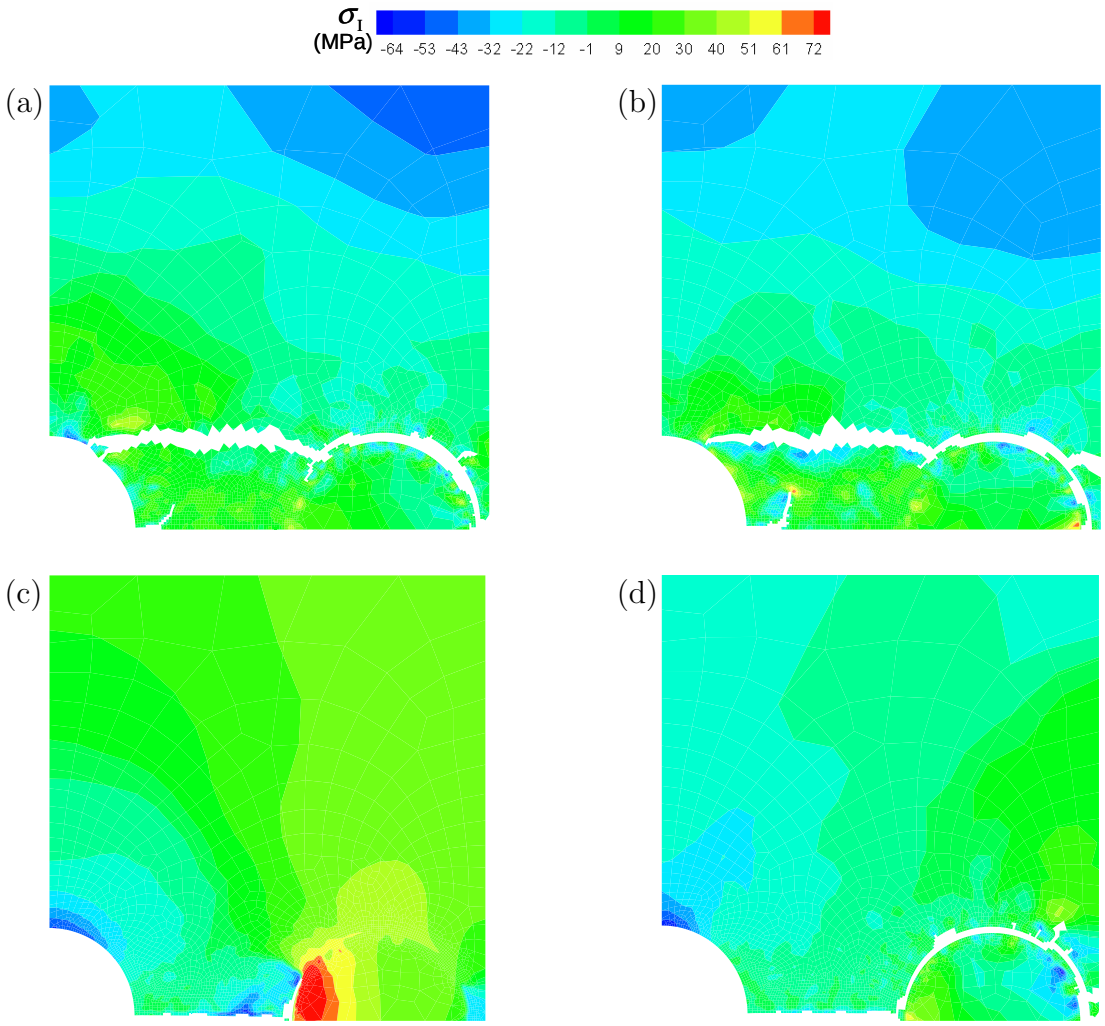

Fig. 70. Crack propagation patterns for the $l_f/r_v = 3.6$ at $\dot{E} = 1.0/s$ for different temperatures (a) T= 0^oC (b) T= 25^oC (c) T= 75^oC and (d) T= 90^oC.

Figure 70 shows the maximum principal stress contours and crack propagation

for $l_f/r_v = 3.6$ for T= 0^{o}C, 25^{o}C, 75^{o}C and 90^{o}C at an advance stage of failure. For the low temperature cases of T= 0^{o}C and 25^{o}C a crack initiates due to debonding on the fiber's top edge and propagates towards the void perpendicular to the loading direction. A craze-induced crack from the void's lateral edge is also initiated and diverted towards the other crack, coming from the fiber edge in a parallel plane. The reason for this diversion was discussed in an earlier Section. For the cases of T= 75^{o}C and 90^{o}C the crack initiates through the craze-induced failure mechanism from the lateral edge of the void and propagates perpendicular to the loading, which ends by merging with the fiber followed by the fiber-matrix debonding.

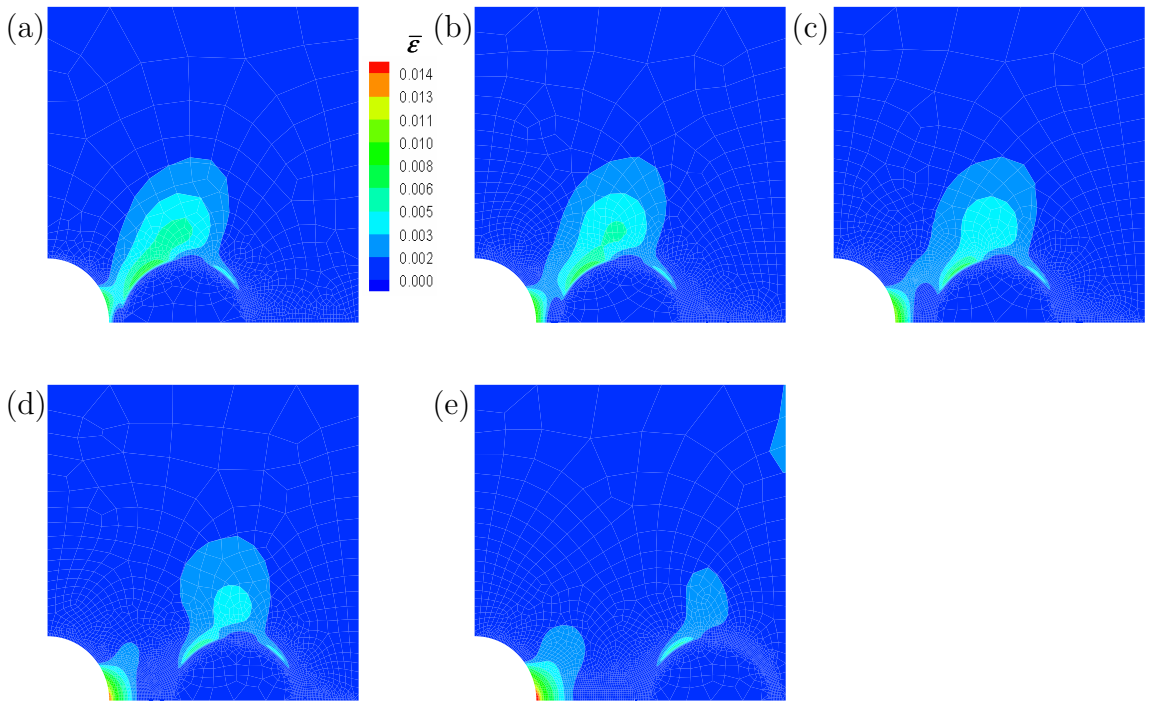

Fig. 71. Effective plastic strain contours at T= 50^{o}C and $E_{22} = 0.01$ for different l_f/r_v ratios of (a) 0.40 (b) 0.72 (c) 1.20 (d) 2.0 and (e) 3.60.

Figure 71 shows the distribution of effective plastic strain, $\bar{\epsilon}$, at $E_{22} = 0.01$ for different fiber distances at T= 50^{o}C. As the fiber moves away from the void, effective

plastic strain concentration around the void increases, and that around the fiber decreases (Fig. 71c, 71d, 71e and 71f). The intensity of the plastic strain (maximum $\bar{\epsilon}$ within the unit cell) also increases with the increase of fiber-void distance.

Figure 72 shows the distribution of hydrostatic stress obtained at $E_{22} = 0.01$ for T= 50^{o}C for $l_f/r_v = 0.40, 0.72, 1.20, 2.00$ and 3.60. This figure shows that the stress concentration at the lateral edge of the void increases with the increase of the

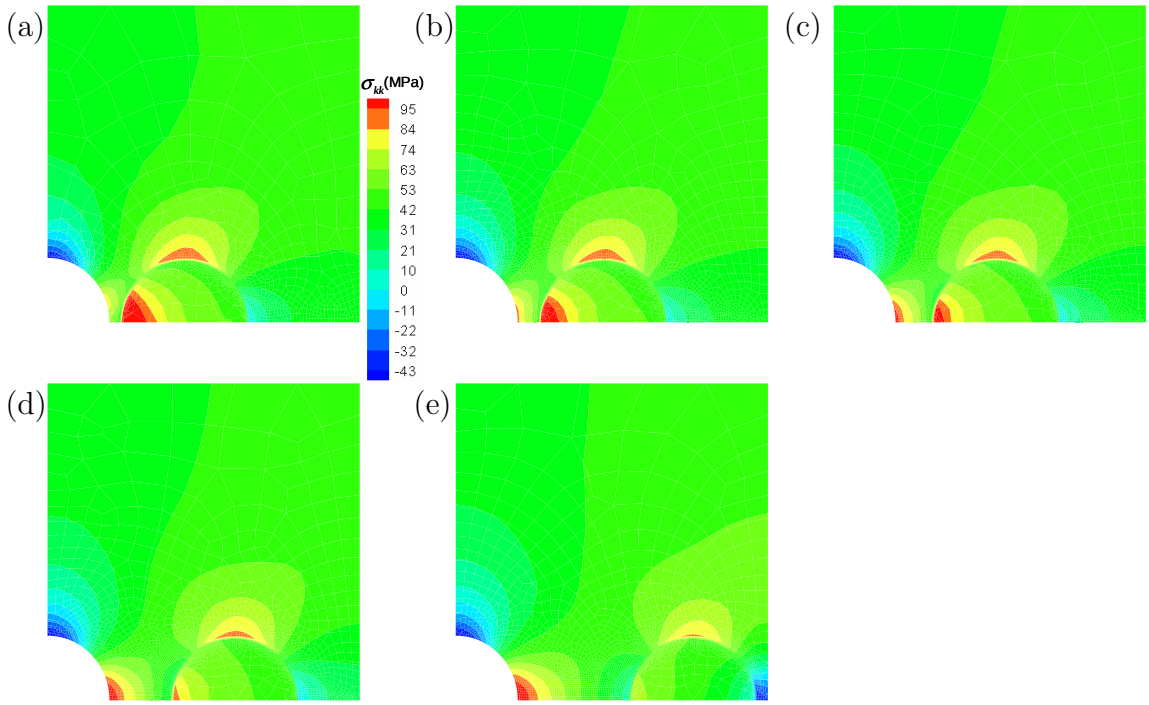

Fig. 72. Hydrostatic stress contours at a temperature of 50^{o}C at $E_{22} = 0.01$ for different fiber distance with the void , l_f/r_v ratio of (a) 0.40 (b) 0.72 (c) 1.20 (d) 2.0 and (e) 3.6.

l_f/r_v ratios. Increasing the distance of the fiber from the void edge also decreases the hydrostatic stress concentration at the fiber top edge, which is critical for causing the cavitation-induced debonding. Therefore, moving the fiber away from the void increases the propensity of craze formation around the void edge and decreases the

propensity of debonding from the fiber's top edge.

Figure 73a shows E_i versus the l_f/r_v ratio for different temperatures. The black triangles and the hollow squares correspond to craze-induced and debonding-induced fracture initiations, respectively. The plot illustrates that with an increase in the l_f/r_v ratio, the crack initiation strain increases for all temperatures considered here. The slope of E_i versus the l_f/r_v plot increases with an increase in temperature. For the case of $l_f/r_v = 3.6$ for the temperatures over 25^oC, the change of macroscopic crack initiation strain with respect to fiber-void distance (the slope of the curve) decreases with an increase in the l_f/r_v ratio. This is because for those cases, the crack initiates through the craze-induced fracture from the void's lateral edge. In the rest of the combination of temperatures and l_f/r_v ratios, the slope of the crack initiation strain versus the lf/rv ratio is larger due to the cavitation-induced debonding at the fiber's top edge. To clarify this concept, we have also plotted E_i versus the temperature for different l_f/r_v ratios, as shown in Figure 73b. This figure illustrates that with an increase in the l_f/r_v ratio, up to 2.0, the macroscopic strain at the onset of crack formation increases with an increase in temperature in an exponential manner, due to the fact that debonding is the mechanism of the damage initiation. However, for $l_f/r_v = 3.6$, a change of crack initiation strain occurs in the same pattern up to T= 25^oC because of the debonding crack initiation mechanism. The slope of the normalized crack initiation strain with respect to temperature decreases when the damage initiation mechanism is changed from debonding to crazing.

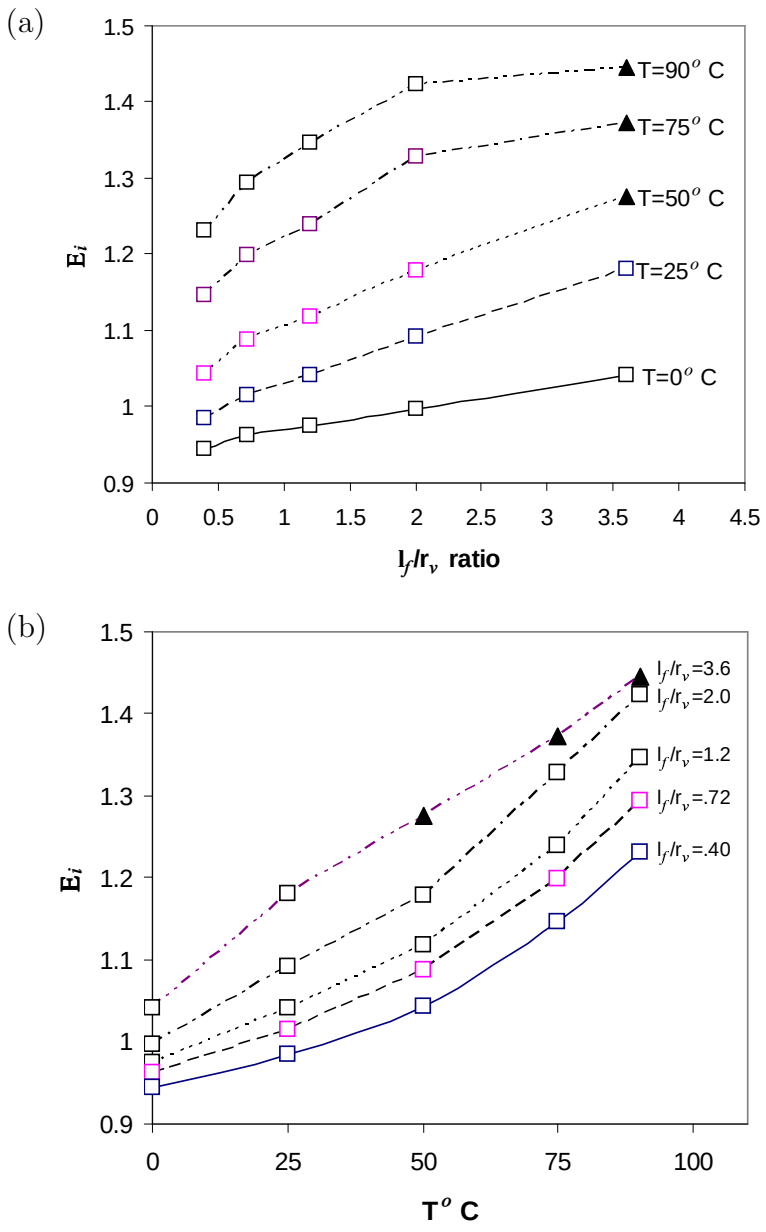

Fig. 73. Plots of (a) Macroscopic crack initiation strain, E_i, vs. l_f/r_v ratio for different temperature, where l_f is the shortest distance between fiber and void edge and r_v is the void radius (b) E_i vs. temperature for different l_f/r_v ratio. The hollow squares and solid triangles corresponds to fracture initiation by debonding at the fiber -matrix interface and craze induced fracture from void, respectively.

Figure 74a exhibits $\Sigma_{\max}$ versus l_f/r_v ratio for different temperature cases. The plot illustrates that the maximum macroscopic stress carried by the unit cell increases with the l_f/r_v ratio, as the fiber moves away from the void. For the T= 50^{o}C, = 75^{o}C and = 90^o cases the change of stress carrying capacity (the slope of the curve) with respect to the l_f/r_v ratio decreases because crack initiation occurs by craze induced fracture from the void edge. the stress carrying capacity also decreases for T= 75^{o}C and = 90^{o}C. Figure 74b shows $\Sigma_{\max}$ versus temperature for different l_f/r_v ratios, which illustrates that the l_f/r_v from 0.4 to 2.0 shows similar patterns of losing the maximum stress carrying capacity of the unit cell with temperature.

For $l_f/r_v = 3.6$ sensitivity of maximum macroscopic stress with an increase of temperature. For $l_f/r_v = 3.6$, the sensitivity of the maximum macroscopic stress increases with the temperature rise, as we observed for $l_f/r_v = 3.6$, and $\Sigma_{\max}$ versus the temperature curve intersects the curve of $l_f/r_v = 2.0$. Where the maximum stress for $l_f/r_v = 3.6$ at T= 90^{o}C drops below the maximum stress carried by $l_f/r_v = 2.0$.

At room temperature the difference in the maximum stress-carrying capacities between $l_f/r_v = 0.40$' and 3.6 is about 11%. The difference in crack initiation strains between $l_f/r_v = 0.40$' and 3.6 is about 19%. Thus, the void-fiber proximity has an effect on the damage initiation mechanism, the crack initiation strain and the stress-carrying capacity. If the fiber is located adjacent to the void, the effects of the void become more severe with an increase in temperature.

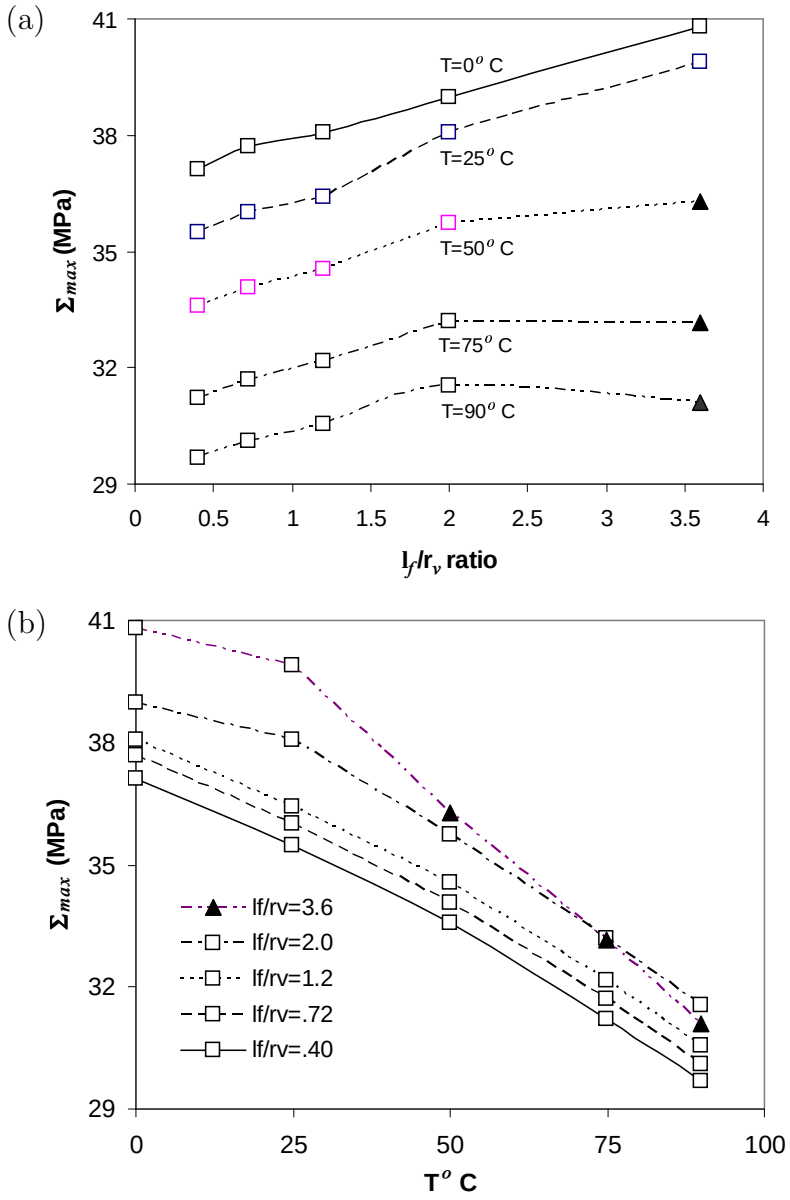

Fig. 74. Plots of (a) $\Sigma_{\max}$ vs. l_f/r_v ratio for different temperatures (b) $\Sigma_{\max}$ vs. temperature for different l_f/r_v ratios.

b. Effects of Temperature and Void Shape

To study the temperature effects of the problem (the effects of different void shapes at room temperature) considered in Section 4.3, we also analyzed the problem at T= 0^oC, 50^oC, 75^oC, and 90^oC. In all temperature cases of the oblate shaped voids of $a/b = 2.0$ and 4.0, damage initiates due to crazing at the lateral edge. Their progression manner is the same as in the T= 25^oC case (discussed earlier, also see Fig. 54b and 55b). The effects of temperature on the mechanism of the crack initiation and propagation for circular-shaped voids ($a/b = 1.0$) have already been discussed in Section 4.3.

Figure. 75 shows the maximum principal stress (σ_{I}) contours and the crack propagation patterns at an advance stage of fracture corresponding to the prolate shaped void ($a/b = 0.5$). For all temperature cases considered here, the main crack initiates from the fiber debonding, followed by craze induced crack accompanied by the formation of several branches. However, for T=0^oC (Fig. 75a)and 75^oC (Fig. 75b) the branched crack arrested after progressing a small distance, on the contrary, for T= 50^oC (Fig. 75c) and 90^oC (Fig. 75d), the branched cracks continued to progress and merged into the void edge. This occurs because at different temperatures the stress levels and their redistribution during crack propagations are different (a detailed discussion of this can be found in Section 1).

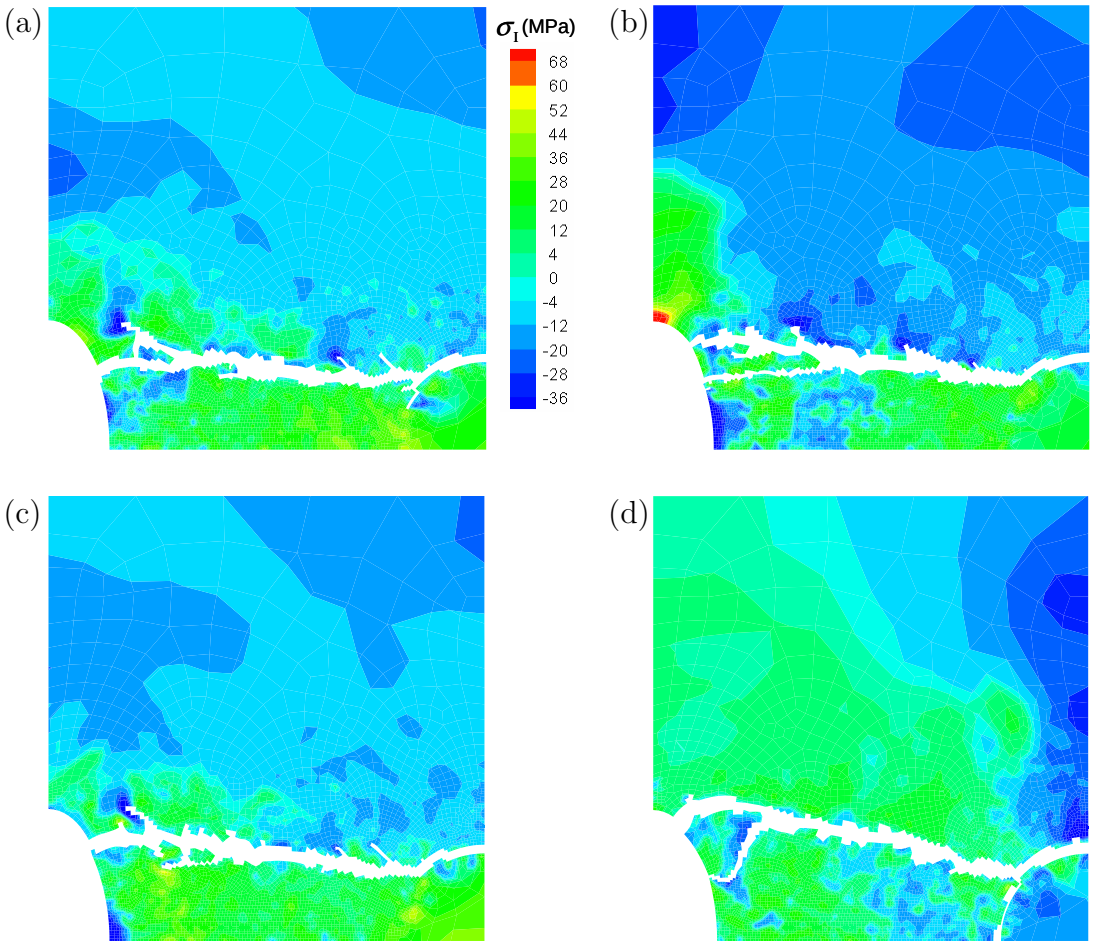

Fig. 75. Crack propagation patterns for $a/b = 0.5$ at $\dot{\mathrm{E}} = 1/\mathrm{s}$ at T=(a) 0^oC (b) 50^oC (c) 75^oC and (d) 90^oC.

Figure 76a shows E_i versus the a/b ratio for different temperatures. The black solid triangles and the hollow squares are corresponding to the craze–induced and debonding–induced fracture initiations, respectively. The plot illustrates that the crack initiation strain decreases with an increases in the a/b ratio for all temperatures except for T= 0^oC and 25^oC up to $a/b = 1$. For $a/b = 0.5$ and 1.0 at T= 0^oC and 25^oC the macroscopic crack initiation strain increases with the a/b ratios. This is because in those cases the crack initiates through the cavitation-induced debonding at the fiber's top edge. For the rest of the combination of temperatures and a/b ratios, the crack initiation strain decreases with an increase in the a/b ratio because the craze-induced failure at the void's edge is the crack initiation mechanism. For further clarification, we have also plotted E_i versus the temperature for different a/b ratios, as shown in Figure 76b. For $a/b = 0.5$ the macroscopic strain at the onset of the crack formation increases with the increase in temperature in a linear fashion, due to the crack initiation from the fiber-matrix debonding. However, for $a/b = 1.0$, the change in crack initiation strain occurs linearly up to T= 25^oC because of the debonding crack initiation mechanism. However, after T = 25^oC the slope of the curve decreases because there is a transition between the damage initiation mechanism from debonding to crazing.

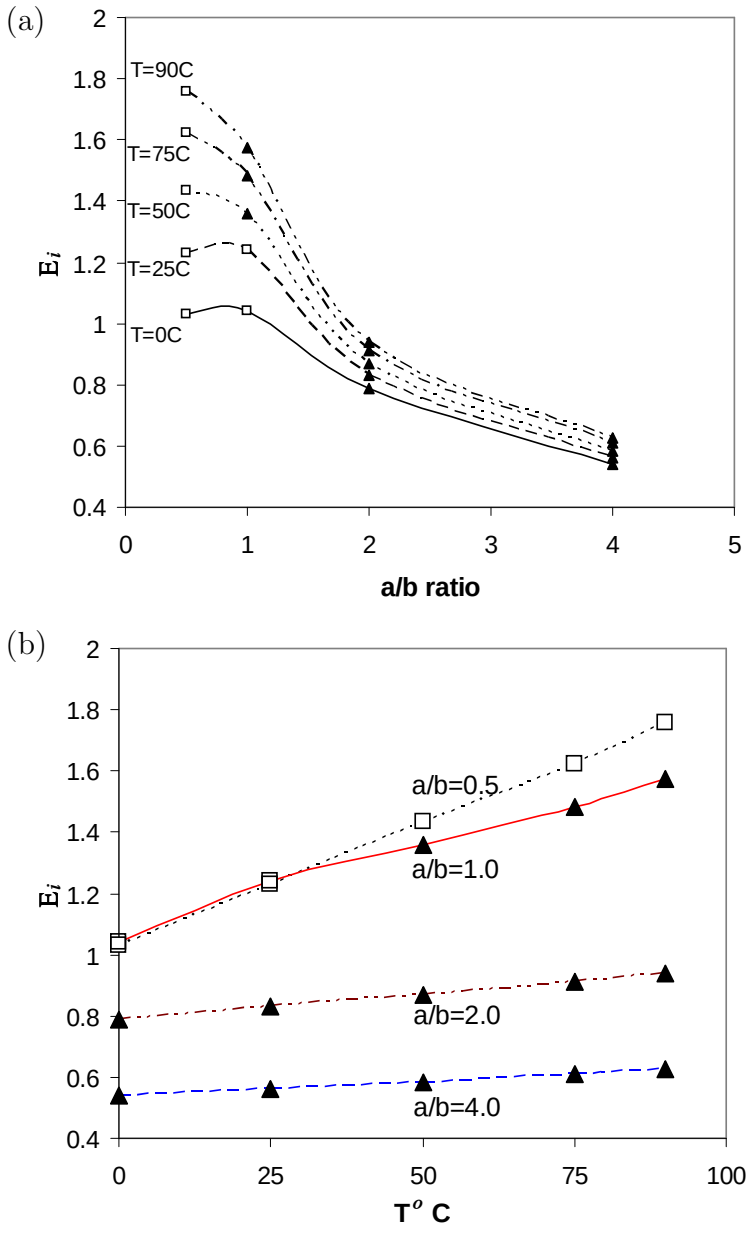

Fig. 76. Plots of (a) E_i vs. a/b ratio for different temperatures (b) E_i vs. temperature for different a/b ratios. The hollow squares and solid triangles correspond to fracture initiation by debonding from at the fiber -matrix interface and craze induced fracture from void, respectively.

For the higher a/b ratios of 2.0 and 4.0, the increase in crack initiation strain with the temperature also follows a linear pattern, but their magnitude is much lower than for $a/b = 0.5$ and 1.

Figure 77a exhibits the maximum macroscopic stress ($\Sigma_{\max}$) versus the a/b ratio for different temperatures. The plot illustrates that $\Sigma_{\max}$ carried by the microstructure decreases with increase of the a/b ratio. Change of stress carrying capacity with respect to a/b ratio decreases for crack initiation dominated by craze induced fracture from the void edge. Stress carrying capacity drops drastically as a/b ratio increases. Figure 77b shows $\Sigma_{\max}$ versus the temperature for different a/b ratios, which illustrates that $a/b = 0.5$ and 1.0 show more temperature sensitivity on $\Sigma_{\max}$ than $a/b =$ 2.0 and 4.0. For the high a/b ratios, temperature becomes less effective, since for $a/b = 4.0$, the stress that drops with the increase in temperature is almost negligible compared to the other a/b ratios.

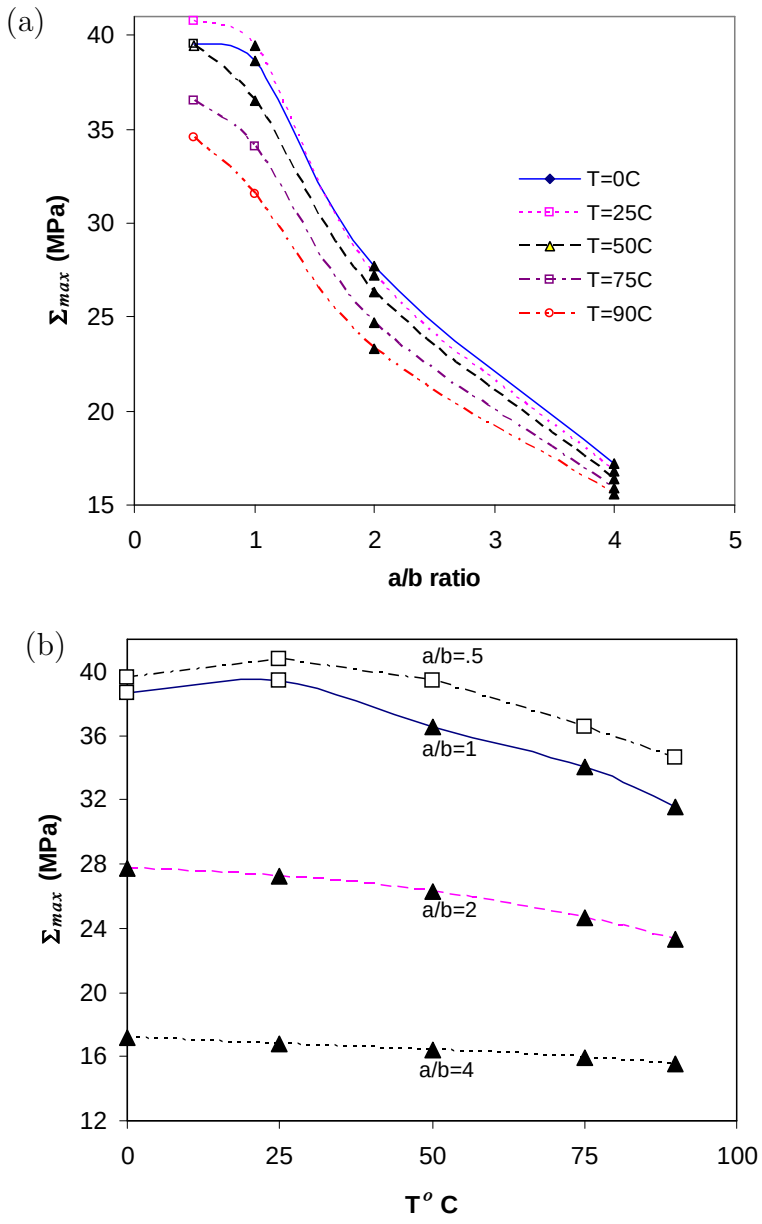

Fig. 77. (a) $\Sigma_{\max}$ vs. a/b ratio for different temperatures (b) $\Sigma_{\max}$ vs. temperature for different a/b ratios.

3. Prediction at Varying Strain Rate

To investigate the change in the damage mechanism under the strain rate variation, we have considered a moderate temperature (T= 90^oC) case. The composite microstructure in our example contains a void and a fiber of $a/b = 1$, $r_v/r_f = 1$ and $l_f/r_v = 6$.. Figure 78 shows the stress–strain responses for four different strain rates of $\dot{\mathrm{E}} = 1/s, 0.1/s, 0.01/s$ and $0.001/s$ at T= 90^oC, which illustrates that decreasing the strain rate causes a more ductile response. A decrease in the strain rate results in

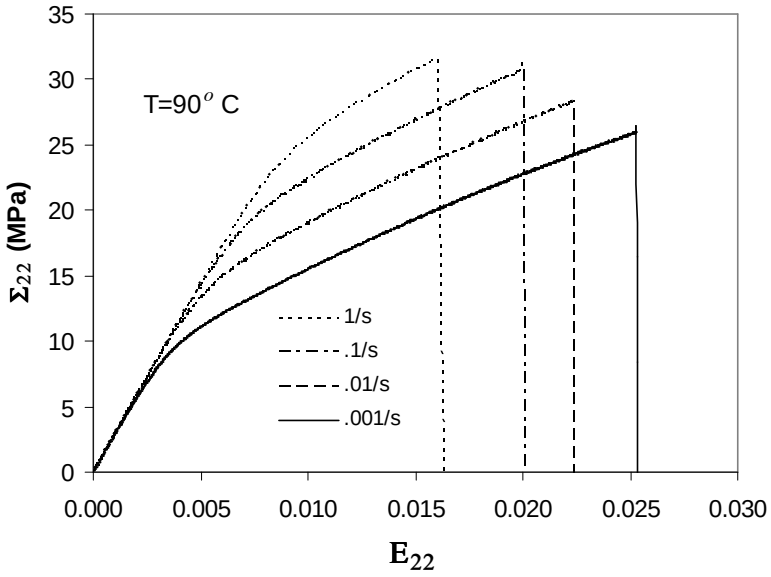

Fig. 78. Macroscopic stress strain responses at T= 90^oC for different strain rates.

a larger strain and a lower stress failure. There is an interesting transition in the damage mechanism observed under variations of the strain rate at higher temperatures. Previously we observed that at low temperatures damage initiation is governed by cavitation-induced debonding. With the increase in temperature, a transition in the damage initiation mechanism from debonding (from the fiber) to the craze-induced crack (from the void) occurs at the strain rate of $1.0/s$. Another transition, from craze-induced to debonding-induced fracture initiation, occurs with the decrease of

the strain rate at moderate temperatures.

Figure 79 shows the σ_{I} contours and fracture pattern for different strain rates. The crack initiates due to the crazing from the void edge for the macroscopic strain rate, $\dot{\mathrm{E}}$, 1.0/s, decrease in the strain rate to $0.1/s$, $0.01/s$ and $0.001/s$ show crack initiations from debonding through cavitation induced matrix cracking. At moderate temperatures the polymer behavior is very ductile. In addition to this, a decrease

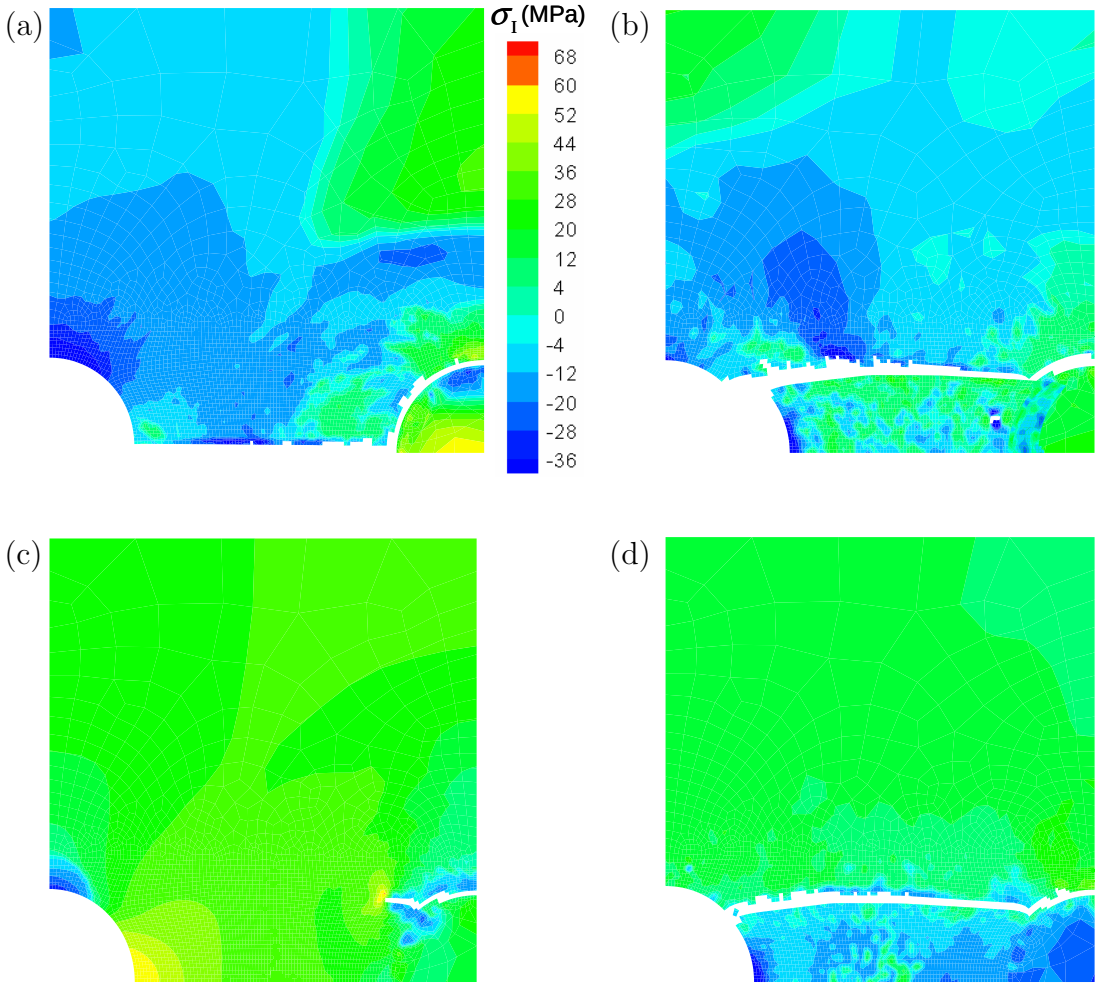

Fig. 79. Damage propagation patterns at T= 90^{o}C and $\dot{\mathrm{E}}$ of (a) 1.0/s (b) 0.1/s (c) 0.01/s and (d) 0.001/s.

in the strain rate causes the polymer behavior to be more ductile and the crazing is suppressed. The homogenous stress-strain responses at different temperatures at a strain rate of 0.001/s, as shown in Chapter III (see Figure 32), illustrates that at moderate temperatures and a low strain rate, a large strain polymer deformation involving a peak yield, strain softening and orientational hardening occurs. Here, for the composite problem, at T= 90^oC and at a strain rate lower than 1/s the local behavior around the void does not reach the state of initiating craze, while the local material approaching the peak yield point, the interface region reaches the critical value of dilatational energy density to initiate fracture by the cavitation-induced cracking.

Figure 80a shows macroscopic crack initiation strain, E_i, versus $\dot{E}$ plot, which illustrates that the crack initiation strain decreases with an increase in strain rate. Figure 66b exhibits Σ_{max} versus the strain rate plot, where Σ_{max} is the maximum macroscopic stress carried by the microstructure. The plot illustrates that the maximum macroscopic stress carried by the microstructure increases with the increase in the strain rate. The rate of increase of Σ_{max} with respect to the strain rate decreases when damage initiation mechanism changes from debonding to crazing. The investigation of the effect of the strain rate for the same loading condition is also done for an oblate shaped void of $a/b = 4.0$ at T= 90^oC. The numerical simulation conducted by considering $\dot{E} = 0.001$/s and 1.0/s are compared for the analysis. Figure 81a shows the stress strain responses corresponding to the strain rate of 1.0/s and 0.001/s, which exhibits the fact that for the lower strain rate the unit cell behaviors are more ductile and the drop in stress due to crack formation occurs at a much larger strain.

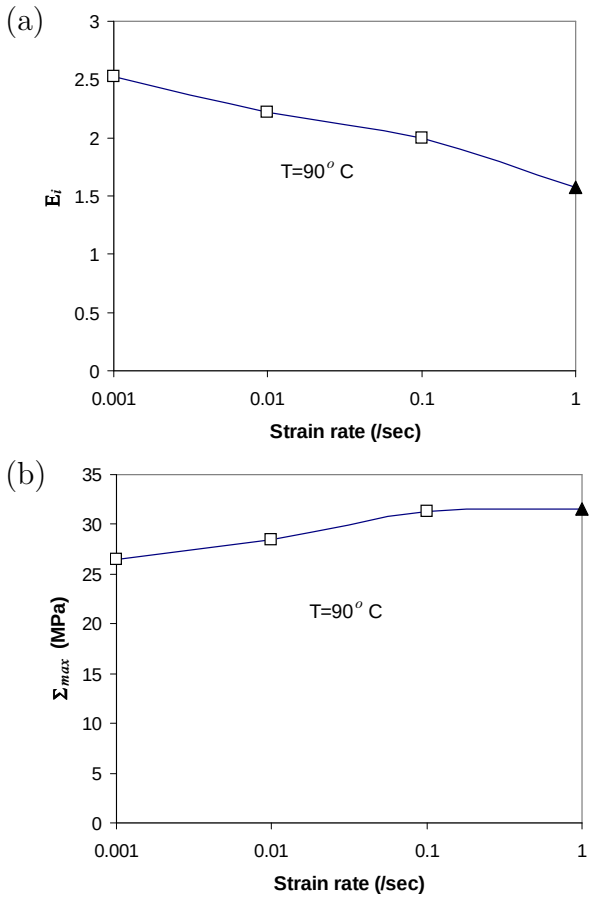

Fig. 80. (a) E_i vs. macroscopic strain rate plot (b) plot of Σ_{max} vs. strain rate at T= 90^{o}C. Here E_i and Σ_{max} is crack initiation strain and maximum macroscopic stress carried by unit cell, respectively.

Figure 81b, c and d show the maximum principal stress, σ_{I}, contours and crack progressions at different stages of straining for the $\dot{\text{E}} = 0.001/\text{s}$ case. Figure 81b shows the distribution of σ_{I} just before the crack initiation, which shows that at the lateral edge of the void there exists a small high stress zone due to orientational hardening, then a strain-softened zone due to crazing, followed by a high stress concentrated zone. At this strain rate the immediate location around the void's lateral edge undergoes shear yielding. Because of this, the craze-induced crack initiates at a small distance away from the void's lateral edge (Fig. 81c). The craze-induced crack then progresses towards the fiber, perpendicular to the loading direction, and separates the fiber from the matrix after merging into the fiber's lateral edge. For better understanding of the shear yielding occurrence, the effective plastic strain, $\bar{\epsilon}$, contours are plotted in the figure. 82 at different stages of straining. At $\text{E}_{22} = 0.012$ (Fig. 82a) the plastic strain immediately around the void edge is about 0.12, upon continuing deformation at a E_{22} of 0.014 the plastic strain at that zone increases to 0.2, which is a clear indication of shear yielding in that zone. This is because the uniaxial tension at 90^oC at $\dot{\text{E}} = 0.001/\text{s}$ PMMA reaches the peak yield position approximately at a $\bar{\epsilon}$ of $0.13 - .14$. Since the immediate edge of the void suffers $\bar{\epsilon} = 0.20$, this zone undergoes intrinsic softening followed by orientational hardening. Upon continuing deformation due to the orientational hardening, subsequent plastic deformation corresponding to shear yielding expanded into the material (Figs. 82c and 82d) but was soon arrested due to the formation of a craze-induced fracture initiation and progression into the neighboring zone.

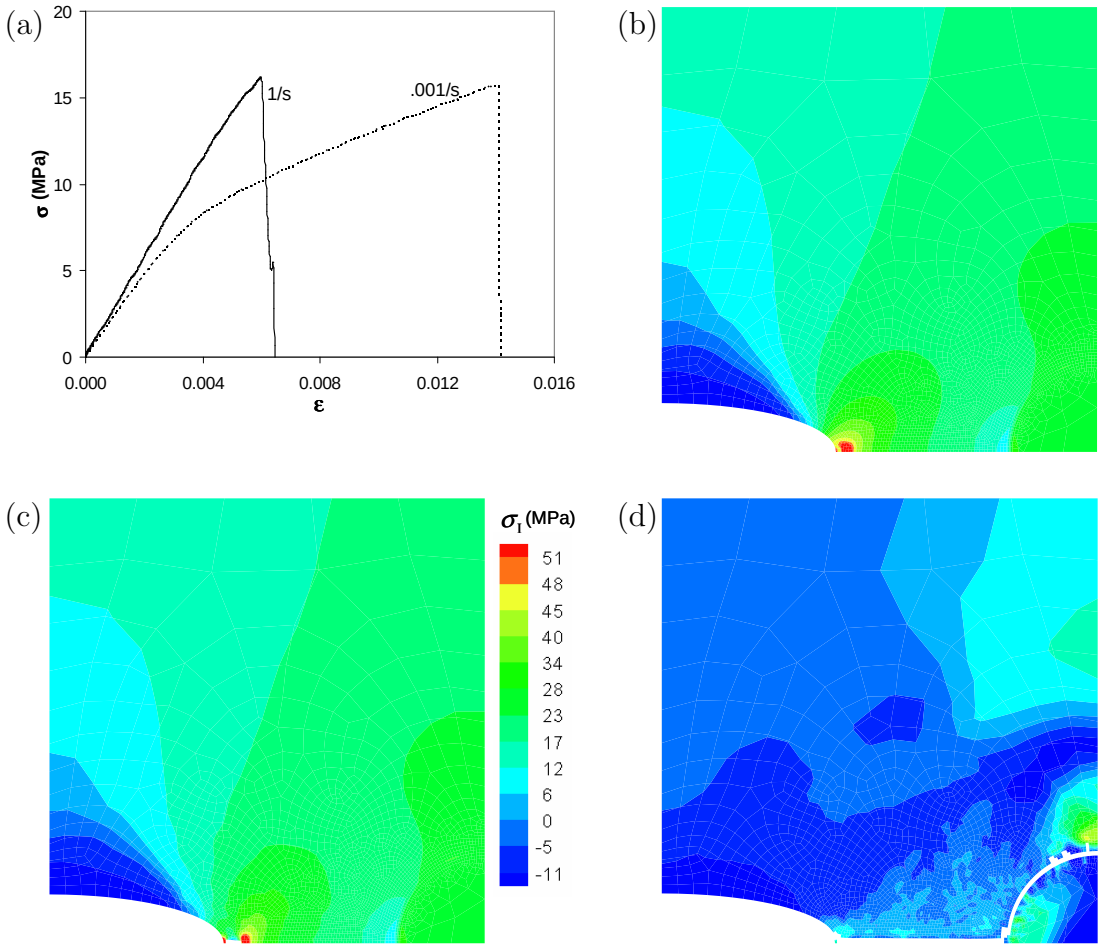

Fig. 81. (a) Macroscopic stress strain responses for moderate and low strain rate loading at T= 90^{o}C. (b), (c) and (d) Development of fracture and σ_{I} contours for $a/b = 4.0$ at $\dot{\mathrm{E}} = 0.001/\mathrm{s}$ and T= 90^{o}C.

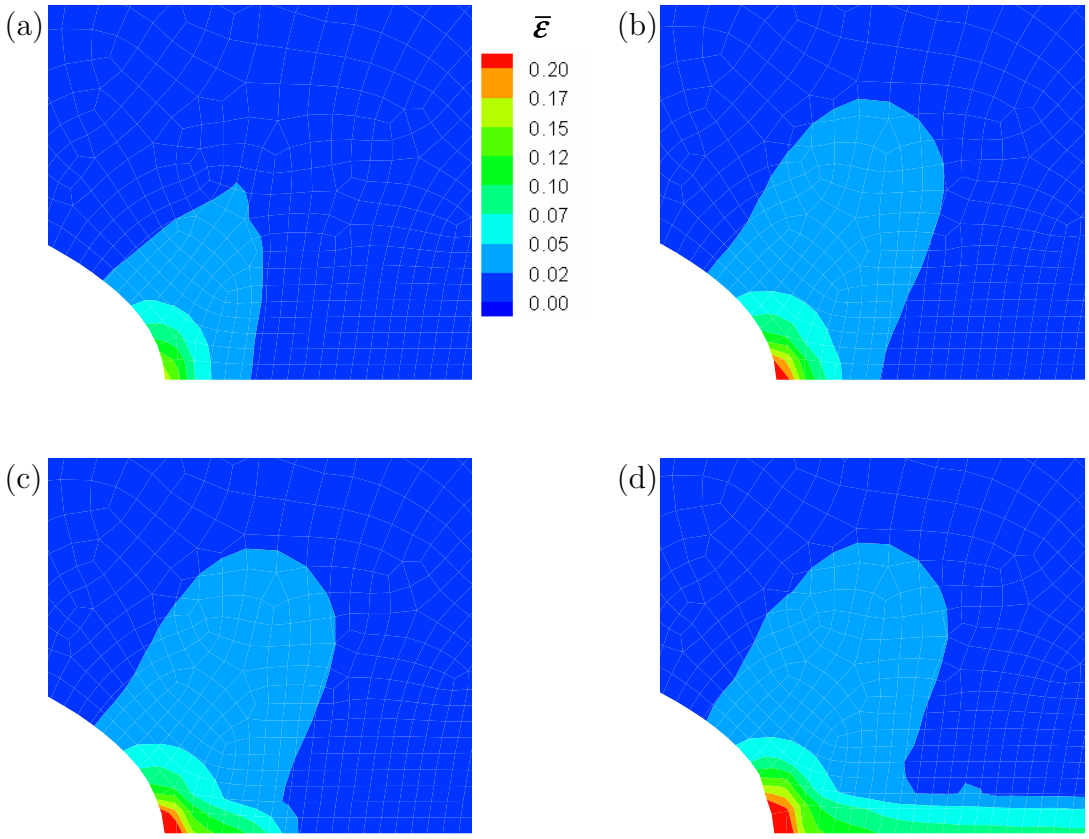

Fig. 82. Effective plastic strain contours and the development of plastic strain at different stages of straining for an oblate shaped void ($a/b = 4.0$) at T= 90^{o}C and $\dot{\text{E}} = 0.001$/s (a) $\text{E}_{22} = 0.0120$ (b) $\text{E}_{22} = 0.0140$ (c) $\text{E}_{22} = 0.01408$ and (d) $\text{E}_{22} = 0.01413$.

E. Discussion

In this chapter the effects of the presence of void, its distribution, geometry, size and location on damage initiation and progression in a thermoplastic polymer matrix composite system subjected to different temperatures and loading rates under plane strain uniaxial tension were investigated. Voids and fibers embedded in a PMMA polymer matrix were explicitly represented in the microstructure. For transverse loading of unidirectional composites, matrix plays a major role in initiating micro-scale damage; hence, the physically based constitutive equations (the modified macromolecular model) for polymer deformation and fracture (the new crazing model and the cavitation-induced debonding criterion) were implemented in a finite element computational framework at a finite strain . In the polymer matrix composite system, the distribution, shape and size of the micro-constituents (voids and fibers) in the microstructure under different temperatures and strain rates played a significant role in the initiation and progression of damage. The competition between debonding and craze-induced failures was observed in this analysis. At low homologous temperatures the propensity of fiber-matrix debonding occurring due to the cavitation-induced matrix crack is higher and at moderate temperatures the propensity to craze formation is higher. If cracks initiate due to debonding, they initiate at the fiber's top edge and after traveling a short distance on the fiber surface, they arrest and a craze-induced crack initiates. The craze-induced crack then propagates while arrested debonding zones unlock themselves and continue to proceed on the fiber-matrix interface. Another crack may form at the lateral edge of the void and travel in a parallel plane towards the craze-induced crack traveling in the opposite direction from the fiber. When the tips of the two approaching cracks come closer, they perturb each other's stress fields and the crack that originated from the void turns toward the other crack.

First the effects of the presence of voids in a composite microstructure at room temperature at a fixed strain rate were investigated considering a change in the void size, shape and distribution relative to fiber geometry. The presence of a void of the same size and shape, and located at the side of the fiber, shows a larger crack initiation strain and a smaller stress than in the 'without void' case. Bringing the fiber very near the void causes an increase in the effect by reducing the crack initiation strain to be even smaller than in the 'without void' case. However, the crack initiation mechanism is the same as in the 'without void' case.

Increasing the size of the void relative to the fiber size decreases the crack initiation strain and the maximum macroscopic stress-carrying capacity of the microstructure, as well as the change of the crack initiation mechanism from debonding at the fiber's top edge to the craze-induced fracture at the void's lateral edge. Void size relative to the fiber size plays an important role in the mechanism of damage initiation and development. Multiple cracking modes (debonding, craze induced cracks and their branching) were observed during the process of damage development depending on the size of the void to fiber ratio. Crack initiation strain increases and stress-carrying capacity decreases with the increase of the void radius relative to the fiber radius.

Debonding is the dominant crack-initiation mechanism for a void radius less then 1.5 times the fiber radius. A larger void, more than $r_v/r_f = 1.5$, causes crazing in the dominant crack initiation mechanism.

The presence of different shapes of void causes major changes in the damage initiation and progression patterns as compared to the 'without void' case. The crack initiation strain and stress-carrying capacity are both larger. As the void becomes more oblate, a transition of the crack initiation mechanism from the cavitation-induced debonding at the fiber's surface to the craze-induced crack initiation at the void

occurs significantly reducing the crack initiation strain and stress-carrying capacity.

Effects of the fiber location on damage initiation and propagation were also investigated by placing the fiber on top of the void, keeping the same distance between the void and the fiber. In that case, the void acts as a shield to the fiber from the initiation of the debonding and facilitates the craze formation around the void's edge and subsequent craze-induced crack propagation. Changes in fiber location from the side to the top do not show significant effects on crack initiation strain and maximum stress-carrying capacity.

The investigation of the effects of the void was extended to analyze the effects of temperature and strain rate. To understand the temperature effect, the composite microstructure containing a void and a fiber of the same size and shape, and located side by side subjected to different temperatures, were all considered. The responses of the microstructure showed an increased amount of ductility with the rise in temperature (Fig. 61) due to polymers with a temperature sensitive yield and deformation behavior. At the low temperature of T= 0^oC and 25^oC debonding and at the moderate temperature of T= 50^oC, 75^oC, 90^oC and 110^oC crazing was the failure initiation mechanism (Fig. 63). Macroscopic crack initiation strain increases with an increase in temperature, and the macroscopic stress-carrying capacity increases as long as damage is initiated by debonding, and decreases if crazing at the void is the cause of damage initiation.

The effects of fiber closeness with the void on damage initiation and progression were also investigated at different temperatures. Debonding is the cause of crack initiation for l_f/r_v less than 3.6 for all temperature cases considered here. For l_f/r_v = 3.6, a craze induced crack is dominant only for the moderate temperature (T=50^oC, 75^oC and 90^oC) cases. At low temperatures with a decrease in the fiber-void distance, the crack initiation strain and the maximum stress-carrying capacity decrease and

debonding induced damage initiation is observed.

To investigate the temperature effects, the composite microstructure containing a void and a fiber of the same volume fraction, located side by side for different void shapes from prolate to oblate (a/b ratio varies from 0.5 to 4.0) and subjected to different temperatures were considered. For all temperatures considered here, the prolate shaped void caused debonding induced damage first. On the other hand, for oblate shaped voids, crazing induced a crack from the void first. Crack initiation strain and maximum macroscopic stress decreased drastically with a change in the void shape from prolate to oblate, except in low temperature cases of T= 0^oC and 25^oC, because of debonding initiating fractures for $a/b = 0.5$ and 1.0 (Fig. 76). For the presence of an oblate shaped void of $a/b = 4.0$, the crack initiation strain and stress carrying capacity dropped by 50% and 60%, respectively. For the presence of a prolate shaped void of $a/b = 0.5$, the stress carrying capacity increased about 12%. As the void became more oblate, the temperature effects became less dominant as compared to the shape effect.

The effects of the loading rate were investigated by choosing a spheroid (a/b = 1 and oblate shaped void ($a/b = 4.0$) at T = 90oC under different strain rates. For both the moderate temperature cases, crazing was the dominant crack initiation mechanism at a moderate strain rate of 1/s, but for the low strain rate case the local behavior corresponding to two shapes of void showed a substantially different behavior. For the spheroidally shape void, four strain rates of 1/s, 0.1/s, 0.01/s and 0.001/s were considered for this analysis. Crack initiation through the cavitation-induced debonding phenomenon, which occurs at low temperatures, returns as the applied strain rate decreases. For the oblate shaped void, at moderate temperatures and low strain rates, shear yielding occurs at the void tip before the craze-induced crack initiates slightly away from the void tip. A low strain rate response at moderate

temperatures also shows large amounts of ductility in the stress-strain response and large differences in macroscopic crack initiation strains.

F. Conclusion

Constitutive models that account for large strain polymer deformation and damage due to shear yielding, crazing and debonding were employed to investigate the effects of voids on damage initiation in a polymer matrix composite microstructure. The modified macromolecular model for polymer deformation, the new crazing model for craze-induced fractures and linear elastic critical dilatational energy density criterion for debonding were all employed for the studies corresponding to this Section. Full transient analyses were carried out at finite strains in a finite element code within a unifying framework.

Based on the analyses, the following conclusions are drawn.

- In a PMMA composite microstructure the presence of voids allows larger crack initiation strains and smaller stress carrying capacity for the fiber-void distance ratio of l_f/r_v greater than 2.0 and void aspect ratio of a/b less than 2.0.

- Void shape has a significant effect on damage. The presence of a prolate shaped void causes a debonding-induced damage initiation and an oblate shaped void causes a craze-induced damage initiation.

- At room temperature, if the fiber is situated at the side of the void, debonding is the crack initiation mechanism, and if the fiber location is above the void, the crazing from the void is the crack initiation mechanism.

- Crack initiation strain and the stress carrying capacity decreases when the fiber moves closer to the void.

- The presence of circular shaped voids may cause multiple damage modes in a composite microstructure depending upon temperature.

- Temperature has major effects in determining the damage initiation mechanism. At low temperatures, damage initiation is caused by fiber-matrix debonding, while at moderate temperatures, damage initiation is caused by crazing. However, at moderate temperatures and low strain rates (i.e., lesser than 0.1/s), debonding-induced fracture returns. Also, the occurrence of shear yielding through large strain deformation of polymers at the edge of the void may be observed depending upon the void shape.

CHAPTER V

CONCLUSION

In this research the effects of voids, their location, shape and size with respect to fiber geometry on damage in a polymer matrix composite microstructure subjected to transverse loading under different temperatures and loading rates were investigated in a computational framework that incorporates the matrix deformation and fracture behavior at governing scales of physical mechanisms.

The large strain deformation behavior of polymers is implemented in an explicit finite element code within a unifying framework using two distinct constitutive models: (i) a reference model, which is a Drucker-Prager [106] type phenomenological Bodner model [80, 82] (DPB model) that accounts for the rate and pressure-sensitive yielding, followed by isotropic hardening; and (ii) a macromolecular model that accounts for intrinsic softening, followed by kinematic orientational hardening, where yielding is rate, temperature and pressure sensitive [55, 59, 78, 79, 121]. They were compared through analyses of the impact and plane strain compression responses of a planar block of material and local behavior of a composite unit cell with a void under plane strain tension. For the impact problem, the models show substantial differences in predicting local behaviors though both model exhibits similar in macroscopic behavior under low and moderately high velocity impact loadings. The intrinsic softening behavior characteristics of the macromolecular model at small strains favors (i) the formation and propagation of bands of intense deformation in plane strain compression of a block and (ii) irregular shape changes, i.e., the "bulging out" of voids under tension in a composite like microstructure. These local behaviors are not captured by the DPB model. However, the original macromolecular model exhibits linear elastic behavior before peak yield and predicts yield as a sudden event rather

than as a distributed event in the experimental observation. Modification of the original macromolecular model is obtained through introducing hyperbolic functions in the evolution equation of the athermal shear strength. As a result, the modified macromolecular model successfully captures the initial viscoplastic behavior prior to peak yield as well as to the smooth yielding event.

The computational framework is extended to include craze-induced polymer fractures by implementing two continuum constitutive models (i) a reference craze model, developed by Gearing-Anand [60] and (ii) a physically based, new craze model. Both crazing models account for craze initiation, craze widening and craze breakdown. The reference model's craze breakdown criterion is an ad hoc criterion. However, the new craze model associates the craze breakdown with the craze growth process, where fracture occurs as a natural outcome of the solution. In order to demonstrate the capability of fracture models, three combinations of macromolecular models and crazing models were tested numerically in a plate with a hole problem, i.e., (i) the original macromolecular model with the new craze, (ii) the modified macromolecular model with the reference craze, and (iii) the modified macromolecular model with the new craze model. In a thermoplastic (PMMA) plate with a hole subjected to tension, a crack initiates at the lateral edge of the void and progresses laterally, soon after the crack branches out from the main crack path. Both craze models with the modified macromolecular model capture this crack progression pattern. However, the macroscopic behavior is significantly different. The new craze model also is able to capture the macroscopic nonlinear behavior of the plate with a hole structure. The development of the new craze model simplifies the numerical implementation of the crazing model in a finite element program beyond being more physical than currently used empirical failure criteria. Debonding through fracture in fiber-matrix interfaces due to cavitation is demonstrated by implementing the dilatational energy density

criterion.

The study of the effects of the void is conducted using the modified macromolecular model, the new crazing model and the dilatational energy density criterion for matrix deformation, craze-induced fractures and cavitation-induced debonding, respectively. Competition between craze-induced fractures from voids and cavitation-induced debonding through matrix cracks at the fiber–matrix interface are all observed depending upon void size, shape and distribution under variations in the temperature and loading rates. For the 'without void' case, debonding is the only crack initiation mechanism. However, the presence of a void causes a variation in the crack initiation mechanism. Voids situated far and very close to the fibers cause 14% increase and 9% reduction in macroscopic crack initiation strains relative to the 'without void' case. Increases in void size relative to fiber exhibits increase in ductility in macroscopic responses as well as increase in crack initiation strains. After a certain void size is larger than the fiber size the result is a transition of damage initiation mechanisms from fiber-matrix debonding to crazing from the void edge. The presence of an oblate shaped void has the most significant effect. At room temperature an oblate shaped void of a major axis to a minor axis, a/b, ratio of about 4.0 shows approximately 40% and 60% reduction in crack initiation strain and maximum stress-carrying capacity, respectively, with respect to the 'without void' case. However, a prolate shaped void of the $a/b = 0.5$ exhibits a 12% increase in crack initiation strain and no change in the maximum stress-carrying capacity with respect to the 'without void' case. Changes in the crack initiation mechanism from debonding to crazing the void were also observed when the void shape changed from prolate to oblate.

Temperatures and strain rates play a major role in determining damage initiation mechanisms in the strain and strength of composite microstructures with or without the presence of a void. At a moderately low strain rate (1/s) with an increase of

temperature, the composite microstructure illustrates a more ductile response and a larger crack initiation strain. The effects of temperature become more significant as fiber-void distances increase because of alterations to the damage initiation mechanism. Interestingly, for the oblate shaped voids, the temperature effect is negligible as the crack initiation strains and mechanisms are almost the same for all temperature cases. Void shape has shown to have a significant effect at moderate temperatures with a variation in the strain rate from moderately low to very low. For a circular shaped void at a 1/s strain rate at a low temperature debonding and at moderate temperature crazing from the void is the crack initiation mechanism. Interestingly, lowering the strain rate at a moderate temperature brings back the debonding at the fiber-matrix interface as a crack initiation mechanism. On the other hand, for an oblate shaped void, the simultaneous presence of a shear-yielded zone that goes under significant deformation around the immediate lateral edge of the void and the craze-induced fracture initiation a little ways away from the void are observed at moderate temperatures and low strain rates.

Interesting changes in the crack initiation strain with crack initiation mechanisms are noticed as well. When crack initiation mechanism is fiber–matrix debonding, crack initiation strains increase with an increase in the void-fiber distance, but decrease if the initiation mechanism governs by crazing at the void's edge. This phenomenon was observed during the study of the effect of void shape and the void-fiber distance under different temperatures. Maximum stress-carrying capacity always decreases with an increase in the void shape ratio, void-fiber distance, void size, temperature and decrease in the strain rate when damage initiation mechanisms are craze induced failures at the lateral edge of the void.

Therefore, the presence of manufacturing-induced voids in a thermoplastic polymer based composite, have a significant effect on damage initiation, strain and the

stress-carrying capacity, depending upon a void's structural parameters, i.e., void size, shape and distribution relative to fiber and loading parameters such as temperature and strain rate. The presence of void is beneficial when void situated away from the fiber, void size is smaller relative to fiber and void aspect ratio is lower than the fiber aspect ratio. On the contrary, the presence of void is deleterious when voids are closely placed with fibers, void size is bigger and void aspect ratio is larger than fiber aspect ratio.

The finite element computational framework developed here is a versatile, easy to use tool for investigating many interesting boundary value problems regarding polymer composite microstructures. This framework has been formulated by incorporating the fine scale polymer deformation and fracture mechanisms that are implemented into a large strain explicit finite element program also capable of handling both quasi-static and dynamic problems. There are few limitations to its capabilities with respect to modeling and finite element details, i.e., fiber fracture and fiber-matrix debonding through sliding are not incorporated. Only plane strain problems can be analyzed. Furthermore, within a well-defined unit cell structure or representative volume, most mechanisms of matrix damage attributed to the initiation and growth of cracks can be captured. Because of this, the computational framework can potentially curtail the necessity for extensive laboratory experimentation regarding matrix cracking, since it successfully captures the fundamental deformation and fracture behavior of the composite matrix. This feature provides a considerable advantage over those analyses which are based on linear elastic matrix deformation and fracture behavior.

In the future in terms of finite elements, the code should be expanded for handling axisymmetric elements, plane stress elements and three dimensional problems, which will be a challenging but necessary task, especially for the micro-mechanical analysis of composite laminates. Cohesive elements also may be incorporated in order to

capture fiber matrix debonding through decohesion. In terms of the prediction of damage in composites, the microscopic computational results should be utilized to develop improved continuum damage mechanics models that will account for damage initiation mechanisms and their propagation patterns.

REFERENCES

[1] R. K. Goldberg, G. D. Roberts, and A. Gilat, "Incorporation of mean stress effects into the micromechanical analysis of the high strain rate response of polymer matrix composites," *Composites Part B: Engineering*, vol. 34, pp. 151–165, 2003.

[2] P. W. J. Heuvel, T. Peijs, and R. J. Young, "Failure phenomena in two-dimensional multi-fibre model composites: 5. a finite element study," *Composites Part A*, vol. 29A, pp. 1121–1135, 1998.

[3] P. Hope, I. Ward, and A. Gibson, "The hydrostatic extrusion of polymethylmethacrylate," *J. Mat. Sci.*, vol. 15, p. 2207, 1980.

[4] W. A. Spitzig and O. Richmond, "Effect of hydrostatic pressure on the deformation behavior of polyethylene and polycarbonate in tension and compression," *Polymer Engineering and Science*, vol. 19, pp. 1129–1139, 1979.

[5] C. G'Sell, "Strength of metals and alloys," in *Proceedings of ICSMA 7* (H. J. McQueen, J. P. Bailon, J. I. Dickson, and J. J. Jonas, eds.), vol. 3, pp. 1943–1982, Pergamon Press, Oxford, 1985.

[6] E. M. Arruda, M. C. Boyce, and H. Quintus-Bosz, "Effects of initial anisotropy on the finite straindeformation behavior of glassy polymers," *International Journal of Plasticity*, vol. 9, pp. 783–811, 1993.

[7] S. S. Sternstein and F. A. Meyers, "Yielding of glassy polymers in the second quadrant of principal stress space," *Journal of Macromolecular Science*, vol. B8, pp. 539–571, 1973.

[8] J. Varna, R. Joffe, L. Berglund, and T. S. Lundstrom, "Effect of voids on failure mechanisms in RTM laminates," *Composites Science and Technology*, vol. 53, no. 2, pp. 241–249, 1995.

[9] G. Nilsson, S. P. Fernberg, and L. A. Berglund, "Strain field inhomogeneities and stiffness changes in GMT containing voids," *Composites Part A: Applied Science and Manufacturing*, vol. 33, pp. 75–85, January 2002.

[10] F. C. Campbell, A. R. Mallow, and C. E. Browning, "Porosity in carbon fiber composites: An overview of cause," *Journal of Advanced Materials*, vol. 18, p. 33, 1995.

[11] N. C. W. Judd and W. W. W., "Voids and their effects on the mechanical properties of composites - an appraisal," *SAMPE Journal*, vol. 10, p. 4, 1978.

[12] C. A. Howe, R. J. Patton, and A. A. Goodwin, "A comparison between voids in RTM and prepeg carbon/epoxy laminates," (Gold Coast, Queensland, Australia), 1997. In ICCM-11 Conference Proceedings.

[13] B. D. Harper, G. H. Staab, and R. S. Chen, "A note on the effects of voids upon the hygral and mechanical properties of AS4/3502 graphite/epoxy," *Journal of Composite Material*, vol. 21, pp. 280–289, March 1987.

[14] K. J. Bowles and S. Frimpong, "Void effects on the interlaminar shear strength of unidirectional graphite-fiber-reinforced composites," *Journal of Composite Materials*, vol. 26, pp. 1487–1509, 1992.

[15] J. C. Suarez, F. Molleda, and A. Guemes, "Void content in carbon fiber/epoxy resin composites and its effects on compressive properties," in *Proceedings of Ninth International Conference on Composite Materials* (A. Miravete, ed.),

vol. 6, (Madrid, Spain), pp. 589–596, ICCM-9, Woodhead Publishing Limited, July 1993.

[16] J. G. Berryman, "Role of porosity in estimates of composite elastic constants," vol. 53, pp. 223–235, American Society for Mechanical Engineers, 1993. In Composite Material Technology Conference Proceedings.

[17] T. Mura, H. M. Shodja, and Y. Hirose, "Inclusion problems," *Applied Mechanics Reviews*, vol. 49, pp. 118–127, 1996.

[18] S. Nemat-Nasser and M. Hori, *Micromechanics: Overall Properties of Heterogeneous Materials*. Amsterdam: Elsevier Science, 1999.

[19] A. Farouk, N. A. Langrana, and G. J. Weng, "Modulus prediction of a cross-ply fiber reinforced fabric composites with voids," in *Plastics and Plastic Composites: Material Properties, Part Performance and Process Simulation*, vol. 29, pp. 207–308, ASME, 1991.

[20] Y. A. Gowayed, "The effect of voids on the elastic properties of textile reinforced composites," *Journal of Composites Technology and Research*, vol. 19, pp. 168–173, 1997.

[21] H. Huang and R. Talreja, "Effects of void geometry on elastic properties of unidirectional fiber reinforced composites," *Composites Science and Technology*, vol. 65, pp. 1964–1981, 2005.

[22] M. Wisnom, T. Reynolds, and Gwillam, "Reduction in interlaminar shear strength by discrete and distributed voids," *Composites Science Technology*, vol. 56, pp. 93–101, 1996.

[23] A. R. Chambers, J. S. Earl, C. A. Squires, and S. M. A., "The effect of voids on the flexural fatigue performance of unidirectional carbon fibre composites developed for wind turbine applications," *International Journal of Fatigue*, vol. 28, pp. 1389–1398, October 2006.

[24] C. T. Sun and J. Chen, "A simple flow rule for charaterizing nonlinear behavior of fiber composites," *Journal of Composite Material*, vol. 23, no. 10, pp. 1009–1020, 1989.

[25] T. S. Gates and C. T. Sun, "Elastic/viscoplastic constitutive model for fiber reinforced thermoplastic composite," *AIAA Journal*, vol. 29, pp. 457–463, 1991.

[26] V. Srikanth, Thiruppukuzhi, and C. T. Sun, "Models for the strain-rate-dependent behavior of polymer composites," *Composites Science and Technology*, vol. 61, pp. 1–12, January 2001.

[27] G. Dvorak and Y. A. Bahei-El-Din, "Plasticity analysis of fibrous composites," *J. Appl. Mech.*, vol. 49, pp. 327–335, 1982.

[28] G. Odegard, K. Searles, and M. Kumosa, "A continuum elastic-plastic model for woven-fabric/polymer-matrix -composite materials under biaxial stresses," *Composite Science and Technology*, vol. 61, pp. 2501–2510, 2001.

[29] M. Megnis and J. Varna, "Micromechanics based modeling of nonlinear viscoplastic response of unidirectional composite," *Composites Science and Technology*, vol. 63, pp. 19–31, January 2003.

[30] J. Aboudi, "Micromechanical analysis of the finite elastic-viscoplastic response of multiphase composites," *Int. J. Solids Structures*, vol. 40, pp. 2793–2817, June 2003.

[31] M. S. Al-Haik, H. Garmestani, and A. Savran, "Explicit and implicit viscoplastic models for polymeric composite," *International Journal of Plasticity*, vol. 20, pp. 1875–1907, 2004.

[32] G. Spathis and E. Kontou, "Nonlinear viscoelastic and viscoplastic response of glassy polymers," *Polym. Eng. Sci.*, vol. 41, no. 8, p. 1337, 2001.

[33] G. Spathis and E. Kontou, "Non-linear viscoplastic behavior of fiber reinforced polymer composites," *Composites Science and Technology*, vol. 64, no. 15, pp. 2333–2340, 2004.

[34] E. Kontou and G. Spathis, "Application of finite strain viscoplasticity to polymeric fiber composites," *International Journal of Plasticity*, vol. 22, pp. 1287–1303, July 2006.

[35] L. Kachanov, "Time of rupture process under creep conditions," *Izy Akad Nank S.S.R. Otd Tech Nauk*, vol. 8, pp. 26–31, 1958.

[36] Y. N. Rabotnov, "Creep rupture," in *Proceedings of the XII International Congress Applied Mechanics.*, pp. 342–349, 1968.

[37] J. L. Chaboche and P. M. Lesne, "A non-linear continuous fatigue damage model," *Fatigue Fract. Engng. Mater. Struct.*, vol. 11, pp. 1–17, 1988.

[38] R. Talreja, "A continuum mechanics characterization of damage in composite materials.," *Proc. R. Soc. Lond.*, vol. A339, pp. 195–216, 1985a.

[39] R. Talreja, "Transverse cracking and stiffness reduction in composite laminates," *J. Composite Mater*, vol. 19, pp. 355–375, 1985b.

[40] R. Talreja, S. Yalvac, L. D. Yats, and D. G. Wetters, "Transverse cracking and stiffness reduction in cross ply laminates of different matrix toughness," *J. Composite Mater.*, vol. 26, p. 1644, 1992.

[41] J. Fish, Q. Yu, and K. Shek, "Computational damage mechanics for composite materials based on mathematical homogenization," *Int. J. Numer. Meth. Engng.*, vol. 45, pp. 1657–1679, 1999.

[42] S. Li, S. R. Reid, and P. D. Soden, "A continuum damage model for transverse matrix cracking in laminated fibre-reinforced composites," *Phil. Trans. R. Soc. Lond. A*, vol. 356, pp. 2379–2412, 1998.

[43] A. Boutaous, B. Peseux, L. Gornet, and A. Blaidi, "A new modeling of plasticity coupled with the damage and identification for carbon fibre composite laminates," *Composite Structures*, vol. 74, pp. 1–9, July 2006.

[44] L. Lannucci and J. Ankersen, "An energy based damage model for thin laminated composites," *Composites Science and Technology*, vol. 66, pp. 934–951, June 2006.

[45] Z. Hashin and A. Rotem, "A fatigue failure criterion for fiber reinforced materials," *J. Compos. Mater.*, vol. 7, pp. 448–464, Oct. 1973.

[46] Z. Hashin, "Failure criteria for unidirectional fiber composites," *J. Appl. Mech.*, vol. 47, pp. 329–334, June 1980.

[47] S. E. Yamada and C. T. Sun, "Analysis of laminate strength and its distribution," *J. Compos. Mater.*, vol. 12, pp. 275–284, July 1978.

[48] Shahid, Iqbal, Chang, and Fu-Kuo, "Failure and strength of laminated composite plates under multiple in-plane loads.," in *38th Int. SAMPE Symp.*, pp. 967–

977, May 1993.

[49] Shahid, Iqbal, Chang, and Fu-Kuo, "An accumulative damage model for tensile and shear failures of laminatedcomposite plates," *J. Compos. Mater.*, vol. 29, no. 7, pp. 926–981, 1995.

[50] R. M. Christensen, "Stress based yield/failure criteria for fiber composites," *J. Solids and Struct.*, vol. 34, no. 5, pp. 529–543, 1997.

[51] H. D. Chandler, I. M. D. Campbell, and M. A. Stone, "An assessment of failure criteria for fibre-reinforced composite laminates.," *Int. J. Fatigue*, vol. 17, no. 7, pp. 513–518, 1995.

[52] A. Gilat, R. K. Goldberg, and G. D. Roberts, "Experimental study of strain-rate-dependent behavior of carbon/epoxy composite," *Composites Science and Technology*, vol. 62, pp. 1469–1476, 2002.

[53] P. W. J. Heuvel, T. Peijs, and R. J. Young, "Failure phenomena in two-dimensional multi-fibre microcomposites.Part 4: A raman spectroscopic study on the influence of the matrix yield stress on stress concentrations," *Composites Part A*, vol. 31, pp. 165–171, 2000.

[54] J. C. S. Roman, "Experiments on epoxy, polyurethane and ADP adhesives," Technical Report CCLab2000. 1b/1, Ecole Polytechnique, France, 2005.

[55] M. C. Boyce, D. M. Parks, and A. S. Argon, "Large inelastic deformation of glassy polymers, Part I: rate dependent constitutive model," *Mech. Mater.*, vol. 7, pp. 15–33, 1988.

[56] J. D. Ferry, *Viscoelastic properties of polymers*. New York: Wiley, 1962.

[57] S. Rabinowitz, I. Ward, and J. Perry, "The effect of hydrostatic pressure on the shear yield behavior of polymers," *J. Mater. Sci.*, vol. 5, p. 29, 1970.

[58] J. Sauer, K. Pae, and S. Bhateja, "Influence of pressure on yield and fracture in polymers," *J. Macromol.*, vol. B8, p. 631, 1973.

[59] A. S. Argon, "A theory for the low temperature plastic deformation of glassy polymers," *Phil. Mag.*, vol. 15, pp. 28–39, 1973.

[60] B. P. Gearing and L. Anand, "On modeling the deformation and fracture response of glassy polymers due to shear yielding and crazing," *Int. J. Solids Structures*, vol. 41, pp. 3125–3150, 2004.

[61] P. B. Bowden, *The yield behavior of glassy polymers, The physics of glassy polymers.* Essex,England: Applied Sci. Publishers, 1973.

[62] J. Lu and K. Ravi-chandar, "Inelastic deformation and localization in polycarbonate under tension," *Int. J. of Solids and structures*, vol. 36, pp. 391–425, 1999.

[63] K. Ravi-Chandar and Z. Ma, "Inelastic deformation in polymers under multiaxial compression," *Mechanics of Time-Dependent Materials*, vol. 4, pp. 333–357, 2000.

[64] E. M. Arruda and M. C. Boyce, "Evolution of plastic anisotropy in amorphous polymers during finite straining," *International Journal of Plasticity*, vol. 9, pp. 697–720, 1993.

[65] E. M. Arruda, M. C. Boyce, and R. Jayachandran, "Effects of strain rate, temperature and thermomechanical coupling on the finite strain deformation of glassy polymers," *Mechanics of Materials*, vol. 19, pp. 193–212, 1995.

[66] L. Anand and M. E. Gurtin, "A theory of amorphous solids undergoing large deformations, with application to polymeric glasses," *Int. J. Solids Structures*, vol. 40, pp. 1465–1487, 2003.

[67] S. Sarva, A. D. Mulliken, and M. C. Boyce, "The mechanics of large-strain inhomogeneous deformation of polymeric materials under dynamic loading conditions," *Journal de Physique IV*, vol. 134, pp. 95–101, 2006.

[68] J. Rottler and M. O. Robbins, "Yield conditions for deformation of amorphous polymer glasses," *Physical Review E*, vol. 64, pp. 1–8, November 2001.

[69] H. Eyring, "Viscosity, plasticity and diffusion as examples of absolute reaction rate," *Journal of Chemical Physics*, vol. 4, pp. 283–291, April 1936.

[70] R. A. Duckett, S. Rabinowitz, and I. M. Ward, "The strain-rate, temperature and pressure dependence of yield of isotropic poly(methylmethacrylate) and poly(ethylene terephthalate)," *J. Mater. Sci.*, vol. 5, pp. 909–915, 1970.

[71] R. E. Robertson, "Theory for the plasticity of glassy polymers," *J. Chem. Phys.*, vol. 44, pp. 3950–3956, May 1966.

[72] M. G. Brereton, R. A. Duckett, S. H. Joseph, and P. J. Spence, "An interpretation of the yield behaviour of polymers in terms of correlated motion," *J. Mech. Phys. Solids*, vol. 25, pp. 127–136, April 1977.

[73] J. C. Bauwens, "Attempt to correlate the formation of free volume and the plastic deformation process in glassy polymers," *Polymer*, vol. 21, p. 699, 1980.

[74] K. C. Rusch and R. H. J. Beck, "Yielding behavior of glassy polymers. I. Free-volume model," *Journal of Macromolecular Science, Part B*, vol. 3, pp. 365–383, 1969.

[75] P. Bowden and S. Raha, "A molecular model for yield and flow in amorphous glassy polymers making use of a dislocation analogue," *Philosophical Magazine*, vol. 29, no. 1, pp. 149–166, 1974.

[76] Z. H. Stachurski, "Yield strength and anelastic limit of amorphous ductile polymers. I. Amorphous structure and deformation," *J. Mater. Sci.*, vol. 21, pp. 323–3236, 1986.

[77] R. N. Haward and G. Thackray, "The use of a mathematical model to describe isothermal stress-strain curves in glassy thermoplastics," *Proc. Royal. Soc*, vol. 302, p. 453, 1968.

[78] E. M. Arruda and M. C. Boyce, "A three-dimensional constitutive model for large stretch behaviour of rubber materials," *J. Mech. Phys. Solids*, vol. 41, pp. 389–412, 1993.

[79] P. D. Wu and E. Van der Giessen, "On improved network models for rubber elasticity and their applications to orientation hardening in glassy polymers," *J. Mech. Phys. Solids*, vol. 41, pp. 427–456, 1993.

[80] R. K. Goldberg and D. C. Stouffer, "Strain rate dependent analysis of a polymer matrix composite utilizing a micromechanics approach," *Journal of Composite Materials*, vol. 36, pp. 773–793, 2002.

[81] L. Zhu, A. Chattopadhyay, and R. K. Goldberg, "Nonlinear transient response of strain rate dependent composite laminated plates using multiscale simulation," *Int. J. Solids Structures*, vol. 43, pp. 2602–2630, 2006.

[82] S. R. Bodner and Y. Partom, "Constitutive equations for elastic-viscoplastic

strain-hardening materials," *Journal of Applied Mechanics*, vol. 42, pp. 385–389, 1975.

[83] I. Narisawa and A. F. Yee, *Structure and properties of polymers, material science and technology: A comprehensive treatment*, vol. 12. Weinheim: VCH Verlag, 1993.

[84] C. C. Chau and J. C. M. Li, "Slip processes in the deformation of polystyrene," *J. Mater. Sci.*, vol. 11, pp. 434–444, 1976.

[85] A. S. Argon, R. E. Cohen, and T. M. Mower, "Mechanisms of toughening brittle polymers," *Materials Science and Engineering A*, vol. 176, pp. 79–90, March 1994.

[86] R. N. Haward, ed., *The physics of glassy polymer*. London: Applied Science Publishers Ltd., 1973.

[87] N. Haward, R, *Critical stages in the fracture of an organic glass*. London: John Wiley, 1972.

[88] A. S. Argon, J. G. Hannoosh, and M. M. Salama, "Initiation and growth of crazes in glassy polymers," *Fracture*, vol. 1, pp. 445–470, 1977.

[89] A. M. Donald and E. J. Kramer, "The entanglement network and craze micromechanics in glassy polymers," *J. Polymer Sci.*, vol. 20, pp. 1129–1141, 1982.

[90] H. H. Kramer, "Microscopic and molecular fundamentals of crazing," *Advances in Polymer Science*, vol. 52, pp. 1–56, 1983.

[91] H. H. Kramer and L. L. Berger, "Craze growth and fracture," *Adv. Polym. Sc.*, vol. 91, pp. 1–68, 1990.

[92] W. Doll, "Optical inference measurements and fracture mechanics analysis of crack tip craze tip crack zones," *Adv. Polym. Sc.*, vol. 52, pp. 105–168, 1983.

[93] J. Rottler and M. O. Robbins, "Growth, microstructure and failure of crazes in glassy polymers," *Phys. Rev. E*, vol. 64, no. 011801, 2003.

[94] R. N. Haward and R. J. Young, *The physics of glassy polymer*. London: Chapman and Hall, 2nd ed., 1997.

[95] A. S. Argon and J. G. Hannoosh, "Initiation of crazes in polystyrene," *Philosophical Magazine*, vol. 36, pp. 1195–1216, 1977.

[96] A. S. Argon and M. M. Salama, "Growth of crazes in glassy polymer," *Philosophical Magazine*, vol. 36, no. 5, pp. 1217–1234, 1977.

[97] A. J. Kinloch and R. J. Young, *Fracture behavior of polymers*. London: Elsevier Applied Science, 1983.

[98] J. G. Williams, *Fracture mechanics of polymers*. Chichester: Ellis Horwood, 1984.

[99] R. Estevez, M. G. A. Tijssens, and E. Van der Giessen, "Modeling of the competition between shear yielding and crazing in glassy polymers," *J. Mech. Phys. Solids*, vol. 48, pp. 2585–2617, 2000.

[100] P. Krawczak and J. Pabiot, "Fracture mechanics applied to glass fiber/epoxy matrix interface charaterization," *Journal of Composite Materials*, vol. 29, no. 17, pp. 2230–2253, 1995.

[101] L. E. Asp, L. A. Berglund, and R. Talreja, "A criterion for crack initiation in glassy polymers subjected to a composite-like stress state," *Composites Science and Technology*, vol. 56, pp. 1291–1301, 1996.

[102] S. S. Sternstein and L. Ongchin, "Yield criteria for plastic deformation of glassy high polymers in general stress fields," *Polymer Preprints*, vol. 10, pp. 1117–1124, 1969.

[103] R. J. Oxborough and P. B. Bowden, "A general critical-strain criterion for crazing in amorphous polymers," *Philosophical Magazine*, vol. 28, pp. 547–559, 1973.

[104] J. Lai and E. V. d. Giessen, "A numerical study of crack-tip plasticity in glassy polymers," *Mechanics of Materials*, vol. 25, pp. 183–197, 1997.

[105] S. Basu, D. Mahajan, and E. Van der Giessen, "Micromechanics of the growth and failure of a craze fibril in glassy polymers," *Polymer*, vol. 46, pp. 7504–7518, 2005.

[106] D. C. Drucker and W. Prager, "Soil mechanics and plastic analysis or limit design," *Quarterly of Applied Mathematics*, vol. 10, no. 2, pp. 157–165, 1952.

[107] S. R. Bodner, *Unified plasticity for engineering applications.* New York: Kluwer Academic/Plenum, 2002.

[108] A. Needleman, "Dynamic shear band development in plane strain," *J. App. Mech.*, vol. 56, pp. 1–9, 1989.

[109] T. Belytschko, R. L. Chiapetta, and H. D. Bartel, "Efficient large scale non-linear transient analysis by finite elements.," *Int. J. Numer. Meths. Engrg.*, vol. 10, pp. 579–596, 1976.

[110] D. Peirce, C. F. Shih, and A. Needleman, "A tangent modulus method for rate dependent solids," *Comput. Structures*, vol. 18, pp. 875–887, 1984.

[111] A. E. Green and W. Zerna, *Theoretical elasticity*. Oxford: Clarendon Press, 1954.

[112] A. Needleman and V. Tvergaard, *Finite elements-special problems in solid mechanics*, vol. 5, ch. Finite element analysis of localization of plasticity, pp. 94–157. Englewood Cliffs, NJ: Prentice Hall, 1983.

[113] N. M. Newmark, "A method of computation for structural dynamics," *J. Engineering Mechanics Division. ASCE*, vol. 85, pp. 67–94, July 1959.

[114] T. J. R. Hughes and T. Belytschko, "A precis of developments in computational methods for transient analysis," *ASME, Transactions, J. App. Mech.*, vol. 50, no. 4b, pp. 1033–1041, 1983.

[115] J. C. Simo, N. Tarnow, and K. K. Wong, "Exact energy-momentum conserving algorithmsand symplectic schemes for nonlinear dynamics," *Comp. Meth. Appl. Mech.*, vol. 100, pp. 63–116, 1992.

[116] C. Kane, J. E. Marsden, M. Ortiz, and M. West, "Variational integrators and the newmark algorithm for conservative and dissipative mechanical systems," *Int. J. Numer. Meths. Engrg.*, vol. 49, pp. 1295–1325, 2000.

[117] A. Needleman and V. Tvergaard, "Numerical modeling of the ductile-brittle transition," *Int. J. Frac.*, vol. 101, pp. 73–97, 2000.

[118] A. A. Benzerga, V. Tvergaard, and A. Needleman, "Size effects in the Charpy V-notch test," *Int. J. Frac.*, vol. 116, pp. 275–296, 2002.

[119] A. Needleman, "An analysis of intersonic crack growth under shear loading," *ASME J. Appl. Mech.*, vol. 66, pp. 847–857, 1999.

[120] R. O. Krieg and S. W. Key, "Transient shell response by numerical time integration," *Int. J. Numer. Meths. Engrg.*, vol. 7, pp. 273–286, 1973.

[121] P. D. Wu and E. Van der Giessen, "Computational aspects of localized deformations in amorphous glassy polymers," *Eur. J. Mech.*, vol. 15, pp. 799–823, 1996.

[122] J. M. Powers and R. M. Caddell, "The macroscopic volume changes of selected polymers subjected to uniform tensile deformation," *Polymer Engineering and Science*, vol. 12, pp. 432–436, November 1972.

[123] Z. H. Stachurski, "Deformation mechanisms and yield strength in amorphous polymers," *Progress in Polymer Science*, vol. 22, pp. 407–474, 1997.

[124] P. D. Wu and E. Van der Giessen, "Analysis of shear band propagation in amorphous glassy polymers," *Int. J. Solids Structures*, vol. 31, pp. 1493–1517, 1994.

[125] T. Belytschko and B. J. Hsieh, "Nonlinear transient finite element analysis with convected coordinates," *Int. J. Numer. Meths. Engrg.*, vol. 7, pp. 255–271, 1973.

[126] J. Lemaitre and J. L. Chaboche, "A nonlinear model of creep-fatigue damage cumulation and interaction," in *IUTAM Symp. of Mechanics of Visco-elastic Media and Bodies*, (Gothenburg, Sweden), p. 1974, Springer-verlag, 1974.

[127] S. Li and S. Ghosh, "Debonding in composite microstructureswith morphological variations," *International Journal of Computational Methods*, vol. 1, no. 1, pp. 121–149, 2004.

[128] H. Huang and R. Talreja, "Numerical simulation of matrix micro-cracking in

short fiber reinforced polymer composites: Initiation and propagation," *Composites Science and Technology*, vol. 66, no. 15, pp. 2743–2757, 2006.

[129] C. Gonzalez and J. LLorca, "Multiscale modeling of fracture in fiber-reinforced composites," *Acta Materialia*, vol. 54, pp. 4171–4181, September 2006.

[130] R. P. Kambour, "A review of crazing and fracture in thermoplastics," *Journal of Polymer Science*, vol. 7, pp. 1–154, 1973.

[131] M. G. A. Tijssens, E. Giessen, and L. J. Sluys, "Modeling of crazing using a cohesive surface methodology," *Mechanics of Materials*, vol. 32, pp. 19–35, 2000.

[132] W. G. Knauss, "Time dependent fracture and cohesive zones," *J. Eng. Mat. Tech.*, vol. 115, pp. 262–267, 1993.

[133] S. A. Telenkov, "Infrared imaging of stress crazing in rubber modified polystyrene," *Polymer Engineering Science*, vol. 38, pp. 385–391, 1998.

[134] W. E. Warren, "On the accuracy of the calculated stress field arround a craze," *Polymer Engineering Science*, vol. 29, pp. 426–431, 1989.

[135] A. A. Benzerga, "Micromechanics of coalescence in ductile fracture," *Journal of the Mechanics and Physics of Solids*, vol. 50, pp. 1331–1362, 2002.

[136] S. Socrate, M. C. Boyce, and A. Lazzeri, "A micromechanical model for multiple crazing in high impact polystyrene," *Mechanics of Material*, vol. 33, pp. 155–175, 2001.

[137] A. A. Benzerga, J. Besson, and A. Pineau, "Anisotropic ductile fracture: Part II: Theory," *Acta Materialia*, vol. 52, pp. 4639–4650, 2004.

[138] R. P. Kambour, "Stress strain behavior of the craze," *Polymer Engineering and Science*, vol. 8, no. 4, pp. 281–289, 1968.

[139] B. Z. Jang and Y. K. Lieu, "Fracture behavior of short fiber reinforcedthermoplastics i. crack propagation mode and fracture toughness.," *Journal of Applied Polymer Science*, vol. 30, no. 9, pp. 3925–3942, 1985.

[140] N. Sato, T. Kurauchi, and S. Sato, "Microfailure behaviour of randomly dispersed short fibre reinforced thermoplastic composites obtained by direct SEM observation," *J. Mater. Sci.*, vol. 26, pp. 3891–3898, 1991.

[141] C. A. Wood and W. L. Bradley, "Determination of the effect of seawater on the interfacial strength of an interlayer e-glass/graphite/epoxy composite by in situ observation of transverse cracking in an environmental SEM," *Composites Science and Technology*, vol. 57, pp. 1033–1043, 1997.

[142] J. Lindhagen and L. Berglund, "Microscopical damage mechanisms in glass fiber reinforced polypropylene microscopical damage mechanisms in glassfiber reinforced polypropylene," *J. Appl. Polym. Sci.*, vol. 69, no. 7, pp. 1319–1327, 1998.

[143] N. Vejen and R. Pyrz, "Transverse crack growth in glass/epoxy composites with exactly positioned long fibres. Part I: experimental," *Composites Part B: Engineering*, vol. 32, pp. 557–564, October 2001.

[144] L. E. Govaert, H. J. Schellens, H. J. M. Thomassen, R. J. M. Smit, L. Terzoli, and T. Peijs, "A micromechanical approach to time-dependent failure in off-axis loaded polymer composites," *Composites Part A: Applied Science and Manufacturing,*, vol. 32, pp. 1697–1711, December 2001.

[145] W. Lee, "Crack propagation within corrugated interfaces inceramic laminates," *Scripta Materialia*, vol. 47, pp. 295–300, 2002.

[146] G. D. Seidel, D. H. Allen, K. L. E. Helms, and S. E. Groves, "A model for predicting the evolution of damage in viscoelastic particle-reinforced composites," *Mechanics of Materials*, vol. 37, pp. 163–178, 2005.

[147] Y. Zhang, Z. Xia, and F. Ellyin, "Nonlinear viscoelastic micromechanical analysisof fibre-reinforced polymer laminates with damage evolution," *Int. J. Solids Structures*, vol. 42, pp. 591–604, 2005.

[148] S. Sirivedin, D. N. Fenner, R. B. Nath, and C. Galiotis, "Viscoplastic finite element analysis of matrix crack propagationin model continuous-carbon fibre/epoxy composites," *Composites: Part A*, vol. 37, pp. 1922–1935, November 2006.

[149] A. Needleman, "Micromechanical modelling of interfacial decohesion," *Ultramicroscopy*, vol. 40, pp. 203–214, March 1992.

[150] S. Li and S. Ghosh, "Debonding in composite microstructures with morphological variations," *Int. J. Comput. Meth.*, vol. 1, no. 1, pp. 121–149, 2004.

[151] A. Caporale, R. Luciano, and E. Sacco, "Micromechanical analysis of interfacial debonding in unidirectional fiber-reinforced composites," *Computers and Structures*, vol. 84, pp. 2200–2211, 2006.

[152] M. Costa, S. Almeida, and M. Rezende, "The influence of porosity on the interlaminar shear strength of carbon/epoxy and carbon/bismaleimide fabric laminates," *Comp. Sci. Tech.*, vol. 61, pp. 2101–2108, 2001.

[153] L. E. Asp, L. A. Berglund, and R. Talreja, "Prediction of matrix-initiated transverse failure in polymer composites," *Composites Science and Technology*, vol. 56, pp. 1089–1097, 1996.

APPENDIX A

The rate tangent method, to update constitutive equation, summarized in the main section follows the approach proposed by Pierce et al. [110]. In detail formulations corresponding to the DPB and the macromolecular models are described in this appendix. The formulation here based on the forward gradient estimation of effective plastic strain rate $\dot{\bar{\epsilon}}$, which is obtained through eq. 2.33

Rate Tangent Formulation of the DPB model

The forward gradient estimate of effective strain rate at current time is obtained as:

$$\dot{\bar{\epsilon}} = \dot{\bar{\epsilon}}\,(t) + \theta \triangle t \left(\frac{\partial \dot{\bar{\epsilon}}}{\partial \bar{\sigma}} \dot{\bar{\sigma}} + \frac{\partial \dot{\bar{\epsilon}}}{\partial Z} \dot{Z} \right) \tag{A.1}$$

with

$$\frac{\partial \dot{\bar{\epsilon}}}{\partial \bar{\sigma}} = \frac{n}{\bar{\sigma}} \left(\frac{Z}{\bar{\sigma}} \right)^{2n} \dot{\bar{\epsilon}}, \frac{\partial \dot{\bar{\epsilon}}}{\partial Z} = -\frac{n}{Z} \left(\frac{Z}{\bar{\sigma}} \right)^{2n} \dot{\bar{\epsilon}} \tag{A.2}$$

and $\dot{\bar{\sigma}}$ is obtained from the consistency condition by obtaining the time derivative of the plastic potential function equal to zero.

$$\dot{\phi} = 0 = \frac{\partial \phi}{\partial \boldsymbol{\sigma}} \overset{\nabla}{\boldsymbol{\sigma}} + \frac{\partial \phi}{\partial \bar{\sigma}} \dot{\bar{\sigma}} + \frac{\partial \phi}{\partial \gamma} \dot{\gamma} \tag{A.3}$$

that yields

$$\dot{\bar{\sigma}} = -\frac{\mathbf{p} : \overset{\nabla}{\boldsymbol{\sigma}} + \frac{\partial \phi}{\partial \gamma} \dot{\gamma}}{\partial \phi / \partial \bar{\sigma}} \tag{A.4}$$

where $\mathbf{p} : \overset{\nabla}{\boldsymbol{\sigma}}$ is obtained from equation 2.35. Now using equation 2.22, 2.23, 2.35 and A.4, into equation A.1 we obtain,

$$\dot{\bar{\epsilon}}_{t+\triangle t} = \frac{\dot{\bar{\epsilon}}_t}{1+\xi} + \frac{\xi}{1+\xi} \frac{\mathbf{PD}}{H} \tag{A.5}$$

, where

$$H = \mathbf{p} : \mathbf{L}_{\mathrm{e}} : \mathbf{p} - \frac{\partial \phi}{\partial \gamma} q'(\gamma_1 - \gamma) - \left(\frac{\partial \dot{\bar{\epsilon}}}{\partial \bar{\sigma}}\right)^{-1} \frac{\partial \dot{\bar{\epsilon}}}{\partial Z} q(Z_1 - Z) \tag{A.6}$$

and

$$\xi = \theta \triangle t \frac{\partial \dot{\bar{\epsilon}}}{\partial \bar{\sigma}} H \tag{A.7}$$

Finally, the constitutive equation took the form of equation 2.36, where $\mathbf{L}_{\tan}$ and $\dot{\mathbf{Q}}$ are obtained from equation 2.37.

Rate Tangent Formulation of the macromolecular model

The Taylor-series-Expansion of the functional form of equation 2.30 for the macromolecular model, given by

$$\dot{\bar{\epsilon}} = \dot{\bar{\epsilon}}(t) + \theta \triangle t \left(\frac{\partial \dot{\bar{\epsilon}}}{\partial \sigma_{\mathrm{e}}}\ \dot{\sigma_{\mathrm{e}}}\right) \tag{A.8}$$

,where

$$\frac{\partial \dot{\bar{\epsilon}}}{\partial \sigma_{\mathrm{e}}} = \frac{5}{6} \frac{A\left(s - \alpha \sigma_{kk}\right)}{T} \left(\frac{\sigma_{\mathrm{e}}}{s - \alpha \sigma_{kk}}\right)^{5/6} \frac{\dot{\bar{\epsilon}}}{\sigma_{\mathrm{e}}} \tag{A.9}$$

$\dot{\sigma_{\mathrm{e}}}$ is obtained from the rate form of equation 2.25, given by

$$\dot{\sigma_{\mathrm{e}}} = \frac{3}{2\sigma_{\mathrm{e}}} \overset{\nabla}{\boldsymbol{\sigma}}{}'_{\mathrm{d}} : \boldsymbol{\sigma}'_{\mathrm{d}} = \frac{3}{2\sigma_{\mathrm{e}}} \left[\overset{\nabla}{\boldsymbol{\sigma}}{}' - \overset{\nabla}{\mathbf{b}}{}'\right] : \boldsymbol{\sigma}'_{\mathrm{d}} \tag{A.10}$$

where $\overset{\nabla}{\mathbf{b}}{}'$ is the deviatoric part of the back stress rate, $\overset{\nabla}{\mathbf{b}}$. The rate form of the back stress developed by [121], expressed in terms of Jaumann rate of back stress $\overset{\nabla}{\mathbf{b}} = \dot{\mathbf{b}} - \mathbf{W}\mathbf{b} + \mathbf{b}\mathbf{W}$, which is similar to the rate form of the constitutive equation for the Cauchy stress in equation 2.14, has the following form

$$\overset{\nabla}{\mathbf{b}} = \mathbf{R}\mathbf{D} \tag{A.11}$$

where $\mathbf{R}$ is the fourth order back stress moduli tensor, dependant on particular back stress model. For eight-chain model back stress moduli $\mathbf{R}_{8-\mathrm{ch}}$ is obtained using the

equations 2.26 and 2.29, given as

$$R^{ijkl}_{8-\mathrm{ch}} = \frac{1}{3}C^R\sqrt{N}\left[\left(\frac{\xi_c}{\sqrt{N}} - \frac{\Im_c}{\lambda_c}\right)\frac{B^{ij}B^{kl}}{B^{mm}} + \frac{\Im_c}{\lambda_c}\left(g^{ik}B^{jl} + B^{ik}g^{jl}\right)\right] \tag{A.12}$$

where, $\Im_c$ and ξ_c are shorthand notation for

$$\Im_c \equiv \mathcal{L}^{-1}\left(\frac{\lambda_c}{\sqrt{N}}\right), \xi_c \equiv \frac{d}{dx}\mathcal{L}^{-1}\left(\frac{\lambda_c}{\sqrt{N}}\right) = \frac{\Im_c^2}{1 - \Im_c^2\ \mathrm{csch}^2\Im_c} \tag{A.13}$$

For the back stress moduli classical non gaussian three-chain rubber elasticity model is utilized. Using the equations 2.26 and 2.28 the 3-chain back stress modulus tensor is given by

$$R^{ijkl}_{3-\mathrm{ch}} = \begin{cases} \frac{1}{3}C^R\sqrt{N}\lambda_i^2\left(\frac{\xi_i}{\sqrt{N}} + \frac{\Im_i}{\lambda_i}\right)g^{ik}g^{jl} & \text{if } \lambda_i = \lambda_j \\ \frac{1}{3}C^R\sqrt{N}\frac{\lambda_i^2+\lambda_j^2}{\lambda_i^2-\lambda_j^2}(\lambda_i\Im_i - \lambda_j\Im_j)g^{ik}g^{jl} & \text{if } \lambda_i \neq \lambda_j \end{cases} \tag{A.14}$$

where, $\Im_i$ and ξ_i are shorthand notations for

$$\Im_i \equiv \mathcal{L}^{-1}\left(\frac{\lambda_i}{\sqrt{N}}\right), \xi_i \equiv \frac{d}{dx}\mathcal{L}^{-1}\left(\frac{\lambda_i}{\sqrt{N}}\right) = \frac{\Im_i^2}{1 - \Im_i^2\mathrm{csch}^2\Im_i} \tag{A.15}$$

The Langevin inverse function is computed by using the three term Taylor expansion $\mathcal{L}^{-1}(\zeta) = 3\zeta + \frac{9}{5}\zeta^3 + \frac{297}{175}\zeta^5 + \frac{1539}{875}\zeta^7 + ...$ By combining 3-chain and 8-chain moduli linearly, back stress moduli for full network model is given as [121],

$$\mathbf{R} = (1-\rho)\,\mathbf{R}_{3-\mathrm{ch}} + \rho\mathbf{R}_{8-\mathrm{ch}} \tag{A.16}$$

After substituting the rate form of back stress and tedious algebraic manipulation the equation A.10 took the following form

$$\dot{\sigma}_{\mathrm{e}} = \frac{1}{1+\xi}\left[\frac{3\mu_{\mathrm{s}}}{\sigma_{\mathrm{e}}}\boldsymbol{\sigma}'_{\mathrm{d}} : \mathbf{D} - H\dot{\bar{\epsilon}}\right] \tag{A.17}$$

where ξ and H is defined as

$$\xi = \theta \triangle t \frac{\partial \dot{\bar{\epsilon}}}{\partial \sigma_{\mathrm{e}}} H, \;\; H = 3\mu_{\mathrm{s}} + \frac{9}{4} \frac{1}{{\sigma_{\mathrm{e}}}^2} \; {\boldsymbol{\sigma}'}_{\mathrm{d}} : \mathbf{R}' : {\boldsymbol{\sigma}'}_{\mathrm{d}} \tag{A.18}$$

where μ_{s} is elastic shear modulus, $\mathbf{R}'$ is the deviatoric part of the back stress modulus tensor $\mathbf{R}$. Finally, the macromolecular constitutive equation and $\dot{\bar{\epsilon}}$ took the form of equations 2.36 and A.5, respectively.

Rate Tangent Formulation of the Reference Craze Model

The Taylor-series-Expansion of the functional form of equation (3.7)for the craze growth model, given by

$$\dot{\bar{\epsilon}} = \dot{\bar{\epsilon}}(t) + \theta \triangle t \left(\frac{\partial \dot{\bar{\epsilon}}}{\partial \sigma_{\mathrm{I}}} \dot{\sigma}_{\mathrm{I}} \right) \tag{A.19}$$

with

$$\frac{\partial \dot{\bar{\epsilon}}}{\partial \sigma_{\mathrm{I}}} = \frac{\dot{\epsilon}_0^{cr}}{m \sigma_{\mathrm{I}}} \left\{ \frac{\sigma_{\mathrm{I}}}{s_{cr}} \right\}^{\frac{1}{m}} \tag{A.20}$$

from the craze initiation criterion

$$\hbar = \sigma_{\mathrm{I}} - \sigma_c \tag{A.21}$$

Now we obtained $\dot{\sigma}_{\mathrm{I}}$ from the consistency condition by taking time derivative of craze potential function $\hbar$ equal to zero.

$$\dot{\hbar} = 0 = \frac{\partial \hbar}{\partial \boldsymbol{\sigma}} \overset{\nabla}{\boldsymbol{\sigma}} + \frac{\partial \hbar}{\partial \sigma_{\mathrm{I}}} \dot{\sigma}_{\mathrm{I}} \tag{A.22}$$

that yields

$$\dot{\sigma}_{\mathrm{I}} = \mathbf{p} : \overset{\nabla}{\boldsymbol{\sigma}} \tag{A.23}$$

where $\mathbf{p} = \hat{\mathbf{e}}_{\mathbf{1}} \otimes \hat{\mathbf{e}}_{\mathbf{1}}$ is direction of maximum principal stress. Substituting the Jaumann derivative of Cauchy stress, $\overset{\nabla}{\boldsymbol{\sigma}} = \mathbf{L}_e : \mathbf{D} - \mathbf{P}\dot{\epsilon}$, in equation(A.23) and after algebraic

manipulation of equation(3.7), we obtained following form craze strain rate.

$$\dot{\bar{\epsilon}}^{cr}_{t+\triangle t} = \frac{\dot{\bar{\epsilon}}^{cr}_{t}}{1+\xi} + \frac{\xi}{1+\xi}\frac{\mathbf{P}:\mathbf{D}}{H} \tag{A.24}$$

where

$$H = \mathbf{p}:\mathbf{L}_e:\mathbf{p}; \quad \xi = \theta\triangle t\frac{\partial\dot{\bar{\epsilon}}}{\partial\bar{\sigma}}H \tag{A.25}$$

Finally viscoplastic constitutive equation took the form of equation 3.16, where $\mathbf{L}_{tan}$ and $\dot{\mathbf{Q}}$ are obtained from equation 3.17.

Rate Tangent Formulation of the New Crazing Model

The Taylor-series-Expansion of the functional form of equation (3.12)for the mechanism based craze growth model is same as the reference craze model. Rate of change of maximum principal stress $\dot{\sigma}_I$ is obtained by taking rate of change of craze potential function to be zero, given by

$$\dot{\Phi}_c = 0 = \frac{\partial\Phi_c}{\partial\boldsymbol{\sigma}}\overset{\nabla}{\boldsymbol{\sigma}} + \frac{\partial\Phi_c}{\partial\chi}\dot{\chi} + \frac{\partial\Phi_c}{\partial\bar{\sigma}}\dot{\bar{\sigma}} \tag{A.26}$$

yields

$$\dot{\bar{\sigma}} = -\frac{\frac{\partial\Phi_c}{\partial\chi}\dot{\chi} + \frac{\partial\Phi_c}{\partial\boldsymbol{\sigma}}\overset{\nabla}{\boldsymbol{\sigma}}}{\frac{\partial\Phi_c}{\partial\bar{\sigma}}} \tag{A.27}$$

After following the same procedure described before we obtained same form of craze strain rate (equation A.24) at current time and ξ. with

$$H = \mathbf{p}:\mathbf{L}_e:\mathbf{p} - \frac{\partial\Phi_c}{\partial\chi}C\left(\chi_1 - \chi\right) \tag{A.28}$$

and

$$\xi = \theta\triangle t\frac{\partial\dot{\bar{\epsilon}}}{\partial\bar{\sigma}}H\left(\frac{\partial\Phi_c}{\partial\bar{\sigma}}\right)^{-1} \tag{A.29}$$

Considering constant damage or $\chi = Constant$ Gearing-Anand's craze model can be recovered.

VITA

Khairul Chowdhury was born in Bangladesh. He received his B.S. in mechanical engineering from Bangladesh University of Engineering and Technology in 1999. He enrolled in the graduate program in engineering science and mechanics at The University of Alabama in the fall of 2000 and studied under the direction of Dr. John Jackson. He received a M.S. degree in engineering science and mechanics in December 2002. He earned his Ph.D. in aerospace engineering from Texas A&M University in May 2007. His research interests include polymer science, non-linear finite element methods, multiscale modeling, fracture mechanics, and viscoplasticity. Mr. Chowdhury can be reached at his office address: Department of Aerospace Engineering , H.R. Bright Building, Rm. 701, Ross Street - TAMU 3141, College Station, TX 77843.

The typist for this thesis was Khairul Chowdhury.